

**DESIGN OF A SPOKE TYPE PMSM WITH SMC STATOR CORE
FOR TRACTION APPLICATIONS**

Mohanraj Muthusamy

A Thesis

In the Department

of

Electrical and Computer Engineering

Presented in Partial Fulfillment of the Requirements

For the Degree of

Doctor of Philosophy (Electrical and Computer Engineering) at

Concordia University

Montréal, Québec, Canada

July 2023

© Mohanraj Muthusamy, 2023

CONCORDIA UNIVERSITY
SCHOOL OF GRADUATE STUDIES

This is to certify that the thesis prepared

By: Mohanraj Muthusamy

Entitled: Design of a Spoke Type PMSM with SMC Stator Core for Traction Applications

and submitted in partial fulfillment of the requirements for the degree of

Doctor of Philosophy (Electrical and Computer Engineering)

complies with the regulations of the University and meets the accepted standards with respect to originality and quality.

Signed by the final examining committee:

_____	Chair
Dr. Carol Fung	
_____	External Examiner
Dr. Joseph Olorunfemi Ojo	
_____	External to program
Dr. Ursula Eicker	
_____	Examiner
Dr. Chunyan Lai	
_____	Examiner
Dr. Luiz. A.C. Lopes	
_____	Thesis Supervisor
Dr. Pragasen Pillay	

Approved by: _____

Dr. Jun Cai, Graduate Program Director

July 7, 2023

Dr. Mourad Debbabi, Dean,
Gina Cody School of Engineering and Computer Science

ABSTRACT

Design of a Spoke Type PMSM with SMC Stator Core for Traction Applications

Mohanraj Muthusamy, Ph.D.

Concordia University, 2023

The requirement of a clean energy environment has created the need for electric vehicles in the automotive industry. Electrical machines are the most vital component in traction applications as they provide electromechanical energy conversions. Traction applications require motor drive systems that can operate with high torque and high-power densities with reduced maintenance costs and losses. Since the 20th century, induction machines (IMs) have been a popular choice owing to ruggedness and reduced cost (absence of commutators and slip rings). But it is less efficient when compared to the other kinds of AC machines such as the permanent magnet synchronous machines (PMSM). In the IM, a part of the rotor flux is created by the currents flowing in the rotor conductors, made up of either aluminium or copper bars. But in PMSMs, the rotor flux is created by the permanent magnets (PMs) mounted on the rotor structure. The absence of the rotor cage reduces the mass of the PMSMs, resulting in lower inertia and faster torque response when compared to IMs. Also, the lack of rotor currents eliminates the rotor losses leading to higher efficiency.

In PMSM machines, a realistic value of the copper fill factor ranges between 35% to 40% with the laminated stator for air cooling. A higher current rating is required for a low voltage machine to meet the torque and power specifications. Higher current rating machines usually utilize parallel windings to reduce the number of strands. With the parallel winding pattern, the turns per coil will be multiplied with the number of parallel paths reducing the wire diameter and increasing the copper fill factor. The high copper fill factor increases the contact between the wires, and this allows for better heat transfer from the conductors. Therefore, the temperature of the windings is reduced, the resistance decreases and also the copper losses.

This thesis compares the performance of the SMC and laminated steel-based design for a radial flux outer rotor permanent magnet synchronous machine (PMSM) and its impact on the core loss at higher frequencies. Also, this thesis examines two different winding patterns (distributed and fractional) for field weakening operation with a surface mount outer rotor PMSM.

This thesis presents a cold spray additive manufacturing technique to spray the NdFeB magnet on to the rotor laminations. With this technique, magnet shaping is more feasible. The magnets are sprayed in a cobra shape to obtain better electromagnetic performances. This cold spray technique is developed at NRC Canada which makes the magnet shaping inexpensive.

This thesis presents a modified spoke type rotor that significantly reduces the torque ripple, back electromagnetic force (EMF) harmonics, and cogging torque from conventional spoke type designs. The effectiveness of the modified spoke type rotor is proved with state-of-the-art designs such as Toyota Prius and Honda Accord motors. Three different SMC materials are compared for the same machine specification. The tooth body length of SMC stator is varied from 36 mm to 56 mm to analyze the performance of the motor.

Along with the modified spoke type rotor focus is on a segmented soft magnetic composite (SMC) stator core to improve the copper fill factor and improve torque density by reducing the tooth length to allow additional space for the end windings within the stack length of the motor. A comparison between the laminated steel stator and SMC stator is presented. The laminated motor is capable of producing higher torque than the SMC motor when both machines are designed to operate with the same temperature, though the torque density in terms of volume of SMC motor is higher than the laminated motor. In all cases, the machines are designed to fit into the same frame. A cost comparison is presented between the SMC and laminated motors, which shows that SMC motors can be manufactured at lower cost than laminated motors. Also, the SMC stator includes axial magnet segmentation, flux weakening capability, thermal analysis, stator stress analysis due to electromagnetic forces, and a rotor mechanical stress analysis.

Finally, this thesis aims to present the development of SMC teeth considering manufacturing and assembling challenges. It briefly presents the SMC tooth manufacturing including the heat treatment. Also, it presents the rotor manufacturing with prototype pictures. Finally, it presents the experimental results for the SMC motor, along with the simulation results.

ACKNOWLEDGMENT

First and foremost, I would like to thank my supervisor ***Professor Pragasen Pillay*** for giving me a chance to pursue a PhD under his supervision. I am grateful for the opportunity to learn from someone as knowledgeable and experienced as you. Thanks a lot for your motivation, care, financial support, and recommendation letters. Thanks for being like an advisor, father, and mentor, at just the right moments. Also, I thank you for showing me the path of Yoga.

I would like to express my heartfelt gratitude to my mother, father, sister, brother-in-law, my little nephew ***Nikash***, and my beloved grandmother (Amichi) for their unwavering encouragement, support, and prayers.

In addition to my supervisor, I would like to extend my gratitude to the other members of my thesis committee: ***Dr. Chunyan Lai, Dr. Luiz A.C. Lopes, Dr. Ursula Eicker, and Dr. Joseph Olorunfemi Ojo*** for their encouragement, insightful feedback, and valuable time.

I express my heartfelt gratitude to ***Dr. Mathews Bobby*** and ***Dr. Akrem Mohamed Aljehaimi*** for their invaluable assistance in conducting the experiments.

I extend my sincere appreciation to all the members of the CRD project for their support in motor prototyping specially ***Dr. Maged Ibrahim, Dr. Fabrice Bernier, Dr. Jean-Michel Lamarre, and Dr. Serge Grenier***. Special thanks to ***Mr. James Hendershot*** for validating and prototyping the design.

It is my pleasure to acknowledge my PEER group colleagues: ***Bassam S. Abdel-Mageed, Ashutosh Patel, Sumeet Singh, Tamanwe Payarou, Yupeng Liu, Bigyan Basnet, Gayathri Tanuku, Dwaipayan Barman, Rajendra Thike, Amitkumar, Benoit Blanchard, Neetusha, Koteswara Rao, Solihah, Amir, Tolga, Talha, Nil Patel, Gael, Nazanin, Ying, Shiva, & Ahmad*** for their support and interactions during studies. Also, I thank my roommates for their support during both the good and the challenging times over the past four years.

I thank ***Dr. Sundaram, Dr. Vinod, Dr. Anand & Dr. Chelladurai*** for their recommendation letters and their great support. Also, I thank CEMPE members of PSG college of Technology: ***Jayaraam, Varun, Dinesh, Subash, Jayanthan, and Aravind*** for their support.

This research work is done as a part of the InnovÉÉ/NSERC CRD Project entitled "Novel permanent magnet motor topologies using advanced magnetic materials". This research work is done as part of the NSERC/Hydro-Quebec Senior Industrial Research Chair entitled "Design and Performance of Special Electrical Machines" held by Professor Pragasen Pillay at Concordia University, Montreal. This research is also partly funded by the NSERC Discovery Grant entitled "Novel Electric Machine Design Topologies for Electrified Transportation". I would like to acknowledge the support of the National Research Council of Canada (NRC).

CONTENTS

LIST OF FIGURES	xi
LIST OF TABLES	xxi
LIST OF ABBREVIATIONS	xxiv
LIST OF SYMBOLS	xxv
CHAPTER – 1	1
Introduction	1
1.1 Introduction	1
1.2 Different types of lamination material	5
1.3 Application of SMC in Electric Machine Design	7
1.4 Cold Spray Additive Manufacturing of Permanent Magnets.....	8
1.5 Objectives.....	12
1.6 Limitations:	12
1.7 Organization and outline of the dissertation	13
1.8 Original contributions in this dissertation	14
CHAPTER – 2	18
Design of an Outer Rotor with SMC Stator Core	18
2.1. Introduction to Outer Rotor PMSM for traction applications.....	18
2.2. Comparison of laminated steel and SMC Based design	20
2.3. Different Winding pattern for flux weakening.....	27
2.4. Conclusions	30
CHAPTER – 3	31
Benchmarking of State-Of-The-Art Traction Motors & Slot/Pole Selection for the Twizy Motor	31

3.1. Introduction to state-of-the-art traction motors	31
3.2 Commercial traction motors (Recent activities).....	31
3.3 Benchmarking of BMWi3 [4]	33
3.4 Benchmarking of 2005 Honda Accord [6].....	36
3.5 Analytical Design of Interior PMSMs	39
3.6 Stator dimension calculations	45
3.7 Initial designs for Twizy	48
3.7.1 2-D FEA of Higher Pole and Lower Pole configurations	48
3.7.2 Using BMW-i3 rotor for Twizy motor design using NdFeB ($B_r = 1.2$ T).....	50
3.7.3 Using BMW-i3 rotor for Twizy motor using coldspray magnet	51
3.7.4. 12 slot 8 pole with Commercial magnet and cold spray magnet.....	52
3.7.5. 12 slot 8 pole with modified stator tip thickness and rotor air barrier with commercial magnet and cold spray magnet	56
3.7.6. 12 slot 8 pole with closed slots and open slots	58
3.8 Conclusions	61
CHAPTER – 4	63
Design and Analysis of a Cobra Shaped Spoke Type Rotor using 3D-FEA.....	63
4.1. Introduction to Cobra Rotor Design.....	63
4.2. Electromagnetic design and slot pole selection of cobra shaped rotor	64
4.3. 2-D & 3-D analysis of 12-slot/10-pole with conventional & cobra rotors.....	70
4.4. Cobra type rotor with laminated stator and SMC stator.....	75
4.5. Mechanical stress analysis of cobra rotor	80
4.6. Optimal flux weakening of cobra rotor with smc stator.....	81
4.7. Optimizing cobra rotor design.....	81
4.8. Multiobjective optimization of cobra rotor	85

4.9. Conclusion.....	87
CHAPTER – 5.....	88
Design and Analysis of a Spoke Type Rotor with Commercial Magnets for the Twizy Car	88
5.1. Introduction to spoke type rotor.....	88
5.2. Comparison of spoke-type PMSM with different slot/pole configurations.	89
5.3. Air gap flux density in spoke type PMSM.....	96
5.4. Selection of rotor and stator parameters.....	97
5.5. Conventional and modified spoke type rotor	104
5.6. Design case for proving the effectiveness of the proposed rotor design.....	109
A. Case Study with Toyota Prius 2010 design	109
5.7. Conclusion.....	117
CHAPTER – 6.....	119
Design of a SMC Stator Core for Traction Applications for Twizy Car	119
6.1. Introduction to soft magnetic composite stator (SMC).....	119
6.2 SMC material properties and machine specification.....	121
6.3. SMC material comparison using 3D FEA method.....	122
6.4. Characterization of SMC-B material.....	126
6.5. Performance comparison of higher poles with SMC-B stator and laminated stator for the same specifications with same current density	128
6.6. Selection of tooth body length for the smc stator design	131
6.7. 3D FEA design of smc stator core and comparison with the laminated steel design for the required specifications.....	135
6.8. Loss analysis of SMC and laminated stator designs	141
A. Iron losses and copper loss.....	141
6.9. Thermal analysis of (Design-3) laminated and (Design-4) SMC stator design at the base speed.....	144

6.10. Electromagnetic and thermal analysis of design-5 (Laminated stator) with higher current	146
6.11. Wastage and cost comparison of laminated stator and SMC stator	151
6.12. Axial magnet segmentation, optimal flux weakening and mechanical stress analysis of SMC stator design	153
6.13. Conclusion.....	158
CHAPTER – 7	161
Prototype and Experiment	161
7.1. Introduction	161
7.2. Evolution of SMC tooth.....	162
7.3. SMC Stator fabrication.....	164
7.4. Experimental validation	168
7.5. Phase resistance and copper loss calculation	178
7.6. Current density calculation.....	179
7.7. Simulation Vs Measurement	181
7.8. Comparison of Simulation and measurement results with and without tooth tip:	183
7.9. Conclusion.....	186
CHAPTER – 8	188
Conclusions and Future Work	188
8.1. Conclusion.....	188
8.2. Future Work	194
References	196

LIST OF FIGURES

Fig. 1.1	Different types of electric vehicles	2
Fig. 1.2	Electric motor in an EV drivetrain	2
Fig. 1.3	Different types of PMSM motors (a) Surface mount (b) IPM with lateral magnets (c) Spoke type rotor (d) IPM with variable orientation magnets.	2
Fig. 1.4	Surface mount PMSM rotor	3
Fig. 1.5	Different parts of a surface mount PMSM (a) Inner rotor (b) Outer rotor or out runner	3
Fig. 1.6	Schematic structure of NOSS and SMC	7
Fig. 1.7	Recycling motors with SMC core and lamination core	8
Fig. 1.8	Typical hysteresis curve obtained during the magnetic measurements	10
Fig. 1.9	Hysteresis curve of coatings produced using two different powder mix ratios: Blue—90% MQFP-B, 10% H15, Red—75% MQFP-B, 25% H15	10
Fig. 1.10	(a) Comparison of the remanence obtained for NdFeB fabricated by different manufacturing processes [3] (b) Comparison of the ultimate tensile strength obtained for NdFeB fabricated by different manufacturing processes	11
Fig. 2.1	Outer Rotor Configuration (Assembly drawing)	20
Fig. 2.2 – 2.4	Outer Rotor PMSM (a) 24 Slot 22 pole (b) YZ plane (c) B-H Curve of Steel & SMC.	20
Fig. 2.5	Back EMF of M-36 26Ga design	23
Fig. 2.6	Back EMF of SMC design	23
Fig. 2.7	Torque Comparison of SMC and M-36 26Ga	24
Fig. 2.8	Air gap Flux Density Comparison	24
Fig. 2.9	N-T Efficiency map of laminated stator	25
Fig. 2.10	N-T Efficiency map of SMC stator	25
Fig. 2.11	N-T Iron loss of laminated stator	26
Fig. 2.12	N-T Iron loss of SMC stator	26
Fig. 2.13	N-T copper loss of laminated stator	26

Fig. 2.14	N-T copper loss of SMC stator	26
Fig. 2.15	Voltage and Current Loop of Outer Rotor PMSM with SMC	28
Fig. 2.16	Torque vs Speed vs Power ($\psi_m \approx L_d * I_s$ of (a)Design 1 (b)Design 2	29
Fig. 3.1 to 3.4	Commercial traction motors (3.1) BMW i3 (3.2) Toyota Prius (3.3) Nissan Leaf (3.4) Honda Accord	32
Fig. 3.5 to 3.9	BMWi3 motor rotor	33
Fig. 3.10	BMWi3 motor stator	33
Fig. 3.11	BMWi3 in MotorSolve	34
Fig. 3.12	BMWi3 stator end windings	34
Fig. 3.13	Magnet Torque and Reluctance Torque of BMWi3	35
Fig. 3.14	Speed Vs Torque & Speed Vs Power	35
Fig. 3.15	No load flux density of BMWi3 motor	35
Fig. 3.16	Full load flux density of BMWi3	35
Fig. 3.17	Stator disassembly showing daisy-chain lamination design	36
Fig. 3.18	Rotor with close view of bobbins	36
Fig. 3.19	Accord Model in MotorSolve	37
Fig. 3.20	Winding Model of Accord motor in Motor-CAD	37
Fig. 3.21	Honda Accord Model in MotorSolve (No load flux plot)	38
Fig. 3.22	Honda Accord Model in MotorSolve (Full load flux plot)	38
Fig. 3.33	Efficiency Map of Honda Accord	38
Fig. 3.24	Speed Vs Torque of Accord Motor	38
Fig. 3.25	Torque per unit rotor volume (TRV) and air-gap shear stress	40
Fig. 3.26	Slot geometry for the radial flux motor topology	46
Fig. 3.27	24 slot 20 pole with SMC	48
Fig. 3.28	Speed Vs Torque and Speed Vs Power	48
Fig. 3.29	Torque ripple of 24 slot 20 pole machine	48
Fig. 3.30	Back EMF of 24 slot 20 pole machine	48

Fig. 3.31	24 slot 20 pole with Laminated Steel	48
Fig. 3.32	Speed Vs Torque and Speed Vs Power	48
Fig. 3.33	Torque ripple of 24 slot 20 pole machine	48
Fig. 3.34	Back EMF of 24 slot 20 pole machine	48
Fig. 3.35	12 slot 8 pole with SMC	49
Fig. 3.36	Speed Vs Torque and Speed Vs Power	49
Fig. 3.37	Torque ripple of 12 slot 8 pole SMC machine	49
Fig. 3.38	Back EMF of 12 slot 8 pole SMC machine	49
Fig. 3.39	Twizy motor with BMW i3 rotor with 48 slots	50
Fig. 3.40	Twizy motor with BMW i3 rotor with 48 slots	50
Fig. 3.41	Twizy motor with BMW i3 rotor with 48 slots (thinner magnets)	50
Fig. 3.42	Full load flux density plot of Twizy motor with BMW i3 rotor with 48 slots	50
Fig. 3.43	Full load flux density plot of Twizy motor with BMW i3 rotor with 12 slots	50
Fig. 3.44	Full load flux density plot of Twizy motor with BMW i3 rotor with 48 slots (thinner magnets)	50
Fig. 3.45	Twizy motor with BMW i3 rotor with 48 slots	51
Fig. 3.46	Twizy motor with BMW i3 rotor with 12	51
Fig. 3.47	Twizy motor with BMW i3 rotor with 48 slots (thinner magnets)	51
Fig. 3.48	Scallop design with coldspray magnet	51
Fig. 3.49	Flux density plot of Scallop design with coldspray magnet	51
Fig. 3.50	Phase back EMF of Scallop design	52
Fig. 3.51	Torque angle curves of scallop design	52
Fig. 3.52	NT vs NP curve for scallop design	52
Fig. 3.53	12-slot/8-pole PMSM with laminated stator (NdFeB)	52
Fig. 3.55	12-slot/8-pole PMSM with SMC stator (NdFeB)	52
Fig. 3.56	12-slot/8-pole PMSM with SMC stator using cold spray magnet (Coldspray)	52
Fig. 3.57	Flux density of 12-slot/8-pole PMSM with laminated stator (NdFeB)	53

Fig. 3.58	Phase back EMF of 12-slot/8-pole PMSM with laminated stator (NdFeB)	53
Fig. 3.59	Torque of 12-slot/8-pole PMSM with laminated stator (NdFeB)	53
Fig. 3.60	NT and NP of 12-slot/8-pole PMSM with laminated stator (NdFeB)	53
Fig. 3.61	Flux density of 12-slot/8-pole PMSM with SMC stator (NdFeB)	53
Fig. 3.62	Phase back EMF of 12-slot/8-pole PMSM with SMC stator (NdFeB)	53
Fig. 3.63	Torque of 12-slot/8-pole PMSM with SMC stator (NdFeB)	53
Fig. 3.64	NT and NP of 12-slot/8-pole PMSM with SMC stator (NdFeB)	53
Fig. 3.65	Flux density of 12-slot/8-pole PMSM with laminated stator (NdFeB)	54
Fig. 3.66	Phase back EMF of 12-slot/8-pole PMSM with laminated stator (NdFeB)	54
Fig. 3.67	Torque of 12-slot/8-pole PMSM with laminated stator (NdFeB)	54
Fig. 3.68	NT and NP of 12-slot/8-pole PMSM with laminated stator (NdFeB)	54
Fig. 3.69	Modified 12 slot 8 pole designs with commercial and coldspray magnets	56
Fig. 3.70	Closed slot 12 slot 8 pole designs with commercial and coldspray magnets	58
Fig. 3.71	Open slot 12 slot 8 pole designs with commercial and coldspray magnets	58
Fig. 3.72	Open slot 12 slot 8 pole designs with commercial and coldspray magnets	59
Fig. 4.1	Laminated stator with 12 slots	65
Fig. 4.2	Flux density plots at full load (a) 12-slot/8-pole (b) 12-slot/10-pole	66
Fig. 4.3	Phase back EMF of 12-slot/8-pole & 12-slot/10-pole configurations	66
Fig. 4.4	Phase back EMF harmonics of 12-slot/8-pole & 12-slot/10-pole	66
Fig. 4.5	Cogging torque of 12-slot/8-pole & 12-slot/10-pole configurations	67
Fig. 4.6	Torque of 12-slot/8-pole & 12-slot/10-pole configurations	67
Fig. 4.7	(a & b) Conventional spoke type rotor (c) Full load flux density plot	70
Fig. 4.8	(a & b) Cobra spoke type rotor. (c) Full load flux density plot	71
Fig. 4.10	2-D- Phase back EMF of conventional rotor and cobra rotor	72
Fig. 4.11	3-D- Phase back EMF of conventional rotor and cobra rotor	72
Fig. 4.12	2-D- Electromagnetic torque of conventional rotor and cobra rotor	72
Fig. 4.13	3-D- Electromagnetic torque of conventional rotor and cobra rotor	73

Fig. 4.14	Phase back EMF harmonics of 2-D and 3-D designs.	74
Fig. 4.14	4. 14. B-H Curve of laminated Steel & SMC	76
Fig. 4.15	3-D printed dummy tooth using plastic	76
Fig. 4.16	(a) Laminated stator with end winding (b) SMC stator with encapsulated end winding	76
Fig. 4.17	(a) SMC stator with compacted end winding (b) Laminated stator with end winding	77
Fig. 4.18	Efficiency map of laminated stator with cobra rotor	79
Fig. 4.19	Efficiency map of SMC stator with cobra rotor	79
Fig. 4.20	Mechanical stress analysis of cobra rotor at 10000 rpm	80
Fig. 4.21	Speed Vs Torque & Power of SMC Stator	81
Fig. 4.22	Cobra rotor with various magnet thickness and rotor structure	82
Fig. 4.23	Flux density plot of various cobra rotor designs.	83
Fig. 4.24	Phase back EMF of various cobra rotor designs.	83
Fig. 4.25	Electromagnetic torque of various cobra rotor design	84
Fig. 4.26	Parameters for multiobjective optimization	85
Fig. 4.27	Optimization results	86
Fig. 5.1	Different Slot/Pole schematic (a) 12-slot/4-pole (b) 36-slot/6-pole (c) 12-slot/8-pole (d) 12-slot/10-pole.	90
Fig. 5.2	Flux density plot at full load (a) 12-slot/4-pole (b) 36-slot/6-pole (c) 12-slot/8-pole (d) 12-slot/10-pole.	90
Fig. 5.3	Open circuit flux density of different slot pole designs.	91
Fig. 5.4	Torque ripple of different slot/pole designs	92
Fig. 5.5	Phase back EMF of different slot/pole designs	92
Fig. 5.6	Cogging torque of different slot/pole designs	93
Fig. 5.7	Losses of different slot/pole designs	94
Fig. 5.8	Efficiency maps (a) 12-slot/4-pole (b) 36-slot/6-pole (c) 12-slot/8-pole (d) 12-slot/10-pole	95
Fig. 5.9	Turns per coil Vs Peak phase fundamental voltage from the drive.	97
Fig. 5.10	B-H curve of N30SH magnet grade at 100 deg C	98
Fig. 5.11	Magnetic field strength with respect to magnet thickness	98

Fig. 5.12	Speed Vs Torque and Speed Vs Power for different magnet thickness	99
Fig. 5.13	One rotor pole and one stator slot	100
Fig. 5.14	Rotor optimization results	101
Fig. 5.14	Stator sensitivity analysis results (average torque Vs torque ripple)	102
Fig. 5.15	Stator sensitivity analysis results (average torque Vs hysteresis loss)	103
Fig. 5.16	Laminated stator core	104
Fig. 5.17	Laminated stator teeth	104
Fig. 5.18	Rotor designs (a) Design-1 (b) Design-2 (c) Design-3	105
Fig. 5.19	Flux density (a) Design-1 (b) Design-2 (c) Design-3	105
Fig. 5.20	Open circuit air-gap flux density of design 1,2 and 3	106
Fig. 5.21	Back EMF of Designs-1,2 &3	106
Fig. 5.22	Phase back EMF harmonics of Designs-1, 2 and 3	107
Fig. 5.23	Cogging torque of design 1,2 and 3.	107
Fig. 5.24	Electromagnetic torque of Designs- 1,2 and 3	107
Fig. 5.25	Toyota Prius stator with proposed rotor design (a) Design-3_1(same magnet mass) (b) Design-3_2(increased magnet mass)	109
Fig. 5.26	(a) Toyota Prius stator with proposed rotor design (a) Design-3_1(same magnet mass) (b) Design-3_2(increased magnet mass)	111
Fig. 5.27	Electromagnetic torque of Toyota Prius, Design-3_1(same magnet mass), Design-3_2(increased magnet mass), & Design-3_3(increased magnet mass with SMC)	111
Fig. 5.28	Phase back EMF of Toyota Prius, Design-3_1 (same magnet mass), Design-3_2 (increased magnet mass), & Design-3_3 (increased magnet mass with SMC)	112
Fig. 5.29	(a) Honda Accord Rotor (b) Design-3 rotor	114
Fig. 5.30	Full load flux density plot (a) Honda Accord Rotor (b) Design-3 rotor	114
Fig. 5.31	Electromagnetic torque of Honda Accord and Design-3 rotor	116
Fig. 5.32	Phase back EMF of Honda Accord and Design-3 rotor	116
Figs. 6.1-6.2	Lamination Tooth	122

Figs. 6.3-6.4	SCM tooth	122
Fig. 6.5	(a&b). Electromagnetic torque of SMC (A,B,C) and Phase Back EMF at 3400 rpm	123
Fig. 6.6	(a) Selected spoke type rotor (b, c & d) Eddy current density of SMC – A, B & C at 3400 RPM	124
Fig. 6.7	Loss analysis of SMC (A,B,C) at 3400 RPM	124
Fig. 6.8	Loss analysis of SMC (A,B,C) at 10000 RPM	125
Fig. 6.9	Efficiency map (a) SMC-A (b) SMC-B (c) SMC-C	125
Fig. 6.10	(a) SMC-B sample ring (b) Experimental setup with a SMC-B toroid sample	127
Fig. 6.11	Measured iron loss values of SMC-B material	127
Fig. 6.12	Higher slot/pole designs (a) 24-slot/16-pole (b) 36-slot/30-pole	128
Fig. 6.13	Phase Back EMF of 24/20 & 36/30 with lamination & SMC stator	129
Fig. 6.14	Cogging torque of 24/20 & 36/30 with lamination & SMC stator	129
Fig. 6.15	Electromagnetic torque of 24/20 & 36/30 with lamination & SMC stator	130
Fig. 6.16	Flux density plot of SMC stator different tooth length	131
Fig. 6.17	Torque of SMC stator with different tooth length	132
Fig. 6.18	Phase Back EMF of SMC stator with different tooth length	132
Fig. 6.19	Back EMF harmonics of SMC stator with different tooth length	133
Fig. 6.20	Cogging torque of SMC stator with different tooth length	133
Fig. 6.21	Complete SMC stator and its flux density plot with 56 mm tooth body length with back iron.	134
Fig. 6.22	Complete SMC stator and its flux density plot with 56 mm tooth body with no back iron.	135
Fig. 6.23	(a) Laminated steel flux path (b) SMC flux path (c) SMC tooth	136
Fig. 6.24	B-H Curve of laminated Steel & SMC	136
Fig. 6.25	SMC stator	136
Fig. 6.26	Loss curves of laminated and SMC stator.	136
Fig. 6.27	Design – 3 (Laminated steel with coil end winding)	137
Fig. 6.28	Design-4 (SMC stator with compacted end winding)	137
Fig. 6.29	Design -3 (Flux density plot for both stator and rotor)	138

Fig. 6.30	Design -4 (Flux density plot for both stator and rotor)	138
Fig. 6.31	Full load flux density plots (a) Laminated stator (b) SMC stator	139
Fig. 6.32	3D Cogging torque of Design -3 & 4 (Laminated and SMC)	139
Fig. 6.33	3D Phase back EMF of Design-3&4 (Laminated and SMC).	139
Fig. 6.34	Electromagnetic torque of Design -3 & 4 (Laminated and SMC)	140
Fig. 6.35	3D eddy current density plot of SMC stator with reduced tooth body	142
Fig. 6.36 (a)	Efficiency map of Laminated stator	143
Fig. 6.36 (b)	Efficiency map of SMC stator	144
Fig. 6.37	Schematic for cooling with a fan coupled to the shaft	144
Fig. 6.38	(a) Temperature distribution in laminated steel stator (b) Temperature distribution in one coil side of a laminated stator (c) Temperature distribution in SMC stator (d) Temperature distribution in one coil side of a SMC stator.	145
Fig. 6.39	Thermal analysis of the SMC stator design	145
Fig. 6.40	Thermal comparison between the laminated stator and SMC stator design	146
Fig. 6.41	RMS current Vs copper and iron loss at the base speed (3400 RPM) for Design-4(SMC stator) & Design-5(Lami stator)	147
Fig. 6.42	Total loss Vs temperature at the base speed (3400 RPM) for Design-4(SMC stator) & Design-5(Lami stator)	147
Fig. 6.43	RMS current Vs copper and iron loss at the base speed (3400 RPM) for Design-4(SMC stator) & Design-5(Lami stator)	147
Fig. 6.44	Electromagnetic torque of Design -5 (Lami stator)	148
Fig. 6.45	Efficiency map of Design-5 (Lami stator) with higher current	150
Fig. 6.46	Thermal distribution of Design -5 (Lami stator) at the base speed (a) Temperature for different parts (b) Temperature of copper conductor	150
Fig. 6.47	Laminated stator (a) Square shape laminations (ready to wire cut) (b) Final laminated stator after wire cut	151
Fig. 6.48	Assembly drawing of SMC stator design	152
Fig. 6.49	Magnet Segments (a) Four (b) Flux plot of rotor	153

Fig. 6.50	Magnet eddy current loss density (a) No segment (b) Two segments (c) Four segments (d) Eight segments	154
Fig. 6.51	Magnet losses of SMC stator with various segments at 10000 rpm	154
Fig. 6.52(a)	Speed Vs torque & Speed Vs Power (JMAG – 3D FEA)	155
Fig. 6.52(b)	Speed Vs torque & Speed Vs Power (MATLAB analytical)	155
Fig. 6.53	SMC tooth (a) Without fillet (b) With fillet radius (2mm)	156
Fig. 6. 64(a)	Mechanical stress analysis of SMC-B stator with no fillet.	157
Fig. 6.54(b)	Mechanical stress analysis of SMC-B stator with fillet (radius 2mm)	157
Fig. 6.55	Rotor mechanical stress at 10000 rpm (a) Rotor view without magnets (b) Rotor view with magnets.	158
Fig. 7.1	SMC tooth evolution	162
Fig. 7.2	Tooth-2 (SMC tooth) views with 3D printed plastic tooth	162
Fig. 7.3	Tooth-3 (3D Printed) SMC tooth using plastic	163
Fig. 7.4	Tooth-3 with 3 axial segments sketched using CAD software.	164
Fig. 7.5	SMC material original shape	164
Fig. 7.6	SMC tooth (a) Manufactured tooth segments (b) Glued tooth segments.	165
Fig. 7.7	SMC tooth parts in assembly with screw (b) SMC tooth assembly in the oven	165
Fig. 7.8	Fabricated SMC stator core (complete) 12 slots	166
Fig. 7.9	SMC stator core is assembled and placed inside the motor frame with windings	167
Fig. 7.10	Fabricated spoke type rotor (a) One piece of lamination (b) Stacked rotor laminations	168
Fig. 7.11	Test setup for torque vs angle measurement	169
Fig. 7.12	Measured phase back EMF at 200 RPM.	169
Fig. 7.13	Measured phase back EMF at 500 RPM.	170
Fig. 7.14	Measured phase back EMF at 1000 RPM	170
Fig. 7.15	Measured phase back EMF at 1500 RPM	171
Fig. 7.16	Measured phase back EMF at 2500 RPM	171
Fig. 7.17	Measured phase back EMF at 3400 RPM.	172

Fig. 7.18	Phase back EMF (Simulation Vs Measurement)	173
Fig. 7.19	Measured torque angle curve for SMC motor	174
Fig. 7.20	Load torque measurement setup of SMC motor	175
Fig. 7.21	Measured torque at various current and speed	176
Fig. 7.22	Current waveforms at $I_s = 195$ A, 1000 rpm (83.33 Hz)	176
Fig. 7.23	Current waveforms at $I_s = 195$ A, 3300 rpm (275 Hz)	177
Fig. 7.24	Measured Torque vs Simulated Torque	177
Fig. 7.25	Fig.7.25. Simulated Vs Measured Torque angle curves at (Left) 15 A and (Right) 45 A	181
Fig. 7.26	Simulated Vs Measured Torque angle curves at (Left) 60 A and (Right) 75 A	181
Fig. 7.27	Simulated Vs Measured Torque angle curves at (Left) 120 A and (Right) 150	181
Fig. 7.28	Simulated Vs Measured Torque angle curves at (Left) 170 A and (Right) 195 A	182
Fig. 7.29	Simulated Vs Measured Torque angle curves at 45A, 60A, 120A and 195 A	182
Fig. 7.30	SMC stator (Left) tooth tip length same as back iron length (Right) tooth tip length same as tooth body length.	183
Fig. 7.31	SMC stator (Left) tooth tip length same as back iron length (Right) tooth tip length same as tooth body length.	183
Fig. 7.32	Electromagnetic torque of SMC stator with tooth tip and without tooth tip	184
Fig. 7.33	Simulated Vs Measured torque components	184

LIST OF TABLES

Table 1.1	Summary of motors in the state-of-the-art electric vehicles [2]	4
Table 1.2	Fabrication cost distribution of an automotive electric motor [5]	9
Table 2.1	Outer rotor pmsm specifications	21
Table 2.2	Outer rotor pmsm dimensions	23
Table 2.3	Iron loss(w/kg) for m-36 26ga	24
Table 2.4	Iron loss(w/kg) for SMC	25
Table 2.5	Iron loss comparison of smc & m-36 26ga (@1.0T)	26
Table 2.6	Copper loss comparison of smc & M-36 26Ga	28
Table 2.7	Efficiency comparison of smc & M-36 26Ga	29
Table 2.8	Comparison of Distributed and Fractional Winding for optimal flux weakening	29
Table 3.1	Design comparison of different commercial electric traction motors	31
Table 3.2	BMW i3 motor specifications [4]	34
Table 3.3	Key design parameters for the Accord PMSM [21]	37
Table 3.4	Typical values of σ for different types of machines	40
Table 3.5	Comparison of higher pole and lower pole configurations	49
Table 3.6	Comparison of Twizy motor designed with BMW i3 rotor	51
Table 3.7	Comparison of 12-slot 8 pole - commercial magnet & cold spray magnet with SMC and laminated stator	55
Table 3.8	Comparison of modified 12-slot 8 pole - commercial & cold spray magnet with SMC & laminated stator	57
Table 3.9	Comparison of tooth width for open slot configuration	59
Table 4.1	Machine specifications	65
Table 4.2	12/8 AND 12/10 CONFIGURATIONS	68
Table 4.3	Back EMF Harmonics	69
Table 4.5	Torque components	70
Table 4.6	Conventional & cobra specifications	71
Table 4.7	Back EMF Harmonics	73

Table 4.8	Torque components	74
Table 4.9	Laminated & smc stator specifications	75
Table 4.10	Iron loss(W/Kg) For M-36 29Ga	77
Table 4.11	Iron loss(W/Kg) For SMC	77
Table 4.12	Laminated stator loss analysis	78
Table 4.13	SMC stator loss analysis	78
Table 4.14	Optimal flux weakening conditions	81
Table 4.15	Torque Ripple comparison	84
Table 4.16	Optimization Range	85
Table 4.17	Optimization Objectives	85
Table 4.18	Selected parameter	86
Table 5.1	Required specifications	89
Table 5.2	Performance metrics of slot pole selection	95
Table 5.3	Rotor Parameters for optimization	100
Table 5.4	Objectives for optimization	101
Table 5.6	Selected parameters after optimization	101
Table 5.7	Stator parameters for sensitivity	102
Table 5.8	Selected Parameters for stator core	103
Table 5.9	Design parameters of the analysis models	106
Table 5.10	Phase back EMF harmonics	108
Table 5.11	Performance metrics of Design 1, 2 &3	108
Table 5.12	key dimensions of the Toyota Prius & proposed design	110
Table 5.13	Performance metrics of case study with Toyota PRIUS	112
Table 5.14	Toyota Prius Cost comparison with 48-slot/8-pole	112
Table 5.15	key dimensions of the Honda accord & proposed designs	115
Table 5.16	Performance metrics of case study with Honda Accord Motor	115
Table 6.1	Machine specifications	121
Table 6.2	SMC material properties	122
Table 6.3	Design paramaters of SMC material (A,B,C)	123
Table 6.4	Design paramaters of 24/20 and 36/30	128

Table 6.5	FEA based Iron loss comparison of SMC – B & M-36 29 Ga at 3400 rpm	130
Table 6.6	Performance metrics of SMC stator with different tooth body length	134
Table 6.7	Phase back EMF harmonics of SMC stator with different tooth body length	134
Table 6.8	Laminated & smc stator specifications	137
Table 6.9	Performance metrics of slot/pole selection	140
Table 6.10	Design 3 & 4 (laminated and SMC)	141
Table 6.11	Design 3 & 4 (Loss comparison)	143
Table 6.12	Design-3(Lami stator_1) specifications	148
Table 6.13	Design-5 (Lami stator)	149
Table 6.14	Design-5(Lami Stator) losses	149
Table 6.15	Laminated steel waste	151
Table 6.16	Cost Comparison of Laminated motor and SMC moto	152
Table 6.17	Optimal flux weakening conditions	156
Table 7.1	Measured back-EMF vs RPM	172
Table 7.2	Simulated Vs measured Back EMF	173
Table 7.3	Simulated torque components	184
Table 7.4	Simulated Vs measured torque components	185

LIST OF ABBREVIATIONS

EV	Electric vehicle
HEV	Hybrid electric vehicle
PHEV	Plug-in hybrid electric vehicle
BEV	Battery electric vehicle
IM	Induction machine
PMSM	Permanent magnet synchronous machine
PM	Permanent magnet
IPM	Interior permanent magnet
CRML	Cold Rolled Motor Laminations Steel
GOSS	Grain Oriented Silicon Steel
NOSS	Non- Oriented Silicon Steel
TGNOSS	Thin Gauge Non- Oriented Silicon Steel
NIA	Nickel- Iron Alloys
CIA	Cobalt- Iron Alloys
AA	Amorphous Alloys
SMC	Soft Magnetic Composites
NdFeB	Neodymium iron boron
UTS	Ultimate tensile strength
Back EMF	back electromagnetic force
3D FEA	Three-dimensional Finite element analysis
RPM	Revolution per minute
TRV	Torque to rotor volume

LIST OF SYMBOLS

S_r	Mechanical speed
N_m	Number of phase
f_e	Fundamental electrical frequency
ω_e	Electrical speed
P_{hp}	Power
ω_m	Mechanical speed rad/s
N_{spp}	Number of slots /pole/phase
α_{cp}	Coil pole fraction
θ_p	Angular pole Pitch
θ_s	Angular slot Pitch
N_s	No of slots
θ_{se}	Slot pitch in electrical radians
N_{sm}	Number of slots per magnet pole
R_{si}	Inside stator radius
R_{ro}	Rotor outside radius
τ_p	Pole pitch
τ_c	Coil pitch
ω_t	Tooth width
ω_s	Slot opening
k_d	Distribution factor
k_p	Pitch factor (k_p)
k_s	Skew factor
C_\emptyset	Flux concentration factor
α_m	Magnet fraction
P_c	Permeance coefficient
l_m	Magnet length
g	Air gap length

k_{ml}	Magnet leakage factor
μ_r	Relative permeability
τ_s	Slot pitch
g_c	Effective air-gap for carter's coefficient
K_c	Carter's coefficient
k_{ml}	Magnet leakage factor
B_g	Air gap flux density (T)
B_r	Magnet remanence
ϕ_g	Air-gap flux
w_{bi}	Stator back iron width
w_{tb}	Tooth width (w_{tb})
d_s	Total slot depth
R_{SO}	Outside stator radius
R_{sb}	Stator back iron radius
R_{ri}	The rotor inside radius
w_{sb}	Slot bottom width
d_s	Slot depth
d_3	Conductor slot depth
A_s	Conductor area
L	Axial length

CHAPTER – 1

Introduction

This chapter presents an introduction to permanent magnet electric motors for electric traction applications. It presents an overview of different types of PMSMs for traction applications. It introduces different types of lamination materials and soft magnetic composite materials and their properties along with the organization of the dissertation and original contributions.

1.1 *Introduction*

The world is moving towards electric traction as the principal means of sustaining the comfort, convenience, and efficiency of the transportation systems used in our modern life. Electric vehicles (EVs) will contribute to promoting sustainable energy development while addressing air quality and climate change. For instance, 41% of CO₂ emissions in a typical city are due to transportation [1]. There are three types of electric vehicles in general including the hybrid electric vehicle (HEV), battery electric vehicle (BEV) and plug-in hybrid electric vehicle (PHEV). A schematic for the three different vehicles is shown in Fig.1.1. The hybrid electric vehicle may not have an external electrical connection. It derives some of its driving power from a conventional gasoline engine and some from an electric motor. On the other hand, a battery electric vehicle gets its driving power exclusively from an electric motor, and that energy is generated from a larger battery bank that has been recharged from the grid. The plug-in hybrid electric vehicle can first run entirely on electricity from the battery for a short period of time and then it can switch to a gasoline to recharge the battery when it gets low. Compared to conventional ICEs, electric vehicles (BEVs) and hybrid electric vehicles (HEVs) have lower emissions at point of use. Fig. 1.2 shows the electric motor in an EV drive train. Electric motors are the heart of electric vehicles. Electrical machines are a vital component in traction applications as they provide electromechanical energy conversion. Traction applications require motor drive systems that can operate with high torque density and high-power density with reduced maintenance costs and losses. Since the 20th century, induction machines (IMs) have remained a popular choice owing to ruggedness and reduced

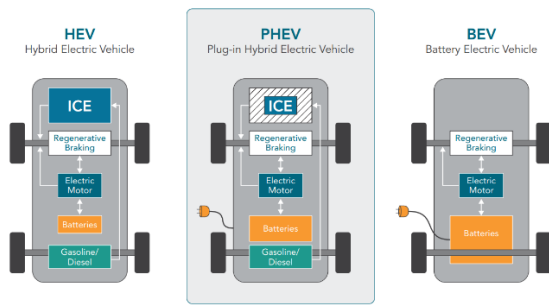


Fig. 1.1. Different types of electric vehicles



Fig. 1.2. Electric motor in an EV drivetrain [3]

cost (absence of commutators and slip rings). But it is less efficient when compared to the other kinds of AC machines such as PMSM machines. In the IM, a part of the rotor flux is created by the currents flowing in the rotor conductors, made up of either aluminium or copper bars. But in PMSMs, the rotor flux is created by the permanent magnets (PMs) mounted on the rotor. The absence of the rotor cage reduces the mass of the PMSMs, resulting in lower inertia and fast torque response when compared to IMs. Also, the lack of rotor currents reduces the rotor losses leading to higher efficiency.

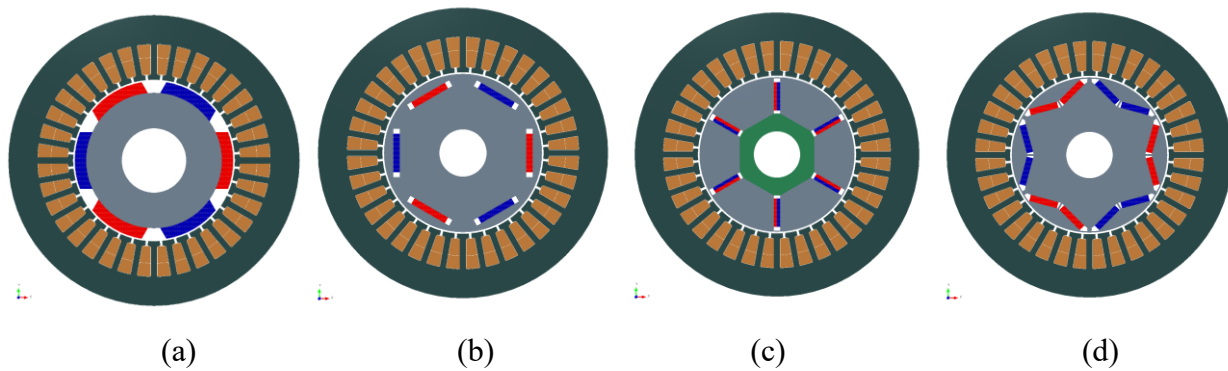


Fig. 1.3 Different types of PMSM motors (a) Surface mount (b) IPM with lateral magnets (c) Spoke type rotor (d) IPM with variable orientation magnets.

There are different types of motor topologies, such as radial, axial and transverse flux motors. But predominantly radial flux motors are used in traction motors. Figure 1.3 shows the different types of radial permanent magnet synchronous motors (PMSM). Fig. 1.3 (a-d) show the surface mount PM motor, interior permanent magnet motor (IPM) with lateral magnets, spoke type motor, and IPM motor with variable orientation magnets.

The surface mount PM machines are non-salient pole machines which means, it does not have reluctance torque, it just has the magnet torque.

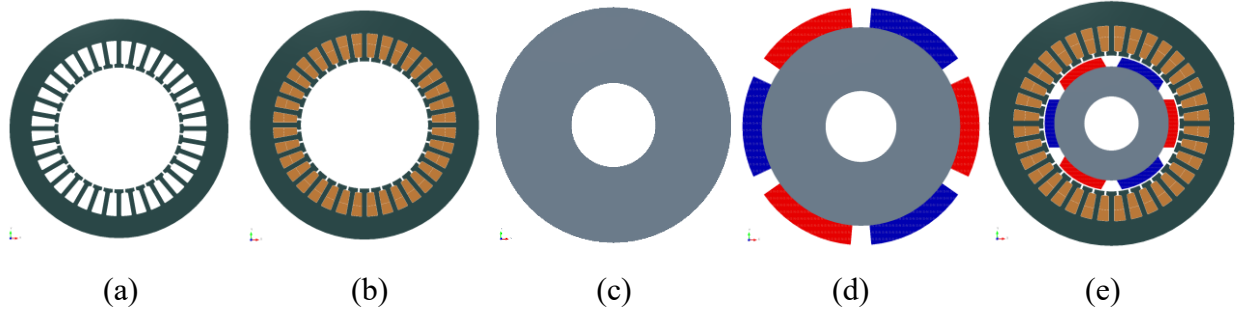


Fig. 1.4 Surface mount PMSM rotor

PMSM motors will have magnets on the rotor either buried into the rotor core or placed on the surface of the rotor core. Fig. 1.4 shows the different parts of the surface mount rotor. Fig. 1.4(a) shows the stator core without copper conductor, (b) shows the stator core with copper conductors, (c) shows the rotor core (d) shows the magnets placed on the rotor core (e) shows the complete surface mount PMSM with rotor, stator, copper and magnets to form a complete motor.

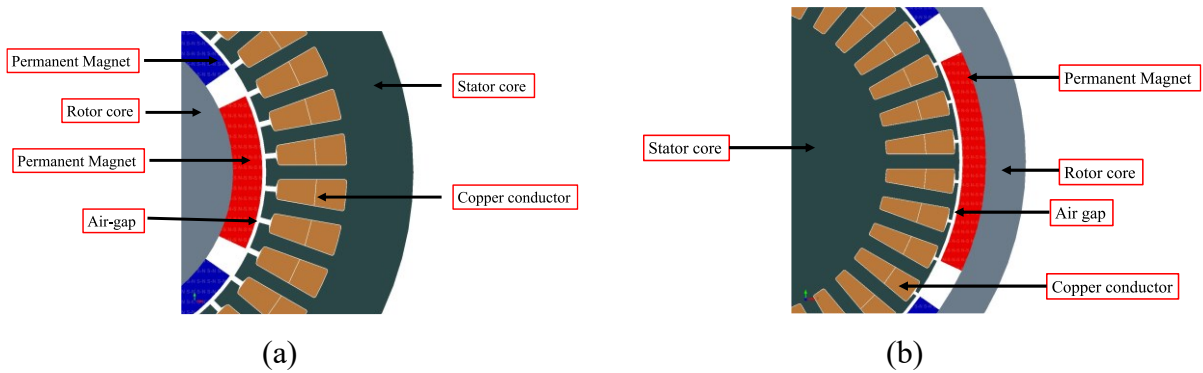


Fig. 1.5 Different parts of a surface mount PMSM (a) Inner rotor (b) Outer rotor or out runner

Fig. 1.5 shows the different parts of an inner rotor and outer rotor surface mount PMSM motor. The stator and rotor are made up of silicon steel material. Usually, magnet is a Neodymium iron boron (NdFeb), copper is used for the winding. The airgap between the stator and rotor are usually small to reduce the flux leakage. Performance of the motor will be decided based on the magnet, rotor and stator materials. The surface mount PMSM motor employs magnets that are affixed to the rotor surface. As the amount of magnet flux determines the torque, the SPM motor utilizes a significant amount of magnet material to achieve the required torque density and efficiency.

Surface motors PMSM motor require considerable field weakening when operating at high speeds, which diminishes their overall efficiency as a traction drive. Also, to protect the magnet during high-speed operation, a sleeve arrangement is necessary for the surface mount PMSM motor. Fig. 1.5 (b) shows the outer rotor PMSM motor. Most of the heat in PM machines arises from the stator winding and stator core, so, the outer rotor PM machines will need a better cooling option to cool the stator, as it is not close to the enclosure.

Fig. 1.3 (b-d) shows IPM motors. In general, IPM motors are salient-pole motors. This means that it has a component of torque - the reluctance torque – that comes from the shape of the lamination steel and not from the magnets. The total torque is a combination of the reluctance and magnet alignment torques. Fig. 1.3 (c) shows the spoke type rotor which is a good candidate for flux concentration, however this does not have a reluctance torque due to non-saliency.

Table 1.1. Summary of motors in the state-of-the-art electric vehicles [2]

Parameters	Honda Insight 2000	Honda Civic 2003	Honda Accord 2005	Honda Civic 2006	Toyota Camry 2007	Lexus 2005	Toyota Prius 1998	Toyota Prius 2004	BMW i3 2016	Nissan leaf 2012
Stator	CW	CW	CW	CW	DW	DW	DW	DW	DW	DW
Rotor	SPM	SPM	IPM	IPM	IPM	IPM	IPM	IPM	IPM	IPM
Rating(kW)	9.2 kW	12 kW	14 kW	15.5 kW	105 kW	123 kW	30 kW	50 kW	125 kW	80 kW
DC bus	144 V	144 V	156 V	156 V	244-650V	650V	273 V	200-500V	650V	375V

*CW: Concentrated Winding *DW: Distributed Winding

Table 1.1. shows the summary of the state-of-the-art electric vehicles, almost all the commercial traction vehicle motors utilize the IPM motors with distributed winding. However, the Honda accord uses a concentrated winding. The winding pattern is basically decided by the number of slots and poles. Traction motors generally do not use more than 12 poles, because increasing the pole number increases the losses of the motors also it increases the switching complexity.

Owing to the rapid development of material science, the performance of the electrical machine has been continuously improved in the past decades. For instance, the efficiency, torque density and power density of the motor have been enhanced with the application of rare-earth permanent magnet machines (PMs). The rotor and stator lamination materials decides the performance of the machine, the best lamination material for a particular operation will give best

performance of the machine. Generally, there are different lamination materials popular among the motor manufacturers presented with their properties for the precise selection of the material [3].

1.2 *Different types of lamination material*

Cold Rolled Motor Laminations Steel (CRML)

It has low carbon steels approx. 0.06% or less of carbon content. It is used when cost is the deciding factor and in certain places where high saturation flux density or permeability is required. But it has low core loss.

Grain Oriented Silicon Steel (GOSS)

It is incorporated with 35% silicon to increase the resistivity, which reduces the core losses. The materials are processed carefully to enrich the magnetic properties longitudinally. High silicon content and grain orientation of steel provide extremely low losses.

Non- Oriented Silicon Steel (NOSS)

Silicon content is 1% or less than 3 %, i.e., less than the GOSS. It can provide magnetic properties in both the transverse and longitudinal directions. So, it can give extended life to the laminations. In general, NOSS are of two types such as fully processed and semi-processed.

Fully processed: Annealing is processed before shipping. If there is a necessity, the stress release can be done after stamping. It is costlier than the semi-processed material.

Semi Processed: It is a customer annealing product. It can be annealed after stamping to maintain the flux density.

Thin Gauge Non- Oriented Silicon Steel (TGNOSS)

If the thickness of the material is reduced, which results in a reduction of the eddy current loss and the overall losses also will be reduced. The thickness may be around 0.25 mm, which is very low, and it does not satisfy any of the standards. It is best suited for high speed and very high-frequency excitation systems. It is classified into another two types with silicon less than 3% and

with silicon 6%. The silicon material can be annealed and stress relief annealed after stamping, but the material with 6% silicon will not be annealed after stamping. It is pre-annealed while manufacturing.

Nickel- Iron Alloys (NIA)

Alloying iron with nickel significantly reduces the core losses in the steel, especially improving the material's permeability. NIA is the best of all materials used in laminations to provide very low losses.

48 – 49% Nickel: 49% of nickel will be used in motor laminations with low loss requirements such as dental and medicinal surgical equipment's where it is closely related to the thermal environments.

80 % Nickel: It is used in motors and resolvers. It must undergo high temperature annealing along with the oxide layer coating to develop magnetic properties.

Cobalt- Iron Alloys (CIA)

Cobalt iron alloys with cobalt range from about 15% to 49%, and it includes 2% of vanadium which offers the highest saturation flux density of any lamination steel material. It is annealed after stamping. Its applications include airborne motors, power generation systems, oil field and specialized automotive valve actuated systems.

Amorphous Alloys (AA)

Amorphous materials are metallic alloys that are cooled during production at a high rate to avoid crystallization. It is also available in very thin size 0.25 mm and exhibits low core loss and high permeability. Due to its non-crystalline structure, it is complicated to have flat laminations. It is best suited for toroidal transformers. New technologies must be incorporated for the lamination stampings.

Soft Magnetic Composites (SMC)

From the above classification of different lamination steels, it is clear that the NOSS with 0-3% silicon as an additive is widely used to manufacture magnetic cores of electric machines. Another important impulse promoting electrical machine development comes from the SMC,

whose mechanical and magnetic properties are improved drastically in the last decades. In contrast to the laminated steel, the SMC comprises many fine iron particles coated with insulation material, as illustrated in Figure. 1.6.

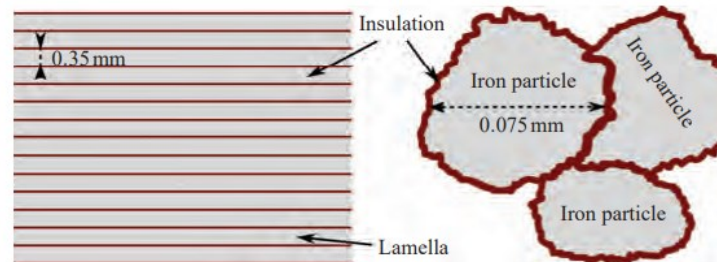


Figure 1.6. Schematic structure of NOSS and SMC

SMC are isotropic in nature, implying that the physical properties are independent of the flux orientation. This characteristic is valid for both thermal and magnetic properties. So, the heat derived from the machine losses will be more easily dissipated. Due to this magnetic isotropy, electrical machines with complex 3-dimensional magnetic patterns can be realized, which are difficult or even impossible to be manufactured with conventional laminated steels [4]. The electrical resistance of SMC is much higher than that of NOSS because of the thin insulation layer around each iron particle, which will effectively reduce the eddy current losses. This indicates that SMC core machines are best suited for higher operating frequencies, where eddy current losses become a more dominant iron loss component. The stator fill factor of the motor can be improved from 40% to 60%, which reduces the current density and the copper losses of the machine.

1.3 *Application of SMC in Electric Machine Design*

The SMC has higher electrical resistance than the NOSS because it has thin insulation layers around each particle, effectively reducing the eddy current losses. This shows that the SMC based electrical machines will have advantages at the high operating frequency.

High slot fill factor can be achieved in SMC, which will eventually reduce the copper loss of the machine.

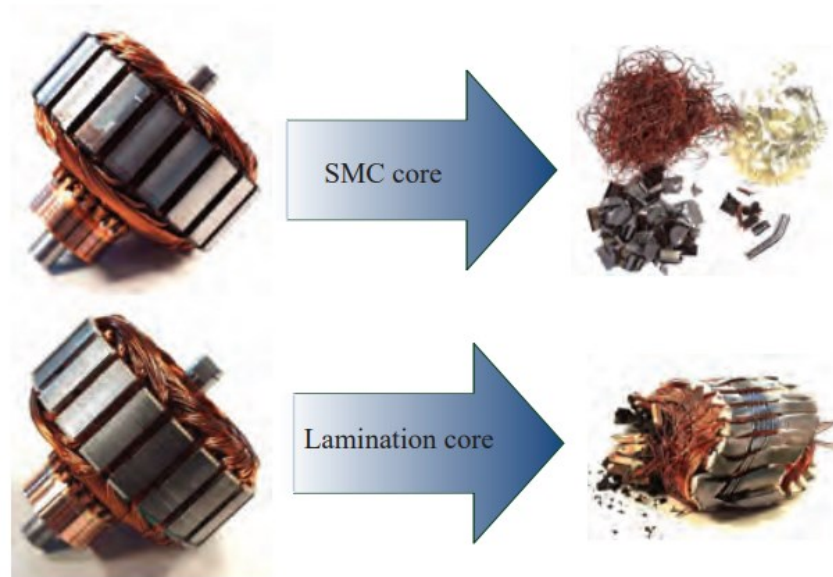


Figure 1.7. Recycling motors with SMC core and lamination core

The SMC core can be recycled, and the copper winding can be separated from SMC, as shown in 1.7 but the laminated core copper winding cannot be easily recycled. Considering the above advantages, it can be concluded that the components with 3D magnetic flux conductivity and complex shape can be manufactured with SMC. However, SMC has some disadvantages such as low magnetic permeability, high hysteresis losses, inferior mechanical properties, and limited geometrical size of the available parts. A trade-off has to be made between the merits and demerits.

1.4 *Cold Spray Additive Manufacturing of Permanent Magnets*

With the global trend towards electrification of transport, various configurations of electric motors have been developed. Unfortunately, the low versatility of the motor magnet fabrication technologies limits the development of new motor geometries. Cold spray additive manufacturing is used to shape PMs for the direct fabrication of electric motor parts without additional assembly steps. This novel technique allows an increase in the design flexibility of electrical machine geometries targeting improved performance [5]. The cost of the magnets in a PM electric motor can represent up to 50% of the total motor cost, as shown in Table 1.2.

Table 1.2: Fabrication cost distribution of an automotive electric motor [5].

Motor Part	Cost fraction, %
Bearings	1
Insulation	1
Shaft	2
Rotor iron	6
Stator iron	9
Stator copper	10
Housing	18
Magnets	53

The high cost of the rare-earth materials necessary to fabricate PMs and the numerous required assembly steps are responsible for that high fraction. Current techniques used for the assembly of PMs in motors such as adhesives, slots or screws are complex, labour-intensive and offer very little flexibility for advanced motor design geometries. Sintered magnets are typically fabricated in straightforward shapes that limit possible designs and thus performance. Consequently, alternative fabrication techniques such as cold spray additive manufacturing are worth exploring. Nowadays, PMs used in electric motors for automotive applications are typically fabricated using high-performance NdFeB alloys. Unfortunately, these materials are prone to high-temperature degradation and are thus very difficult to process using conventional thermal spray systems. The first step towards the high magnetic performance of magnets built by cold spray is to find the parameters leading to the maximal magnetic loading of the composite. Indeed, high magnetic content is needed to obtain a material with good magnetic properties. At the National Research Council of Canada (NRC-CNRC Canada), magnetic remanence and intrinsic coercivity were obtained using a hysteresis graph Permagraph L equipment from Magnet Physik (Fishers, Indiana, USA). Measured magnetic quantities are shown on a typical hard magnetic material complete BH curve in 1.8. [5].

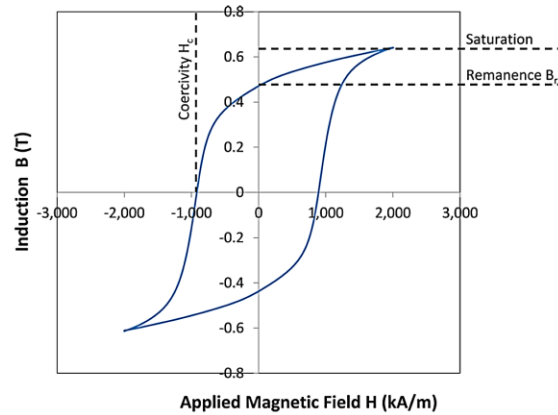


Figure 1.8. Typical hysteresis curve obtained during the magnetic measurements [5]

A good PM should possess both a high remanence (strongly related to the magnet's strength) and a high coercivity absolute value (resistance to demagnetization of the magnet under a magnetic field). Two powder pre-mixes by NRC Canada were cold spray processed using a gas temperature of 600 °C. Figure 1.3. shows the measured magnetic properties obtained from these compositions. Measurement of the samples yielded a negligible change in coercivity (3%) for the two compositions, while the remanence is 70% higher for the 90% pre-mix (90% = 0.45 T, 75% = 0.26 T). Volume fraction analysis showed that the magnetic fraction is 70% higher for the 90% mix and is thus directly responsible for the magnetic properties improvement.

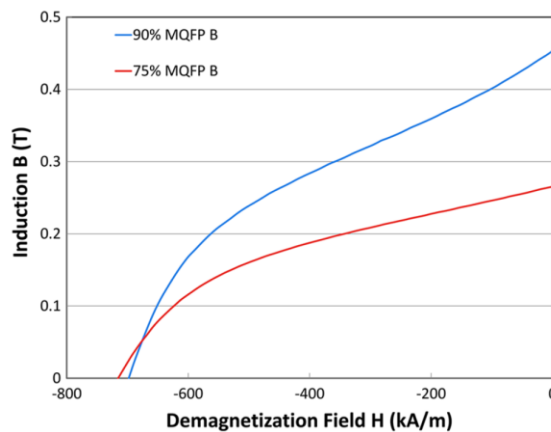


Figure 1.9. Hysteresis curve of coatings produced using two different powder mix ratios: Blue—90% MQFP-B, 10% H15, Red—75% MQFP-B, 25% H15 [5]

The effect of various process parameters on the magnetic properties of cold spray additive PMs was tested at NRC Canada laboratories. The highest obtained remanence of 0.49 T was for a

magnet volume fraction of 68%. Figure 1.9. presents the maximum remanence value obtained for different fabrication techniques compared to the industry standard sintered magnets.

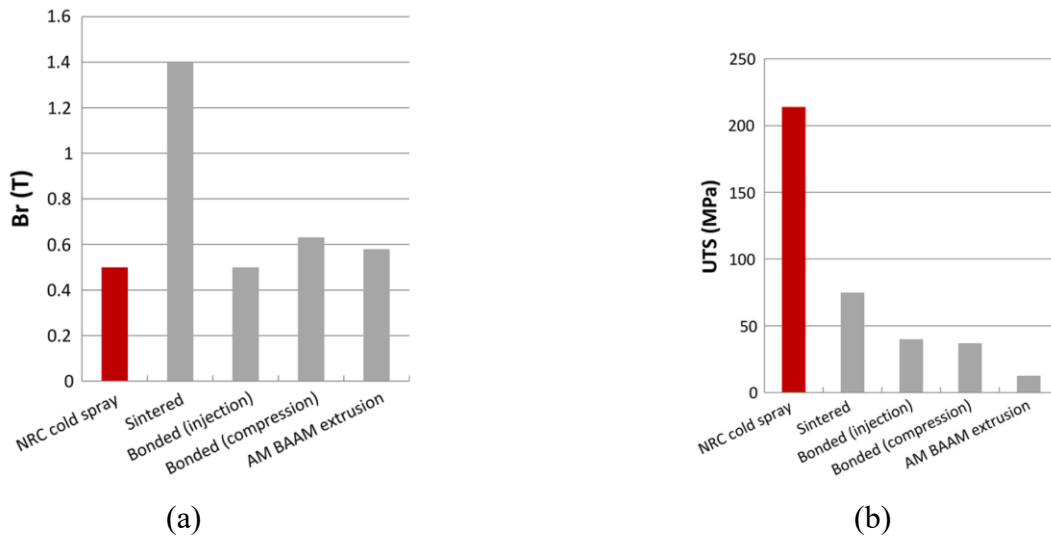


Figure 1.10. (a) Comparison of the remanence obtained for NdFeB fabricated by different manufacturing processes [3] (b) Comparison of the ultimate tensile strength obtained for NdFeB fabricated by different manufacturing processes [5]

At this point, sintered magnets offer the best remanence with values reaching up to 1.4 T. This is mainly due to the use of aligned anisotropic powder and volume fraction density of 95 + % obtained by pressing and sintering. Other techniques such as bonded magnets and additive manufacturing require the use of a binder material. This limits the maximum magnetic material volume fraction. While the obtained magnetic properties are interesting, there is still improvement needed to reach the industry's best values. Ultimate tensile strength (UTS) values for permanent magnets fabricated by different techniques are presented in Figure 1.10 (a). Cold spray-fabricated magnets exhibit the best performance with UTS above 200 MPa which is shown in Fig. 1.10 (b). This value can be attributed to the use of a metallic binder and the excellent inter-particle cohesion obtained via the high particle deformation in the cold spray process. As their adhesion and cohesion are higher than that of commercial glues, cold spray-fabricated magnets are a strong candidate to be used in applications where high mechanical integrity is required. The above-discussed analysis shows the potential of cold spray additive manufacturing of PMs for the realization of complex electric motor parts.

1.5 Objectives

The objectives of this thesis are:

- To design and analyse an outer rotor design for Twizy motor specifications.
- To design and analyse a cobra shaped spoke type rotor design using coldspray magnets for Twizy motor specifications.
- The objective is to create and construct a spoke-type motor for the Twizy electric car adhering to the following specifications: a torque rating of 20 N-m at the base speed, the capability for wide flux weakening, a constant power speed region (CPSR) of 3, torque ripple below 2%, and a DC link voltage of 96 volts. The design will incorporate commercial magnets, laminated steel for the rotor core, and an SMC (Soft Magnetic Composite) stator core.
- To compare the final spoke type rotor design with state-of-the-art traction motors such as Honda Accord and Toyota Prius to demonstrate the effectiveness of the proposed rotor design.
- After finalising the rotor design, to compare three different SMC materials for the stator core to select the best material for the SMC stator core. To analyse different tooth body lengths to select the best length with respect to electromagnetic torque.
- To compare the SMC stator design with the laminated stator design with rotor design being fixed. To perform magnetic segmentation, optimal flux weakening, thermal & mechanical analysis for the final design. Finally, to manufacture and test the final design.

1.6 Limitations:

The limitations of this thesis are:

- Outer rotor design and cobra rotor design are not manufactured due to the difficulties and costs in manufacturing.
- In the design process of the SMC stator core, thin components are not taken into account due to the difficulties involved in their manufacturing.
- The motor's testing is restricted to 3300 RPM because of the voltage limitations associated with the sine PWM method that is currently available in the laboratory.

1.7 *Organization and outline of the dissertation*

This dissertation is divided into eight chapters. It is organized as follows,

Chapter 1: This chapter provides an introduction to permanent magnet electric motors in traction applications, including an overview of DC and AC motors. It also discusses the various types of PMSM machines used for traction and covers different materials such as silicon steel and soft magnetic composite material. In addition, the section explores the characteristics of cold spray magnets.

Chapter 2 : This chapter compares the performance of the SMC and laminated steel-based designs for a radial flux outer rotor permanent magnet synchronous machine (PMSM) and its impact on the core loss at higher frequencies. Also, this chapter examines two different winding patterns (distributed and fractional) for optimal field weakening operation.

Chapter 3: This chapter presents the benchmarking of commercial vehicle traction motors such as BMWi3, and Honda Accord. Also, it presents detailed analytical equations for the PMSM design. Finally, it presents the initial designs of the Twizy motor with commercial and cold spray magnets using a lamination stator and SMC stator.

Chapter 4: This chapter focuses on reducing the torque ripple, and harmonic content of back EMF utilizing cold spray additively manufactured magnets. The electromagnetic performance of the conventional spoke and the cobra-shaped spoke type rotor are compared for the same specifications. Also, this chapter focuses on the design of a segmented SMC stator core to improve the copper fill factor to 60%. A comparison between the laminated stator core and the SMC stator core has been presented. The tooth body of the SMC stator core is reduced on both sides to compact the end winding within the stack height, increasing the torque density in terms of motor volume.

Chapter 5: This chapter presents four different slot/pole configurations to select the best slot/pole for a traction application with a wide speed range. The electromagnetic performances are improved for the selected slot/pole configuration. This chapter presents a modified spoke type rotor that significantly reduces the torque ripple, back electromagnetic force (EMF) harmonics,

and cogging torque from conventional spoke type designs. The effectiveness of the modified spoke type rotor is proved with state-of-the-art designs such as Toyota Prius and Honda Accord motors.

Chapter 6: This chapter focuses on a segmented soft magnetic composite (SMC) stator core to improve the copper fill factor and improve torque density by reducing the tooth length to allow additional space for the end windings within the stack length of the motor. A comparison between the laminated steel stator and SMC stator is presented with the selected spoke type rotor. The laminated motor is capable of producing higher torque than the SMC motor when both machines are designed to operate with the same temperature, though the torque density in terms of volume of SMC motor is higher than the laminated motor. In all cases, the machines are designed to fit into the same frame. A cost comparison has been presented between the SMC and laminated motors, which proves that the SMC motors can be manufactured at lower cost than the laminated motors. Also, the SMC stator design presents axial magnet segmentation, flux weakening, thermal analysis, stator stress analysis due to electromagnetic forces, and a rotor mechanical stress analysis.

Chapter 7: This chapter presents the evolution of SMC teeth considering the manufacturing and assembling challenges. It briefly presents the SMC tooth manufacturing including the heat treatment. Also, it presents the rotor manufacturing with prototype pictures. Finally, experimental results are presented for the SMC motor, along with the simulation results.

Chapter 8: This chapter presents the conclusion of the research work and provides recommendations for possible future research work.

1.8 *Original contributions in this dissertation*

The research contributions achieved in this Ph.D. work can be summarized as follows:

Chapter 1: This chapter presents a detailed overview of different types of motors, such as AC and DC motors. Also, it summarizes the electric motors used in the state-of-the-art vehicles. In addition, it provides a detailed overview of the materials for traction motors.

Chapter 2:

M. Muthusamy and P. Pillay, "Design of an Outer Rotor PMSM with Soft Magnetic Composite Stator Core," 2021 IEEE Energy Conversion Congress and Exposition (ECCE), Vancouver, BC, Canada, 2021, pp. 3987-3992, doi: 10.1109/ECCE47101.2021.9594954.

The contribution in this chapter is to design, analyze and compare the outer rotor with SMC and laminated stator for Twizy motor. This chapter presents a 24 -slot/20-pole outer rotor PMSM for the required Twizy specifications. Initially the motor is designed with a lamination stator core, then the motor is analyzed with the SMC stator core for the same specifications. The iron losses are compared between the laminated stator and SMC stator design. The iron loss is reduced 32% with SMC core when it is operated at the maximum speed. After selecting the SMC stator design, two different winding patterns such as concentrated winding and distributed winding are analyzed to obtain the wide flux weakening regions.

Chapter 3:

The contribution in this chapter is to analyze existing commercial vehicles and utilize the techniques to incorporate for the Twizy motor design with analytical equations. This chapter presents a detailed literature survey of existing commercial vehicle traction motors such as BMW i3 and Honda Accord. Detailed analytical equations are presented for the PMSM motor design. Also, commercial motor designs are validated using FEA software. The Twizy motor is designed using BMW i3 rotor and Nissan Leaf rotor. 24-slot/20-pole and 12-slot/8-pole have been designed and compared for the same specifications. It presents the evolution of the Twizy motor with 12-slot/8-pole using laminated and SMC stator designs.

Chapter 4:

M. Muthusamy and P. Pillay, "Design and analysis of cobra shaped spoke type rotor with SMC stator core for traction applications," 2022 IEEE Energy Conversion Congress and Exposition (ECCE), Detroit, MI, USA, 2022, pp. 1-6, doi: 10.1109/ECCE50734.2022.9947645.

The contribution in this chapter is to utilize the coldspray magnet for Twizy motor. This chapter focuses on reducing the torque ripple, and the harmonic content of back EMF utilizing cold spray additively manufactured magnets. The electromagnetic performance of conventional spoke and the cobra-shaped spoke type rotor are compared for the same specifications. Also, this paper

focuses on the design of a segmented SMC stator core to improve the copper fill factor to 60%. A comparison between the laminated stator core and the SMC stator core has been presented. The tooth body of the SMC stator core is reduced on both sides to compact the end winding within the stack height, increasing the torque density in terms of motor volume.

Chapter 5 :

M. Muthusamy, J. Hendershot and P. Pillay, "Design of a Spoke Type PMSM With SMC Stator Core for Traction Applications," in IEEE Transactions on Industry Applications, vol. 59, no. 2, pp. 1418-1436, March-April 2023, doi: 10.1109/TIA.2022.3223636.

The contribution in chapter 5 is to analyze different slot/pole combinations to select the best slot/pole combinations for Twizy motor. Also, to optimize the rotor design, and to validate the effectiveness of the proposed design with commercial motors such as Toyota Prius and Honda Accord. This chapter presents four different slot/pole configurations to select the best slot/pole for a traction application with a wide speed range. The electromagnetic performances are improved for the selected slot/pole configuration.

This paper presents a modified spoke type rotor that significantly reduces the torque ripple, back electromagnetic force (EMF) harmonics, and cogging torque from conventional spoke type designs. The effectiveness of the modified spoke type rotor is proved with state-of-the-art designs such as Toyota Prius and Honda Accord motors.

Chapter 6 and 7 :

M. Muthusamy, B. S. Abdel-Mageed and P. Pillay, "Impact of Soft Magnetic Composite Material for Traction Applications using 3D FEA," 2022 International Conference on Electrical Machines (ICEM), Valencia, Spain, 2022, pp. 1117-1123, doi: 10.1109/ICEM51905.2022.9910639.

M. Muthusamy, B. S. Abdel-Mageed and P. Pillay, "Impact of Soft Magnetic Composite Material for Traction Applications using 3D FEA," Under preparation to be submitted IEEE transactions on Energy Conversion.

M. Muthusamy, M. Bobby, J. Hendershot and P. Pillay, " Design of a novel SMC spoke-type PM machine with vertical-shaped copper conductors," Accepted to ECCE 2023.

The contribution in this chapter is to analyze the impact of Soft Magnetic Composites (SMC) for traction applications. A sensitivity analysis has been done to select the parameters for the SMC stator. Three different SMC materials are compared for the same machine specification. Eddy current loss density is plotted using a 3D FEA analysis for all three different materials. The magnet and copper losses are plotted along with the total iron losses. Efficiency maps are presented for the three designs for a maximum speed range of 10000 rpm. This chapter also presents a comparison of the SMC stator with the laminated stator design which is designed to fit into the same frame. Higher pole designs such as 24-slot/16-pole and 36-slot/30-pole has been designed and analyzed with laminated stator and SMC stator design to prove the effectiveness of the SMC material at elevated frequencies. In all cases the SMC stator is designed with 60% copper fill factor, whereas the laminated stator is designed with 40% copper fill factor. The core loss of an SMC material is tested using a toroidal measurement setup. The SMC stator is designed with a 3D flux carrying capability to improve the torque density by eliminating the end winding. The tooth body length of SMC stator is varied from 36 mm to 56 mm to analyze the performance of the motor. Nodal force and mechanical stress is calculated for the final SMC stator design with and without fillet. Finally, the manufacturing steps of the SMC stator is presented for the final design.

This contribution in chapter 7 is that it presents the design of SMC stator considering manufacturing constraints including the manufacturing steps of the SMC stator core. Finally, it compares the simulation and the experimental results for the SMC motor design.

Chapter 8 :

This chapter has the conclusions and the possible future work.

CHAPTER – 2

Design of an Outer Rotor with SMC Stator Core

This chapter compares the performance of the SMC and laminated steel-based design for a radial flux outer rotor permanent magnet synchronous machine (PMSM) and its impact on the core loss at higher frequencies. Also, this chapter examines two different winding patterns (distributed and fractional) for the optimal field weakening operation.

2.1. *Introduction to Outer Rotor PMSM for traction applications.*

Electric machines are used widely in traction applications. Improved performance and reduced weight are two main criteria that decide the electric machine design to satisfy specifications. Electrical steels play a vital role in the manufacturing of electric machines. The various characteristics of the electrical steel include core loss, saturation flux density, permeability, cost, and the manufacturing facility to produce certain parts, and its marketability. The power density of the machine depends on the electrical steel in the machine. The electric steels are broadly classified into three types such as soft magnetic alloys (SMA), amorphous metal (AM), and soft magnetic composites (SMC). The soft magnetic alloys are further classified into three types such as cold-rolled steels (CRS), Grain-oriented silicon steel [GOSS], non-oriented silicon steel (NOSS). CRS are low carbon steels, which have very high core loss and is suitable for industrial motors and generators. GOSS steels have 3% silicon content with magnetic flux oriented in the rolling direction, which is suitable for transformer core design. The high content of silicon makes it very abrasive, so tool life will be reduced. NOSS laminations are used in the stator and rotor cores of the motor, which is alloyed with 1% to 3% silicon to increase the resistivity, and thus reduces the core loss of the machine [6]. The AM has high permeability, and thinner laminations have lower iron losses. The authors in [7] compared the SMC and AM and found a 2% increase in efficiency with the AM. Due to its material hardness, it is best suited for transformer applications to obtain high efficiency. The powdered alloys otherwise called SMC, in which the metallic particles are insulated by insulation with the aim to make a smaller material section, thus reducing the eddy currents in the core. They have the potential to provide low core losses at higher frequencies at low manufacturing costs. Segmented stator cores with SMC reduces wastage, also

it allows an increase in copper slot fill factor of the motor [8]. However, the magnetic permeance of SMC is lower than electrical steel, a higher current is required to obtain the same performance which leads to an increase in the ohmic losses, but the total losses of SMC can be lower than laminated silicon steel [9]. Punching laminated steel causes grain distortions thus changing the magnetic behavior and increasing the core loss of the machine. Annealing reduces the effect of punching [10] but it increases the manufacturing cost of the laminations.

For an application like water pumping, the PM motor is designed for operating at a constant speed. Generally, the surface-mounted, non-salient pole AC machine is chosen for this application. But in traction applications, the permanent magnet motor is required to operate above the rated speed for a certain interval of time. To increase the speed above the rated speed, flux weakening is performed. Flux weakening uses the stator current components to counter the flux generated by the rotor magnets, similar to field weakening in a separately excited DC motor. The surface permanent magnet machines are considered as a poor candidate for the flux weakening operation to achieve constant power in the above base speed region [11]. The surface-mounted PMSM has lower inductance because the permanent magnets on the rotor surface behave like a large air gap. To achieve constant power the characteristic current I_{ch} must satisfy the relationship.

$$I_{ch} = \frac{\psi_m}{L_d} A \text{ rms} \quad (2.1)$$

where L_d is the d-axis inductance, and ψ_m is the magnet d-axis flux-linkage. The motor must be designed with high inductance to match the d-axis flux linkage to equate the magnet d-axis flux linkage with the peak current and the d-axis inductance. The most common winding patterns used in SPM machines is a distributed winding or a fractional winding, of which the fractional winding is a promising candidate for EV applications to operate with constant power [12]-[13]. Fig.1 shows the outer rotor motor with a frame. A 24 slot, 22 pole configuration has been proposed for the design of the outer rotor PMSM. The outer rotor PMSM is widely used for in-wheel traction applications, but it is less commonly used in standard traction applications. The outer rotor can be designed with high torque density [14], as it utilizes the complete outer diameter of the rotor.

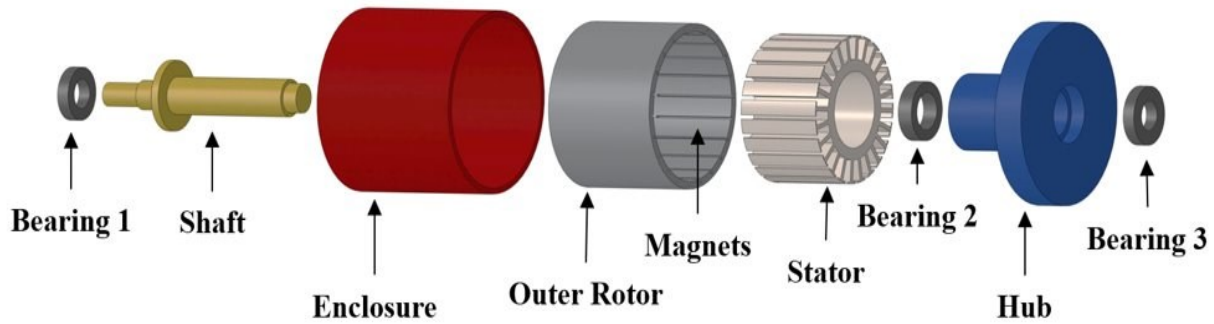


Fig. 2. 1. Outer Rotor Configuration (Assembly drawing)

The outer rotor configuration consists of three bearings, one hub arrangement for supporting the stator, the rotor is supported with bearing-1, which is connected to the frame of the motor, the rotor is made up of laminated steel and the rotor magnets are mounted using a novel cold spray additive manufacturing technique [15]-[17]. Bearing-2 holds the rotor from the inside of the stator and bearing-3 holds the rotor at the end bell. Most iron losses are circulated in the stator steel. To reduce the iron loss at the stator the silicon steel has been replaced by a SMC stator.

2.2. Comparison of laminated steel and SMC Based design

Thin steels are used for reducing the losses, but it increases the cost of the steel core. SMC core can be used to reduce the losses at the higher speed, also SMC has benefits such as high copper fill factor, and 3D flux carrying capability. A comparison has been made between the laminated stator core and the SMC score. Fig. 2. 3 shows the outer rotor PMSM with 24 slots & 22 pole. A comparison has been made with the laminated stator and SMC stator for a 24 slot 20 pole PMSM.

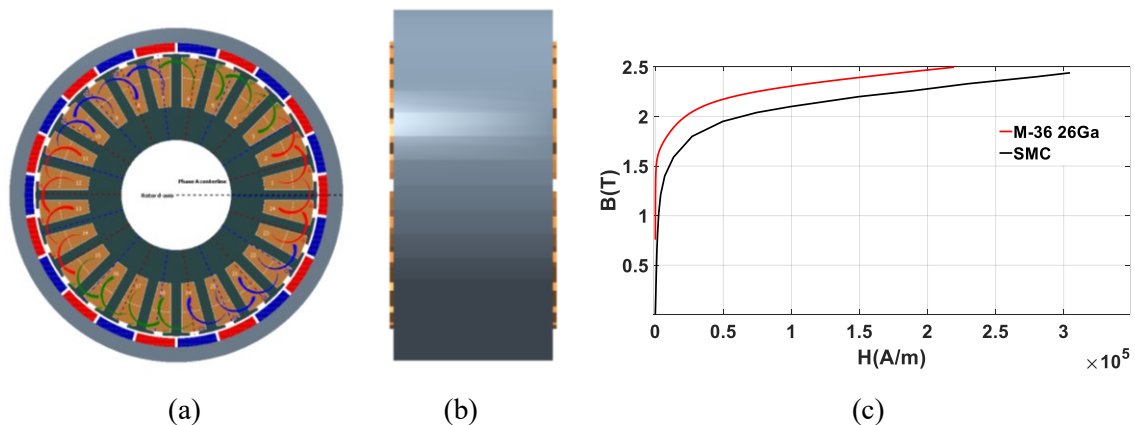


Fig. 2. 3&4 Outer Rotor PMSM (a) 24 Slot 22 pole (b) YZ plane (c) B-H Curve of Steel & SMC.

Fig. 2. 3(c) shows the B-H curve of the laminated steel and the SMC core. The SMC core is less permeable when compared to the laminated steel core, also the peak flux density of SMC is lower than the laminated steel.

Table 2.1: OUTER ROTOR PMSM SPECIFICATIONS

Motor Specifications	Values
Rated Power	7.1 kW
Rated Torque	20 N-m
Rated Speed	3400 rpm
Maximum Speed	10,000 rpm
Supply Voltage	96 volt
Cooling type	Air Cooled
Class of Insulation	F class

Table 2.1 shows the specifications of the outer rotor PMSM with 24 slots 20 pole. The rated speed of the motor is 3400 rpm and the maximum speed of the motor is 10,000 rpm. The motor is rated at 7.1kW with rated torque of 20 N-m.

Table 2.2: OUTER ROTOR PMSM DIMENSIONS

Motor Specifications	M-36 26Ga & SMC
Rotor Outer Diameter (mm)	165
Rated RMS Current (A)	104
Stator Outer Diameter (mm)	139
Stack Length (mm)	85
Magnet Thickness (mm)	4.3
Air Gap Length (mm)	1
Turns per coil	3
Number of Strands in hand	30
Strand diameter (mm)	0.813
Number of parallel paths	1
Number of layers	2

Table 2.2 shows the design specifications of the outer rotor PMSM. The 24 slots 20 pole PMSM has a slot/pole/phase (SPP) of 2/5, best suited for traction applications.

Table 2.3

IRON LOSS(W/ kg) FOR M-36 26GA

[W/kg]	60	200	300	600	1000	2000
	Hz	Hz	Hz	Hz	Hz	Hz
0.5T	0.55	2.69	4.78	14.13	30.85	93.4
1.0T	1.74	9.3	17.38	54.69	127.96	426.8

Table 2.4

IRON LOSS(W/kg) FOR SMC

[W/kg]	60	200	300	600	1000	2000
	Hz	Hz	Hz	Hz	Hz	Hz
0.5T	1.8	6	9	20	36	86
1.0T	5.9	21	32	68	125	307

Table 2.5

IRON LOSS COMPARISON OF SMC & M-36 26GA (@1.0T)

Parameters	M-36 26Ga	SMC
Rated Torque (N-m)	23	20
Iron Loss @ 3400 RPM (W)	231.7	252.4
Iron Loss @ 10,000 RPM (W)	2000	1350

Table 2.3& 2.4 shows the iron loss (W/KG) for the laminated steel M-36 26GA and the SMC. The iron loss at the lower frequencies is higher for the SMC, but the iron loss at the higher frequency is less for SMC than the laminated steel. The outer rotor PMSM machine is designed to operate at a rated speed of 3400 rpm and a maximum speed of 10,000 RPM. The rated torque of the machine is 20N-m. The core loss analysis has been carried out using JMAG Software [18]. The comparison has been done with the same machine dimensions. The laminated steel produced higher torque than the SMC, but the iron loss at the maximum speed is higher in laminated steel.

SMC is the better material to operate at a high frequency. The comparison has been made with the same dimensions and same current. The copper loss will be the same because the machine current remains the same.

Table 2.6

COPPER LOSS COMPARISON OF SMC & M-36 26GA

Parameters	M-36 26Ga	SMC
Rated Torque (N-m)	23	23
Copper Loss @ 3400 RPM (W)	156.03	192.3

The rated torque of the SMC and laminated steel are equated with the increase in the current of the SMC stator to analyze the copper loss of the two machines. Table VI shows the copper loss at the rated speed for laminated stator and SMC stator.

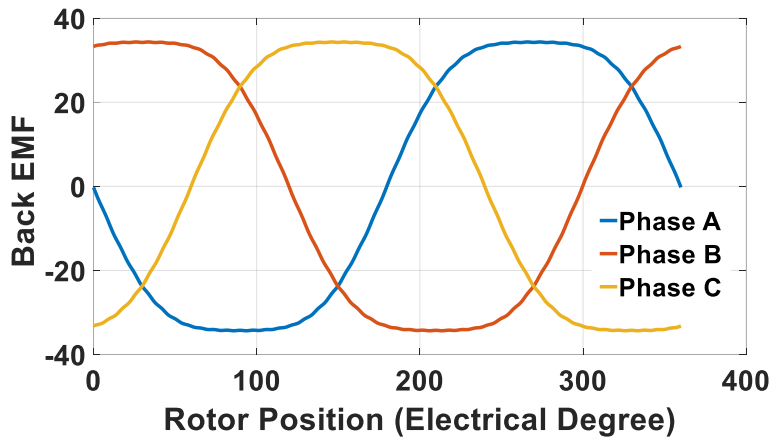


Fig. 2. 5. Back EMF of M-36 26Ga design

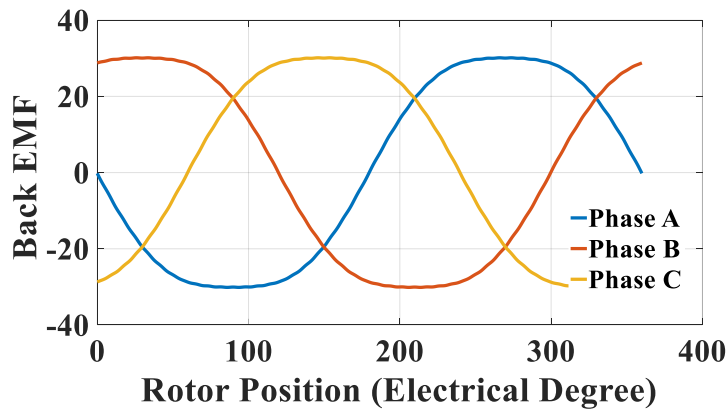


Fig. 2. 6. Back EMF of SMC design

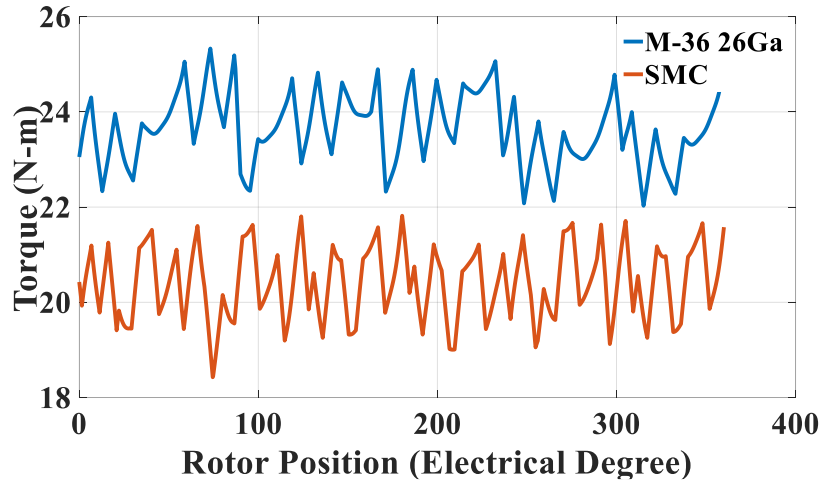


Fig. 2. 7. Torque Comparison of SMC and M-36 26Ga

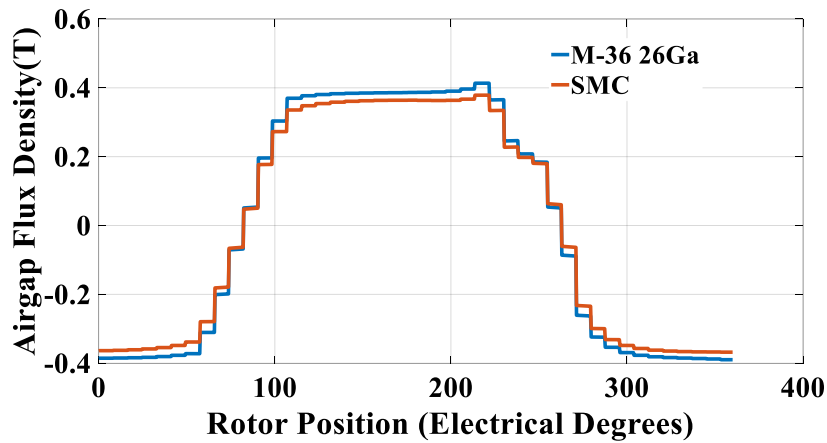


Fig. 2. 8. Air gap Flux Density Comparison

Table 2.6 shows the copper loss of SMC and laminated steel, the SMC has higher copper losses for the same rated torque at 3400 rpm. Fig. 2. 5& 6 shows the phase back EMF of the laminated stator and the SMC stator. The back EMF of the SMC design is lower than the laminated steel design. Fig. 2. 7 shows the torque ripple of the SMC stator and laminated stator. The average torque of the laminated stator is 23.52 N-m, and the SMC stator is 20.76 N-m. The torque ripple is 7% for both machines. Fig. 2. 6, shows the air gap flux density of the SMC and laminated stator. Fig. 2. 9 & 10 show the efficiency map of the laminated stator and the SMC stator. The efficiency at the rated power for laminated stator and SMC stator are 95% and 94%. The efficiency at the maximum power for laminated stator and SMC stator is 77% and 81%.

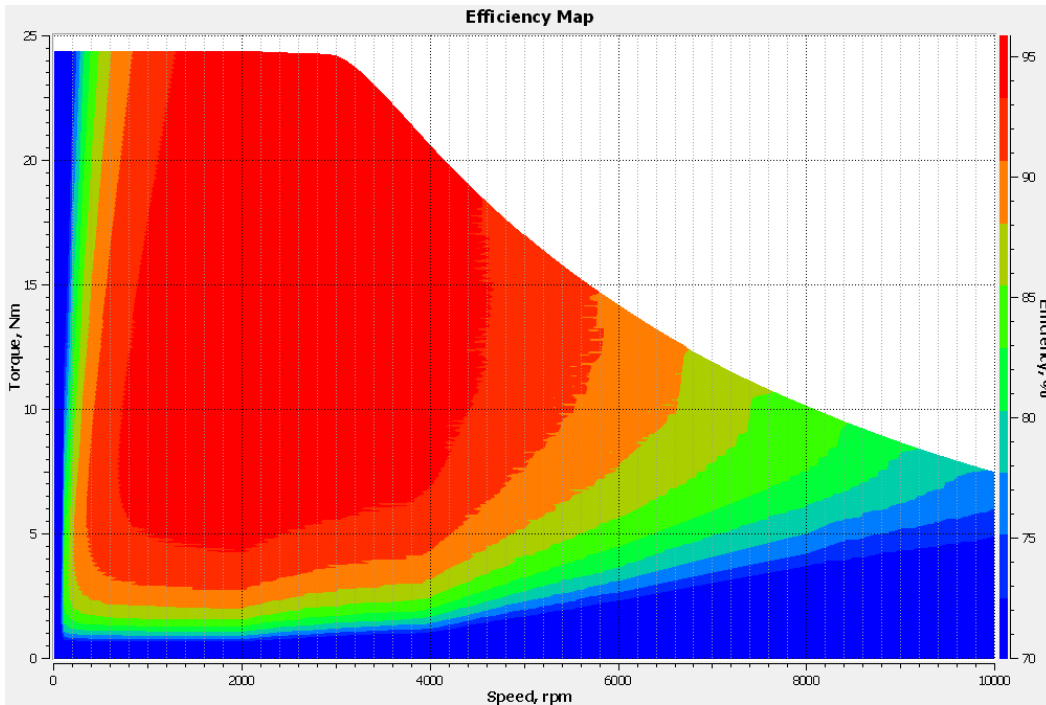


Fig. 2. 9. N-T Efficiency map of laminated stator

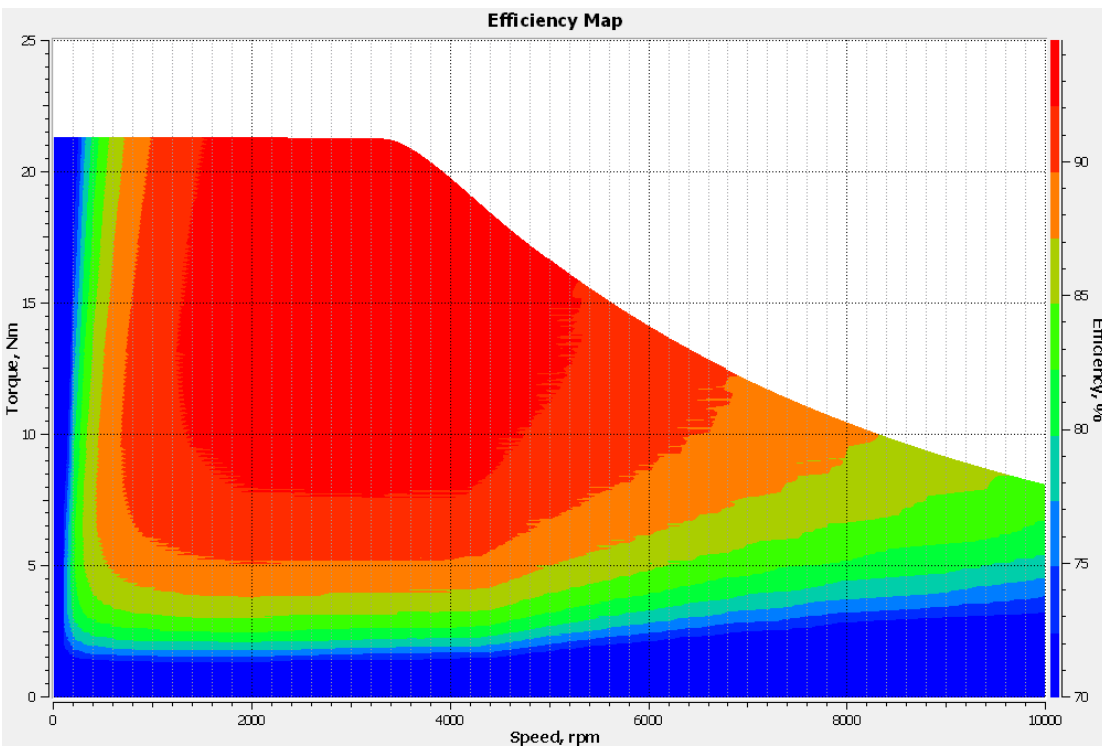


Fig. 2. 10. N-T Efficiency map of SMC stator

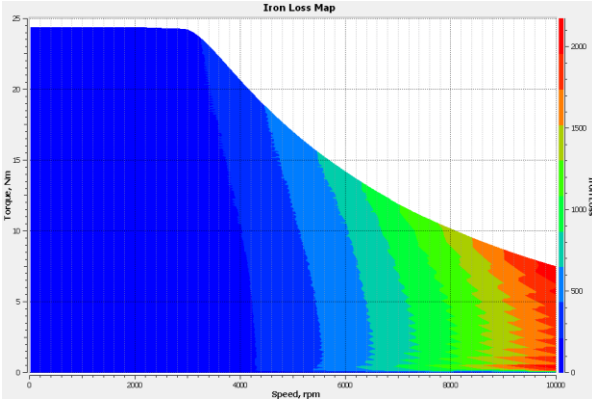


Fig. 2. 11. N-T Iron loss of laminated stator

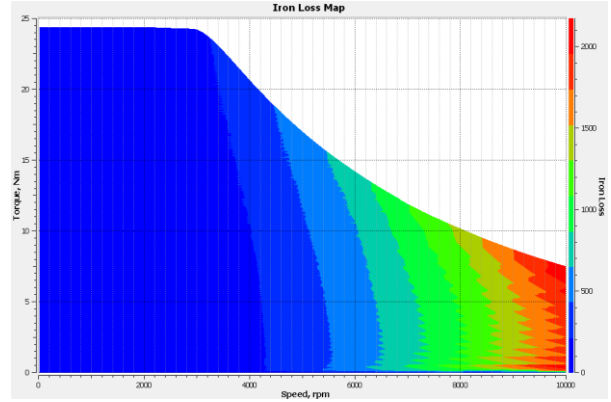


Fig. 2. 12. N-T Iron loss of SMC stator

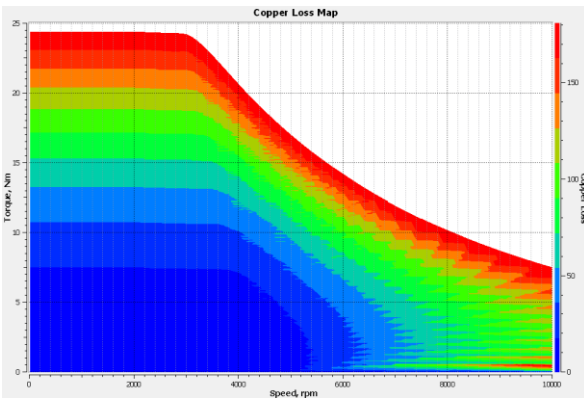


Fig. 2. 13. N-T copper loss of laminated stator



Fig. 2. 14. N-T copper loss of SMC stator

The efficiency of the SMC stator at the maximum power increased by 5% from the laminated stator. Fig. 2. 11 & 12 shows the iron loss map of the laminated stator and the SMC stator. The iron loss at the rated speed for the laminated stator and SMC stator are 231.7 W and 252.4 W. The iron loss at the maximum speed for the laminated stator and SMC stator are 2.0kW and 1.35kW. The iron loss at the SMC stator is reduced by 32.5% at the maximum speed. Fig.13 & 14 shows the copper loss map of the laminated stator core and the SMC stator core. The rated torque of both the machines are equated to 23 N-m to analyze the copper loss of both the machines. The torque of 20 N-m is achieved in the SMC stator with 155 A peak current. The peak current is increased to 175 A to equate the torque of laminated steel. The copper loss of laminated stator at the rated speed is 156 W and the copper loss of SMC stator is 192.3 W. The copper loss of the SMC stator is 18% increased from the laminated stator.

Table 2.7 shows the overall efficiency comparison of laminated steel stator and SMC stator. The efficiency of the laminated stator is less at the maximum speed due to the higher iron loss at the maximum speed. The efficiency of the SMC stator is improved by 6.5 % in the maximum speed flux weakening region.

Table 2.7: EFFICIENCY COMPARISON OF SMC & M-36 26GA

Parameters	M-36 26Ga	SMC
Rated Torque (N-m)	23	23
Efficiency @ 3400 RPM	95.07 %	94.30 %
Efficiency @ 10,000 RPM	77.01 %	83.59 %

2.3. *Different Winding pattern for flux weakening*

Traction motors are required to operate in the field weakening mode to produce constant power. There are two different winding patterns commonly used in traction motors namely concentrated windings and distributed windings. The distributed winding motors naturally have lower inductance, but the concentrated winding has higher inductance which makes it a better candidate for field weakening operation with wide constant power. After selecting the SMC stator core, two different winding configurations are considered to select the winding pattern which is best suited for the optimum flux weakening. The basic equations of the SPM machines for field weakening can be derived by dividing the voltage and current into the d-axis and q-axis. From the equivalent circuit, the voltage equations can be written as,

$$E_s = \omega_e \Psi_m \quad (2.2)$$

$$V_s = I_s R_s + j\omega_e L_s I_s + E_s \quad (2.3)$$

$$V_s = j\omega_e L_s I_s + E_s \text{ (stator resistance ignored)} \quad (2.4)$$

$$i_q = I_s \cos\delta, i_d = I_s \sin\delta \quad (2.5)$$

$$v_q = E_s + I_d L_d \omega_e, v_d = -I_q L_q \omega_e \quad (2.6)$$

$$V_s^2 = v_d^2 + v_q^2 \quad (2.7)$$

$$V_s^2 = (i_q L_q \omega_e)^2 + (E_s + i_d L_d \omega_e)^2 \quad (2.8)$$

$$\frac{V_s^2}{(\omega_e L_d)^2} = \frac{(i_q L_q \omega_e)^2}{(\omega_e L_d)^2} + \frac{(E_s + i_d L_d \omega_e)^2}{(\omega_e L_d)^2} \quad (2.9)$$

$$\frac{V_s^2}{(\omega_e L_d)^2} = \left[\frac{i_q^2 L_q^2}{L_d^2} \right] + \left[\frac{\Psi_m}{L_d} + i_d \right]^2 \quad (2.10)$$

where, E_s is the Back EMF, I_s & V_s are source current and voltage, v_q & v_d are the q-axis and d-axis voltage, i_q & i_d are the q-axis and d-axis current, L_q & L_d are the q-axis and d-axis inductances, Ψ_m is the flux linkage, and ω_e is the rotational frequency. Equation (2.10) forms the voltage loop, by increasing the speed of the machine the voltage will drop, this makes the voltage circle shrink as the speed of the machine increases which is shown in Fig. 2. 15.

The motor which is designed to operate inside the current limit and volt limit circles does not exceed the voltage and current requirement. In Fig. 2. 15, the voltage loops are shown for three different speeds. The small voltage loop is formed for a maximum speed of 10,000 rpm.

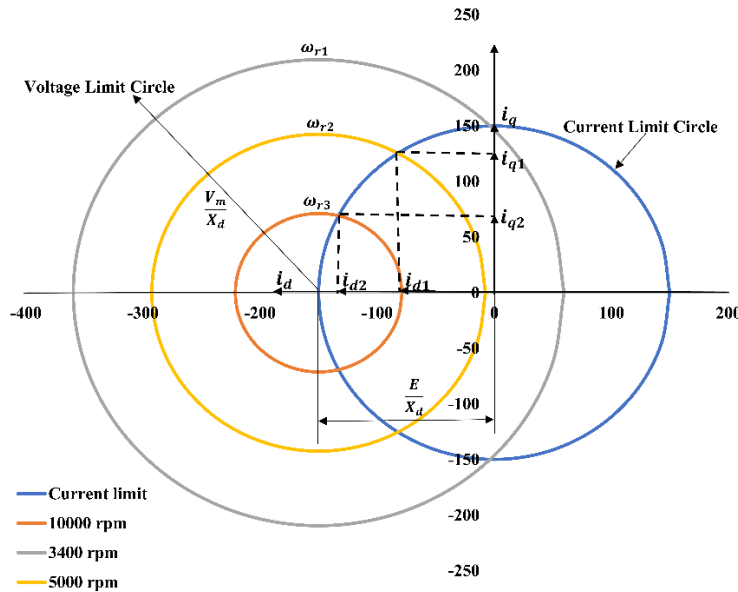
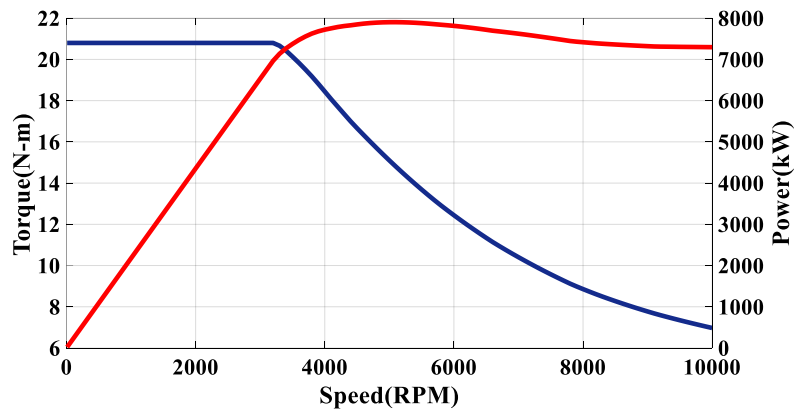


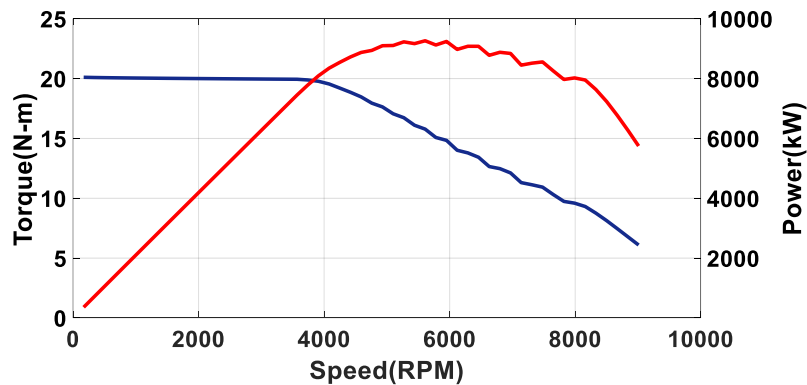
Fig. 2. 15. Voltage and Current Loop of Outer Rotor PMSM with SMC

Table 2.8 COMPARISON OF DISTRIBUTED AND FRACTIONAL WINDING FOR OPTIMAL FLUX WEAKENING

Parameters	Design 1 (24 slot 22 pole)	Design 2 (24 slot 8 pole)
Winding Type	Concentrated	Distributed
Slot/Pole/Phase (SPP)	0.36	1
d-axis induc(mH) (L_d)	0.0612	0.122
Peak current(A) (I_s)	150	150
Flux linkage (Wb) (φ_m)	0.0101	0.0283
$L_d * I_s$	0.00918	0.0183
Diff between φ_m & $L_d * I_s$	0.0009	0.01



(a)



(b)

Fig. 2.16. Torque vs Speed vs Power ($\psi_m \approx L_d * I_s$ of (a)Design 1 (b)Design 2

Table 2.8 shows a comparison between the distributed and concentrated windings, the difference between the flux linkage and the d axis inductance and current of concentrated winding is 2% but the distributed winding is 45%. With a concentrated winding the condition for constant power [1] is achieved, to make the power constant in the field weakening region. Fig. 2. 16 shows the speed Vs torque Vs power for distributed and concentrated winding machines. The power curve in Fig. 2.16 (b) exhibits non-smoothness due to a reduced number of plotted points. The power in the field weakening region of distributed winding (right) drops due to lower inductance and the power in the concentrated winding (left) is constant in the field weakening region. The concentrated winding will provide higher inductance for the same magnet flux linkage. It's proved that in concentrated winding the d-axis inductance is 6.56 increased for the same magnet flux linkage [12]. The concentrated winding is shown to be a better candidate for traction applications with wide constant power.

2.4. *Conclusions*

In this chapter, a radial flux outer rotor PMSM is designed and compared with laminated steel (M36 26Ga) and SMC. The iron loss is reduced 32% with SMC core when it is operated at the maximum speed. The efficiency is found to be increased by 6.5% with the SMC core at the maximum speed of 10,000 rpm. SMC has other advantages such as 3D flux paths, reduced wastage of materials, higher fill factor. The two winding techniques have been analyzed with the SMC core. The concentrated winding in design 2 with fractional SPP is found to be better in the flux weakening mode. The difference between the flux linkage and the product of d-axis inductance and current is found to be 2 % in the concentrated winding and 45 % in the distributed winding. The lower difference in the concentrated winding makes it more suitable for traction applications.

CHAPTER – 3

Benchmarking of State-Of-The-Art Traction Motors & Slot/Pole Selection for the Twizy Motor

This chapter presents the benchmarking of commercial vehicle traction motors such as BMWi3, and Honda Accord. Also, it presents detailed analytical equations for the PMSM design. Finally, it presents the initial designs of Twizy motor with commercial and cold spray magnet using lamination stator and SMC stator.

3.1. *Introduction to state-of-the-art traction motors*

Nowadays, electrical motors account for 65 % of worldwide energy consumption. As environmental concern increases, electrical drives with higher efficiency are desirable. Thus, replacing conventional induction machines with PMSMs has recently gained great interest. Indeed, PM machines have no rotor winding which results in lower copper losses and therefore feature a higher efficiency than induction machines.

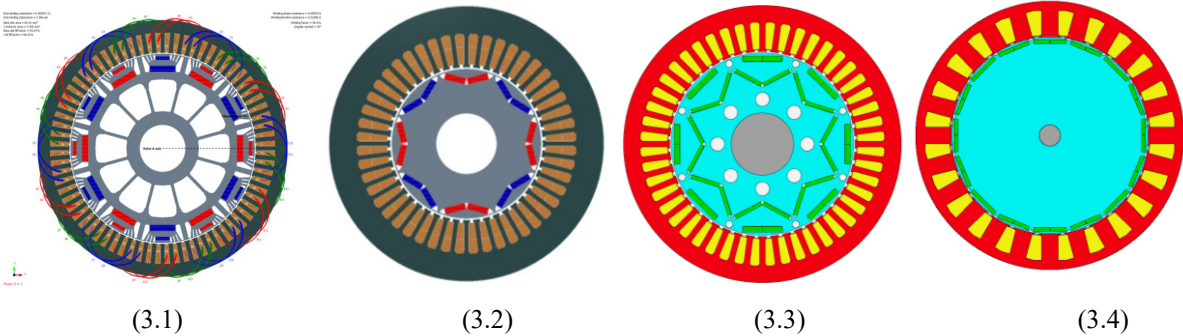
For low-speed applications, below 500 rpm, PM machines may further eliminate the need of a gearbox. To adapt the speed and torque of the machine, a gearbox is traditionally coupled to a standard induction machine. It is advantageous to remove this mechanical element because it is costly, decreases the drive efficiency, and needs maintenance.

3.2 *Commercial traction motors (Recent activities)*

Table 3.1. Design comparison of different commercial electric traction motors

Parameter	BMW _{i3}	Toyota Prius	Nissan Leaf	Honda Accord
No of stator slots	72	48	48	24
No of poles	12	8	8	16
Maximum Speed	12000 rpm	6000 rpm	10000 rpm	5000 rpm
Rotor Type	Buried PM	Buried PM	Buried PM	Buried PM
Stator Type	Laminated steel	Laminated steel	Laminated steel	Laminated steel
Magnet Type	NdFeB	NdFeB	NdFeB	NdFeB

The commercial electric motors such as Toyota Prius, Nissan Leaf, BMWi3, Tesla and Honda Accord commonly uses radial flux buried PM motors in their designs.



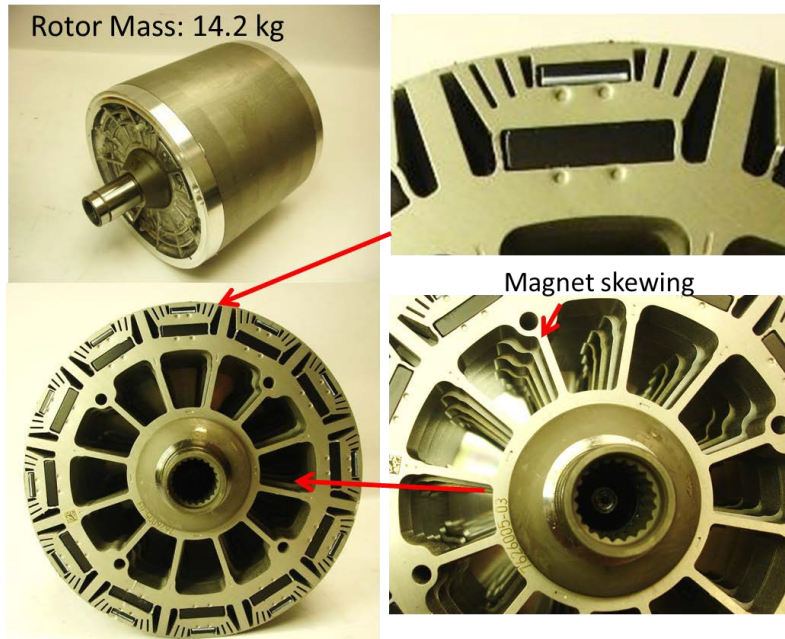
Figs. 3.1- 3.4. Commercial traction motors (3.1) BMW i3 (3.2) Toyota Prius (3.3) Nissan Leaf (3.4) Honda Accord

Figs. 3.1-3.4 show the cross section of the commercial traction motors. Almost all the commercial traction motors are radial flux PM machines which reduces the manufacturing complexity for mass production. A brief comparison of the recent electric traction motors is given below. Table 3.1 shows the comparison of different electric traction motors. The poles have been chosen depending on the operating frequency of drive. Most of the traction motors are designed with 8 poles. The BMWi3 is designed with 12 poles. Most of the commercial vehicle traction motors are designed with distributed windings. The Honda accord is designed with a concentrated winding with 16 poles and also it utilizes segmented teeth which helps to increase the copper fill factor. Lamination steel is commonly used in stator and rotor cores. Usually, the stator cores will have higher core loss when compared to the rotor cores. In most of the cases the rotor core losses will not be considered as its present in negligible amount. The core loss of the laminated steels increases with the increase in the frequency. The poles of the electric motor are directly proportional to the frequency. This is also a reason why a lower number of poles are chosen for the traction motor applications.

The Yokeless and Segmented Armature (YASA) is a new type of axial flux machine which utilizes SMC stator cores for traction application motors. The SMC material has attracted the attention of the traction electric motor market due to its 3D flux carrying capability and improved fill factor with the segmented winding. From the Table 3.1 two machines will be considered for a case study to understand the commercial traction motor design methodologies. The BMWi3 and the Honda accord are considered for the further benchmarking and case study.

3.3 Benchmarking of BMWi3 [4]

The BMW i3 rated at 125 kW and a torque rating of 250 Nm. The motor is liquid-cooled with a spiral channel. BMW i3 uses 72 slots, 12 poles with six slots per pole. The winding is full pitch and concentrically wound with 12 wires (21 AWG) in hand. Each pole is wired in parallel, giving six parallel paths and nine turns per slot [19].



Figs. 3.5-3.9. BMWi3 motor rotor [19]

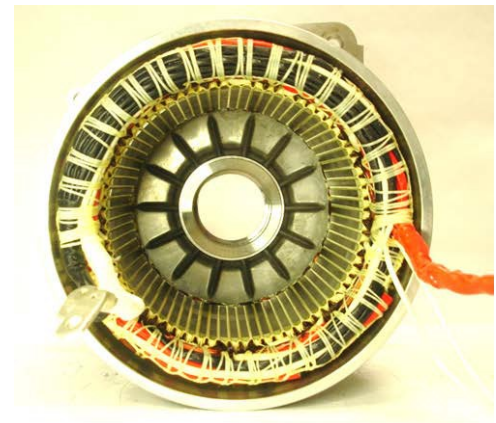


Fig. 3.10. BMWi3 motor stator [19]

The rotor, shown in Figs. 3.5-3.9, has a total mass of 14.2 kg, including the rotor shaft, end plates, end plate bolts, laminations, and magnets. With an outer diameter of 178.60 mm, the lamination design resembles a synchronous reluctance rotor but has one small and one large neodymium iron boron magnet per pole.

Incremental magnet skewing, visible in 3.6(Right), is implemented six times throughout the stack, which is likely to mitigate cogging torque and torque ripple during operation. Figure 3.10 shows the BMWi3 stator with 72 slots with an outer diameter of 243.1 mm, and the overall stack length of the motor is 133.3 mm [19]. Air barriers are used to reduce the area in which lamination steel is not utilized for the flux path. Also, it helps in reducing the weight of the motor. Hence the torque density of the motor is higher for the BMWi3 motor.

Table 3.2: BMWi3 motor specifications [4]

Parameter	BMW i3
Stator OD, cm	24.2
Stator ID, cm	18.0
Stator stack length, cm	13.2
Stator mass, kg	20.2
Stator core mass, kg	13.7
Stator copper mass, kg	7.1
Number of stator slots	72
Stator turns per coil	9
Parallel circuits per phase	6
Coils in series per phase	1 per leg
Number of wires in parallel	12
Wire size, AWG	21
Winding notes	Full pitch

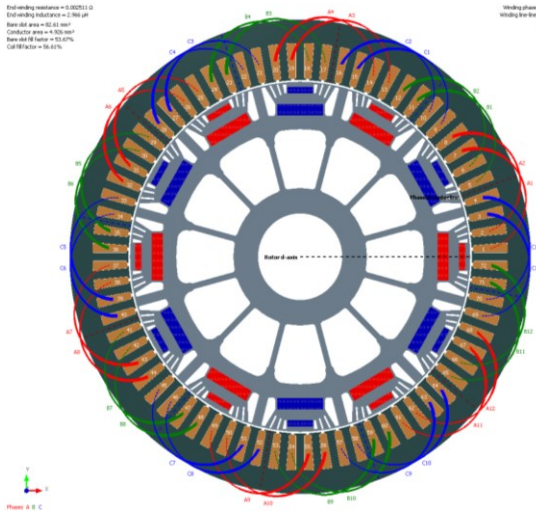


Figure 3.1. BMWi3 in MotorSolve

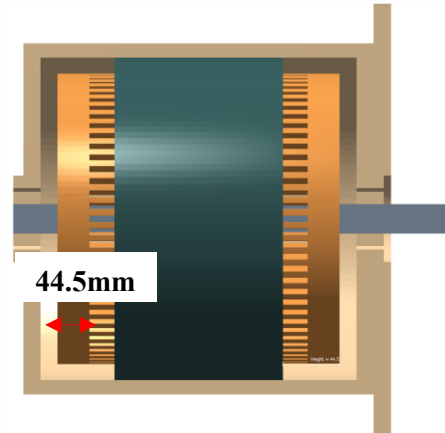


Figure 3.2. BMWi3 stator end windings

Table 3.2 shows the motor design parameters of the BMWi3 motor. The DC link voltage of the motor is 400 V, the rated RMS current is 350 A, the rated speed is 4500 rpm, and the maximum speed is 11,000 rpm. It has six parallel paths, which helps to reduce the number of strands to 13.

Figure 3.11 and 3.12 shows the MotorSolve evaluation of BMWi3 motor. The stator slot fill factor is 53.67 % which is the highest fill factor that can be achieved with the distributed winding. It uses a modern, sophisticated automation technique to incorporate this fill factor. This fill factor is not possible even for other commercial traction manufacturers.

Figure 3.13 shows the magnet and reluctance torques of the BMWi3 motor, d-axis inductance (L_d), and the q-axis inductance (L_q) are not the same for this buried IPM motor. The saliency of the machine is (L_q/L_d) is 3.66, which makes the reluctance torque and the magnet torque close to each other. This motor can be called a PM assisted synchronous reluctance motor.

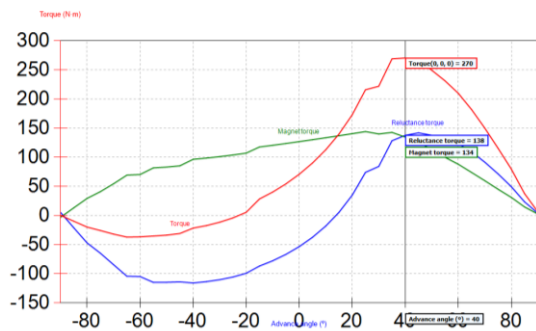


Figure 3.5. Magnet Torque and Reluctance Torque of BMWi3

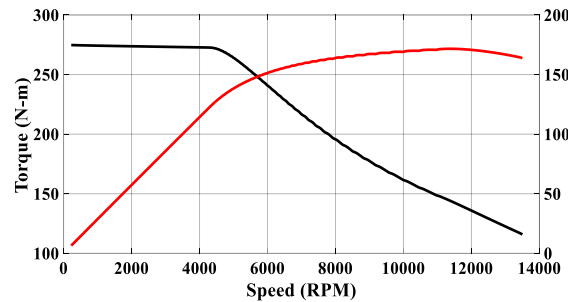


Figure 3.4. Speed Vs Torque & Speed Vs Power

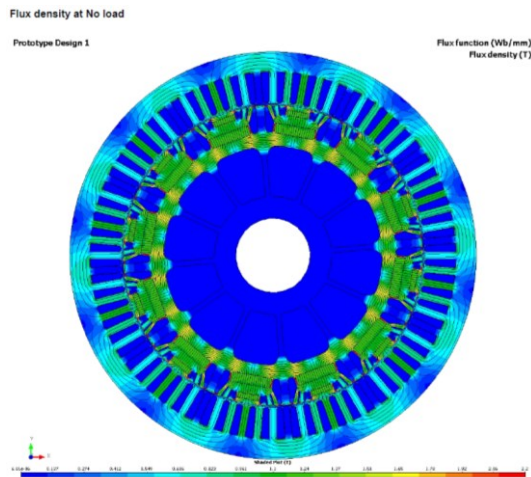


Figure 3.3. No load flux density of BMWi3 motor

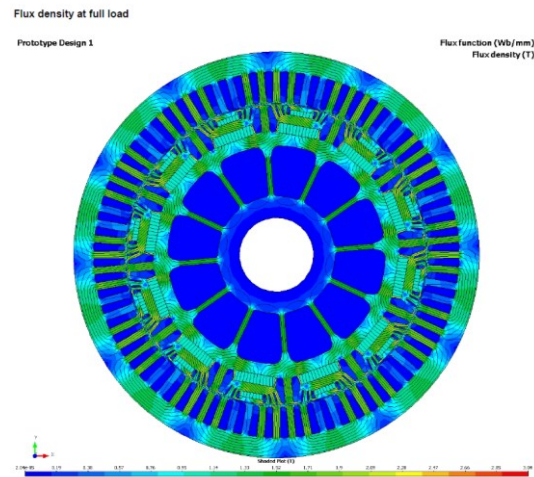


Figure 3.6. Full load flux density of BMWi3 motor

Figure 3.14 shows the constant torque and constant power mode for the BMWi3 motor. The constant power can be achieved by equating the flux linkage with the d-axis inductance and current [20]. Figure 3.15 shows the no-load flux density of the BMWi3 motor, and Figure 3.16

shows the full load flux density of the BMWi3 motor. The yoke flux density and the teeth flux density are designed to be less than 1.5 T, which helps to reduce the iron loss of the motor. The peak open-circuit air gap flux density is 0.6 T which is helpful to achieve maximum speed in the flux weakening mode.

3.4 Benchmarking of 2005 Honda Accord [6]

The 2005 hybrid Accord is an example of how the automotive industry introduces hybrid technology to pre-existing vehicle models. This Accord design is a "mild hybrid" due to the low power rating of the integrated motor assist (IMA) and the fact that it is used only for acceleration to assist the engine [21].

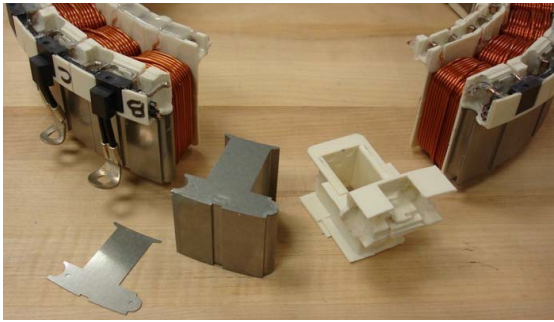


Figure 3.8. Stator disassembly showing daisy-chain lamination design [21]

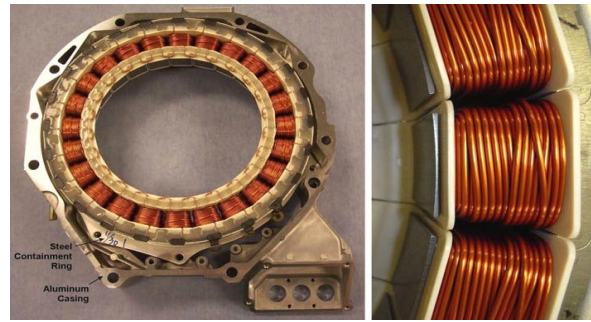


Figure 3.7. Rotor with close view of bobbins

Figure 3.17 shows the Accord motor rotor with the bobbins. Figure 3.18 shows the stator disassembly showing the daisy chain lamination design. Figure 3.18 shows the modular design and assembly of the stator. Small stacks of laminations are assembled for each coil. These are held in place by two plastic shells that are slid over the laminations from the top and bottom of the stack. Each bobbin stack assembly is shaped to hold its position relative to adjacent stacks. The bobbin stack assemblies are held together incidentally by the neutral line and the three-phase wires that circle around the stator and a flexible compound that holds these four wires and secures the connections. However, the primary mechanical support is the steel containment ring with mounting holes (left bottom corner of Fig. 3.17) [21].

Table 3.3: Key design parameters for the Accord PMSM [21]

Parameter	Accord
Stator OD, mm	315.5
Stator ID, mm	232
Rotor OD, mm	230
Rotor ID, mm	188
Rotor stack length, mm	41.2
Stator stack length, mm	40.1
Air gap, mm	1
End-turn length, mm	35
Stator turns per coil	52
Parallel circuit per phase	8
Turns in series per phase	0
Number of poles	16
Number of stator slots	24
Number of wires in parallel	0
Wire diameter	1.55 mm
Slot depth, mm	30.6
Slot opening, mm	4.75
Stator winding mass, kg	3.01
Stator core mass, kg	7.704
Rotor mass, kg	8.02
Magnet mass, g	25

Table 3.2 shows the design specifications of the Accord motor, the DC bus voltage of the motor is 144 V, and the maximum current is 225A, and the maximum torque which can be obtained

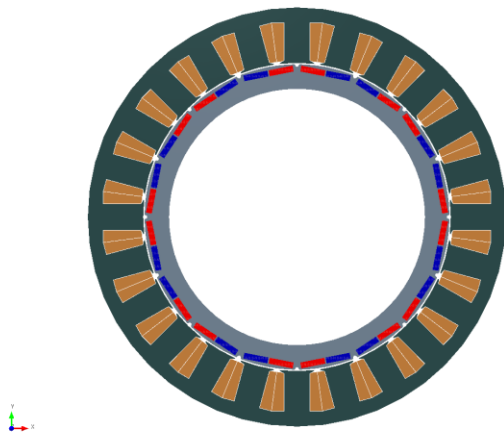


Figure 3.19. Accord Model in MotorSolve

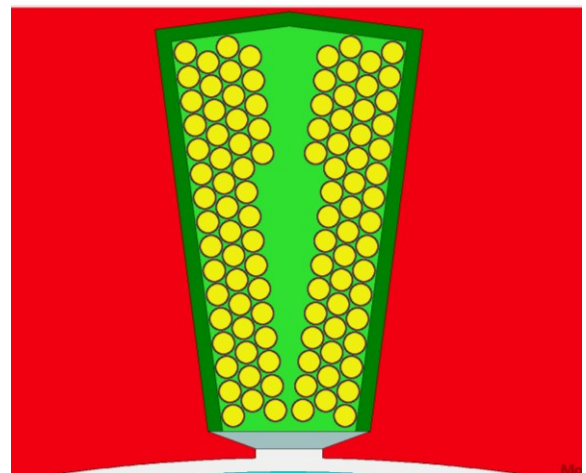


Figure 3.20. Winding Model of Accord motor in Motor-CAD

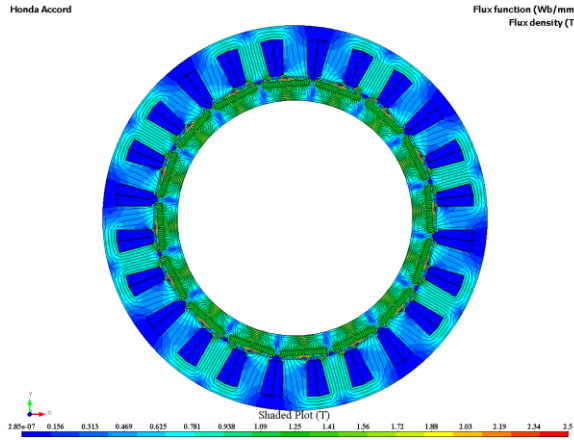


Figure 3.21. Honda Accord Model in MotorSolve (No load flux plot)

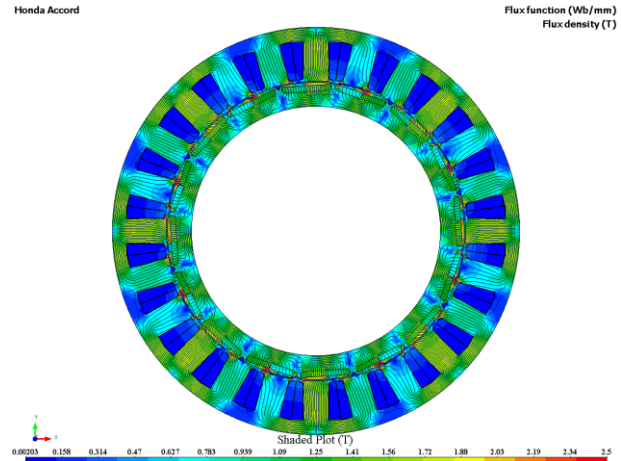


Figure 3.22. Honda Accord Model in MotorSolve (Full load flux plot)

from the motor is 135 N-m. The rated speed of the motor is 850 rpm, and the maximum speed is 6000 rpm. The same machine is simulated in the ANSYS Motor-CAD package, and the results are discussed in the next section. Figure 3.19 and 3.20 shows the Accord model in Motor-CAD. The Accord motor incorporates segmented stator winding, and the copper conductors are pre-wound onto the tooth body. Other commercial machines have a wire diameter of 0.8 mm, but the Accord uses a wire diameter of 1.6 mm with the segmented winding technology, which eventually reduces the copper loss of the motor.

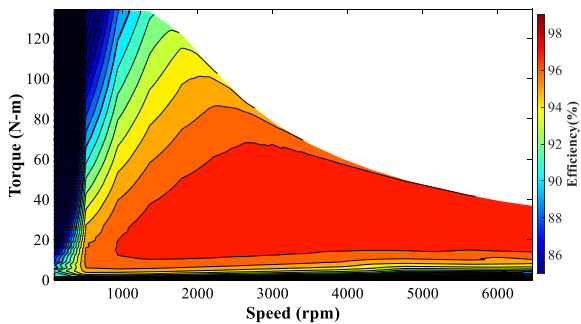


Figure 3.23. Efficiency Map of Honda Accord

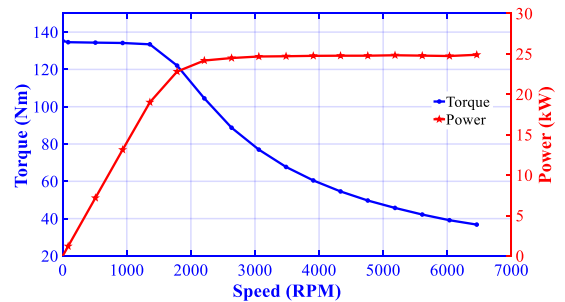


Figure 3.24. Speed Vs Torque of Accord Motor

Figs 3.21 and 3.22 show the no load and full load flux density plot for the Honda Accord motor. Fig. 3.23 and 24 show the efficiency map and speed vs torque characteristics of the Honda Accord Motor. The maximum torque of 130 N-m is achieved at the rated speed of 850 rpm. Constant power is maintained by satisfying the conditions of inductance and flux linkage.

3.5 Analytical Design of Interior PMSMs

The design procedure below [22] [20] shows the calculation for a 12 slot 8 pole PMSM. The same formula is used for other slot/pole combinations. The interior PMSM is designed for the following specifications,

Power = 7.1 kW

DC Bus Voltage = 96 V

Rated Torque = 20 Nm

Pole (N_m) = 8

Slots (N_s) = 12

Base Speed = 3400 RPM

Max Speed = 10000 RPM

The torque as being produced at the rotor surface, the torque per unit rotor volume (TRV) is given by 2-1 and shown in Fig. 3.24,

$$TRV = \frac{T}{V_r} = \frac{T}{\pi r^2 L} \quad (3-1)$$

The torque can be related to average shear stress at the rotor surface. Consider one square unit of area on the rotor surface. If the average shear stress is σ , then the torque is given by,

$$T = 2\pi r^2 L \sigma \quad (3-2)$$

Using equations 2-1 and 2-2,

$$TRV = 2\sigma \quad (3-3)$$

The unit of TRV is kNm/m^3 and of σ is kN/m^2 . In imperial units, σ is usually expressed in p.s.i., and TRV in lb/in^3 . A value of 1 p.s.i. ($6.9 kN/m^2$) corresponds to a TRV of 2 in lb/in^3 ($13.8 kNm/m^3$). Typical values of σ for different types of machines are given in Table 3.4

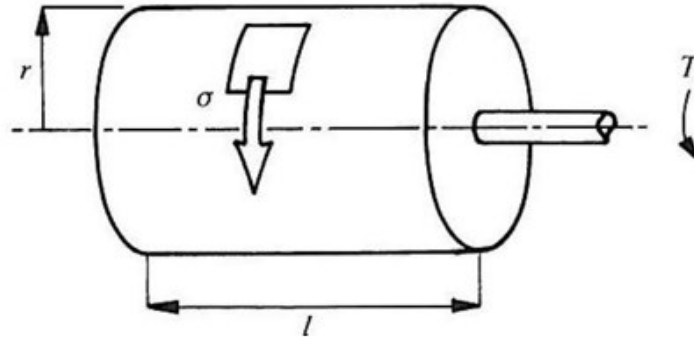


Figure. 3.25 Torque per unit rotor volume (TRV) and air-gap shear stress

Table 3.4 Typical values of σ for different types of machines

Machine type and size	σ [psi] ($1 \text{ psi} = 6.9 \frac{kN}{m^2}$)
Fractional industrial motors	0.1-0.3 psi ($0.69 - 3.07 \frac{kN}{m^2}$)
Integral industrial machines	0.5 - 2 psi ($3.45 - 13.8 \frac{kN}{m^2}$)
High-performance industrial servos	1.5-3 psi ($10.35 - 20.7 \frac{kN}{m^2}$)
Aerospace machines	3-5 psi ($3.45-13.8 \frac{kN}{m^2}$)
Very large liquid-cooled machines	10-15 psi ($69-103.5 \frac{kN}{m^2}$)

- The angular mechanical speed is given by,

$$\omega_m = \left(\frac{\pi}{30}\right) S_r \quad (3.4)$$

where, S_r is the mechanical speed in rpm. Therefore,

$$\omega_m = \left(\frac{\pi}{30}\right) 3400 = 356.047 \text{ rad/sec} \quad (3.5)$$

- The electrical speed is given by,

$$\omega_e = \left(\frac{N_m}{2}\right)\omega_m \quad (3.6)$$

where, ω_m is the mechanical speed, and N_m is the number of poles. Therefore, $\omega_e = \left(\frac{8}{2}\right) 356.047 = 1424.188 \text{ rad/sec}$

- Fundamental electrical frequency is given as,

$$f_e = \frac{\omega_e}{2\pi} \quad (3.7)$$

Where, ω_e is the electrical speed

$$f_e = \frac{1424.188}{2\pi} = 226.66 \text{ Hz} \quad (3.8)$$

- Torque is calculated as,

$$T = \frac{746 * P_{hp}}{\omega_m} = \frac{746 * 9.5212}{356.047} = 20.0 \text{ Nm} \quad (3.9)$$

- No. of slots considered is 13. Therefore, the number of slots /phase (N_{sp}) is four and number of slots /pole (N_{sm}) is 1.5.

- Number of slots /pole/phase (N_{spp}) is given as,

$$N_{spp} = \frac{12}{8 * 3} = 0.5 \quad (3.10)$$

- Coil pole fraction is given as,

$$\alpha_{cp} = \frac{\text{int}(N_{spp})}{N_{spp}} \quad (3.11)$$

where, N_{spp} is the slots per pole per phase.

$$\alpha_{cp} = \frac{0.5}{0.5} = 1 \quad (3.12)$$

- Pole Pitch (θ_p) is given as,

$$\theta_p = \frac{2\pi}{N_m}$$

$$\theta_p = \frac{2\pi}{8} = 0.7853 \text{ rad} = 45^\circ \quad (3.13)$$

- Slot Pitch (θ_s) is given as,

$$\theta_s = \frac{2\pi}{N_s} \quad (3.13)$$

where, N_s is no of slots

$$\theta_s = \frac{2\pi}{12} = 0.5235 \text{ rad} = 30^\circ \quad (3.14)$$

- Slot pitch in electrical radians (θ_{se}) is given as,

$$\theta_{se} = \frac{\pi}{N_{sm}} = \frac{\pi}{1.5} = 3.0943 \frac{\text{rad}}{\text{sec}} = (120^\circ) \quad (3.15)$$

- Inside stator radius (R_{si}) is given as,

$$R_{si} = R_{ro} + g = 59 + 1 = 60 \text{ mm} \quad (3.16)$$

- Pole pitch (τ_p) is given as,

$$\tau_p = R_{si} * \theta_p = 60 * 0.7853 = 47.11 \text{ mm} \quad (3.17)$$

- Coil pitch (τ_c) is given as, and here we have unity winding factor,

$$\tau_c = \alpha_{cp} * \tau_p = 1 * 47.11 = 47.11 \text{ mm} \quad (3.18)$$

- Slot pitch at air gap (τ_s) is given as,

$$\tau_s = R_{si} * \theta_s = 60 * 0.5235 = 31.41 \quad (3.19)$$

Considering the slot opening width (ω_s) as 2 mm

- Tooth width at air gap (ω_t) is given as,

$$\omega_t = \tau_s - \omega_s = 31.41 - 2 = 29.41 \text{ mm} \quad (3.20)$$

- Distribution Factor

$$k_d = \frac{\sin\left(N_{spp} * \frac{\theta_{se}}{2}\right)}{N_{spp} * \sin\left(\frac{\theta_{se}}{2}\right)} = \frac{\sin\left(0.5 * \frac{120}{2}\right)}{0.5 * \sin\left(\frac{120}{2}\right)} = 0.823 \quad (3.21)$$

- Pitch factor (k_p) is given as,

$$k_p = \alpha_{cp} = 1 \quad (3.22)$$

- Skew factor (k_s) is given as,

$$k_s = 1 - \frac{\theta_{se}}{2\pi} = 1 - \frac{3.0923}{2\pi} = 0.667 \quad (3.23)$$

- Flux Concentration factor (C_ϕ) is given as,

The magnet arc is $360^\circ/8 = 45^\circ$. Hence it is reduced to 42° therefore,

$$\alpha_m = 42^\circ/45^\circ = 0.93$$

$$C_\phi = \frac{2 * \alpha_m}{1 + \alpha_m} = \frac{2 * 0.93}{1 + 0.93} = 0.9637 \quad (3.24)$$

- Permeance coefficient (P_c) is given as,

$$P_c = \frac{l_m}{g * C_\phi} \quad (3.25)$$

In a motor, the static operating point lies in the second quadrant, usually at a P_c of 4 or more. Therefore taking P_c value as 5.

$$l_m = P_c * g * C_\phi = 5 * 1 * 0.9637 = 4.82 \text{ mm} \quad (3.26)$$

- Magnet leakage factor (k_{ml}) is given as,

$$k_{ml} = 1 + \frac{4 * l_m}{\pi * \mu_r * \alpha_m * \tau_p} \ln \left[1 + \frac{\pi g}{(1 - \alpha_m) \tau_p} \right] \quad (3.27)$$

$$k_{ml} = 1 + \frac{4 * 4.82}{\pi * 1.06427 * 0.93 * 47.11} \ln \left[1 + \frac{\pi * 1}{(1 - 0.93) * 47.11} \right]$$

$$k_{ml} = 1.043 \approx 1$$

- The effective air-gap for carter's coefficient is given as,

$$g_c = g + \frac{l_m}{\mu_r} = 1 + \frac{4.82}{1.06427} = 5.535 \text{ mm} \quad (3.28)$$

$$g_c = g + \frac{l_m}{\mu_r} = 1 + \frac{4.82}{1.06427} = 5.535 \text{ mm}$$

- Carter coefficient (k_c) is given as,

$$k_c = \left[1 - \frac{1}{\frac{\tau_s}{\omega_s} \left[\frac{5g_c}{\omega_s} + 1 \right]} \right]^{-1} \quad (3.29)$$

$$k_c = \left[1 - \frac{1}{\frac{\tau_s}{\omega_s} \left[\frac{5g_c}{\omega_s} + 1 \right]} \right]^{-1}$$

$$k_c = \left[1 - \frac{1}{\frac{11.93}{3} \left[\frac{5 * 5.535}{3} + 1 \right]} \right]^{-1}$$

$$k_c = 1.004$$

- Air-gap area (A_g) is given as,

$$A_g = \frac{\tau_p L (1 + \alpha_m)}{2} \quad (3.30)$$

$$A_g = 3864 \text{ mm}^2$$

- Air-gap flux density (B_g) is given as,

$$B_g = \frac{C_\phi}{1 + \mu_r K_c k_{ml} / P_c} B_r \quad (3.30)$$

B_r for N35 SH magnet is 1.21

$$B_g = \frac{0.9637}{1 + (1.06427 * 1.0252 * 1) / 5} * 1.21 = 0.7864 \text{ T}$$

- Air-gap flux (ϕ_g) is given as,

$$\phi_g = B_g * A_g \quad (3.31)$$

$$\phi_g = \frac{0.7864 * 3864}{1000000} = 0.0303 \text{ Wb}$$

High-grade materials are always the desired materials since they have the highest resistivity with more silicon percentage and hence the least core losses. A thinner lamination also reduces the losses as the grade number is decreased. Therefore, M35G29 is considered for the design.

Lamination thickness = 0.3556 mm

$B_{max} = 1.4 \text{ T}$

Stacking factor (k_{st}) = 0.95 for lamination

Stacking factor (k_{st}) = 0 for SMC (Solid Steel)

3.6 Stator dimension calculations

- Stator back iron width (w_{bi}) is given as,

$$w_{bi} = \frac{\varphi_g}{2 * B_{max} * k_{st} * L} = \frac{0.012}{2 * 1.2 * 0.95 * 0.85} * 1000 = 6.19 \text{ mm} \quad (3.32)$$

- Tooth width (w_{tb}) is given as,

$$w_{tb} = \frac{2}{N_{sm}} * w_{bi} = \frac{2}{1.5} * 6.19 = 9.066 \text{ mm} \quad (3.33)$$

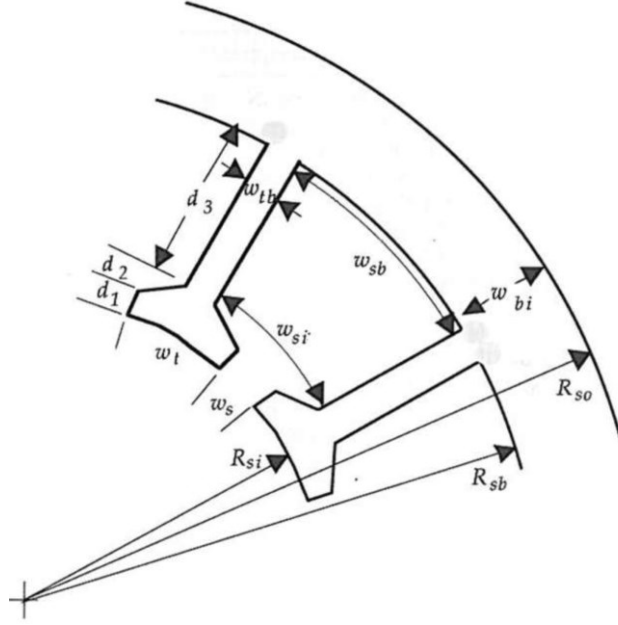


Figure. 3.26. Slot geometry for the radial flux motor topology

Total slot depth (d_s) is assumed to be 19 mm

- Outside stator radius (R_{so}) is given as,

$$R_{so} = R_{si} + w_{bi} + d_s = 60 + 6.19 + 19 = 85.19 \text{ mm} \quad (3.34)$$

- Stator back iron radius (R_{sb}) is given as,

$$R_{sb} = R_{so} - w_{bi} = 85.19 - 6.19 = 79 \text{ mm} \quad (3.35)$$

- The rotor inside radius (R_{ri}) is given as,

$$R_{ri} = R_{ro} - w_{bi} = 59 - 6.19 = 52 \text{ mm} \quad (3.36)$$

- Slot bottom width (w_{sb}) is given as,

$$w_{sb} = R_{sb} * \theta_s - w_{tb} = 79 * 0.2 - 9.06 = 6.74 \text{ mm} \quad (3.37)$$

Assuming $\alpha_{sd} = 0.2$

Again, to ensure slot depth (d_s),

$$d_s = R_{sb} - R_{ro} - g = 79 - 59 - 1 = 19 \text{ mm} \quad (3.38)$$

- Conductor slot depth (d_3) is given as,

$$d_3 = d_s - \alpha_{sd} w_{tb} = 19 - 0.2 * 9.066 = 17.18 \text{ mm} \quad (3.39)$$

Therefore,

$$d_1 + d_2 = \alpha_{sd} w_{tb} = 0.2 * 9.066 = 1.81 \text{ mm}$$

It is assumed that the tooth tip thickness (d_1) is 0.8 mm hence d_2 is 0.36 mm

- Conductor area (A_s) is given as,

$$A_s = d_3 \left[\theta_s \left(R_{sb} - \frac{d_3}{2} \right) - w_{tb} \right] \quad (3.40)$$

$$A_s = 17.18 \left[0.5235 \left(79 - \frac{17.18}{2} \right) - 9.066 \right] = 475.87 \text{ mm}^2$$

- The maximum back-EMF (E_{max}) is taken as $0.45 * 96 \text{ V} = 43 \text{ V}$, so the number of turns per slot is,

$$n_s = \text{int} \left(\frac{E_{max}}{N_m * K_d * K_p * K_s * B_g * L * R_{ro} * N_{spp} * \omega_m} \right) \quad (3.41)$$

$$n_s = \text{int} \left(\frac{43}{8 * 0.823 * 1 * 0.667 * 0.7864 * 0.59 * 0.85 * 0.5 * 356.4} \right)$$

$$n_s = \text{int}(1.2) \approx 2 \text{ turns}$$

The above equations are used to calculate initial slot/pole combinations. These equations helped to determine the parameters analytically. Although magnetic saturation and demagnetization are not considered. However, the aforementioned equations are applied in the preliminary stages of design, whereas for subsequent designs, the FEA package is efficiently employed to choose the appropriate parameters. Twizy is a two-seater electric car. The CRD project is to develop a novel electric motor using novel materials specifically for the Twizy car.

3.7 Initial designs for Twizy

A preliminary analysis has been carried out for higher pole and lower pole configurations. Also, a comparison has been made for both the laminated stator and SMC stator. Also, the comparison has been done for the rectangular magnet arrangement and cobra type arrangement for preliminary results.

3.7.1 2-D FEA of Higher Pole and Lower Pole configurations

The SMC performs better when the operating frequency is higher. To prove the benefits of SMC, the motor has been designed with higher pole configurations. The 24 slots 20 poles have been chosen for the higher pole configuration. This slot pole configuration has an SPP of 0.4, which obeys the conditions for constant power operation [23]. Also, this slot pole combination makes the winding pattern to be concentrated. The commercial NdFeB magnet is chosen for the analysis.

Higher Pole Configurations with SMC Stator

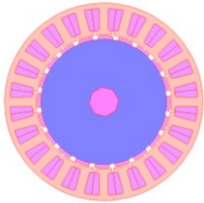


Figure 3.27. 24 slot 20 pole with SMC

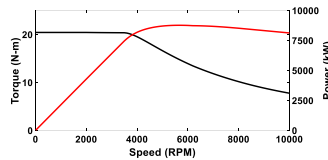


Figure 3.28. Speed Vs Torque and Speed Vs Power

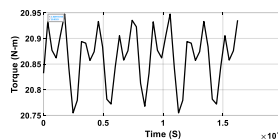


Figure 3.29. Torque ripple of 24 slot 20 pole machine

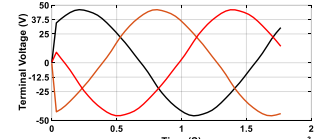


Figure 3.30. Back EMF of 24 slot 20 pole machine

Higher Pole Configurations with Laminated Stator

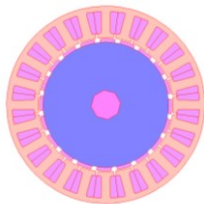


Figure 3.31. 24 slot 20 pole with Laminated Steel

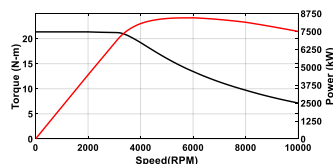


Figure 3.32. Speed Vs Torque and Speed Vs Power

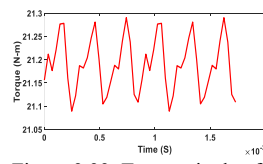


Figure 3.33. Torque ripple of 24 slot 20 pole machine

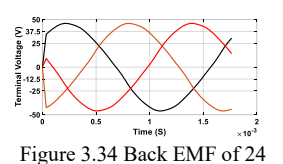


Figure 3.34. Back EMF of 24 slot 20 pole machine

Lower Pole Configurations with SMC Stator

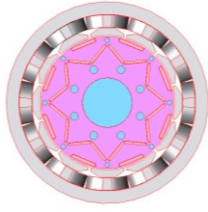


Figure 3.35. 12 slot 8 pole with SMC

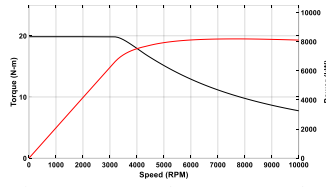


Figure 3.36. Speed Vs Torque and Speed Vs Power

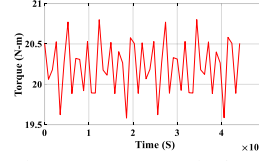


Figure 3.37. Torque ripple of 12 slot 8 pole SMC machine

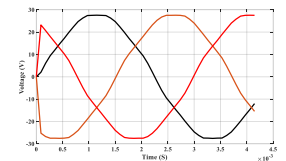


Figure 3.38. Back EMF of 12 slot 8 pole SMC machine

Table 3.5: Comparison of higher pole and lower pole configurations

Parameters	24 slot 20 Pole SPM with Bonded Magnet and Laminated Steel	24 slot 20 Pole SPM with Bonded Magnet and SMC	Twizy IPM – SMC [8 Pole – 12 Slots]	Twizy IPM – Lam. Steel [8 Pole – 12 Slots]
Stator core	Laminated steel (M36G29)	SMC	SMC	Laminated Steel(M36G29)
Rotor core	Laminated steel (M36G29)	Laminated Steel	Laminated Steel	Laminated Steel(M36G29)
Stator OD	180 mm	180 mm	165	180
Rotor OD	120 mm	120 mm	110 mm	120 mm
Airgap length	1 mm	1 mm	1 mm	1 mm
Stacking factor	97%	97%	100 %	97%
Active stack length	87 mm	87 mm	95 mm	105 mm
Overall stack length	120mm	87 mm	95 mm	135 mm
Average torque	20	20	20 Nm	20 Nm
Current (rms)	113 A	130 A	116.6 A	88.3A
Current density (rms)	5.0A/ mm ²	4.0A/ mm ²	5.3 A/mm ²	5.3 A/mm ²
AWG type	SWG 21 (0.812 mm diameter)			
Slot fill factor	40% Concentrated Winding	60 % Concentrated winding	60 % Concentrated winding	40 % Distributed winding
Conductors per slot	172	236	272	200
Resistance				
Phase resistance	0.003219 Ω	0.00213 Ω	0.003574 Ω	0.00461 Ω
Loss @3400 RPM				
Copper loss (3400 rpm)	128.904 W	105.59 W	129.5 W	137.3 W
Iron loss (3400 rpm)	223.4 W	323.61 W	300.60W	86.19 W
Total loss (3400 rpm)	351.30W	428.2 W	430.1 W	223.49 W
Loss @10,000 RPM				
Copper loss (10000 rpm)	118.21 W	81.39 W	129 W	137 W
Iron loss (10000 rpm)	2058 W	1583.5 W	820.15 W	867.81W
Total loss (10000 rpm)	2176.2 W	1609.89	949.1 W	833.8 W
Weight				
Stator	5.50 kg	5.32 kg	5.80 kg	8.71 kg
Winding	3.25 kg	3.403 kg	3.48 kg	3.29 kg
Rotor	6.45 kg	6.45 kg	4.64 kg	6.16 kg
Magnet	0.41 kg	0.415 kg	0.611 kg	0.85 kg
Shaft (Mild steel)	1.34 kg	1.34 kg	1.34 kg	1.34 kg
Total	15.95 kg	16.92 kg	14.87 kg	19.35 kg
Power density	2325.1 kW/ m ³	3207.03 kW/ m ³	3495.24 kW/ m ³	2066.75 kW/ m ³
Torque density (Rot vol)	20.326 kNm/ m ³	20.326 kNm/ m ³	23.981 kNm/ m ³	16.84 kNm/ m ³
Torque density (Mot vol)	5.2 kNm/ m ³	7.64 kNm/ m ³	7.32 kNm/ m ³	5.821 kNm/ m ³
Split Ratio (R/S)	66.6 %	66.6%	66.66%	66.66%
Tip Speed (m/s)	63.8 m/s	63.8 m/s	57.5 m/s	63.8 m/s
Air gap shear stress (lbf/in ²)	1.4	1.4	1.66	1.22

Table 3.5 shows the comparison of the lower pole and the higher pole configurations with lamination stator and the SMC stator. Iron loss is proved to be less in SMC with a higher pole.

The iron loss for laminated steel stator with 20 poles is 2058W, but the iron loss for SMC stator with 20 poles is 1583.5 W. This clearly indicates that the SMC is the best candidate to operate at a higher frequency. Also, the fill factor of the SMC stator can be increased to 60%, but with the laminated steel, the fill factor cannot be increased by more than 40% due to the manufacturing disadvantage. The increase in fill factor helps reduce the machine's phase resistance, which in turn reduces the copper loss of the machine. So, the current density of the SMC machines can be increased over laminated stator machines. From this result and comparison, the 12 slots 8 poles concentrated winding is chosen for further analysis.

3.7.2 Using BMW-i3 rotor for Twizy motor design using NdFeB ($B_r = 1.2 T$)

BMW i3 rotor is used for the design of Twizy motor. In the original BMW motor, liquid cooling is used for cooling the motor. But in this case, the motor is designed to operate without forced cooling. Also, BMW i3 has 12 poles, but in this case the poles are reduced to 8.

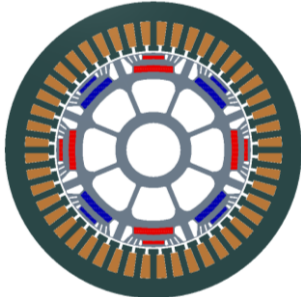


Fig. 3.39. Twizy motor with BMW i3 rotor with 48 slots

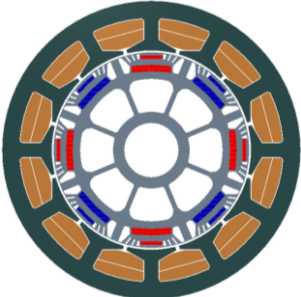


Fig. 3.40. Twizy motor with BMW i3 rotor with 48 slots

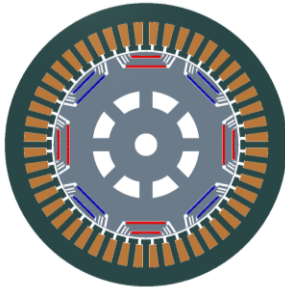


Fig. 3.41. Twizy motor with BMW i3 rotor with 48 slots (thinner magnets)

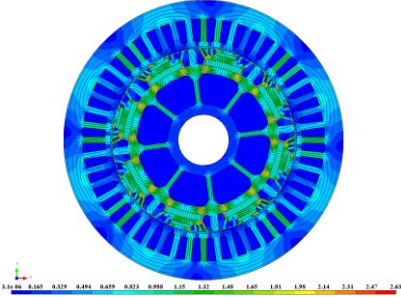


Fig. 3.42. Full load flux density plot of Twizy motor with BMW i3 rotor with 48 slots

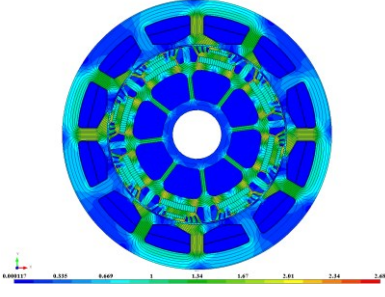


Fig. 3.43. Full load flux density plot of Twizy motor with BMW i3 rotor with 12 slots

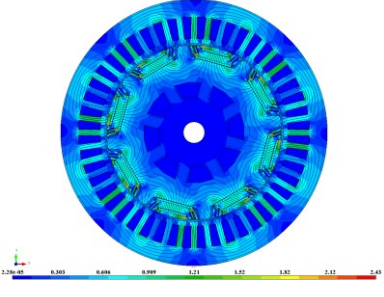


Fig. 3.44. Full load flux density plot of Twizy motor with BMW i3 rotor with 48 slots (thinner magnets)

Fig. 3.39 to 3.41 show the schematic of BMW i3 rotor designs for Twizy motor with NdFeB magnets. Fig. 3.42 to 3.44 show the full load flux density plot of all the three designs.

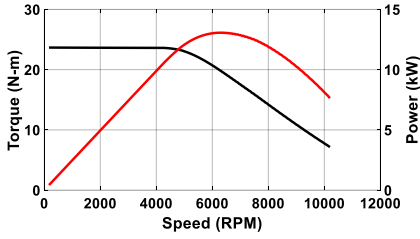


Fig. 3.45. Twizy motor with BMW i3 rotor with 48 slots

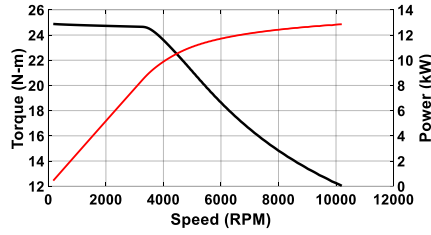


Fig. 3.46. Twizy motor with BMW i3 rotor with 12 slots

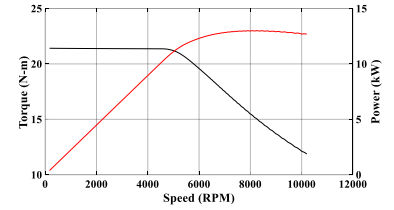


Fig. 3.47. Twizy motor with BMW i3 rotor with 48 slots (thinner magnets)

Table 3.6: Comparison of Twizy motor designed with BMW i3 rotor

Parameters	Twizy with BMWi3 Rotor (48 slot 8 pole)	Twizy with BMWi3 Rotor (48 slot 8 pole) Thinner magnet	Twizy with BMWi3 Rotor (12 slot 8 pole)	Original BMWi3 Motor (72 slot 12 pole)
d-axis Inductance (L_d)	0.0639 mH	0.0831 mH	0.151 mH	0.0763 mH
Peak current (I_s)	155.5 A	155.5 A	155.5 A	500 A
Calculated flux linkage (λ_m)	0.01 Wb	0.012 Wb	0.023 Wb	0.0381 Wb
FEA obtained flux linkage (λ_m)	0.0216 Wb	0.019 Wb	0.0216 Wb	0.0419 Wb

3.7.3 Using BMW-i3 rotor for Twizy motor using coldspray magnet

48 slot 8 pole has been considered for the analysis with coldspray magnets. It can be sprayed to any complex shapes, which significantly reduces the cost of the motor. BMW i3 rotor is shaped to form a scallop design for Twizy motor specifications which is shown in Figs 3.48 and 3.49.

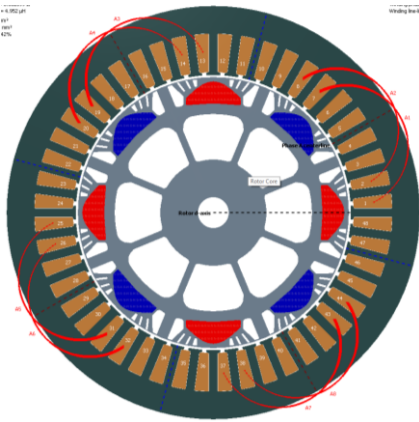


Fig. 3.48. Scallop design with coldspray magnet

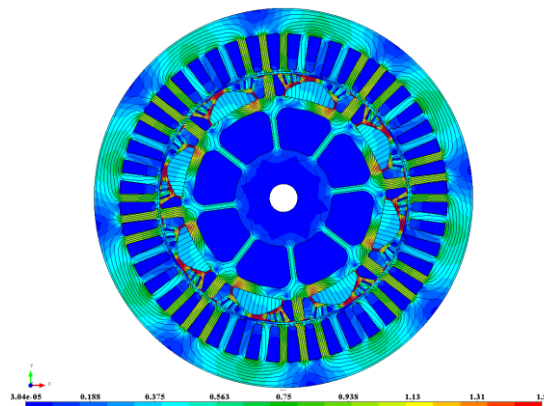


Fig. 3.49. Flux density plot of Scallop design with coldspray magnet

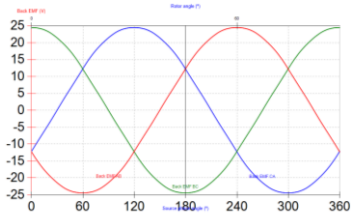


Fig. 3.50. Phase back EMF of Scallop design

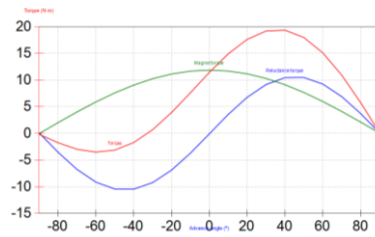


Fig. 3.51. Torque angle curves of scallop design

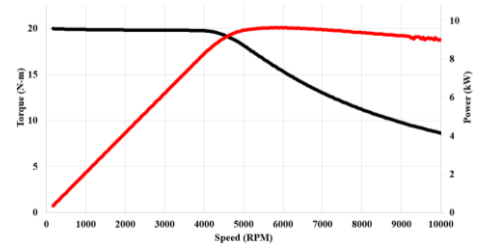


Fig. 3.52. NT vs NP curve for scallop design

Figures 3.50 to 3.52 depict the phase back EMF, torque angle, and NT vs NP curve for a scallop design. In the preceding section, a comparison was made between the 48-slot/8-pole and 12-slot/8-pole configurations for the Twizy motor specifications. The results demonstrated that the 12-slot/8-pole configuration offers greater flux weakening compared to the 48-slot/8-pole configuration for these specifications. However, it is possible to achieve a wider flux weakening with the 48-slot/8-pole motor if it is designed using low Br magnets such as coldspray magnets.

3.7.4. 12 slot 8 pole with Commercial magnet and cold spray magnet

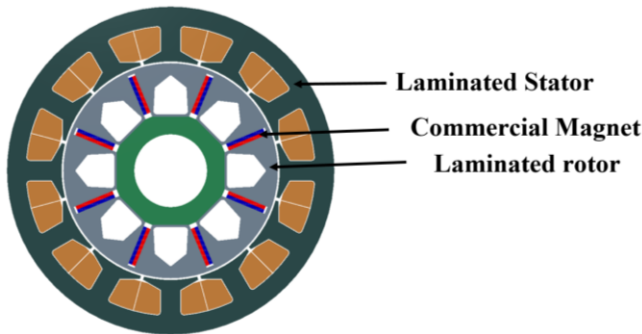


Fig. 3.53. 12-slot/8-pole PMSM with laminated stator (NdFeB)

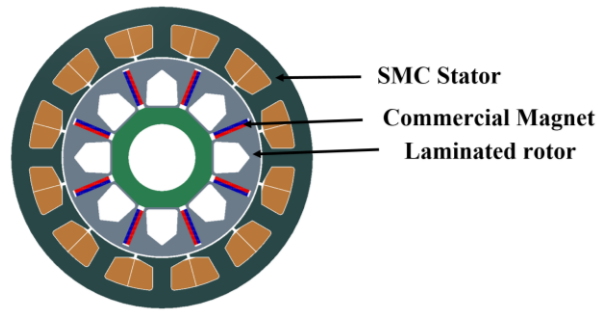


Fig. 3.54 12-slot/8-pole PMSM with SMC stator (NdFeB)

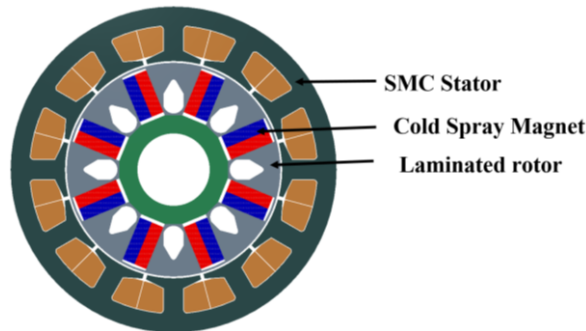


Fig. 3.55 12-slot/8-pole PMSM with SMC stator using cold spray magnet (Coldspray)

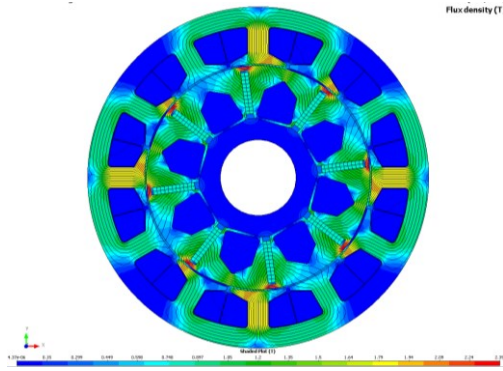


Fig. 3.56 Flux density of 12-slot/8-pole PMSM with laminated stator (NdFeB)

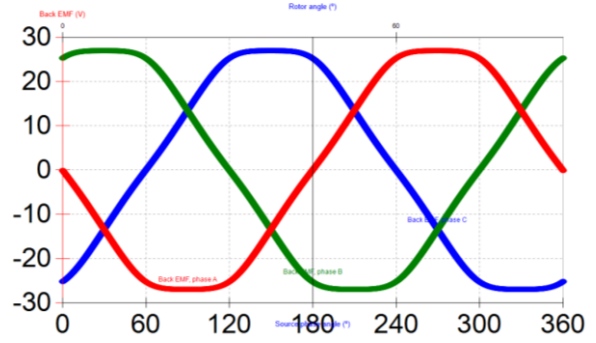


Fig. 3.57 Phase back EMF of 12-slot/8-pole PMSM with laminated stator (NdFeB)

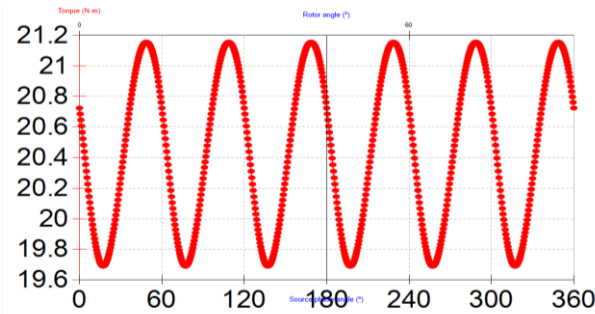


Fig. 3.58 Torque of 12-slot/8-pole PMSM with laminated stator (NdFeB)

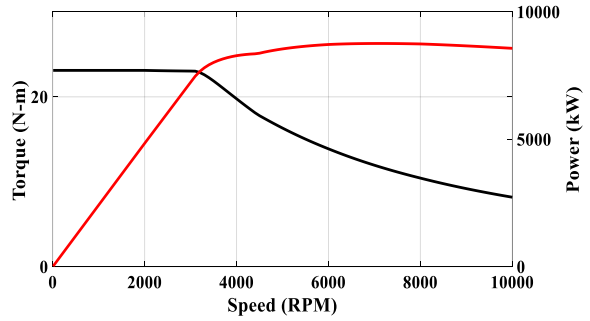


Fig. 3.59 NT and NP of 12-slot/8-pole PMSM with laminated stator (NdFeB)

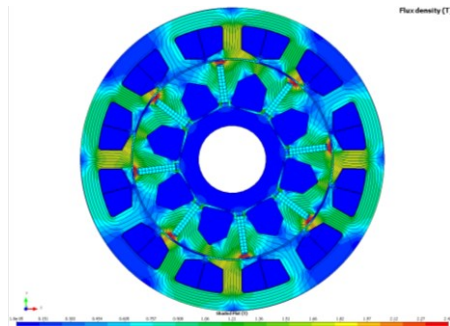


Fig. 3.60 Flux density of 12-slot/8-pole PMSM with SMC stator (NdFeB)

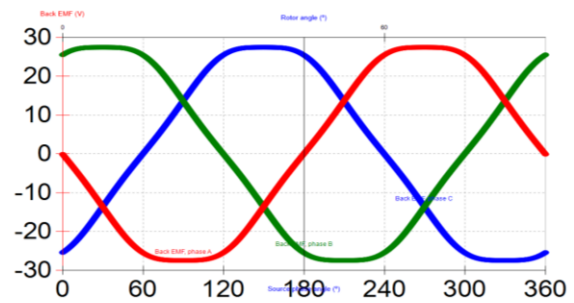


Fig. 3.61 Phase back EMF of 12-slot/8-pole PMSM with SMC stator (NdFeB)

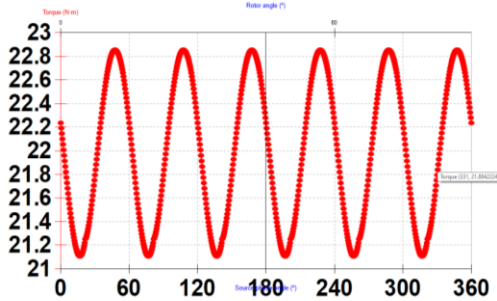


Fig. 3.62 Torque of 12-slot/8-pole PMSM with SMC stator (NdFeB)

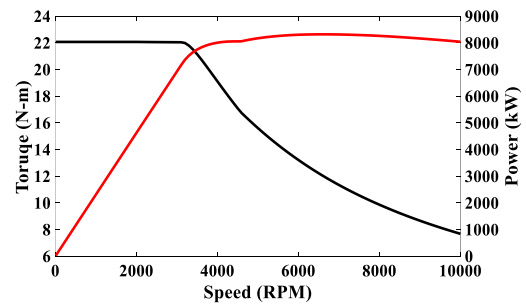


Fig. 3.63 NT and NP of 12-slot/8-pole PMSM with SMC stator (NdFeB)

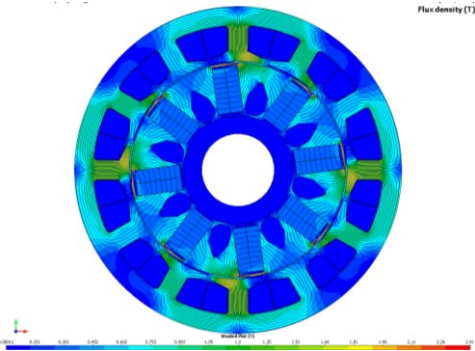


Fig. 3.64. Flux density of 12-slot/8-pole PMSM with laminated stator (NdFeB)

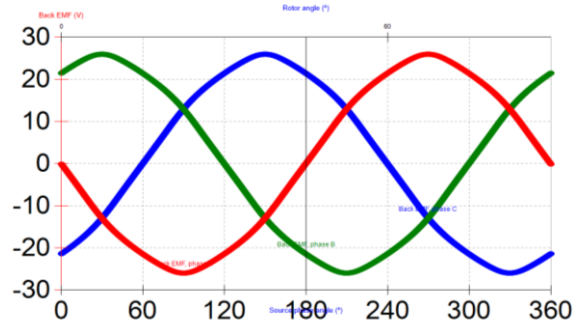


Fig. 3.65. Phase back EMF of 12-slot/8-pole PMSM with laminated stator (NdFeB)

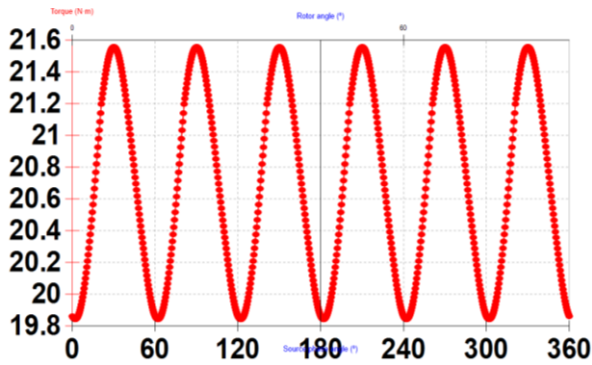


Fig. 3.66. Torque of 12-slot/8-pole PMSM with laminated stator (NdFeB)

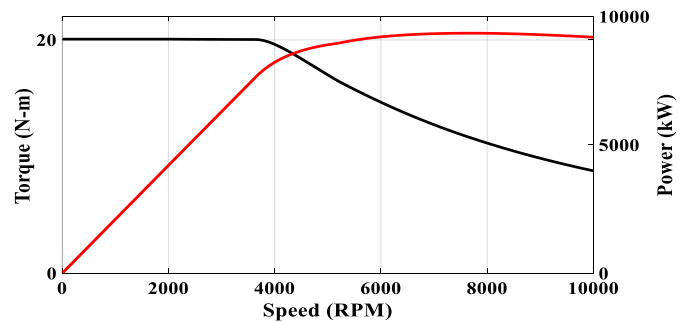


Fig. 3.67. NT and NP of 12-slot/8-pole PMSM with laminated stator (NdFeB)

Figures 3.57 to 3.67 illustrate the 12-slot/8-pole designs for the Twizy motor using both commercial and coldspray magnets. The stator is examined using both laminations and SMC materials, and initially a hub arrangement is considered for the design. The hub is constructed of aluminum to reduce flux leakage. Thicker magnets are required for coldspray magnet designs to achieve the desired performance. In nearly all cases, the machine performs better than the commercial magnet design in flux weakening mode with a wider flux weakening region.

The phase back EMF is closer to a sine wave for coldspray magnets due to their thickness. All other designs also exhibit better back EMF with fewer harmonics. The stator slot is kept constant for all designs, except that the stack length and machine diameter vary based on the required performance. In commercial traction motors, the tooth tip thickness is typically very thin to improve airgap flux density and reduce slot saturation. The stator tooth tip thickness is designed based on lamination stator designs. In addition, a two-layer copper winding is used in all cases to achieve better copper fill factor.

Table 3.7: Comparison of 12-slot 8 pole - commercial magnet & cold spray magnet with SMC and laminated stator

	IPM Laminated stator & NdFeB PM (1 T)	IPM SMC stator & NdFeB PM (1 T)	IPM SMC stator and cold spray PM
Stator core	Laminated	SMC	SMC
Rotor core	Laminated	Laminated Steel	Laminated Steel
Stator OD	200 mm	180 mm	180 mm
Rotor OD	131 mm	118 mm	118 mm
Airgap length	1 mm	1 mm	1 mm
Stacking factor	0.97	0.97	0.97
Active stack length	70 mm	80 mm	100
Overall stack length	100 mm	80 mm	100
Skew angle (Rotor)	15°	15°	15°
Average torque	21.7	22	21
Current (rms)	130	130 A	135 A
Average airgap flux density	0.48 T	0.46 T	0.35 T
Current density (rms)	4.64 A/mm ²	4.47 A/mm ²	4.33 A/mm ²
Power factor	0.74	0.67	0.667
Wire diameter	0.813 mm	0.813 mm	0.813 mm
Slot fill factor	40 % Concentrated winding	60 % Concentrated winding	60 % Concentrated winding
Conductors per slot	390	504	608
Results:			
Phase resistance	0.004006 Ω	0.003796 Ω	0.003094 Ω
Copper loss (3400 rpm)	203 W	193.45 W	169.16 W
Total iron loss (3400 rpm)	140 W	256 W	245 W
Total loss (3400 rpm)	305 W	458.4W	414.16 W
Total loss [cooling – 1.5X]	457.5 W	687.6 W	621.2 W
Loss Analysis at Maximum Speed:			
Copper loss (10000 rpm)	203 W	192 W	169 W
Iron loss (10000 rpm)	820.85 W	863.3 W	786.14 W
Total loss (10000 rpm)	1023.82 W	1054.3 W	828.32 W
Weights (kg):			
Stator	5.9 kg	5.3 kg	6.63 kg
Winding	3.13 kg	3.69 kg	3.73 kg
Rotor	3.03 kg	3.81 kg	3.74 kg
Magnet	0.456 kg	0.422 kg	3.2 kg
Shaft (Mild steel)	1.34 kg	1.34 kg	1.34 kg
Total	13.856 kg	13.56 kg	16.64 kg
Power density (motor vol.)	2260.0 kW/ m ³	3487.6 kW/ m ³	2790.12 kW/ m ³
TRV (rotor vol.)	23.8 kN.m/m ³	25.1 kN.m/m ³	18.9 kN.m/m ³
Torque density (motor vol.)	6.68 kNm/ m ³	9.824 kNm/ m ³	8.25 kNm/ m ³
Rotor OD/Stator OD ratio	66 %	66 %	66 %
Air gap shear stress	1.65 lbf/in ²	1.82 lbf/in ²	1.37 lbf/in ²
Tip speed	68.59 m/sec	61.78 m/sec	61.78 m/sec

The performance of all 12-slot/8-pole designs is compared in Table 3.7, which indicates that the active stack length is increased in coldspray magnet motors to achieve the required performance. As a result, the weight of coldspray magnet motors is greater than that of commercial

magnet motors. Furthermore, SMC motors are designed with a higher fill factor to achieve lower copper losses.

3.7.5. 12 slot 8 pole with modified stator tip thickness and rotor air barrier with commercial magnet and cold spray magnet

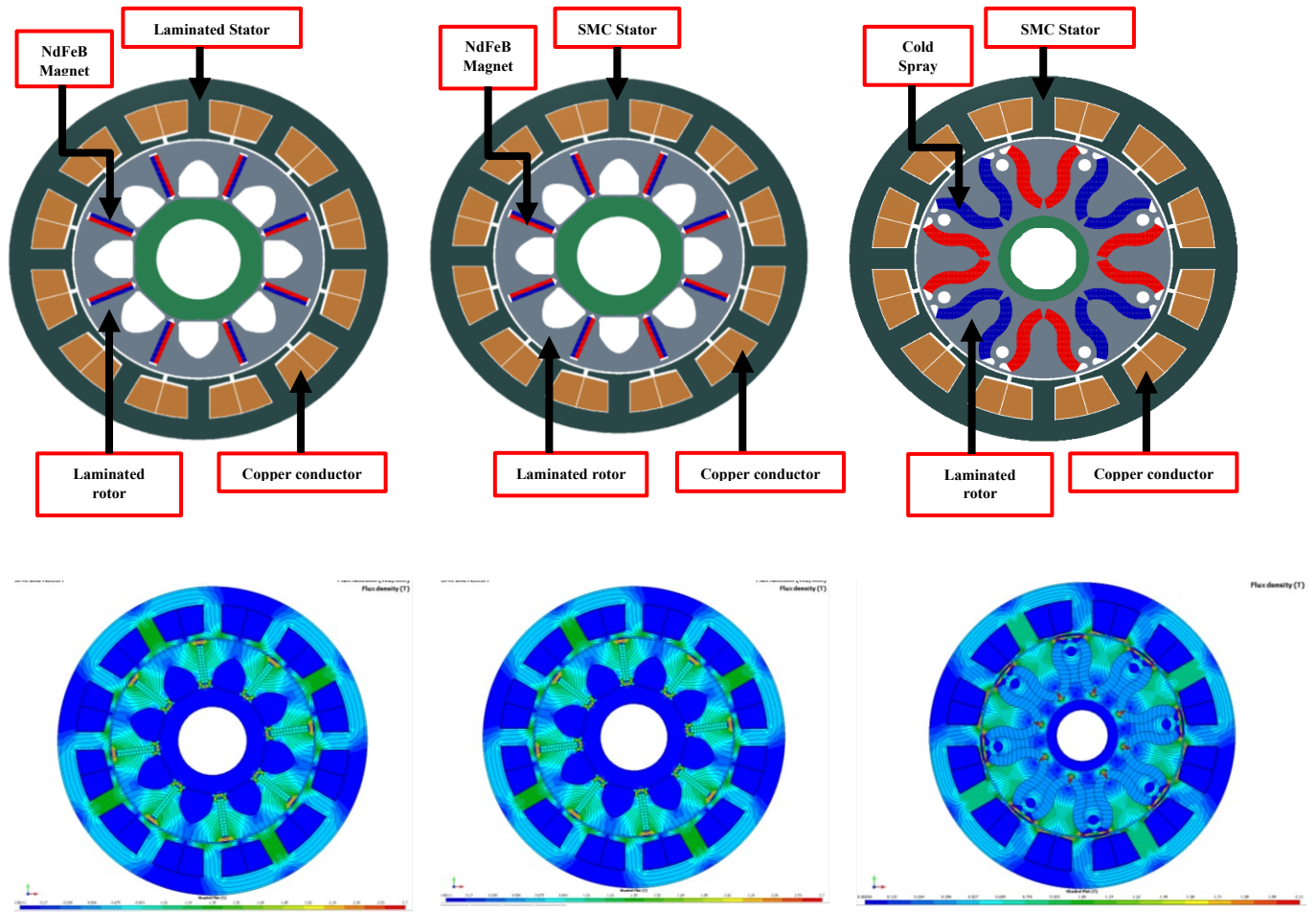


Fig. 3. 68. Modified 12 slot 8 pole designs with commercial and coldspray magnets

Figure 3.68 illustrates the modified 12-slot/8-pole designs for both commercial and coldspray magnets, with laminated stator and SMC stator designs. The rotor air barrier is modified to address manufacturing difficulties, while the stator tooth tip thickness is increased to overcome SMC stator core manufacturing challenges. The hub arrangement is retained in all designs to prevent flux leakage. In all cases, the rotor material is made of lamination steel to handle mechanical stress.

Table 3.8: Comparison of modified 12-slot 8 pole - commercial & cold spray magnet with SMC & laminated stator

	Interior PMSM Laminated steel stator NdFeB PM	Interior PMSM SMC stator NdFeB PM	Interior PMSM Laminated steel stator Cold spray PM	Interior PMSM SMC stator Cold spray PM
Stator core	Laminated Steel	SMC	Laminated Steel	SMC
Rotor core	Laminated Steel	Laminated Steel	Laminated Steel	Laminated Steel
Stator OD	200 mm	180 mm	180 mm	180 mm
Rotor OD	131 mm	118 mm	118 mm	118 mm
Airgap length	1 mm	1 mm	1 mm	1 mm
Stacking factor	97 %	100 %	97 %	100 %
Active stack length	70 mm	85 mm	120 mm	120 mm
Overall stack length	100 mm	85 mm	150 mm	120 mm
Skew angle (Rotor)	15°	15°	15°	15°
Average torque	21 Nm	21 Nm	21 Nm	21 Nm
Current (rms)	130 A	127 A	120 A	127 A
Average airgap flux density	0.48 T	0.45 T	0.35 T	0.34 T
Peak airgap flux density	0.62 T	0.62 T	0.44 T	0.448 T
Current density (rms)	5 A/mm ²	5 A/mm ²	5 A/mm ²	5 A/mm ²
Power factor	0.7	0.75	0.75	0.73
Wire diameter	0.9 mm	0.9 mm	0.9 mm	0.9 mm
Slot fill factor	40% D	60 % C	40% D	60 % C
Lq/ Ld ratio	1.16	1.16	1.3	1.3
Conductors per slot	390	400	280	384
Results:				
Phase resistance	0.004006 Ω	0.003796 Ω	0.00376 Ω	0.002986 Ω
Copper loss (3400 rpm)	203 W	183.6 W	162 W	149 W
Total iron loss (3400 rpm)	140 W	261.1 W	158.7 W	299.8 W
Total loss (3400 rpm)	305 W	444.7 W	320.7 W	448.8 W
Total loss [cooling – 1.5X]	457.5 W	667.05 W	481.05 W	673.2 W
Loss Analysis at Maximum Speed:				
Copper loss (10000 rpm)	203 W	183.6 W	162 W	149 W
Iron loss (10000 rpm)	820.85 W	884.0 W	983.2 W	961.9 W
Total loss (10000 rpm)	1023.82 W	1067.6 W	1144.2 W	1110.9 W
Weights (kg):				
Stator	5.9 kg	5.3 kg	8.21 kg	7.951 kg
Winding	3.13 kg	3.69 kg	3.46 kg	4.755 kg
Rotor	3.03 kg	3.81 kg	5.86 kg	5.86 kg
Magnet	0.456 kg	0.422 kg	3.87 kg	3.877 kg
Shaft (Mild steel)	1.34 kg	1.34 kg	1.34 kg	1.34 kg
Total	13.856 kg	13.56 kg	21.74 kg	23.78 kg
TRV (rotor volume)	23.8 kN.m/m ³	25.1 kN.m/m ³	15.09 25.1 kN.m/m ³	15.09 kN.m/m ³
Power density (motor volume)	2260 kW/m ³	3487.6 kW/m ³	1860.00 kW/m ³	2325.01 kW/m ³
Torque density (motor volume)	6.68 kNm/m³	9.824 kNm/m³	5.23 kNm/m³	6.87 kNm/m³
Torque density (motor weight)	1.5 Nm/kg	1.54 Nm/kg	0.91 Nm/kg	0.92 Nm/kg
Rotor OD/Stator OD ratio	66 %	66 %	66 %	66 %

Table 3.8 shows the design parameters for the modified 12-slot/8-pole spoke type PMSM with commercial and coldspray magnets with SMC and laminated stator designs.

3.7.6. 12 slot 8 pole with closed slots and open slots

Closed slots

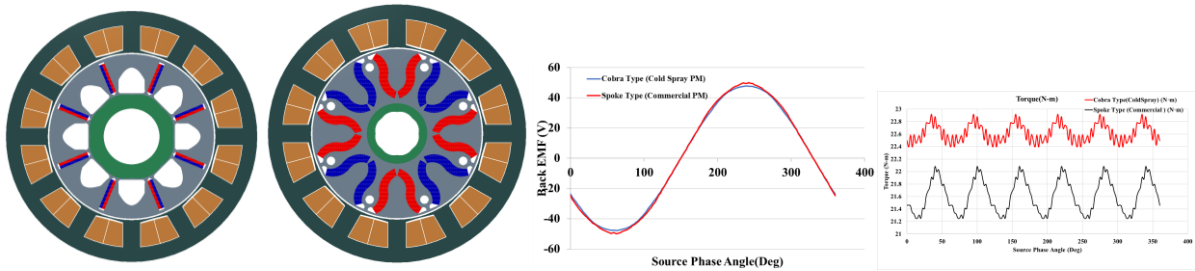


Fig. 3. 69. Closed slot 12 slot 8 pole designs with commercial and coldspray magnets

Torque Ripple

Cobra Type (Cold Spray PM) = 3.30%

Spoke Type (Commercial PM) = 3.83%

Open slots

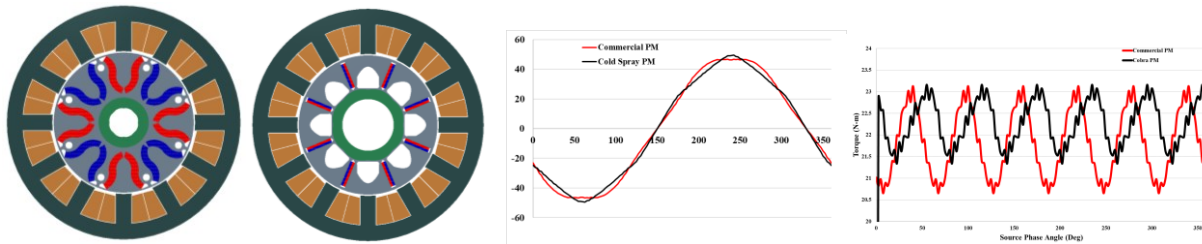


Fig. 3. 70. Open slot 12 slot 8 pole designs with commercial and coldspray magnets

Torque Ripple

Cobra Type (Cold Spray PM) = 8.177 %

Spoke Type (Commercial PM) = 11.37 %

Figures 3.69 and 3.70 display the closed slot and open slot designs, with the former demonstrating lower torque ripple than the latter. In closed slot designs, the tooth tip thickness is typically very thin, around 0.8 mm, but this is not feasible with SMC stator cores. SMC stators require at least 4 mm of tooth tip thickness to enable easy compaction and machining. Thus, a closed slot stator with a 4 mm tooth tip thickness is designed, but the average torque is significantly reduced due to saturation. Fig. 3.71 shows the full load flux density plot for the closed slot with 0.8 mm tooth tip thickness (left side) and 4mm tooth tip thickness (right side). So, considering this, open slot designs are considered for future analysis.

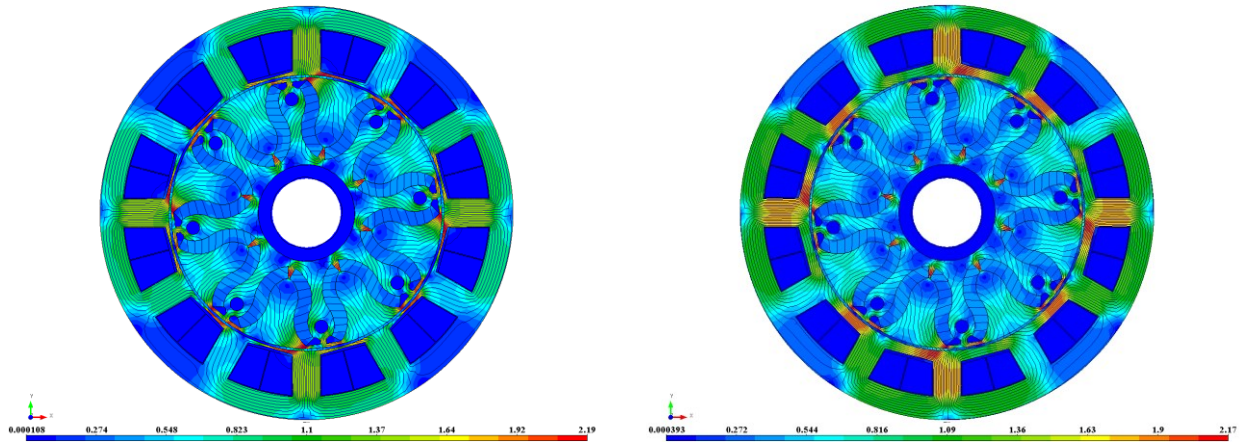


Fig. 3. 71. Open slot 12 slot 8 pole designs with commercial and coldspray magnets

Table 3.9. Comparison of tooth width for open slot configuration

Parameters	Machine	Torque Ripple (%)	Back EMF
Tooth Width = 12		<p>Torque ripple: 11.3%</p>	
Tooth Width = 15		<p>Torque ripple: 9.09%</p>	
Tooth Width = 18		<p>Torque ripple: 7.55%</p>	
Tooth Width = 20		<p>Torque ripple: 5.02%</p>	

After selecting the open slot, the tooth width is varied to check the performance of the motor in terms of torque ripple and phase back EMF which is shown in table 3.9. Varying tooth width eventually will vary the slot opening. However, the torque ripple is 5 % with the tooth width of 20 mm.

Table 3.10. Comparison of 12-slot/8-pole and 12-slot/10-pole [22]

Parameters	12/8	12/10
Winding Factor	0.866	0.966
Slot per pole per phase (SPP)	0.5	0.4 Same as constant power paper(24/20)
Back EMF and Harmonics	<p style="text-align: right;">$N_m=8, N_s=12$ 261</p>	<p style="text-align: right;">$N_m=10, N_s=12$ 281</p>

Table 3.10 shows the comparison of 12-slot/8-pole and 12-slot/10-pole PMSM. 12-slot/10-pole has better winding factor and also it has SPP=0.4 which is most suitable for traction motors to achieve wide flux weakening.

3.8 Conclusions

The commercial motors conclude that the stator fill factor is the key element to improve the performance of the motor by reducing the copper loss of the motor. Also, the two different commercial machines with distributed winding and concentrated winding are studied. The distributed winding in the BMWi3 has better utilization of the reluctance torque component but the concentrated winding with the Honda Accord does not utilize the reluctance torque component. And in terms of copper fill factor the concentrated winding will be better to increase the fill factor. The Honda Accord motor utilizes a segmented stator, each stator can be wound separately, though the fill factor is maintained 40%, because of lamination steel manufacturing capability.

Also, this chapter focuses on comparing the SMC and laminated steel stator core for higher pole and lower pole numbers. The SMC stator core with higher pole numbers exhibits lower iron losses at the maximum operating speed. The BMWi3 rotor is utilized for the Twizy motor designs with commercial magnet and coldspray magnet. 48-slot/8-pole and 12-slot/8-pole designs are analysed with the scale down model of BMW i3 rotor design. Concentrated winding designs always performs better in the flux weakening region. However, a 48-slot/8-pole distributed winding designed using coldspray magnets with a scallop design performs well in the flux weakening mode, its due to that fact that the coldspray magnet is a lower Br magnet.

Considering the manufacturing difficulties, the lower pole number with 12 slots and 8 poles is chosen for the second analysis. In the 12-slot/8-pole configurations, three different designs are analysed. Initial 12-slot/8-pole design, 2nd design with modified stator tip thickness and sine rotor air barrier, and 3rd design with closed and open slots. In all these three designs coldspray rotors are analysed with cobra shaped magnet design. Also, for all the cases, a comparison has been done with the laminated stator and SMC stator for 12 slots 8 poles with the commercial PM and cold spray PM. The SMC stator is always simulated with a 60% fill factor. The active stack length and the overall stack length is the same for the SMC stator, but with the laminated steel stator, the overall stack length is higher than the active length. The torque density in terms of motor volume is the key parameter to define motor performance. The SMC stator has a higher torque density when compared to the laminated stator utilizing the manufacturing technique. The cobra shaped PM motor utilizes the cold spray technique to spray as a single structure without the need for two

pieces of arc magnets, which increases the complexity of the mass production for traction applications. Also, this chapter concludes that 12-slot/8-pole will have higher torque ripple.

CHAPTER – 4

Design and Analysis of a Cobra Shaped Spoke Type Rotor using 3D-FEA

This chapter focuses on reducing the torque ripple, and the harmonic content of back EMF utilizing cold spray additively manufactured magnets. The electromagnetic performance of the conventional spoke and the cobra-shaped spoke type rotor are compared for the same specifications. Also, this chapter focuses on the design of a segmented SMC stator core to improve the copper fill factor to 60%. A comparison between the laminated stator core and the SMC stator core is presented.

4.1. Introduction to Cobra Rotor Design

The electric motor industry always requests the best performing material at competitive cost. The performance of SMC based axial machines were found to be similar to laminated steel designs [24-26]. Alan G. Jack et al. designed radial flux machines with SMC stator cores using a surface mount rotor which was compared with a laminated stator core [27]. The SMC stator was shown to be the best candidate for high-speed applications with reduced core losses [28]. The real advantage of SMC materials for motors can be attained by exploiting the material's original benefits [29].

The advantages of SMC materials include low wastage of materials while cutting the stator and rotor parts, and high copper fill factor by segmenting the stator tooth, 3-D flux carrying capability and recycling of the copper without wastage. The literature does not have any motors designed and analyzed with the SMC stator core for a higher torque rating with low voltage. Low torque ripple, low cogging torque, low ripple in the back EMF, high constant power speed range, better mechanical and thermal performance are the requirements of electric traction motors. Buried PM machines are a better candidate for optimal field weakening compared to surface mounted PM

machines. The spoke type PM is a good option for buried PM machines to utilize flux concentration. Equation (1) shows the optimal flux weakening condition.

$$I_{ch} = \frac{\psi_m}{L_d} A rms \quad (4.1)$$

Where I_{ch} is the characteristic current, ψ_m is the flux linkage, and L_d is the d-axis inductance. The motors' torque pulsation components can be classified into two types: cogging torque and torque ripple. Skewing the rotor will reduce the torque ripple but significantly increase manufacturing costs. The torque ripple reduction for spoke type PMs has been done extensively in the literature [30-32].

A spoke type PM machine has been designed with two layers of PM, each with different thickness. Also designed was a wing-shaped spoke type PM, but the torque ripple percentage has not been studied [33-35]. A flare-shaped spoke type magnet was designed with two individual arc magnets [36]. This chapter utilizes a cold spray additive manufacturing technique to spray the NdFeB magnet on to the rotor laminations. With this technique, magnet shaping is more feasible. The magnets are sprayed in a cobra shape to obtain better electromagnetic performance. This cold spray technique is developed at NRC Canada which makes the magnet shaping inexpensive. The cold spray technique is already proven with a complex petal-shaped magnet design for a surface PM [37].

4.2. *Electromagnetic design and slot pole selection of cobra shaped rotor*

A. Slot pole selection

There are two different types of winding patterns which are common for traction applications. Commercial traction motors such as Toyota Prius, BMWi3, and Nissan leaf uses distributed winding such as 48-slot/8-pole, 72-slot/12-pole, and 48-slot/8-pole. The Honda Accord uses concentrated winding with 24-slot/16-pole. In general, the fractional slot concentrated windings are a better candidate for the wide flux weakening operation [38]. Different slot per pole per phase (SPP) has different machine characteristics. Three different winding patterns are compared regarding the fundamental winding factor, cogging torque, joule losses and winding

MMF harmonics [39]. Each part of the SMC stator can be manufactured separately and assembled at a later stage. Also, the machine performance is improved with the concentrated winding, such as lower copper loss due to a higher copper fill factor [40]. SPP decides the flux weakening characteristics of the PMSM machine [41]. Torque density can be improved with the higher pole configurations, simultaneously the stator core loss will be increased. An optimal slot/pole configuration has to be chosen for an efficient traction motor application. Two different slot/pole configurations such as 12-slot/8-pole and 12-slot/10-pole are analysed to select the best slot/pole for further analysis with the cobra-shaped rotor design.

TABLE 4.1 - MACHINE SPECIFICATIONS

Specifications	Values
Rated Power	7.1 kW
Rated Torque	20 N-m
Rated Speed	3400 rpm
Maximum Speed	10,000 rpm
Supply Voltage	96 volt
Cooling type	Air Cooled
Magnet material	Cold spray NdFeB (0.46 T)
Stator and rotor material	Laminated steel

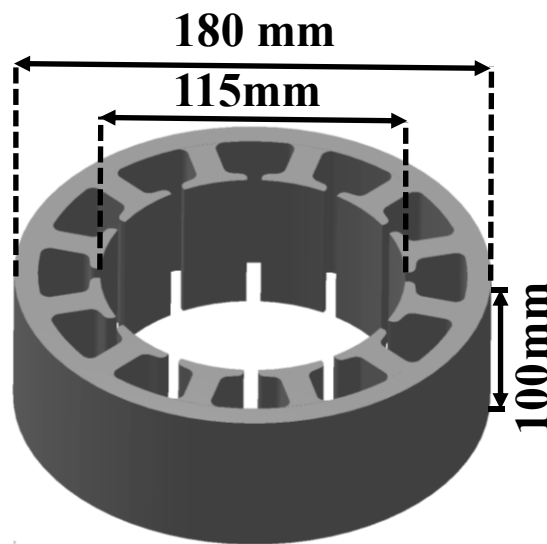


Fig. 4. 1. Laminated stator with 12 slots

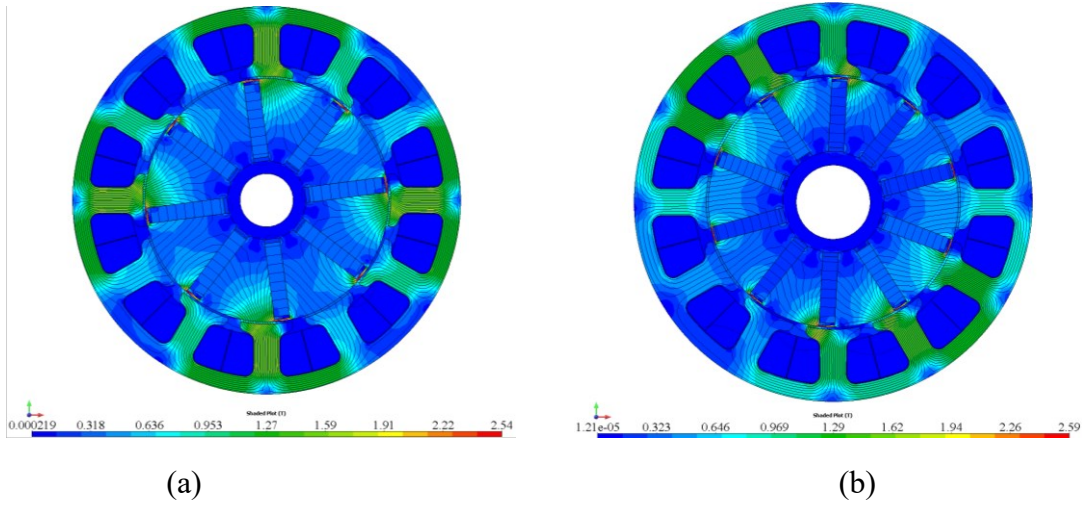


Fig. 4. 2. Flux density plots at full load (a) 12-slot/8-pole (b) 12-slot/10-pole

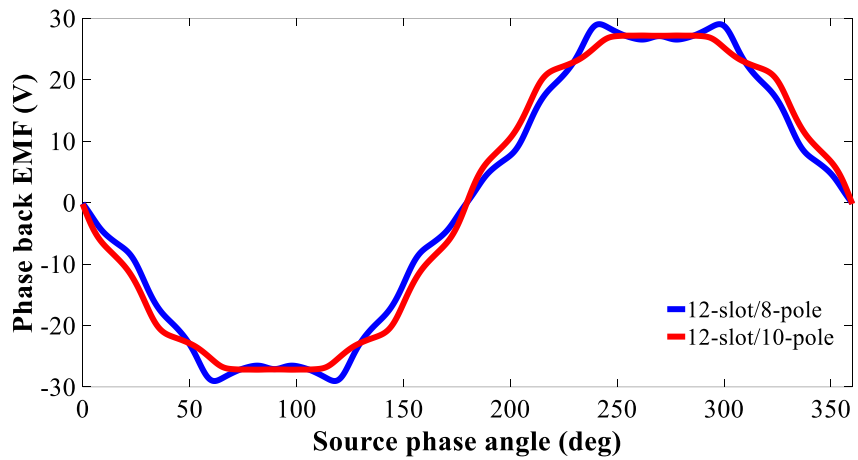


Fig. 4. 3. Phase back EMF of 12-slot/8-pole & 12-slot/10-pole configurations

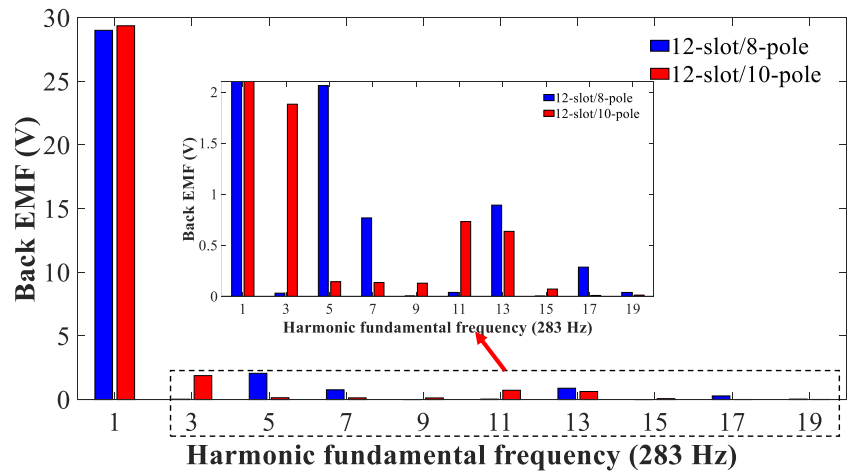


Fig. 4. 4. Phase back EMF harmonics of 12-slot/8-pole & 12-slot/10-pole

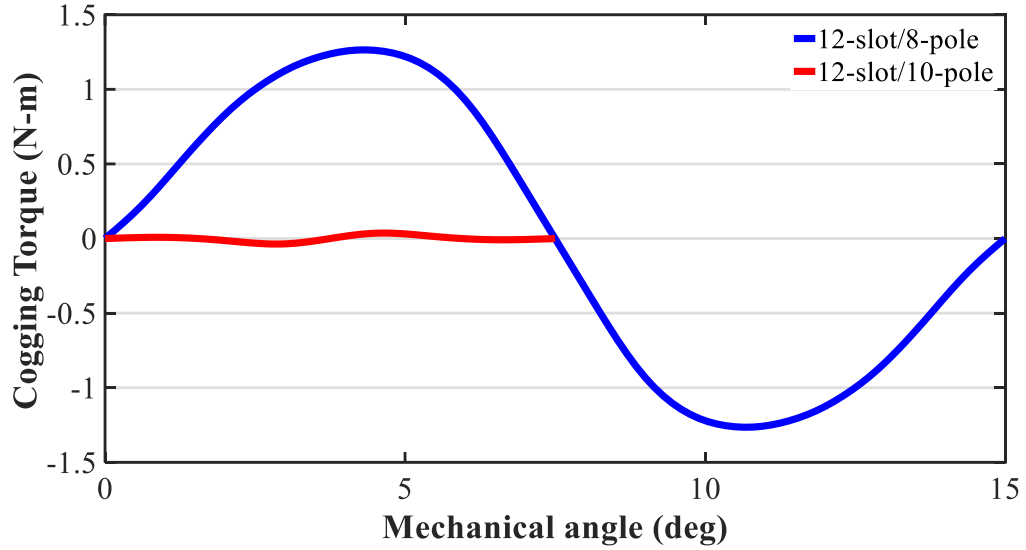


Fig. 4. 5. Cogging torque of 12-slot/8-pole & 12-slot/10-pole configurations

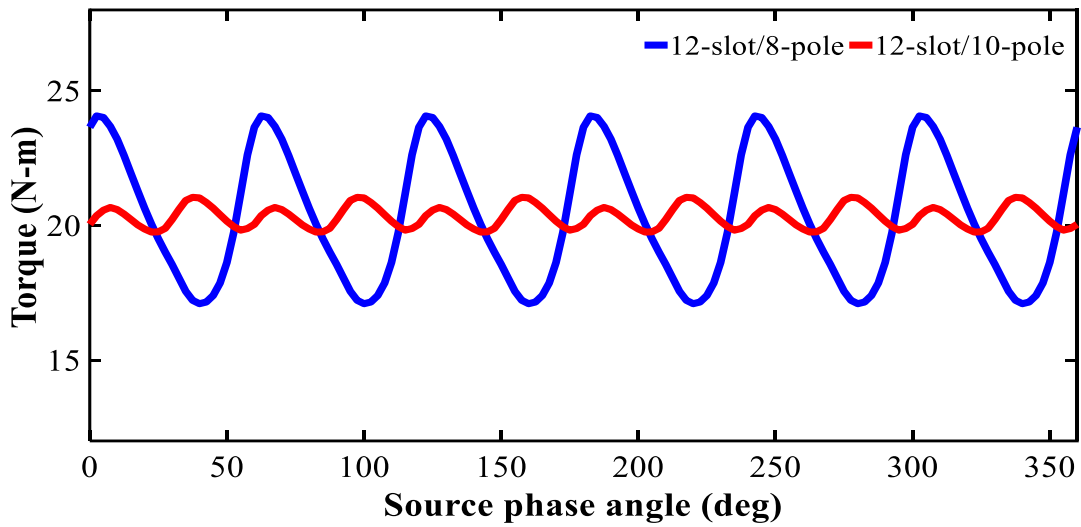


Fig. 4. 6. Torque of 12-slot/8-pole & 12-slot/10-pole configurations

B. Current Density

Current density is defined as an important metric for the slot pole configurations.

$$\text{Current density } (J_{rms}) = \frac{3K_W^{AC}}{2} * \frac{N_{ph}I_{rms}}{D} \quad (4.2)$$

Where K_W^{AC} is the fundamental winding factor, I_{rms} is the winding current, $\frac{3}{2}$ the factor is for a three-phase sinusoidal current set. D is the mean air gap diameter, N_{ph} is the number of the series phase winding turns. The current density is fixed to be 4.5 A/mm^2 for both the slot/pole configurations.

TABLE 4.2- 12/8 AND 12/10 CONFIGURATIONS

Item	12/8	12/10
RMS phase current	120 A	120 A
Stator OD	180 mm	180 mm
Stator ID	115 mm	115 mm
Stack length	100 mm	100 mm
No of turns per coil	16	7
Copper fill factor	40 %	40 %
Wire diameter	0.91 mm	0.91 mm
No of parallel path	4	2
No of winding layer	2	2

Table 4.1 shows the motor specifications. Table 4.2 shows the machine dimensions of 12-slot/8-pole and 12-slot/10-pole configurations. Both machines are designed to fit into the same frame. The machine parameters such as stator outside diameter, stack length and copper fill factor, are kept the same for both designs. Both the designs are analyzed without skewing either rotor or stator. The number of parallel paths is higher for the 12-slot/8-pole configuration due to the fact that greatest common factor (GCF) of 12 and 8 is 4. But for the 12-slot/10-pole configuration, the GCF is 2. As the number of turns per coil increases due to the higher number of parallel paths, the number of strands in hand is reduced for a 12-slot/8-pole configuration to maintain the same copper fill factor. Fig. 4. 2 shows the full load flux density plot for both configurations.

C. Back EMF

The phase back EMF is given by the following equation.

$$E = \frac{\pi^2 * k_{w1} * N_{ph} * B * D * L_{stk} * f}{\sqrt{2} * p} \quad (4.3)$$

N_{ph} is the turns per phase, I is the RMS phase current and D is the stator outer diameter. E is the back EMF, k_{w1} is the harmonic winding factor, L_{stk} is the stack length, f is the frequency, and p is the pole pair. The back EMF decides the control of the motor. Generally, there are two types of back EMF trapezoidal with 120° conduction and sinusoidal with 180° conduction. Back EMF with closer to sinusoidal is the interest of almost of all traction motors. Fig. 4. 3. shows the back EMF of both the designs. Fig. 4. 4 shows the harmonics of phase back EMF.

TABLE 4.3 – BACK EMF HARMONICS

Harmonics	12/8	12/10
1	29.01	29.36
3	0.03	1.88
5	2.06	0.14
7	0.77	0.13
9	0.00	0.13
11	0.04	0.73
13	0.89	0.64
15	0.00	0.07
17	0.29	0.01
19	0.04	0.01
THD(%)	14.19	12.75

Table 4.3 shows the harmonic component of 12/8 and 12/10 designs. The 3rd order harmonics is increased for the 12/10. But the 5th and 7th order harmonics are substantially reduced for the 12/10 design. The overall THD (%) of 12/8 and 12/10 designs are 14 % and 13 %.

D. Cogging Torque

The cogging torque is due to the interaction between the magnets and the stator teeth, which can be expressed as below,

$$\text{Cogging Torque (T)} = -\frac{1}{2}\Phi^2 \frac{dR}{d\theta} \quad (4.4)$$

Where Φ is the magnet flux crossing the air gap, and R is the total reluctance torque through which the flux passes. Fig. 4. 5 shows the cogging torque of 12/8 and 12/10 designs.

E. Electromagnetic torque

The electromagnetic torque of PMSM motor is given by the following equation,

$$\text{Torque} = \frac{3}{2} * \frac{P}{2} [\lambda_m i_q + (L_d - L_q) i_d i_q] \quad (4.5)$$

P is the number of poles, λ_m is the magnet torque, $i_d i_q$ are the d and q-axis current, L_d & L_q are the d and q-axis inductance. The d and q-axis inductance will be closely same for the spoke type PMSM. So spoke type PM utilizes only the magnet torque. Fig. 4. 6 shows the electromagnetic torque of both the designs.

TABLE 4.5– TORQUE COMPONENTS

Item	12-slot/8-pole	12-slot/10-pole
Average torque (Nm)	20.3	20.3
Torque ripple (%)	34.2 %	6.22 %
Peak cogging torque (Nm)	1.26	0.036

Table 4.5 shows the average torque, torque ripple and cogging torque. The torque ripple with the 12-slot/10-pole design is reduced by 81 % from the 12-slot/8-pole design. The peak cogging torque with the 12-slot/10-pole design is reduced by 97% from the 12-slot/8-pole design. The torque ripple and cogging torque are substantially reduced for the 12-slot/10-pole design. The 12-slot/10-pole design is chosen for further analysis with the cobra-shaped rotor.

4.3. 2-D & 3-D analysis of 12-slot/10-pole with conventional & cobra rotors

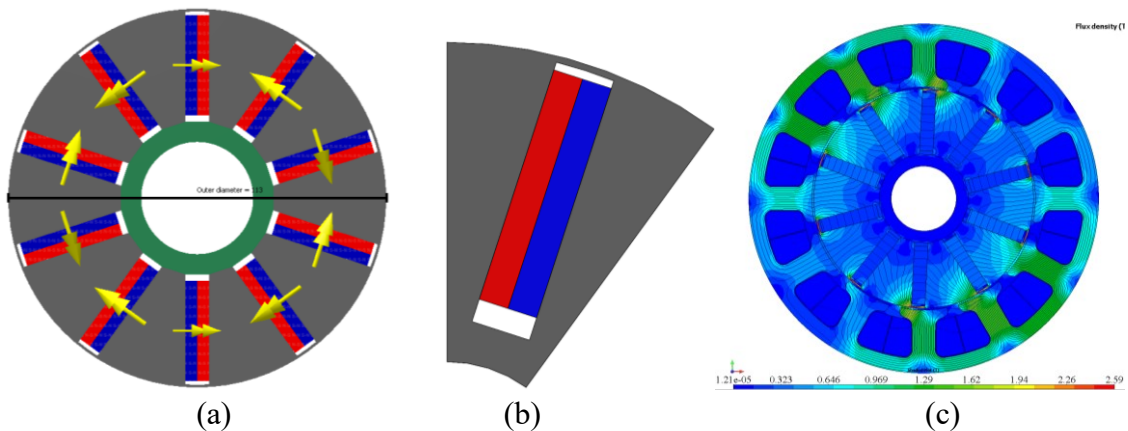


Fig. 4. 7. (a & b) Conventional spoke type rotor (c) Full load flux density plot

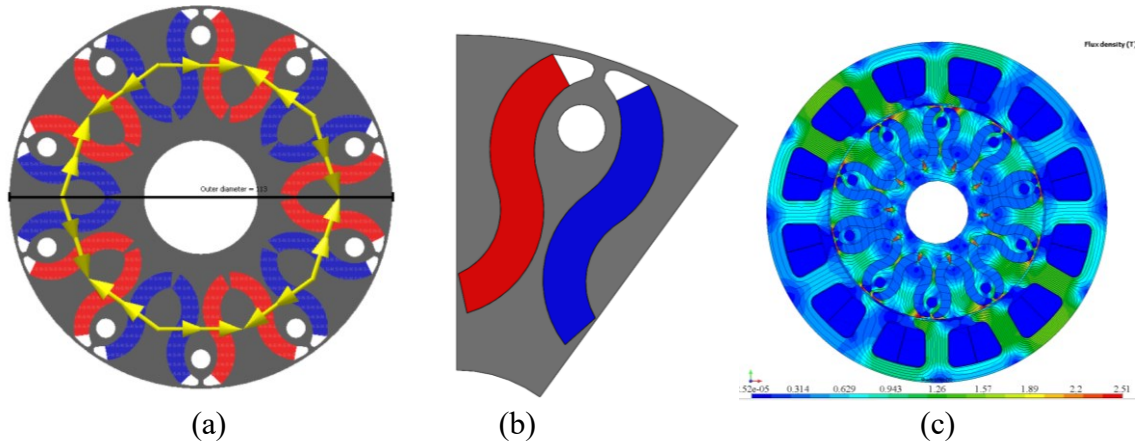


Fig. 4. 8. (a & b) Cobra spoke type rotor. (c) Full load flux density plot

TABLE 4.6- CONVENTIONAL & COBRA SPECIFICATIONS

Item	Conventional rotor	Cobra rotor
RMS phase current	120 A	120 A
Stator OD	180 mm	180 mm
Stator ID	115 mm	115 mm
Stack length	100 mm	100 mm
No of turns per coil	7	7
Copper fill factor	40 %	40 %
Wire diameter	0.91 mm	0.91 mm
No of parallel path	2	2
No of winding layer	2	2
Magnet volume	1.65 kg	2.5 kg

Fig. 4. 7 shows the conventional spoke type rotor and its full load flux density plot. Fig. 4. 8 shows the cobra-shaped rotor and its full load flux density plot. Table 4.6 shows the specifications of the conventional rotor and the cobra-shaped rotor. Laminated steel is used for the rotor and stator core. Cold spray NdFeB (0.46 T) is used for both designs. Machine dimensions such as stator outer diameter, rotor outside diameter, and stack length are fixed the same for both designs. Machine dimensions such as stator outer diameter, rotor outside diameter, and stack length are fixed the same for both the designs. Fig. 4. 9 shows the 3-D flux density plot for both designs. Conventional rotor and cobra-shaped rotor are designed for the same specifications which are presented in Table 4.1.

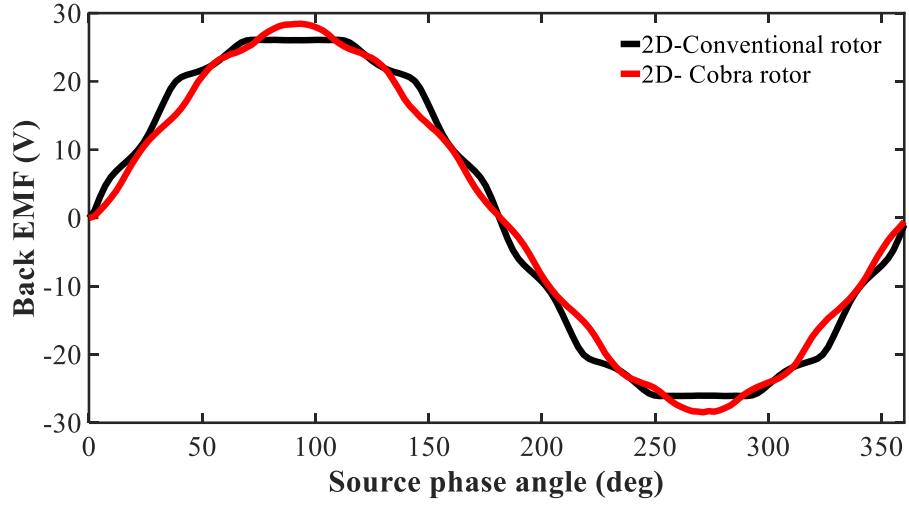


Fig. 4. 10. 2-D- Phase back EMF of conventional rotor and cobra rotor

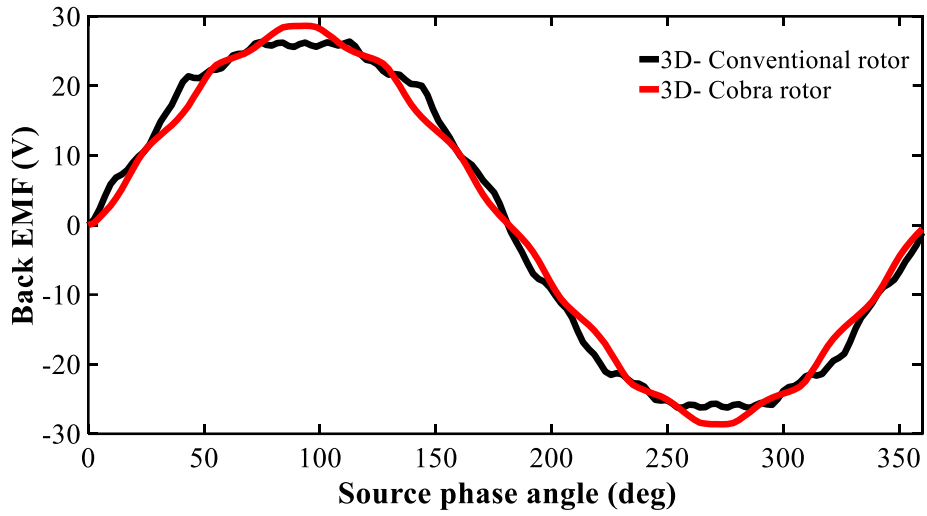


Fig. 4. 11. 3-D- Phase back EMF of conventional rotor and cobra rotor

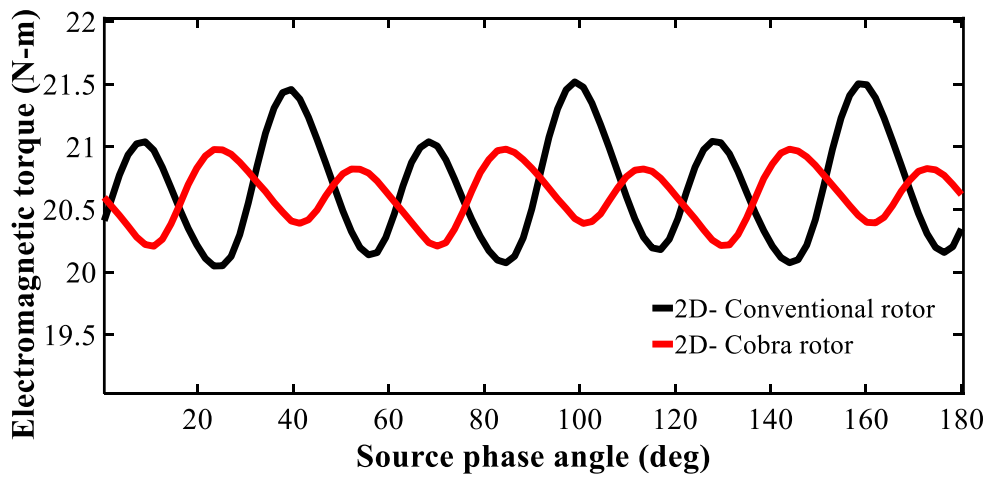


Fig. 4. 12. 2-D- Electromagnetic torque of conventional rotor and cobra rotor

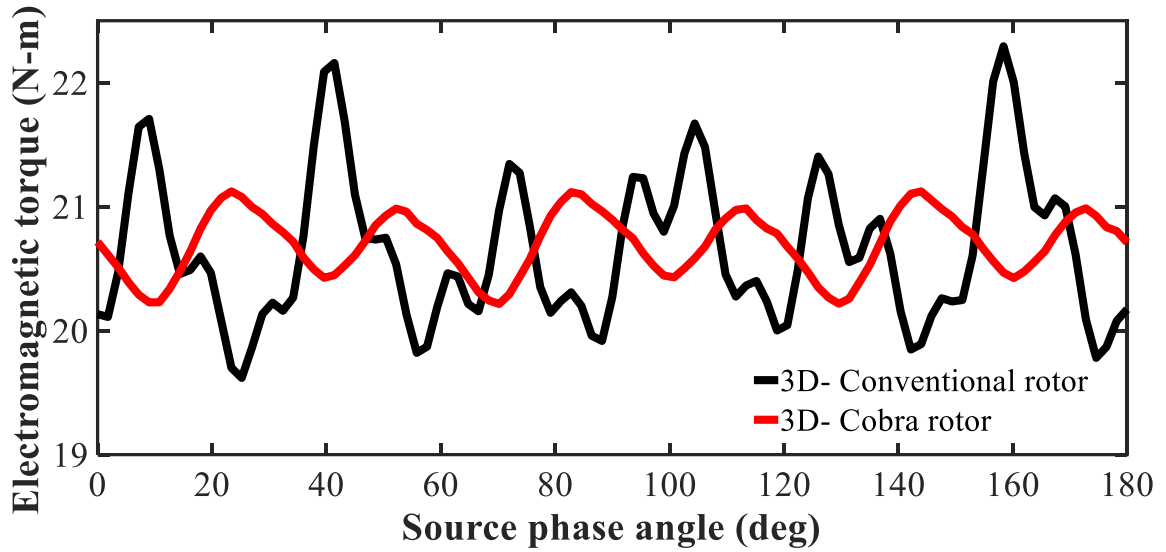


Fig. 4. 13. 3-D- Electromagnetic torque of conventional rotor and cobra rotor

Both designs are analysed using 2-D and 3-D finite element analysis (FEA). The results such as phase back EMF, harmonics in phase back EMF and the electromagnetic torque ripple are presented and compared for both designs.

TABLE 4.7– BACK EMF HARMONICS

Harmonics	2-D- Conv	3-D-Conv	2-D-Cobra	3-D-Cobra
1	28.09	27.80	27.83	27.56
3	1.70	1.48	0.76	0.69
5	0.16	0.18	0.04	0.02
7	0.14	0.13	0.11	0.11
9	0.08	0.05	0.27	0.24
11	0.82	0.77	0.64	0.63
13	0.62	0.36	0.39	0.33
15	0.03	0.06	0.16	0.15
17	0.02	0.01	0.01	0.02
19	0.02	0.01	0.01	0.01
21	0.03	0.09	0.01	0.02
THD (%)	12.8	11.2	8.5	8.0

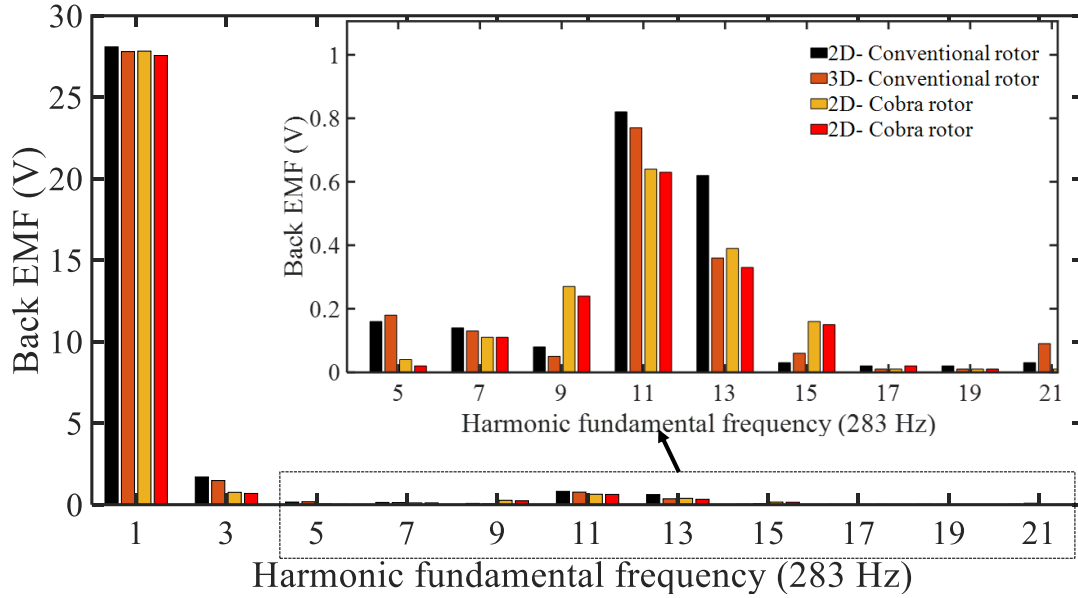


Fig. 4. 14. Phase back EMF harmonics of 2-D and 3-D designs.

Fig. 4. 10 shows the 2-D phase back EMF of the conventional rotor and the cobra rotor. Fig. 4. 11 shows the 3-D phase back EMF of both the rotor designs. Fig. 4. 12 and 13 show the 2-D and 3-D electromagnetic torque ripple of both the designs. Figs. 10 and 11 show the variation in the back EMF waveforms between the two rotor designs. In order to analyse the sinusoidal quality of the back EMF a fast Fourier transform (FFT) analysis is shown in Fig. 4. 14.

TABLE 4.8 – TORQUE COMPONENTS

Item	2-D- Conv	3-D-Conv	2-D-Cobra	3-D-Cobra
Average torque	20.6	20.6	20.6	20.6
Torque ripple (%)	7.1	12.9	3.7	4.3

$$THD = \frac{\sqrt{V_1^2 + V_2^2 + V_3^2 + \dots}}{V_0} \quad (4.6)$$

$$\text{Torque ripple (\%)} = \frac{T_{max} - T_{min}}{T_{avg}} * 100 \quad (4.7)$$

Table 4.7 shows the back EMF harmonic component of all four cases. The stator winding parameters such as number of turns per coil, rms current are fixed the same for both the rotor designs. Due to the adjustment of the magnet volume the rms values of the back EMF are kept the same in four cases for a reasonable comparison of the phase back EMF harmonics and

electromagnetic torque ripple. The harmonic distortions (THD) and electromagnetic torque ripple are calculated by the above equations. The THDs of the four models are 13 %, 11 %, 8 %, and 8 %, respectively. In 2-D FEA the back EMF harmonics with the cobra rotor is reduced by 33% from the conventional rotor. In 3-D FEA the back EMF harmonics with the cobra rotor is reduced by 28% from the conventional rotor. In 2-D FEA the electromagnetic torque ripple with the cobra rotor is reduced by 47 % from the conventional rotor. In 3-D FEA the electromagnetic torque ripple with the cobra rotor is reduced by 66% from the conventional rotor which is shown in Table 4.8. From this section the cobra rotor is chosen as the best candidate for further analysis with the laminated stator and SMC stator design.

4.4. *Cobra type rotor with laminated stator and SMC stator*

The cobra type rotor with 12-slot/10-pole is chosen from the above section for further analysis with SMC stator. The electromagnetic performance between the SMC stator and laminated stator is analyzed for the rated and maximum speed.

TABLE 4.9- LAMINATED & SMC STATOR SPECIFICATIONS

Item	Laminated Steel Design	SMC stator Design
RMS phase current	120 A	140 A
Stator OD	180 mm	180 mm
Rotor OD	113 mm	113 mm
Stack length	100 mm	100 mm
Overall stack length	130 mm	100
Rotor core	M-36 29GA	M-36 29GA
Stator core		SMC
Copper fill factor	40 %	60 %
Phase resistance	0.00259 Ω	0.0148 Ω
Torque density (motor volume)	6.04 KNm/m ³	7.85 KNm/m ³

The SMC stator is designed with a high slot fill factor of 60% with the help of segmented tooth construction and the laminated stator is designed with a slot fill factor of 40 %.

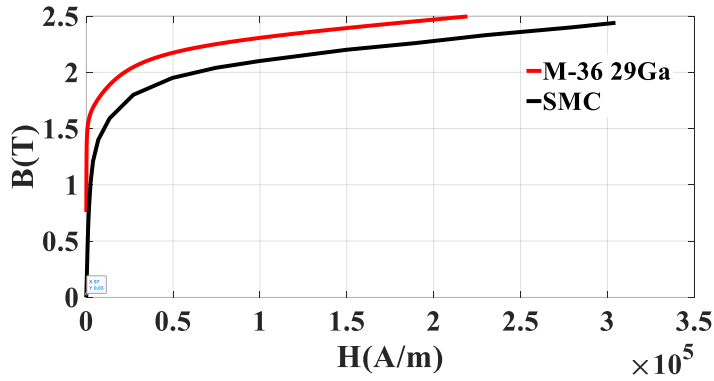


Fig. 4. 14. B-H Curve of laminated Steel & SMC

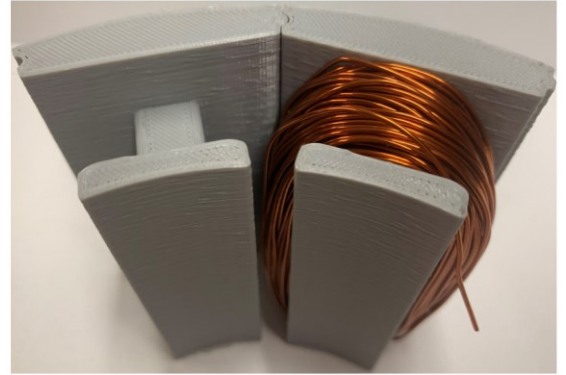


Fig. 4. 15. 3-D printed dummy tooth using plastic

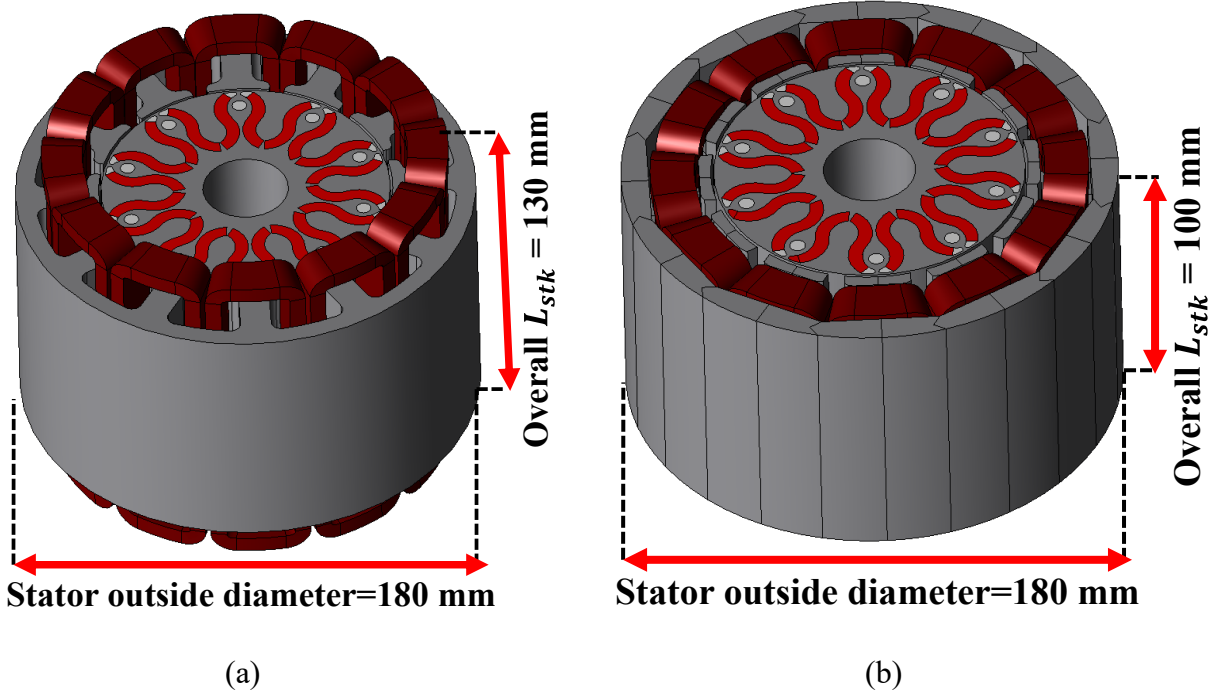


Fig. 4. 16. (a) Laminated stator with end winding (b) SMC stator with encapsulated end winding

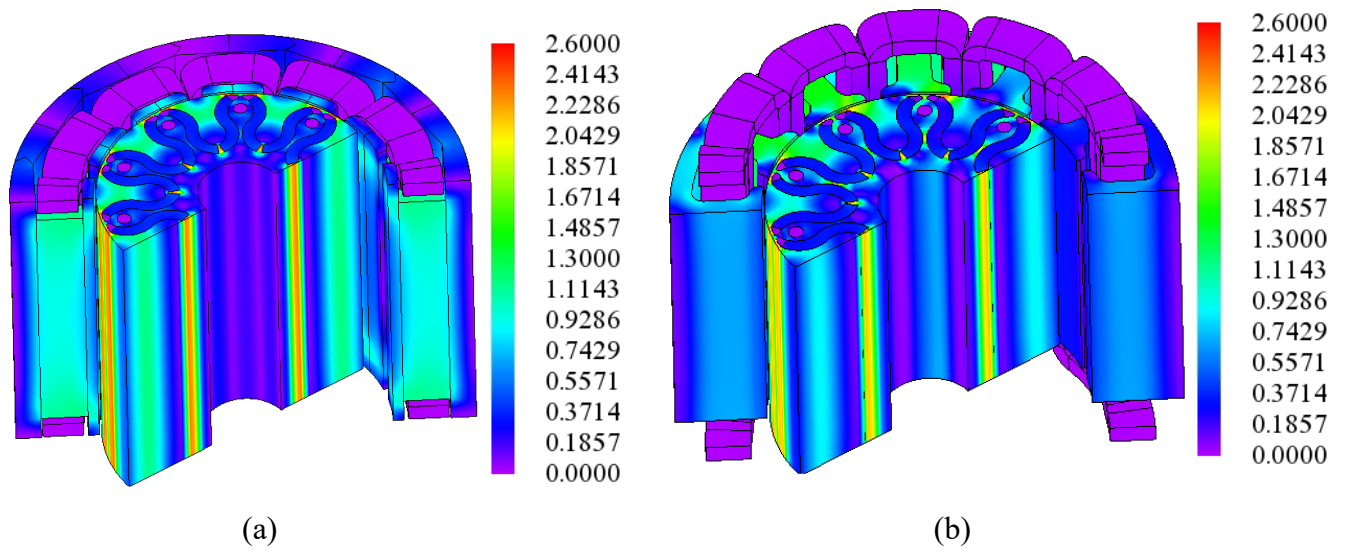


Fig. 4. 17. (a) SMC stator with compacted end winding (b) Laminated stator with end winding

Table 4.10

IRON LOSS(W/KG) FOR M-36 29GA

[W/kg]	60 Hz	200 Hz	300 Hz	600 Hz	1000 Hz	2000 Hz
0.5T	0.55	2.69	4.78	14.13	30.85	93.4
1.0T	1.74	9.3	17.38	54.69	127.96	426.8

Table 4.11

IRON LOSS(W/KG) FOR SMC

[W/kg]	60 Hz	200 Hz	300 Hz	600 Hz	1000 Hz	2000 Hz
0.5T	1.8	6	9	20	36	86
1.0T	5.9	21	32	68	125	307

Table 4.9 shows the design specifications of the laminated stator and the SMC stator designs. Fig. 4. 14 shows the B-H curve of both the material. Fig. 4. 15 shows the SMC tooth and 3-D printed dummy teeth made up of plastic. Both machines are designed to fit into the same enclosure. The

machine dimensions such as stator outside diameter, rotor outside diameter, and stack length are fixed the same for both the designs.

TABLE 4.12 - LAMINATED STATOR LOSS ANALYSIS

Items	Laminated stator at rated speed	Laminated stator at maximum speed
DC copper loss	116 W	116 W
Eddy current loss	83.7 W	346.9 W
Hysteresis loss	46.2 W	60 W
Total iron loss	133.5 W	424.3 W
Efficiency	96 %	94 %

TABLE 4.13- SMC STATOR LOSS ANALYSIS

Items	SMC stator at rated speed	SMC stator maximum speed
DC copper loss	94 W	94 W
Eddy current loss	38 W	232 W
Hysteresis loss	193 W	225 W
Total iron loss	242 W	481 W
Efficiency	95 %	94.5 %

The SMC stator core is less permeable compared to the laminated stator core. Generally, the SMC stator design requires either higher current or bigger machine dimensions to obtain similar performance to the laminated stator design. The copper fill factor is inversely proportional to the current density (A/mm^2). The copper fill factor with the SMC stator is increased by 33% from the laminated stator design. The higher fill factor allows to an increase in the rms current of the motor. The phase resistance with the SMC stator design is reduced by 42% from the laminated stator design. Fig. 4. 16 shows the laminated stator and SMC stator dimensions with end windings. Fig. 4. 17 shows the full load flux density plot of both the stator designs. Table 4.12 and 13 show the copper loss, iron loss and efficiency. The efficiency with the SMC core at the rated speed is reduced by 1% from the laminated stator, but it's improved at the maximum speed. The torque

density in terms of motor volume with the SMC stator core is increased by 23 % from the laminated stator design.

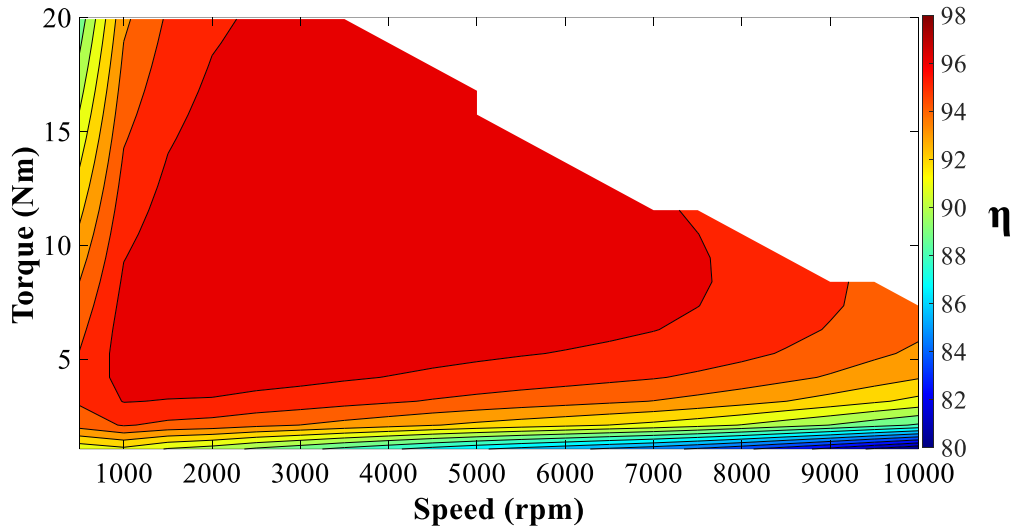


Fig. 4. 18. Efficiency map of laminated stator with cobra rotor

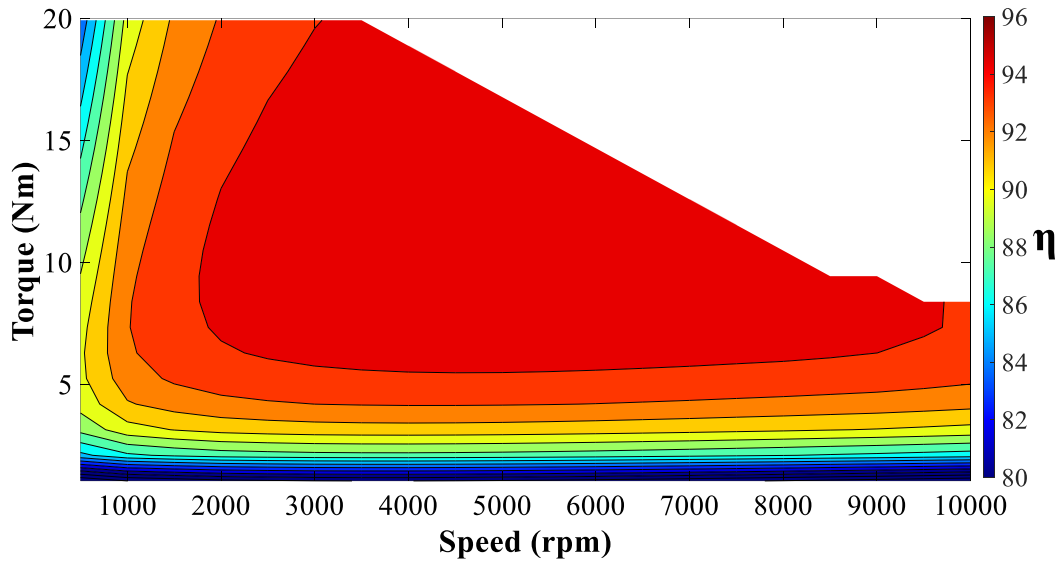


Fig. 4. 19. Efficiency map of SMC stator with cobra rotor

Figs. 18 and 19 show the efficiency map of the laminated stator and the SMC stator design. The iron loss of the laminated stator core will increase with frequency but the iron losses with the SMC stator core will not increase as much at elevated frequencies. SMC machines designed with higher pole numbers tend to perform better, but due to the manufacturing cost and considering the

size of the inverter, lower pole numbers are widely accepted in traction applications. The above analysis and comparison, shows that the SMC stator with the cobra rotor is a good candidate for traction applications.

4.5. Mechanical stress analysis of cobra rotor

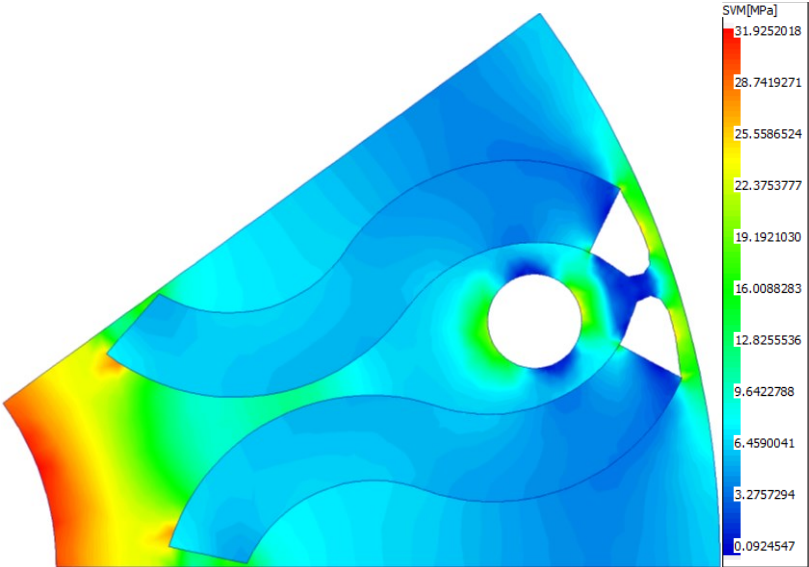


Fig. 4. 20. Mechanical stress analysis of cobra rotor at 10000 rpm

Fig. 4. 20 shows the mechanical stress analysis of the cobra rotor. The rotor is made up of laminated steel. The Young’s modulus of the laminated steel used in the analysis is 210000 MPa. The stress analysis is performed at the maximum speed of 10000 rpm. 32 MPa is the obtained stress value for the cobra rotor which is much lower than the capability of the laminated rotor. The magnets are pre-magnetized with the universal magnetizers before the assembly. JMAG 2-D and 3-D FEA software [42] is used to analyse the conventional and cobra rotor designs with laminated stator core and SMC stator core.

4.6. Optimal flux weakening of cobra rotor with smc stator

TABLE 4.14- OPTIMAL FLUX WEAKENING CONDITIONS

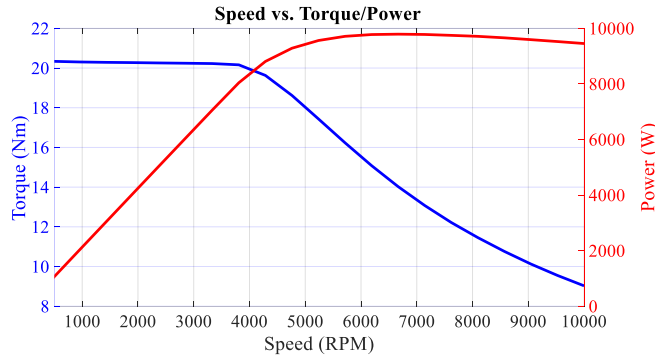


Fig. 4. 21. Speed Vs Torque & Power of SMC Stator

Stator	SMC stator
Winding	Concentrated
SPP slot/pole/phase	0.4
L_d d-axis induc(mH)	0.076
I_s Peak current(A)	198
φ_m Flux linkage (Wb)	0.0146
Diff between φ_m & L_d * I_s	0.0003

Traction motors must operate with the optimal field weakening conditions to attain the constant power in the field weakening mode. A cobra-shaped rotor with 12-slot/10-pole (SPP=0.4) was chosen considering the wide field weakening operations. To achieve wider flux weakening the characteristic current I_{ch} must satisfy the relationship which is shown in equation (4.1). The PMSM machines must be designed with a d-axis high inductance to equate the d-axis flux linkage with the product of d-axis inductance and the peak current which is shown in Table 4.14. Fig. 4. 21 shows the torque speed curve of the cobra rotor with wide flux weakening regions.

4.7. Optimizing cobra rotor design

The cobra rotor is optimized with various magnet shapes. The cold spray magnets can be manufactured in any complex shape. So, different designs have been carried out to select the best design with lower torque ripple and lower harmonics in phase back EMF. Fig. 4. 22 shows 6 different rotor designs with cold spray magnets. Design -1 is the base line design. Design -2 has higher magnet thickness, Design-3 has sine shaped magnet closer to air gap and the rotor pole shape is modified to be close to sine shape. Designs -4 and 5 have thicker magnets and the air barrier near to the air gap is modified. Design- 6 is similar to a conventional design.

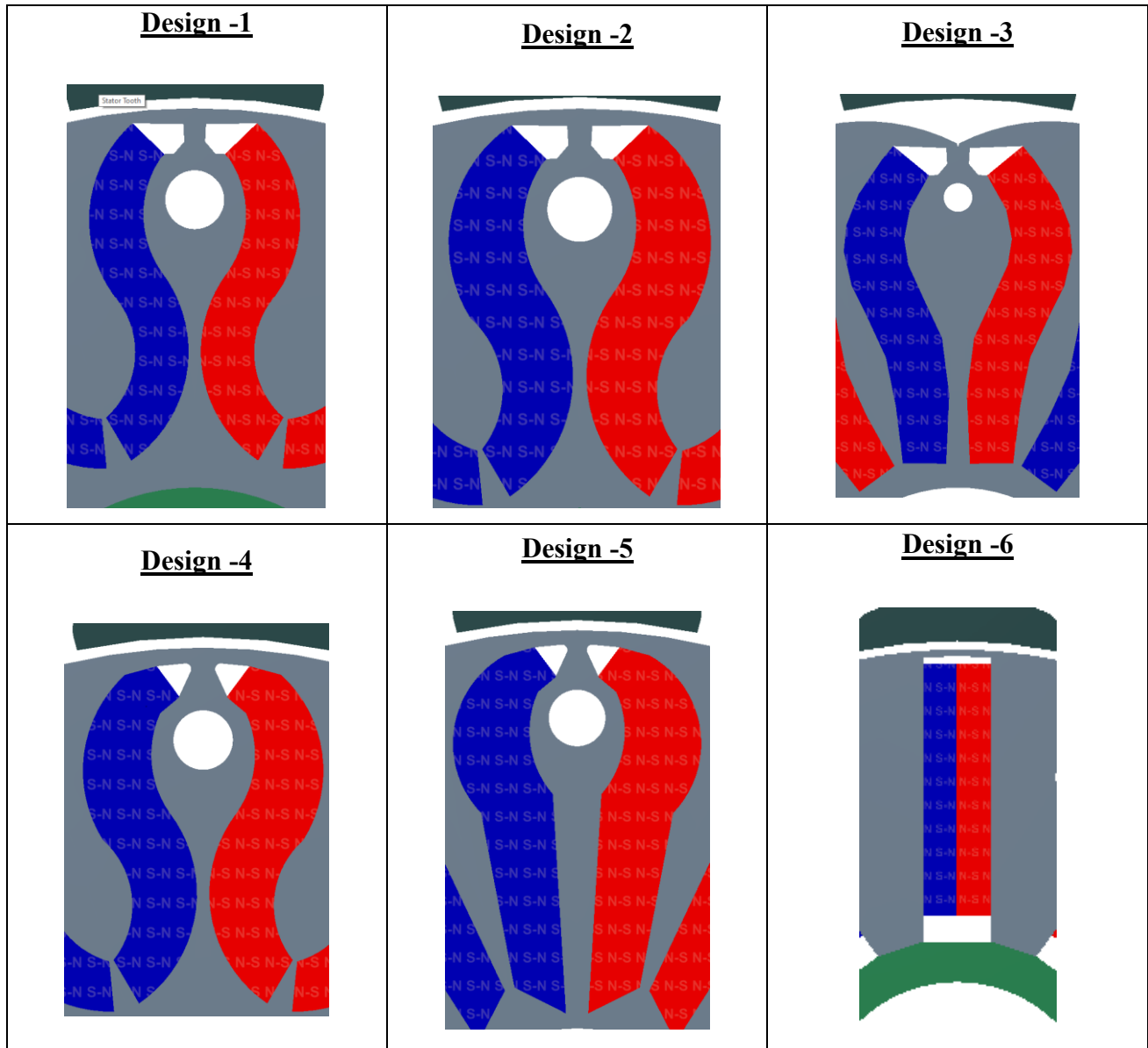


Fig. 4. 22. Cobra rotor with various magnet thickness and rotor structure

Fig. 4. 23 shows the full load flux density plot for all six designs. In all these 6 cases a SMC stator is used with the cold spray motor. The lamination rotor core is used for the analysis. The designs are modified using SOLIDWORKS software and then imported in the FEA software. In all the cases the current and the current density is maintained the same, but the magnet volume is changed. Fig. 4. 24 shows the phase back EMF of all the designs. Design-3 has the lowest phase back EMF due to the rotor pole shaping. All other designs have similar values of the back EMF. Design-2 has the highest value than the other designs.

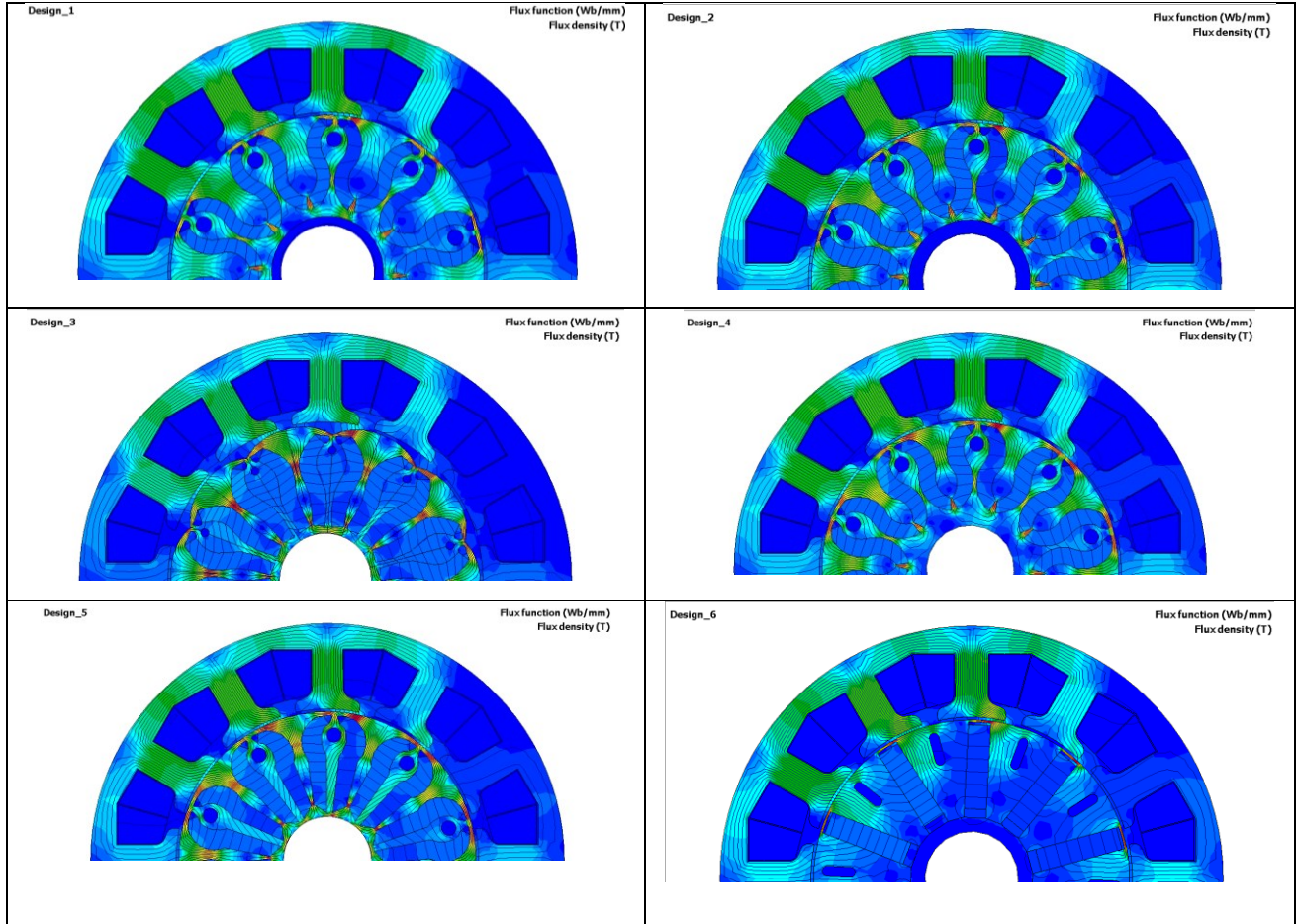


Fig. 4. 23. Flux density plot of various cobra rotor designs.

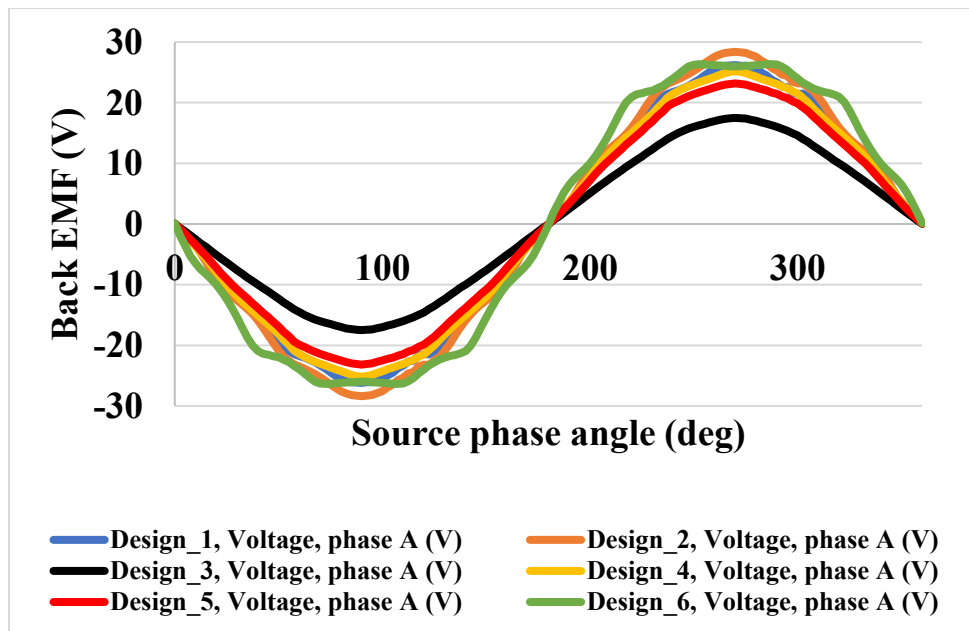


Fig. 4. 24. Phase back EMF of various cobra rotor designs.

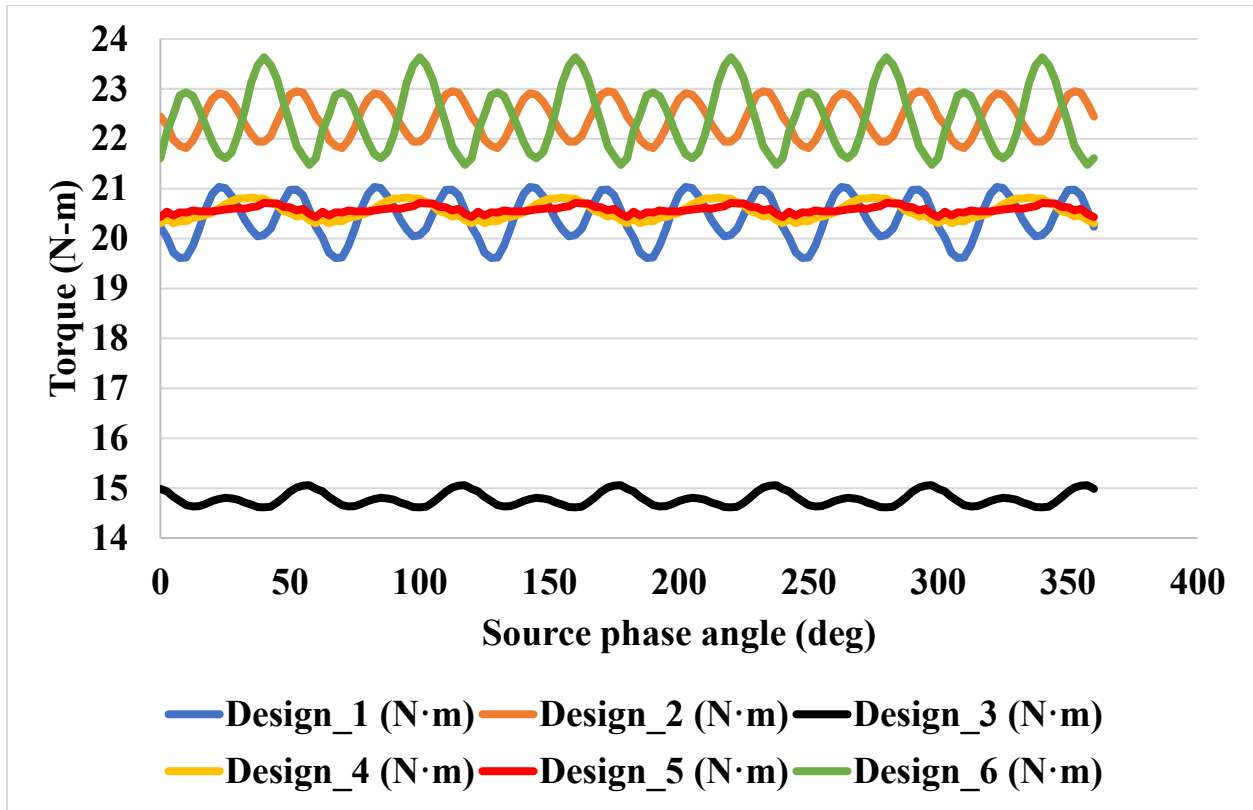


Fig. 4. 25. Electromagnetic torque of various cobra rotor design

TABLE 4.15- TORQUE RIPPLE COMPARISON

Torque Ripple (%)		
Design 1: 6.97 %	Design 2: 5.08%	Design 3: 2.99%
Design 4: 2.50%	Design 5: 1.37%	Design 6: 9.61 %

Fig. 4. 25 shows the electromagnetic torque of all six designs. Table 4.15 shows the torque ripple (%) for all the designs. Design-5 has the lowest torque ripple; however, the average torque of Design-5 is lower than Design-2 and Design-6. Design-2 and Design-6 have higher average torque but in terms of torque ripple, Design-2 is a better candidate. Design-2 emerged as the best candidate. However, this torque ripple is higher than the previous analysis. So the cobra design from section 4.3 is considered for further analysis with JMAG using multiobjective optimization.

4.8. Multiobjective optimization of cobra rotor

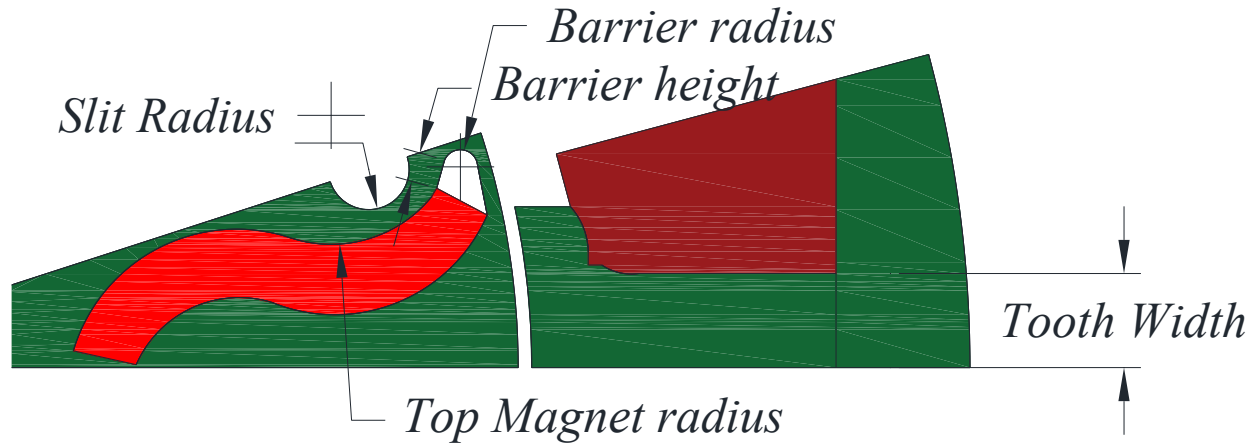


Fig. 4.26. Parameters for multiobjective optimization

Fig. 4.26 shows the multiple parameters which are considered for the optimization. Five parameters are considered, four parameters in the cobra rotor and one parameter from the stator design. Table 4.16 and 4.17 show the optimization range and the optimization constraints.

TABLE 4.16- OPTIMIZATION RANGE

Items	Range
Slit radius (R1)	(2 - 3 mm)
Top magnet radius (R2)	(9.6 – 12 mm)
Barrier height (H1)	(2 – 3 mm)
Barrier radius (R3)	(1 – 1.5 mm)
Tooth width (W1)	(5 – 7 mm)

TABLE 4.17- OPTIMIZATION OBJECTIVES

Items	Range
Torque Ripple	Minimize
Average Torque	Maximize
Stator Loss	Minimize

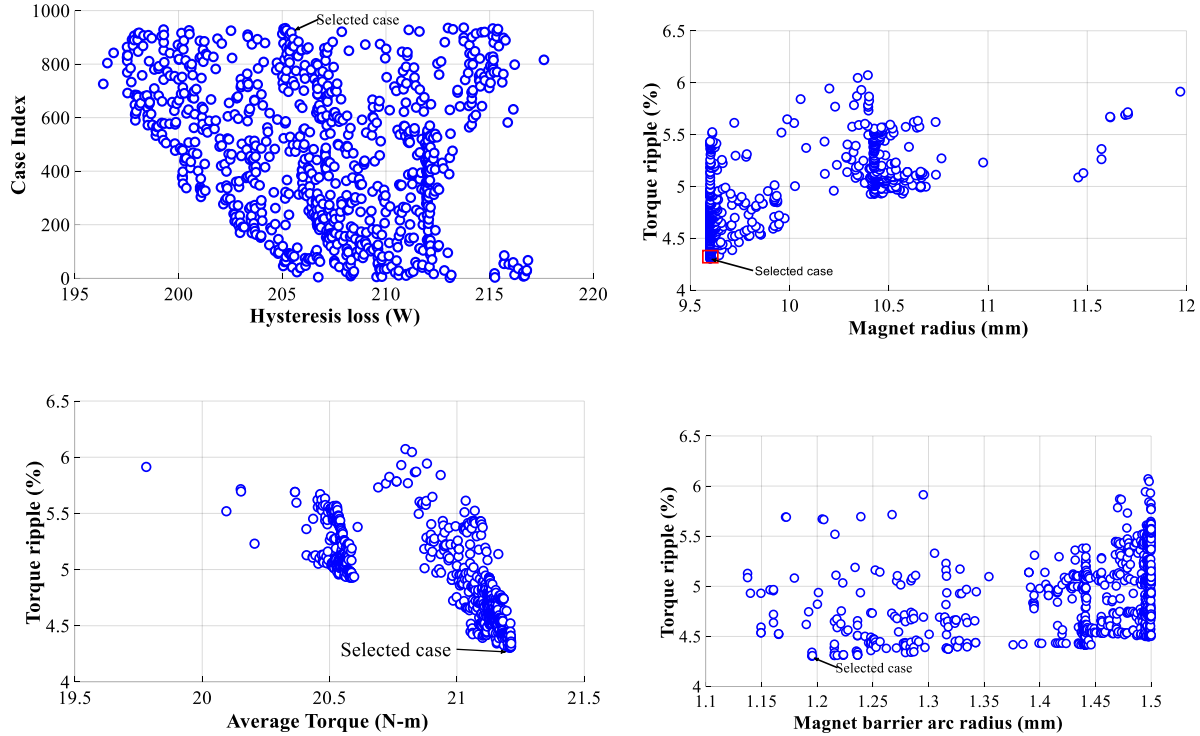


Fig. 4.27. Optimization results

TABLE 4.18- SELECTED PARAMETER

Items	Range
Slit radius (R1)	3 mm
Top magnet radius (R2)	9.9 mm
Barrier height (H1)	2.2 mm
Barrier radius (R3)	1.19 mm
Tooth width (W1)	6.8 mm
Selected case number	923

Fig. 4.27 shows the optimization results for the cobra rotor design. Table 4.18 shows the selected parameters from the optimization. 936 cases have been considered with 100 generations with a population size of 10. Case number 923 is selected as the best case with a torque ripple of 4.3 % and average torque of 21.2 N-m. Compared to the cobra rotor in section 4.3, torque ripple is increased, however the average torque is increased by 3% from the previous design. Also, this optimization shows that the selected design is a better candidate.

4.9. Conclusion

A comparison between the 12-slot/8-pole and 12-slot/10-pole with conventional spoke type rotor is presented. The phase back EMF THD of the 12-slot/10-pole design is reduced by 10% from the 12-slot/8-pole design. The torque ripple with the 12-slot/10-pole design is reduced by 81 % from the 12-slot/8-pole design. The peak cogging torque with the 12-slot/10-pole design is reduced by 97% from the 12-slot/8-pole design. Also, this chapter compares a 12-slot/10-pole conventional spoke type rotor with the 12-slot/10-pole cobra-shaped spoke type rotor. In 3-D FEA torque ripple with the cobra rotor is 66% reduced from the conventional rotor. The phase back-EMF THD of the cobra rotor is 28% reduced from the conventional rotor. A cobra-shaped spoke type rotor is compared with the laminated stator and the SMC stator. The copper loss is 19 % reduced in the SMC stator. Efficiency maps are plotted for laminated stator and SMC stator for a maximum speed of 10000 rpm. Mechanical stress analysis has been performed for a cobra rotor at 10000 rpm. The torque density in terms of motor volume is 23 % increased in SMC stator core with cobra rotor. The optimal flux weakening equation is equated by 97% between the flux linkage and the product of d-axis inductance & current. Finally, optimization has been carried out to select the best parameters. With the optimization technique the torque ripple is increased, however the average torque is increased by 3% from the previous design. Also, this optimization proves that the selected design is a better candidate.

CHAPTER – 5

Design and Analysis of a Spoke Type Rotor with Commercial Magnets for the Twizy Car

This chapter presents four different slot/pole configurations to select the best slot/pole for a traction application with a wide speed range. The electromagnetic performances are improved for the selected slot/pole configuration. This chapter presents a modified spoke type rotor that significantly reduces the torque ripple, back electromagnetic force (EMF) harmonics, and cogging torque from conventional spoke type designs. The effectiveness of the modified spoke type rotor is proved with state-of-the-art designs such as Toyota Prius and Honda Accord motors.

5.1. *Introduction to spoke type rotor*

The desired electromagnetic performance of traction motors includes low torque ripple, lower harmonics in phase back EMF, low cogging torque, and a wide constant power speed range (CPSR). Fractional-slot concentrated windings (FSCW) have attracted attention due to their fault-tolerant capability [43] and high constant power speed ratio (CPSR) [44-46]. Surface permanent magnet (PM) machines are less suitable for flux weakening [47].

The buried interior permanent magnet (IPM) machines are more promising in terms of their resistance to demagnetization and high CPSR ratio. A tangentially magnetized spoke-type interior PMSM machine is an excellent candidate for flux concentration. A 12-slot/10-pole spoke type PMSM machine had been designed with a torque ripple of 2.49% [48]. In the literature, most of the work has been done to minimize the torque ripple, but it does not discuss eliminating the hub arrangement. In spoke type PMSMs, the hub arrangement always increases the manufacturing complexity. This chapter presents a comparison between four different slot/pole configurations. The stack length of the frame used is 120 mm with a stator outer diameter of 180 mm. With this as a baseline, four different slot/poles are analyzed within these outer diameter and stack length constraints. The 12-slot/10-pole design emerges as the best candidate from the 12-slot/4-pole, 36-slot/6-pole, and 12-slot/8-pole designs. By focusing on the 12-slot/10-pole configuration, three

different rotor designs are analyzed to select the best option with improved electromagnetic performance. Design-3 emerges as the best candidate, with a very low torque ripple of 1.12%. In addition, Design-3 is a better candidate than other spoke type motors presented in the literature in terms of torque ripple and cogging torque without skewing either stator or rotor. Moreover, Design-3 eliminates the hub arrangement with a novel barrier shape. Finally, the proposed rotor design is compared with state-of-the-art designs such as Toyota Prius and Honda Accord.

5.2. Comparison of spoke-type PMSM with different slot/pole configurations.

TABLE 5.1–REQUIRED SPECIFICATIONS

Specifications	Values
Rated Power	7.1 kW
Rated Torque	20 N-m
Rated Speed	3400 rpm
Maximum Speed	10,000 rpm
Supply Voltage	96 volt
Cooling type	Air Cooled
Magnet material	NdFeB(N30SH)
Stator and rotor material	Laminated steel (M-36 29Ga)
Current density	4.5 A/mm ²

Four different slot pole configurations were studied to select the best slot pole design for traction applications. All four machines are designed to meet the same specifications presented in Table 5.1. The stator outer diameter (OD) is fixed to 180 mm for all designs. The split ratio guidelines are followed to select the stator inner diameter. Also, the stack length of the motor and rotor magnet dimensions are varied to obtain the specifications. The current density is maintained the same for all four designs. Four different designs such as 12-slot/4-pole, 36-slot/6-pole, 12-slot/8-pole and 12-slot/10-pole are analyzed to select the best slot/pole configuration for the traction application. All four-slot/pole configurations are designed to fit into the same frame. The four different designs were analyzed with different pole numbers. From the geometry aspect, the

machines with higher pole numbers utilize large rotor diameter, which reduces the need for a larger stack length of the machine.

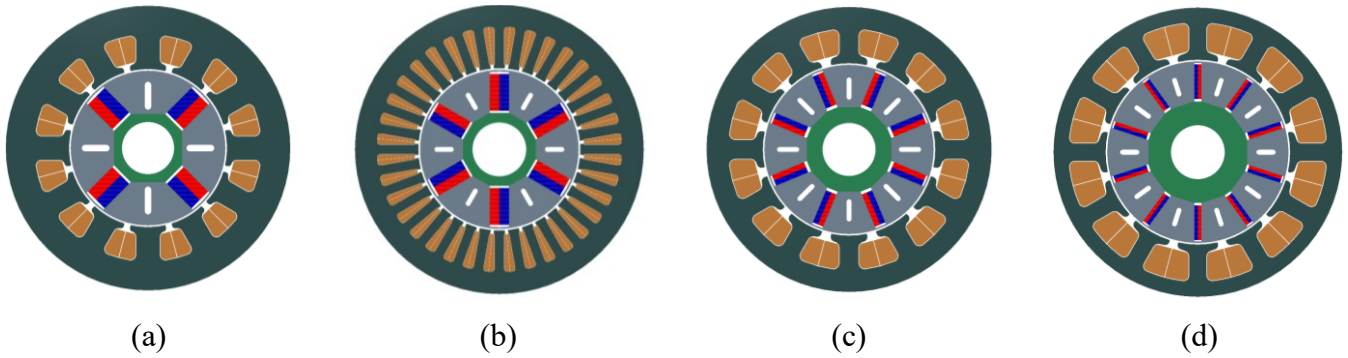


Fig. 5.1. (a) 12-slot/4-pole (b) 36-slot/6-pole (c) 12-slot/8-pole (d) 12-slot/10-pole.

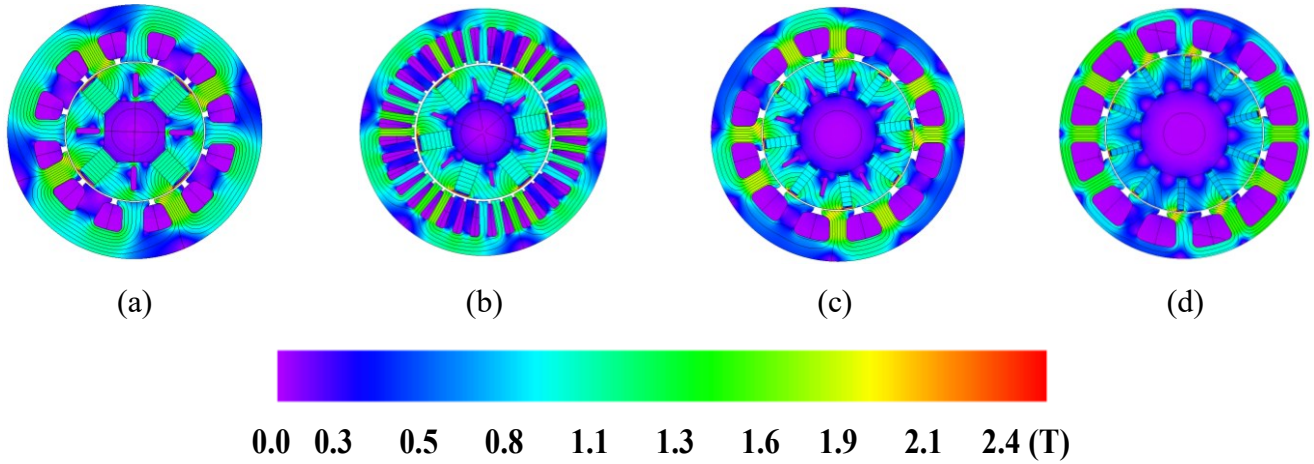


Fig. 5.2. Flux density plot at full load (a) 12-slot/4-pole (b) 36-slot/6-pole (c) 12-slot/8-pole (d) 12-slot/10-pole.

Figs.5.1 and 2 show the geometry and full load flux density plot for all four designs. The rotor diameters and stack length are changed to avoid the saturation in stator tooth and back iron.

A. Current Density

The current density of the electric motor can be defined by,

$$\text{Current density} = \frac{3K_W^{AC}}{2} * \frac{N_{ph}I_{rms}}{D} \quad (5.1)$$

where K_W^{AC} is the fundamental winding factor, I_{rms} is the winding current, $\frac{3}{2}$ the factor is for a three-phase sinusoidal current set. D is the mean air gap diameter, N_{ph} is the number of the series phase winding turns. The current density is designed to be 4.5 A/mm² for all the slot/pole

configurations. All four slot/pole configurations have been designed with a copper fill factor of 40% (defined as ratio of copper area to slot area).

B. Flux Density

The flux density of the spoke type PMSM can be defined as

$$\text{Flux density} = \frac{2 * B_{pk}}{\pi} \quad (5.2)$$

where, B is the magnetic loading, B_{pk} is the peak average flux density. The full load flux density in the stator teeth is maintained to be less than 1.7 T and the flux density in the stator back iron is maintained to be less than 1.5 T for all the slot/pole configurations. The flux value changes with number of poles. The higher the number of poles the lower the flux value. The machines with lower number of poles such as 12-slot/4-pole and 36-slot/6-pole have higher back iron thickness whereas the machines with higher number of poles have a lower back iron thickness. An aluminum hub is used in all the rotor designs. Although it increases the manufacturing cost, it helps to reduce the flux leakage.

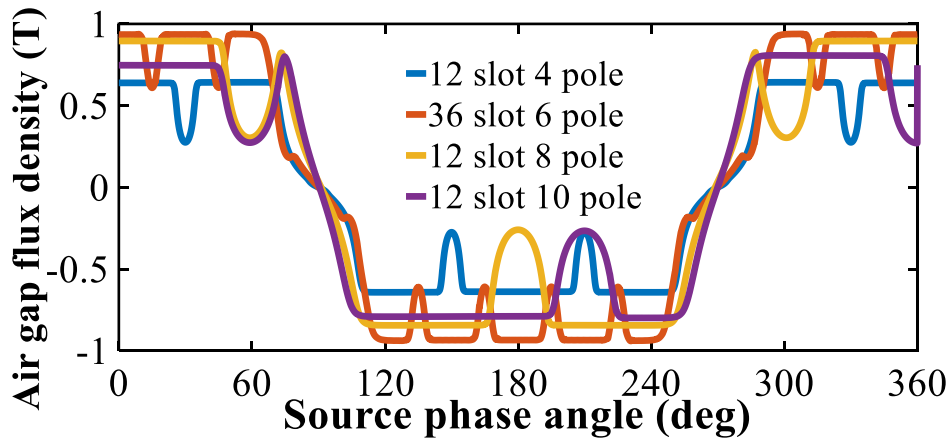


Fig. 5.3. Open circuit flux density of different slot pole designs.

C. Torque ripple

Torque ripple is defined as the ratio of the difference between the maximum and minimum torque divided by the average torque. It can be defined as below,

$$\text{Torque ripple (\%)} = \frac{T_{max} - T_{min}}{T_{avg}} * 100 \quad (5.3)$$

where T_{max} is the maximum torque, T_{min} is the minimum torque, and T_{avg} is the average torque.

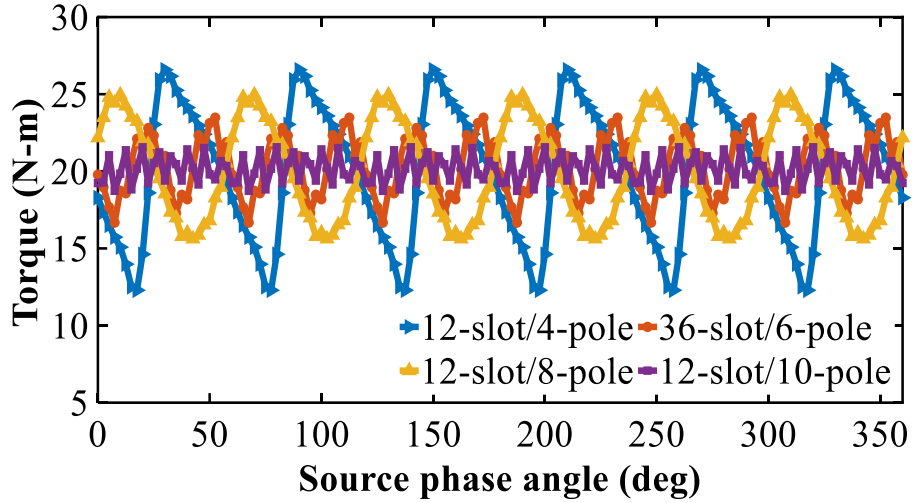


Fig. 5.4. Torque ripple of different slot/pole designs

D. Phase back EMF

The phase back EMF is given by the following equation,

$$\text{Phase back EMF} = \frac{\pi^2 * k_{w1} * N_{ph} * B * D * L_{stk} * f}{\sqrt{2} * p} \quad (5.4)$$

where N_{ph} is the number of the series phase winding turns, k_{w1} is the harmonic winding factor, L_{stk} is the stack length, f is the frequency, and p is the pole pair.

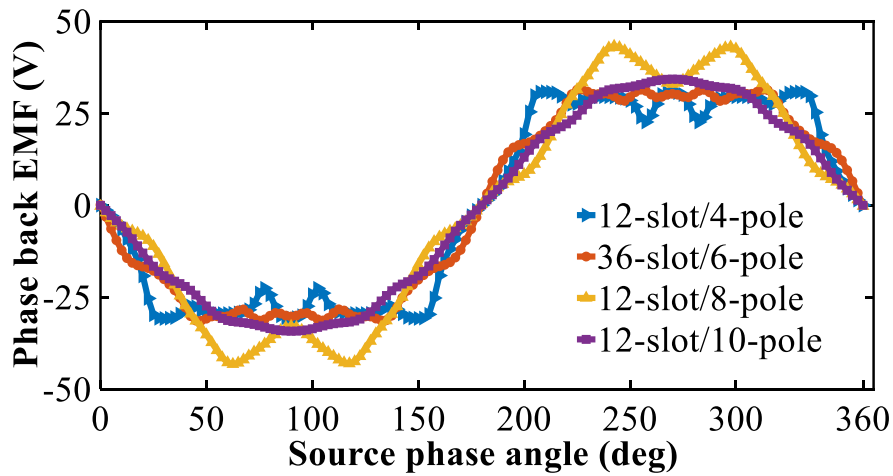


Fig. 5.5. Phase back EMF of different slot/pole designs

E. Cogging Torque

The cogging torque is due to the interaction between the magnets and the stator teeth, which can be expressed as below:

$$\text{Cogging Torque} = -\frac{1}{2}\Phi^2 \frac{dR}{d\theta} \quad (5.5)$$

where Φ is the magnet flux crossing the air gap, and R is the total reluctance torque through which the flux passes.

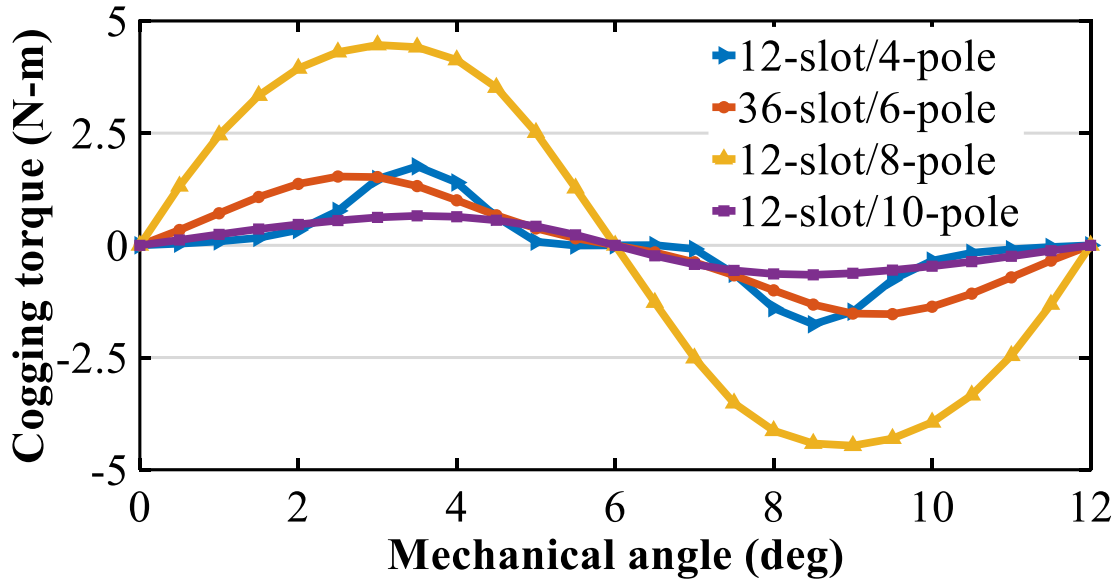


Fig. 5.6. Cogging torque of different slot/pole designs

Fig. 5.3 shows the open circuit air-gap flux density of different slot pole designs. Due to the variation of the magnet thickness, stack length, and turns per coil, the open circuit magnetic loading is not the same. But all the machines are designed to obtain same the electromagnetic torque. Fig. 5.4 shows the torque ripple of different slot pole designs. The torque ripple of the four different slot/pole configurations without skewing the rotor nor the stator is 66.9 %, 226. %, 48.8 %, and 9.56 %. Figs.5. 5 & 6 show the phase back EMF and cogging torque of different slot/pole configurations. The peak cogging torque of different slot/pole configurations is 1.75 N-m, 1.53N-m, 4.46 N-m, and 0.83 N-m.

F. Losses and Efficiency

Losses and efficiency are two important metrics in the design of traction applications. The efficiency of the motor mainly depends on stator copper losses and the iron losses in the stator and rotor core. The copper losses mainly depend on the copper fill factor. The copper fill factor is

limited by the manufacturing constraint. The iron loss of the machine increases with the pole number, but the higher pole machines will have smaller back iron which reduces the total area of the laminated steel, also in the flux weakening mode the air gap flux is suppressed which also benefits to reduce the iron losses of the motor. The copper loss and the core loss of the motor are shown below,

$$\text{Copper loss} = 3I_{rms}^2R \quad (5.6)$$

$$\text{Core loss } P_{core} = P_{hysteresis} + P_{eddy} \quad (5.7)$$

where I_{rms}^2 is the rms current and R is the phase resistance. $P_{hysteresis}$ and P_{eddy} are hysteresis and eddy current losses of the stator and rotor core.

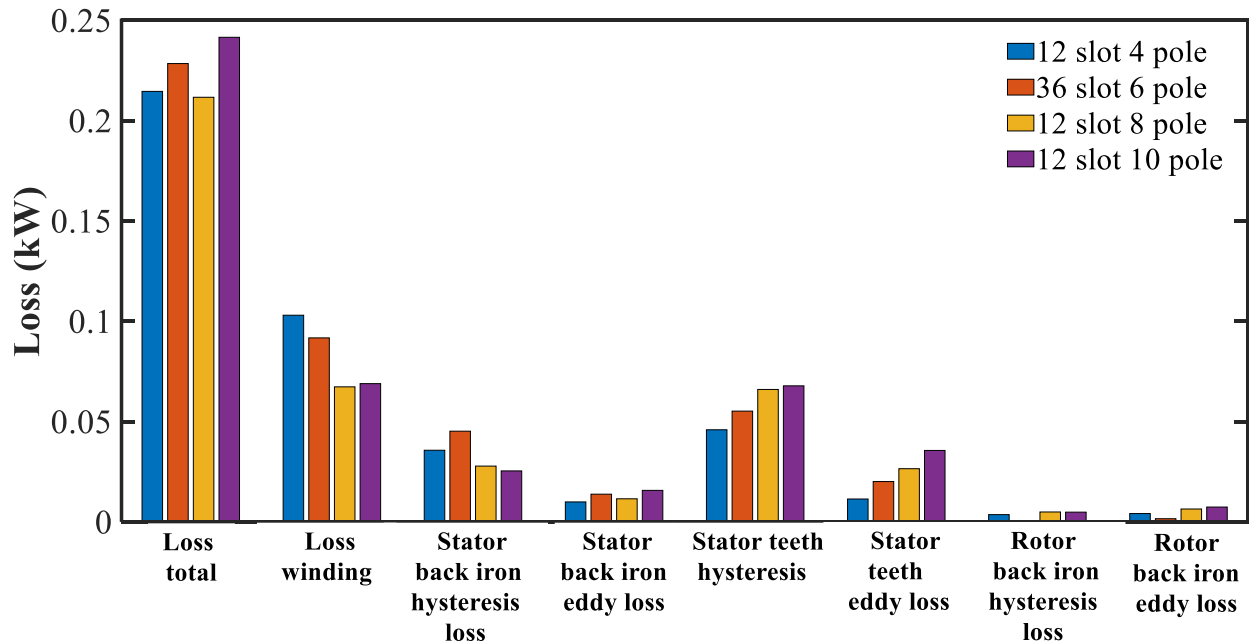


Fig. 5.7. Losses of different slot/pole designs

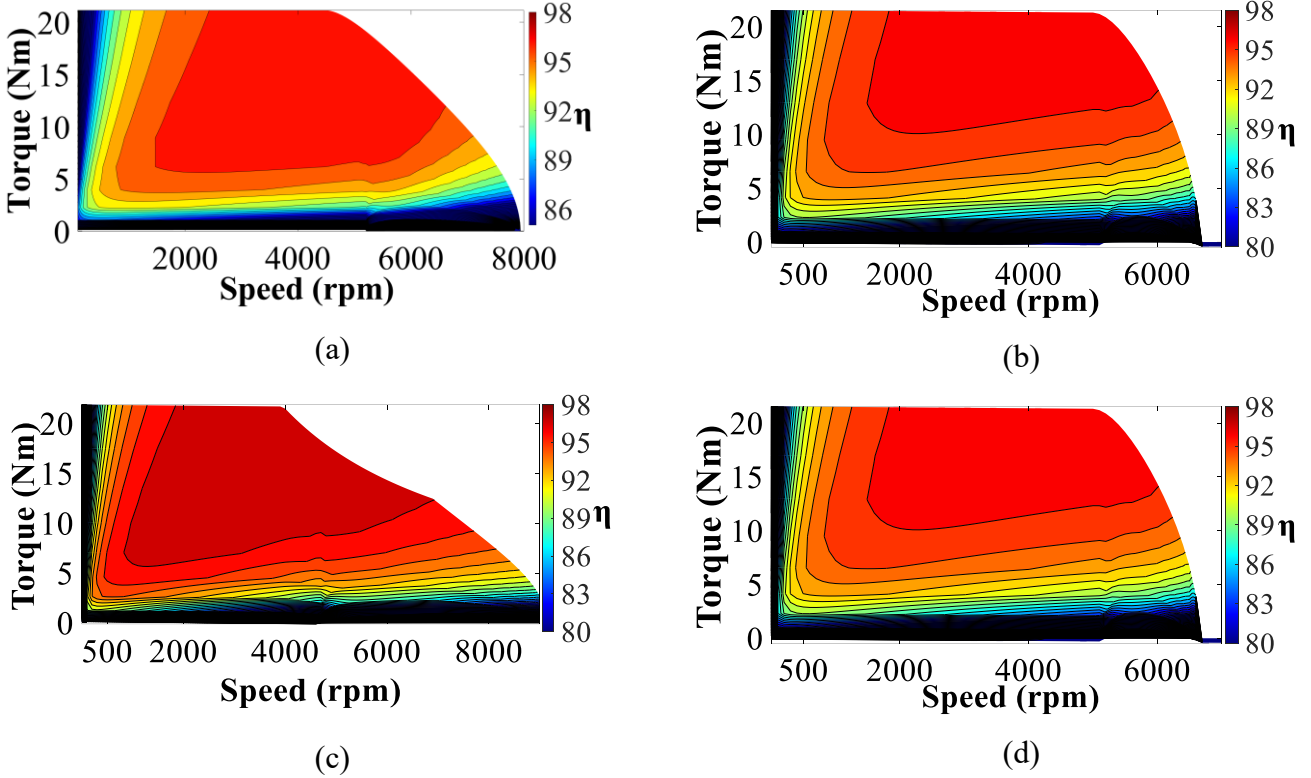


Fig. 5.8. Efficiency maps (a) 12-slot/4-pole (b) 36-slot/6-pole (c) 12-slot/8-pole (d) 12-slot/10-pole

TABLE 5.2 – PERFORMANCE METRICS OF SLOT POLE SELECTION

Items	12/4	36/6	12/8	12/10
Slot/Pole/Phase	1	2	0.5	0.4
Back EMF THD (%)	53.8	28.3	24.3	8.38
Average torque (N-m)	20.06	20.3	20.07	20.15
Torque ripple (N-m) (%)	66.9	22.6	48.8	9.56
Peak cogging torque (N-m)	1.75	1.53	4.46	0.83

Fig. 5.7 shows the loss analysis of the different slot pole combinations, the total loss is found to be higher with the 12- slots/10-pole design. Fig. 5.8 shows the efficiency map for four different slot/pole configurations. It is clear that the machine with a lower number of poles does not exhibit a wide field weakening region. The speed is reduced before the maximum speed of 10000 rpm. The 12-slot/10-pole has (SPP=0.4) achieves the wider flux weakening region. Also, table 5.2 shows the performance comparison between all 4 different pole configurations. The 12-slot/10-pole configuration has better back EMF THD (%), lower torque ripple, lower cogging torque when

compared to all other designs. From this analysis the 12-slot/10-pole design is selected for further analysis with the modified three different spoke type rotors and SMC stator design.

5.3. *Air gap flux density in spoke type PMSM*

The air gap flux density can be increased by arranging the magnets in the spoke-type structure. As the magnets are buried inside the rotor, the air gap flux density can be increased substantially to a value greater than the magnet itself. In spoke -type magnets the flux over the pole arc can be defined as follows [49]

$$B_g \left(\frac{\pi D_{od} - Pt_m}{P} \right) = 2 l_m B_m \quad (5.8)$$

where B_g is the magnet air-gap flux density, D_{od} is the outside diameter of the rotor, P is the number of poles, t_m is the thickness of the magnet, l_m is the length of the magnet, B_m is the flux density within the magnet. The inner radius of the rotor can be defined as follows,

$$r_{ir} = \frac{Pt_m}{2\pi} \quad (5.9)$$

The length of the magnet can be written as follows,

$$l_m = r_{or} - r_{ir} = r_{or} - \frac{Pt_m}{2\pi} = \frac{(2\pi * r_{or}) - Pt_m}{2\pi} \quad (5.10)$$

where r_{or} & r_{ir} are the outer radius and inner radius of the spoke type rotor. Equating (9) and (11) can be expressed as follows,

$$\frac{2 \left(\frac{(2\pi * r_{or}) - Pt_m}{2\pi} \right)}{\left(\frac{\pi D_{od} - Pt_m}{P} \right)} = \frac{(2\pi * r_{or}) - Pt_m}{2\pi} \quad (5.11)$$

$$\frac{B_g}{B_m} = \frac{P}{\pi} \quad (5.12)$$

Equation (5.12) shows that the magnet flux density in the air gap can be increased if the number of poles are chosen as four or more. The magnetomotive force (MMF) developed by the permanent magnet and the armature reaction are fixed, though the magnetic field

distribution in the air gap varies due to the shape of the rotor. The MMF at the air-gap can be expressed as the product of the reluctance and magnetic flux.

$$MMF = R * \varphi \quad (5.13)$$

where R is the reluctance and φ is the flux. The magnetic field distribution can be varied by changing the reluctance. The reluctance in the magnetic circuit can be expressed as follows,

$$R = \frac{l}{\mu_0 * \mu_r * A} \quad (5.14)$$

where l is the magnetic path length, μ_0 is the relative permeability of the vacuum, μ_r is the relative permeability of the material, A is the cross-sectional area of the magnetic path length. The air-gap magnetic flux density can be changed from rectangular to sinusoidal by adjusting the air gap length.

5.4. Selection of rotor and stator parameters

From the above section a 12 slot 10 pole, spoke type PMSM is chosen as the best candidate for this particular traction application. The rotor and stator designs are analyzed interactively to find the best parameters considering wider flux weakening, lower torque ripple and lower mechanical stress values. The stator and rotor diameter are fixed. The stack length of the motor is also fixed for this analysis. The motor terminal voltage primarily depends on the turns per coil, as it's a low voltage motor, the turns per coil is also limited by the voltage. The peak phase fundamental voltage available from the drive is 43V. An iteration has been done in JMAG FEA with different turns per coil to obtain the best turns per coil.

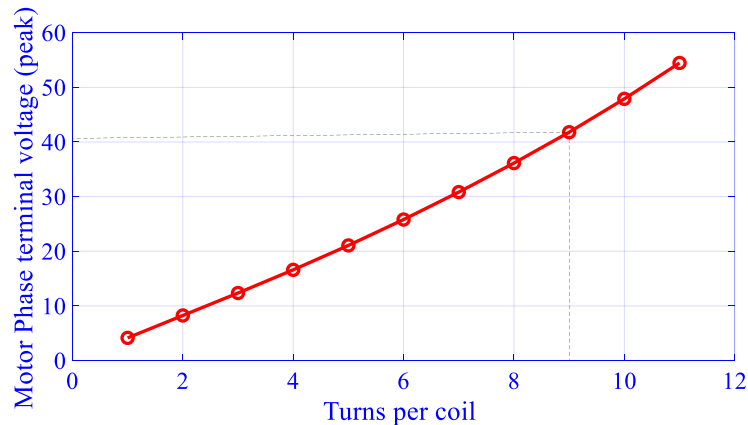


Fig. 5.9. Turns per coil Vs peak phase fundamental voltage from the drive.

Fig. 5.9 shows that the 9 turns per coil is the optimal number to maintain the voltage limits. After fixing the turns per coil, the spoke type PMSM is analyzed with different magnet thickness such as 3, 4, 5 and 6 mm to select the best magnet thickness to achieve a wide flux weakening operations.

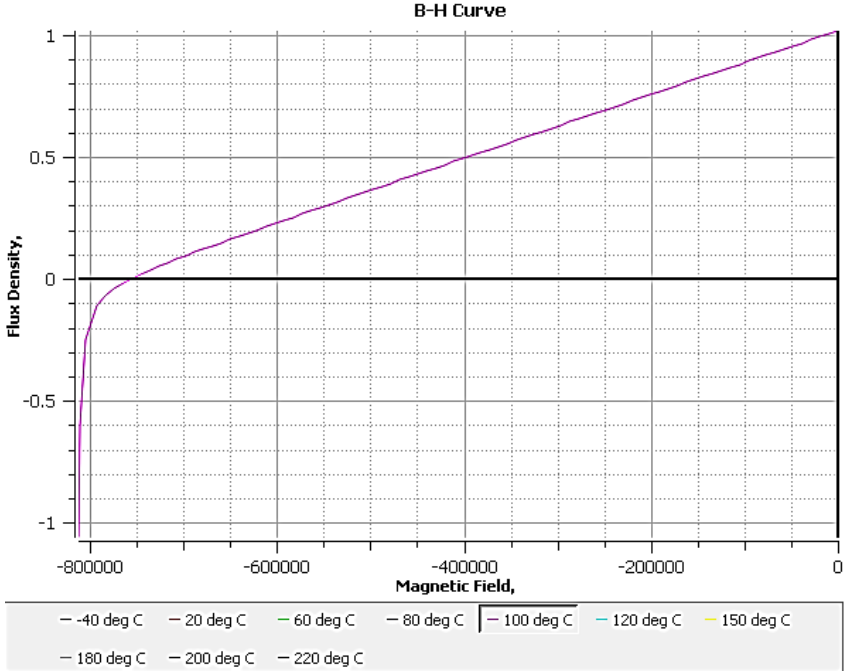


Fig. 5.10. B-H curve of N30SH magnet grade at 100 deg C

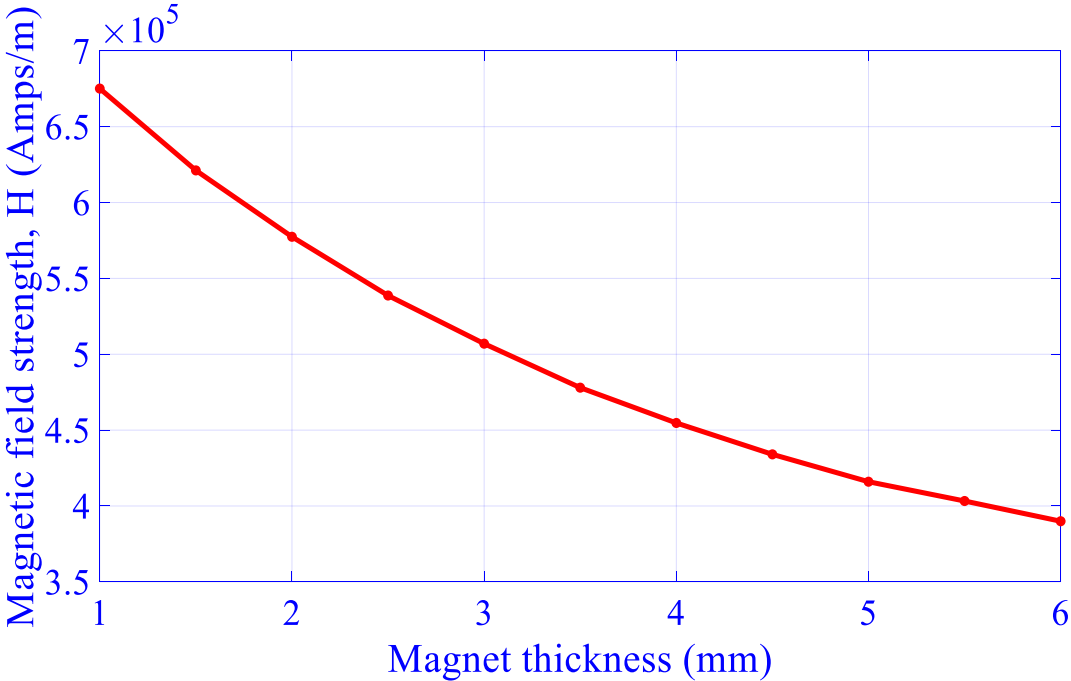


Fig. 5.11. Magnetic field strength with respect to magnet thickness

Fig. 5.10 shows the B-H curve of the selected magnet at 100 deg C. Fig. 5.11 shows the variation of magnetic field strength with respect to the magnet thickness. Magnet thickness is varied from 1mm to 6 mm in which the d axis current is injected with 90 degrees advance angle. The graph shows that when the magnet thickness is 1mm, the magnetic field strength reaches 670,000 H (Amps/m), which is very close to the slope in Fig.10. However, operating the magnet at this point is vulnerable to demagnetization.

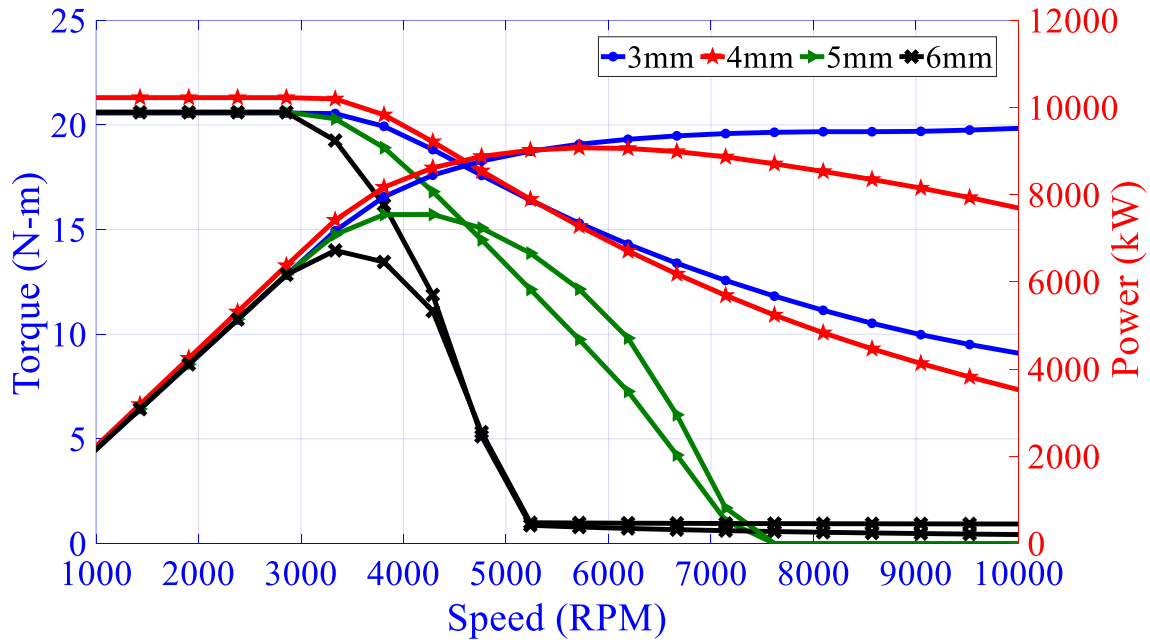


Fig. 5.12. Speed Vs Torque and Speed Vs Power for different magnet thickness

Fig. 5.12 shows the Speed Vs Torque and Power for the different magnet thickness. For this analysis magnet thickness is varied from 3 mm to 6 mm. In all these cases the motor is designed to produce the required torque at constant torque mode. A design with a lower magnet thickness is a good candidate for wider flux weakening, but it is more susceptible to demagnetization. On the other hand, a higher magnet thickness is a better candidate in terms of demagnetization, but it may not be as effective for wider flux weakening. After considering these tradeoffs, a design with a magnet thickness of 4 mm was selected as the best candidate. The magnet dimensions and turns per coil are selected based on the previous sensitivity analysis. Now, the rotor and stator parameters are analyzed. Sensitivity analysis is a technique used to analyze the impact of variations in input parameters on the output response of a motor. As an example, let's consider a motor with three parameters, each parameter having two divisions. In total, there will be eight different cases to examine, employing a factorial design approach.

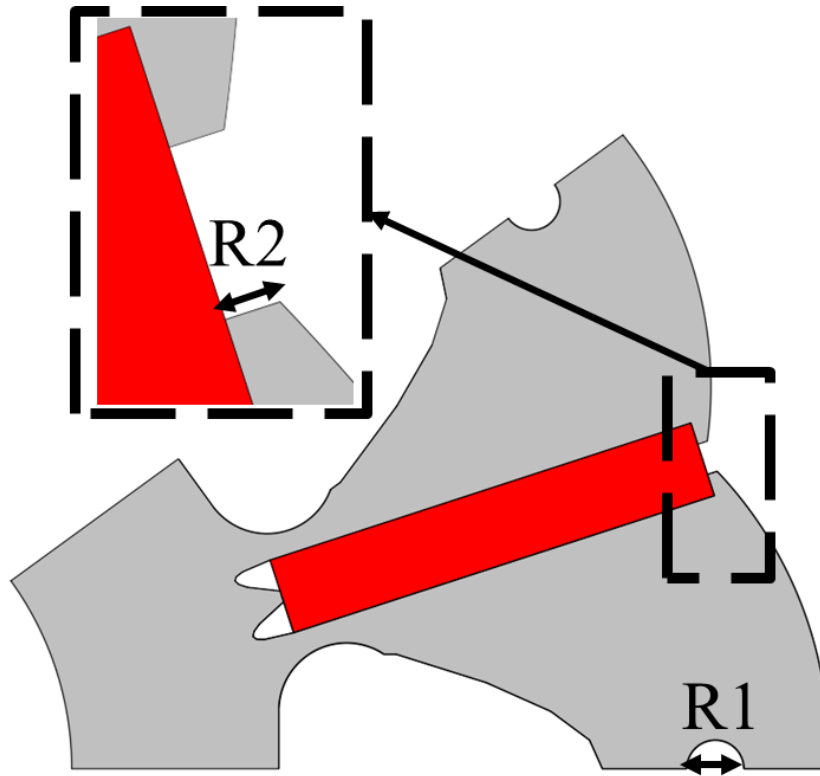


Fig. 5.13. One rotor pole and one stator slot

Fig. 5.13 shows one rotor pole and one stator slot with the parameters such as R2 (rotor magnet inset depth), R1(Rotor top slit radius), S1(Stator half slot opening width), S2(Stator slot depth), and S3 (Stator tooth width). Firstly, two studies are created for electromagnetic analysis and mechanical stress analysis. The two studies are grouped into an analysis group. The electromagnetic study is similar to a normal case, but in mechanical analysis only one pole of the rotor is used for the analysis with similar rotor constraints as the electromagnetic study. Two parameters R1 and R2 are used for multiobjective optimization.

TABLE 5.3 – ROTOR PARAMETERS FOR OPTIMIZATION

Items	Range
Rotor Magnet inset depth (R2)	0.44 – 1.36 (mm)
Rotor Top slit radius (R1)	2 – 4 (mm)

915 cases are simulated in JMAG 2D to optimize the rotor design of spoke type PMSM. The simulation has been carried out with a multiobjective genetic algorithm which is available in

JMAG FEA. The number of generations is 100 and population size used is 10. 915 cases are generated to obtain the best values. Table 5.4 shows the objectives for optimization.

TABLE 5.4– OBJECTIVES FOR OPTIMIZATION

Items	Range
Torque Ripple	Minimize
Average Torque	Maximize
Mechanical stress	Minimize

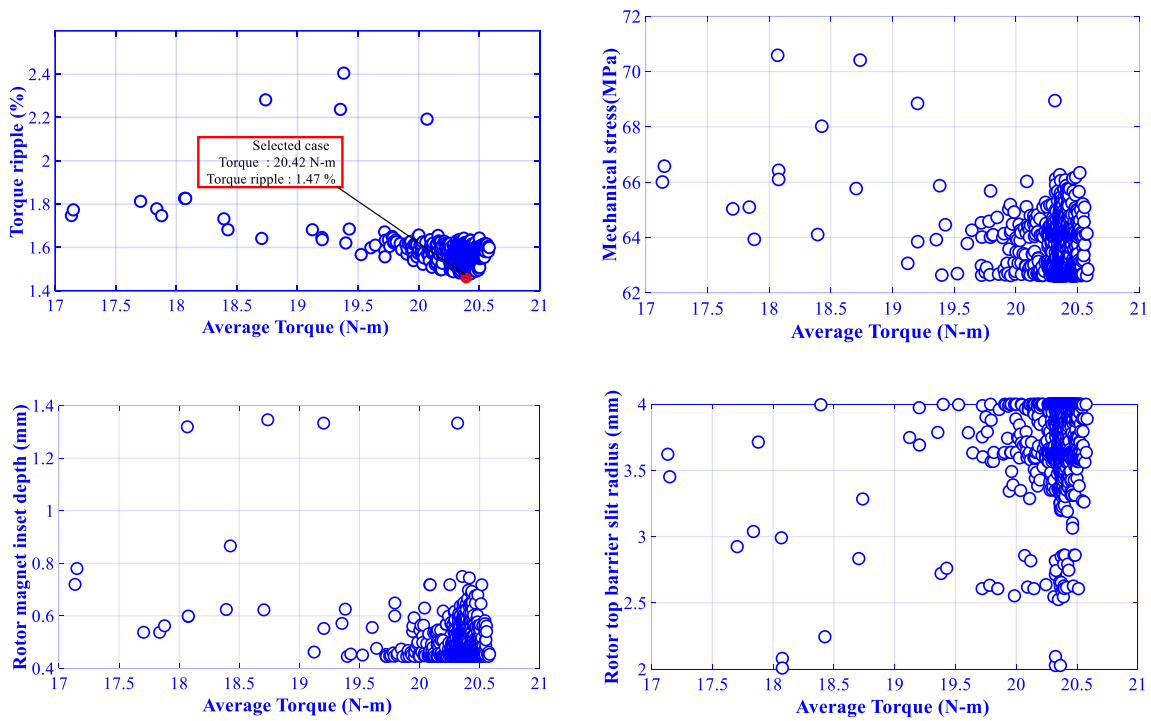


Fig. 5.14. Rotor optimization results

TABLE 5.6 – SELECTED PARAMETERS AFTER OPTIMIZATION

Items	Chosen parameters
Rotor Magnet inset depth (R2)	0.509 mm
Rotor Top slit radius (R1)	3.7 mm
Selected case number	886

Based on the optimization results, the rotor magnet inset depth and the rotor top slit barrier radius were selected. The figures above indicate that the selected design leads to lower rotor stress and lower torque ripple. Using these parameters as a basis, the stator parameters were chosen through sensitivity analysis.

TABLE 5.7 – STATOR PARAMETERS FOR SENSITIVITY

Items	Range
Stator half slot opening width (S1)	2-4 (mm)
Stator slot depth (S2)	23 – 24.5 (mm)
Stator tooth width (S3)	13.92 – 15.55(mm)

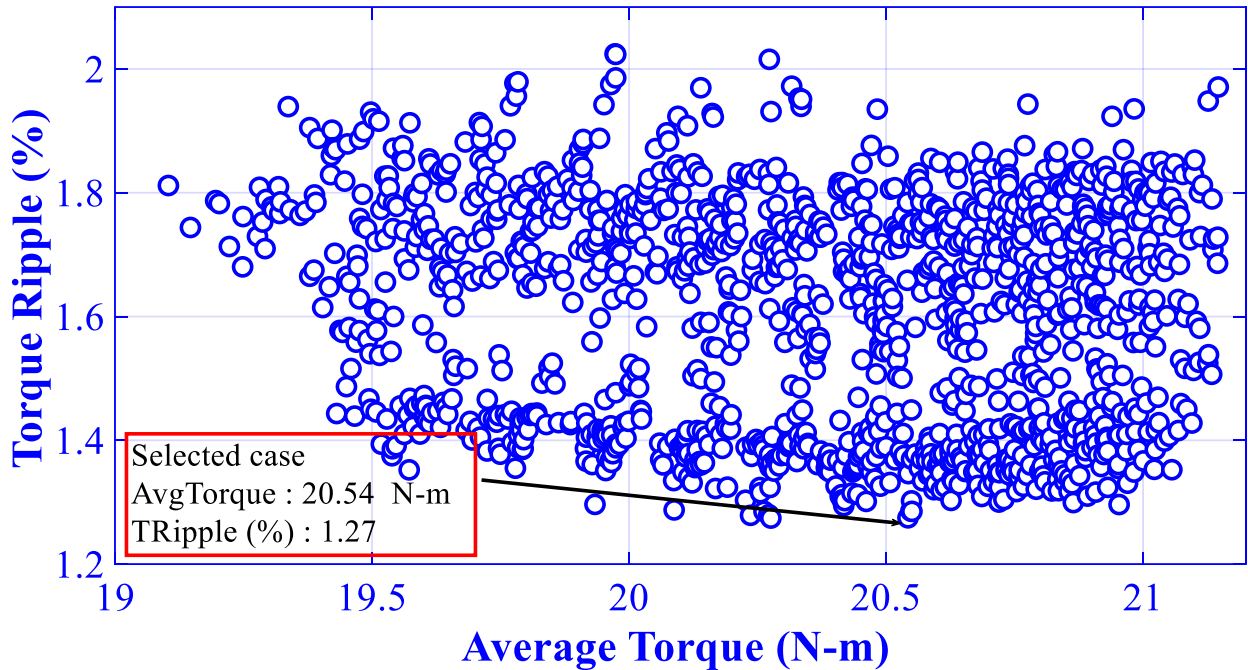


Fig. 5.14. Stator sensitivity analysis results (average torque Vs torque ripple)

To analyze the stator tooth, several parameters were modified including the slot opening, depth of stator slot, and width of stator slot. The sensitivity analysis parameters are listed in Table 5.7. Due to manufacturing constraints, the tooth tip thickness was fixed at 4 mm, while other parameters were varied with an interval of 0.2 mm. The main objective of this sensitivity analysis was to minimize torque ripple and stator hysteresis losses. 1332 cases are considered for analysis.

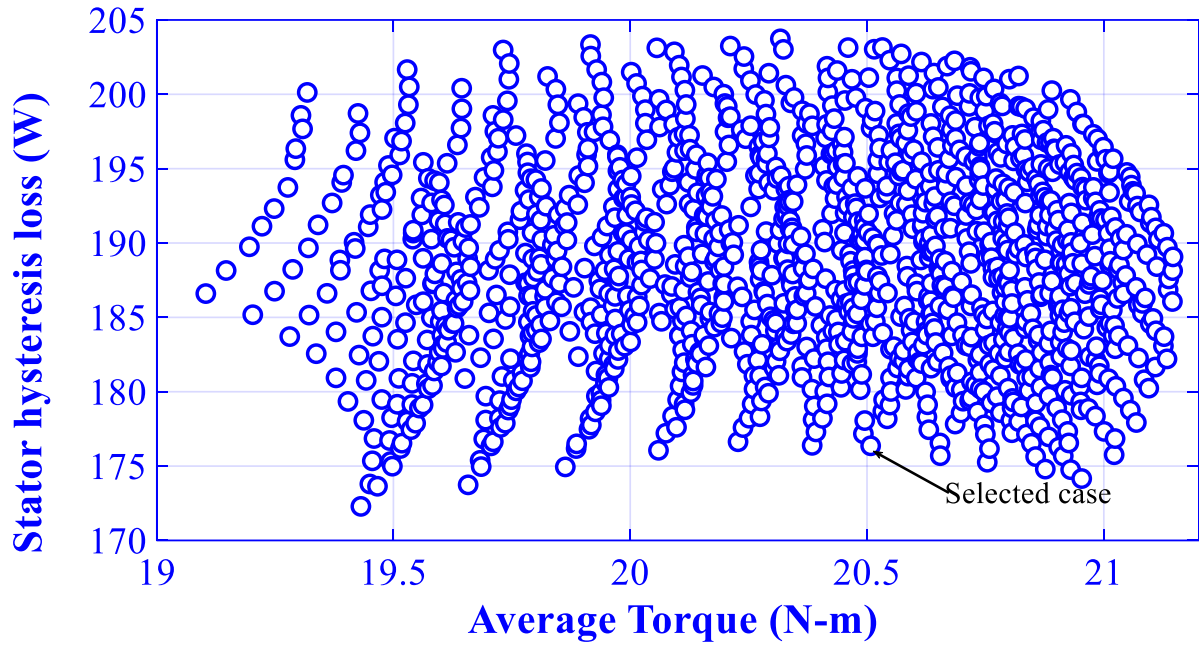


Fig. 5.15. Stator sensitivity analysis results (average torque Vs hysteresis loss)

Generally, the PMSM rotor will have a tendency to align with the slotted stators at various points, which is called as cogging torque. In traction motors skewing is widely employed to reduce the cogging torque which in turn will reduce the torque ripple too. All these cases are analyzed without skewing either the rotor or stator. Figs.5. 14 and 15 show the average torque vs torque ripple and hysteresis loss vs average torque for all the 1332 candidates. Case number 495 is chosen as the best candidate with lower torque ripple and lower hysteresis losses. Table 5.8 shows the selected parameters for the stator core.

TABLE 5.8 – SELECTED PARAMETERS FOR STATOR CORE

Items	Parameters
Slot opening (mm)	3.8
Tooth tip thickness (mm)	4.14
Depth of stator slot (mm)	22.83
Width of stator slot (mm)	14.725

5.5. *Conventional and modified spoke type rotor*

From the above section 12-slot/10-pole is chosen as Design-1. This section focusses on three designs with the same laminated stator design and three different rotor designs.

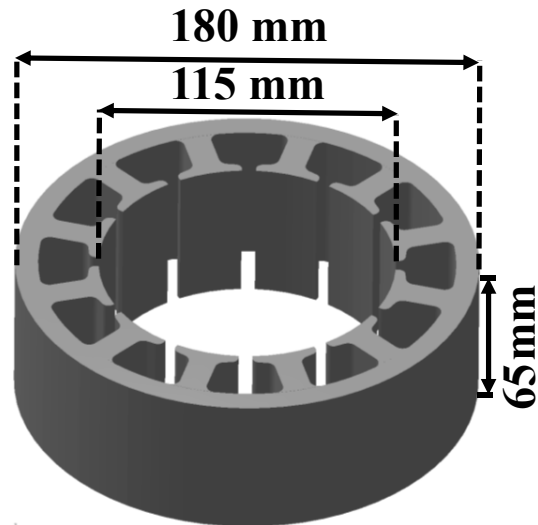


Fig. 5.16. Laminated stator core

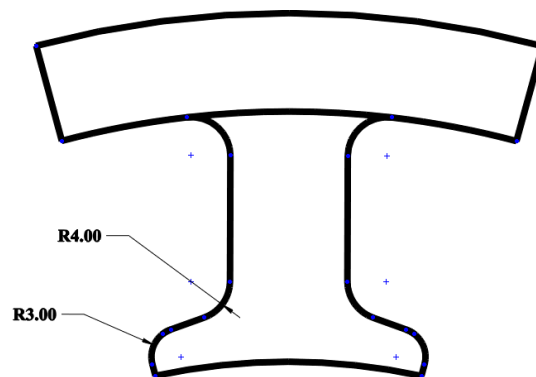


Fig. 5.17. Laminated stator teeth

The design conditions for the comparison are as follows:

- [1] The three designs have the same stator outer diameter and inner diameter. The copper fill factor is maintained the same (40%) for all the three designs. The magnet volume is kept the same for all the three rotor designs.

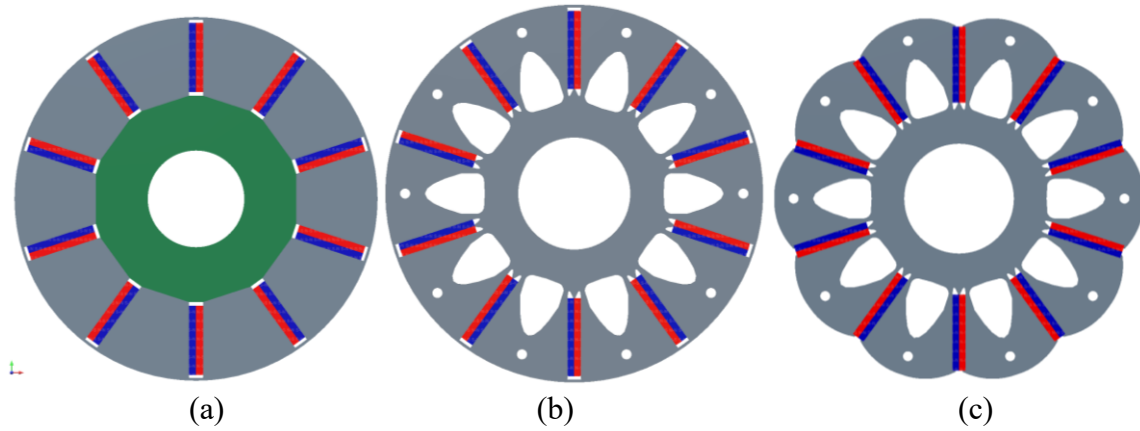


Fig. 5.18. Rotor designs (a) Design-1 (b) Design-2 (c) Design-3

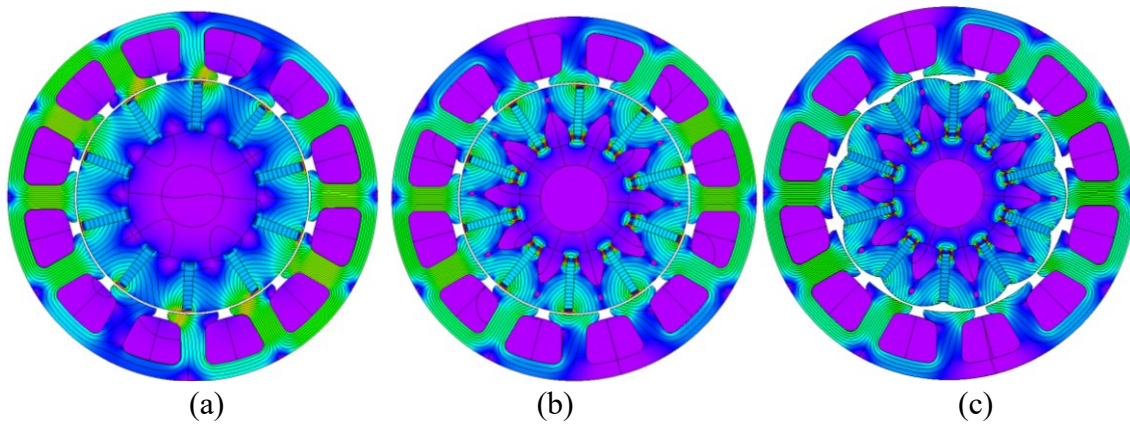


Fig. 5.19. Flux density (a) Design-1 (b) Design-2 (c) Design-3

[2] Also, the current is changed in Design-3, increasing the turns will reduce the number of parallel strands which ultimately pushes the current density to cross the boundary value. Increasing a quarter turn ($1/4$) would be beneficial, but it is unlikely with the 12-slot/10-pole configuration as it cannot have more than two parallel paths due to non-symmetry.

[3] Also, the machine dimensions such as the stack length and the stator diameter outside diameter are fixed. The rms current density is varied within the limit from 4.13 A/mm^2 to 4.86 A/mm^2 .

TABLE 5.9 - DESIGN PARAMETERS OF THE ANALYSIS MODELS

Item	Design-1	Design-2	Design-3
RMS phase current	100	100	107
Rotor magnet mass (kg)	0.47	0.47	0.47
Number of turns per coil	8	9	9
Stator OD (mm)	180	180	180
Rotor OD (mm)	113	113	113
Stack length (mm)	65	65	65
Phase voltage (RMS)	28.6	32.1	27.1

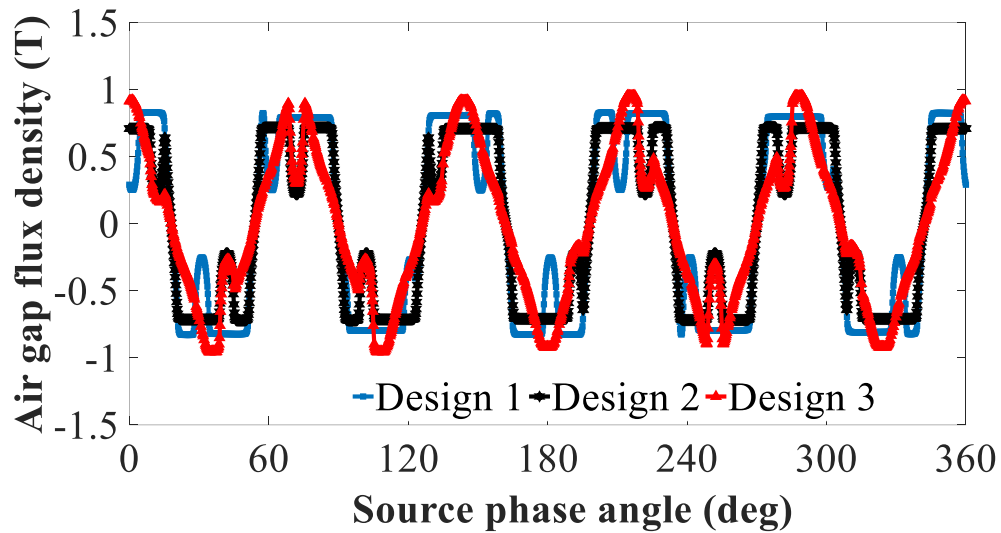


Fig. 5.20. Open circuit air-gap flux density of design 1,2 and 3.

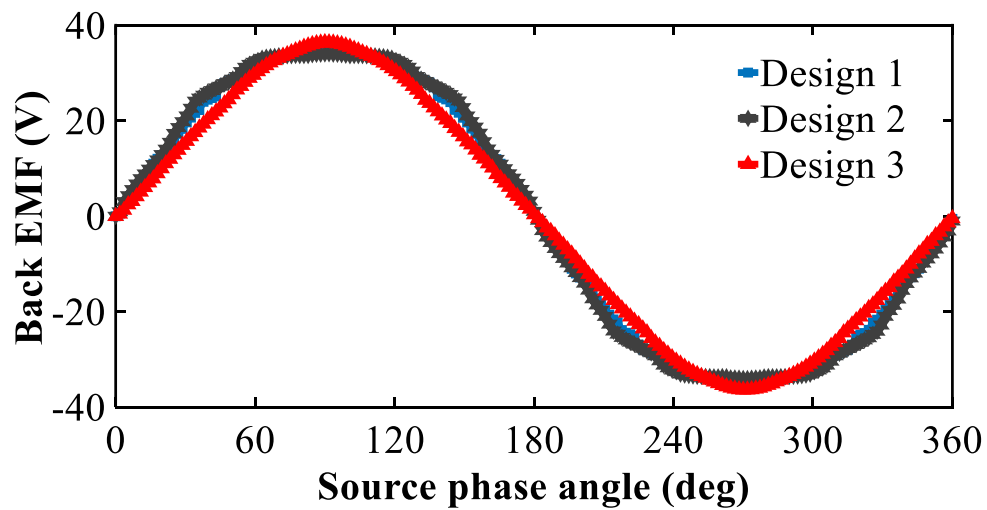


Fig. 5.21. Back EMF of Designs-1,2 &3

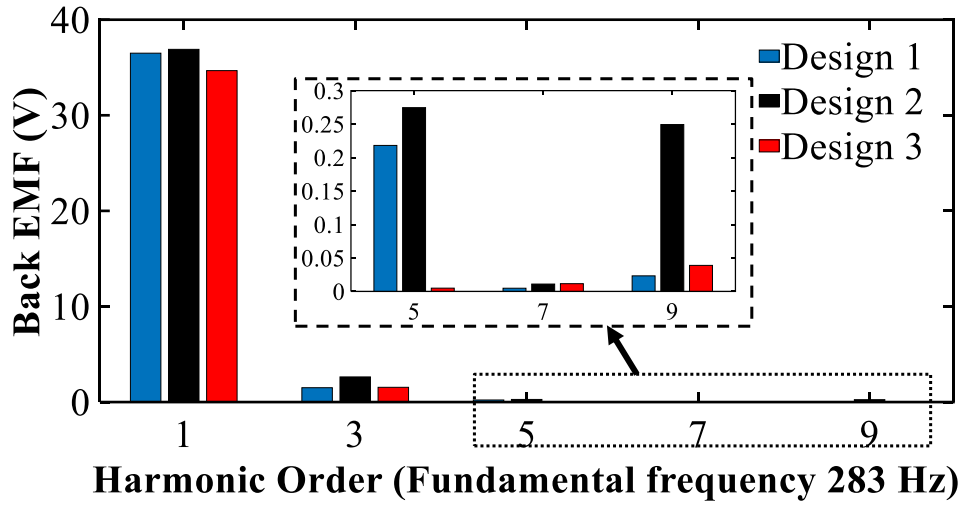


Fig. 5.22. Phase back EMF harmonics of Designs-1, 2 and 3.

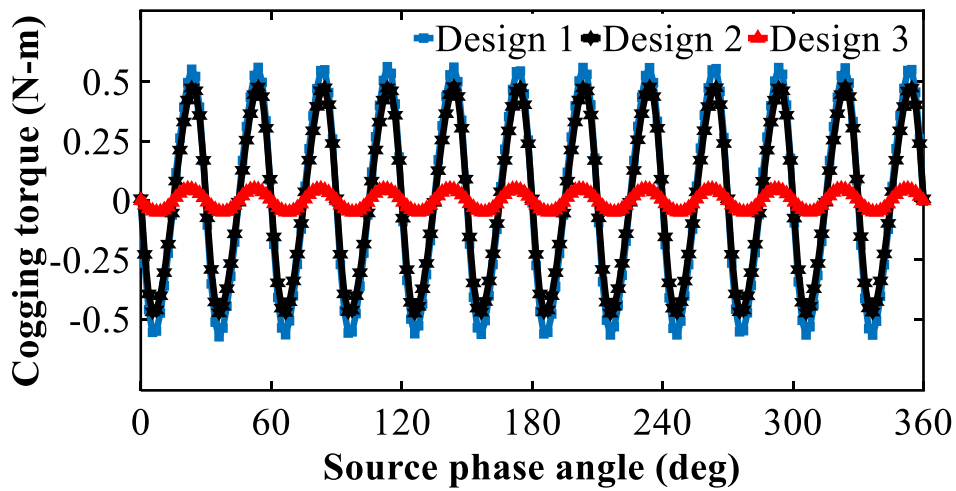


Fig. 5.23. Cogging torque of design 1,2 and 3.

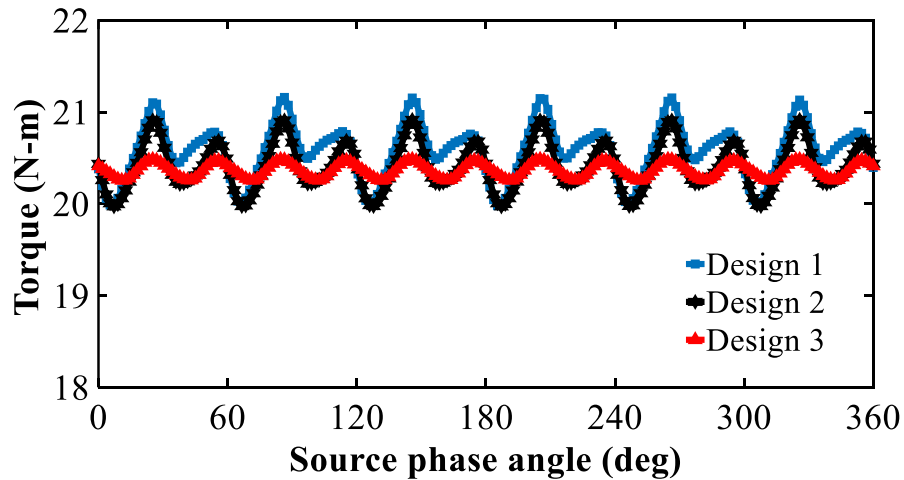


Fig. 5.24. Electromagnetic torque of Designs- 1,2 and 3.

Fig. 5.17 shows the laminated stator with a tooth segment. The same laminated stator is used for the Design-1,2 and 3. Fig. 5.18 shows the three different rotor designs. Fig. 5.19 shows the flux density plot of three different rotor designs. Table 5.9 summarizes the parameters used for the three different designs. Figure 20 shows the open circuit air-gap flux density of Designs 1,2 and 3. The air-gap flux density of Design-3 is closer to sinusoidal when compared to the other two designs. Figs.5.21 and 22 show the back EMF and harmonics of the three designs respectively. Table 5.10 shows the back EMF harmonics of all the three rotor designs. Design-3 has better phase back EMF when compared to the other two designs.

TABLE 5.10– PHASE BACK EMF HARMONICS

Harmonic order	Design-1	Design-2	Design-3
1 st	36.498	36.898	34.673
3 rd	1.502	2.630	1.544
5 th	0.218	0.275	0.005
7 th	0.005	0.011	0.012
9 th	0.023	0.249	0.039
THD (%)	4.79 %	8.57%	4.61%

The dominant harmonics are enlarged in Fig. 5.22. The 3rd harmonic with Design-3 is 2% higher than the Design-1. But the 5th harmonic is significantly reduced in the Design-3. The total harmonic distortion (THD) of the three rotor designs are 4.79 %, 8.57% and 4.61 %. The overall THD with Design-3 is 3.75% reduced from Design-1. The THD can be calculated by using the formula below,

$$\text{THD} = \frac{\sqrt{V_1^2 + V_2^2 + V_3^2 + \dots}}{V_0} \quad (15)$$

TABLE 5.11– PERFORMANCE METRICS OF DESIGN 1, 2 & 3

Items	Design-1	Design-2	Design-3
Average torque (N-m)	20.58	20.40	20.36
Torque ripple (N-m) (%)	5.72	4.62	1.12
Peak cogging torque (N-m)	0.563	0.479	0.049

Figs.5.23 and 24 show the cogging torque and electromagnetic torque of the three rotor designs. The cogging torque of Design-3 is significantly reduced from the other two designs, which is achievable only with the rotor pole shaping. Table 5.11 shows the comparison of average torque, torque ripple and cogging torque of the three rotor designs. The peak-peak cogging torque with Design-3 is 91.29% reduced from Design-1. The average torque and power rating are maintained the same for all three rotor designs. The torque ripple with Design-3 is 80.59 % reduced from Design-1. The electromagnetic torque ripple and the cogging torque are significantly reduced in Design 3. It can be concluded that Design-3 is the best candidate with reduced torque ripple and cogging torque.

5.6. *Design case for proving the effectiveness of the proposed rotor design.*

A. *Case Study with Toyota Prius 2010 design*

A design case is presented here mainly to highlight the advantages of the proposed rotor design without a hub arrangement. The proposed spoke type rotor is designed based on the commercial interior PM synchronous machine Toyota Prius 2010. The Toyota Prius stator is used to have a similar electric loading. The rotor is designed with a proposed spoke- type rotor configuration from Design-3. The rotor poles are changed from 10 pole to 8 pole. The rotor geometry from Design 3 is scaled up to fit into the Toyota Prius stator.

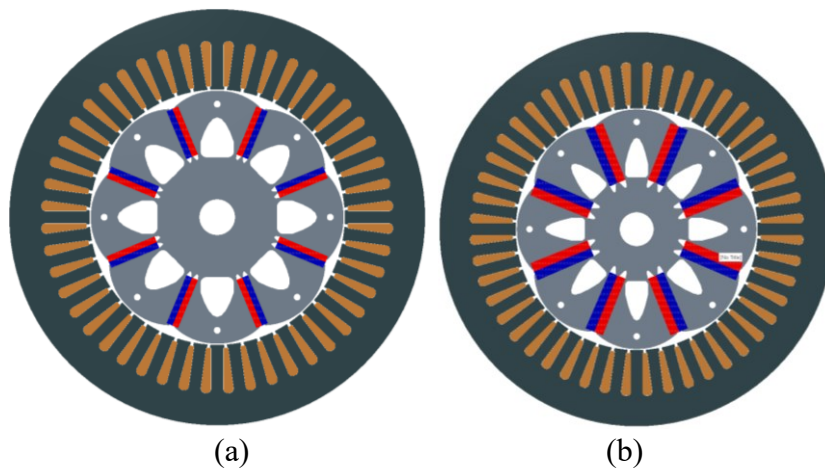


Fig.5.25. Toyota Prius stator with proposed rotor design (a) Design-3_1(same magnet mass) (b) Design-3_2(increased magnet mass)

The key dimensions of the Toyota Prius motor and the proposed rotor designs such as Design-3_1(same magnet mass), Design-3_2(increased magnet mass) and Design-3_3(increased magnet mass with SMC) are shown in Table 5.12. The Toyota Prius dimensions are obtained from an

TABLE 5.12 – KEY DIMENSIONS OF THE TOYOTA PRIUS & PROPOSED DESIGN

Items	Toyota Prius	D-3_1	D-3_2	D-3_3
Stator outside diameter (mm)	264	264	264	264
Stator inside diameter (mm)	162	162	162	162
Rotor outside diameter (mm)	160	160	160	160
Stack length (mm)	50	50	50	54
Air gap length (mm)	0.73	0.73	0.73	0.73
Turns per coil	11	11	11	11
Number of parallel path	0	0	0	0
PM mass (kg)	0.76	0.76	1.4	1.58
Poles	8	8	8	8
Number of stator slots	48	48	48	48
Slot per pole per phase	2	2	2	2
Slot depth (mm)	30.9	30.9	30.9	30.9
Slot opening (mm)	1.88	1.88	1.88	1.88
Rated speed (rpm)	2800	2800	2800	2800
Current density (A/mm ²)	19	19	19	19

ORNL report [50]. Figure 25 shows the proposed rotor design (a) Design-3_1 (with the same magnet mass) of Toyota Prius and (b) Design-3_2 (increased magnet mass) as the Toyota Prius design. The proposed design with the increased magnet mass is further analyzed with the SMC stator core. Figure 26 shows the full load flux density plot of the proposed rotor designs with the same and increased magnet mass compared to the Toyota Prius motor. Figs. 27 and 28 show the electromagnetic torque and the phase back EMF of the four designs such as the Toyota Prius, Design-3_1(same magnet mass), Design-3_2(increased magnet mass) and Design-3_3(increased magnet mass with SMC). The same Toyota Prius stator dimensions are used for the four designs

except the stack length is increased for Design-3_3 (increased magnet mass with SMC). Hence the phase current, number of parallel paths, slot depth, slot opening, and current density remain the same for all the designs.

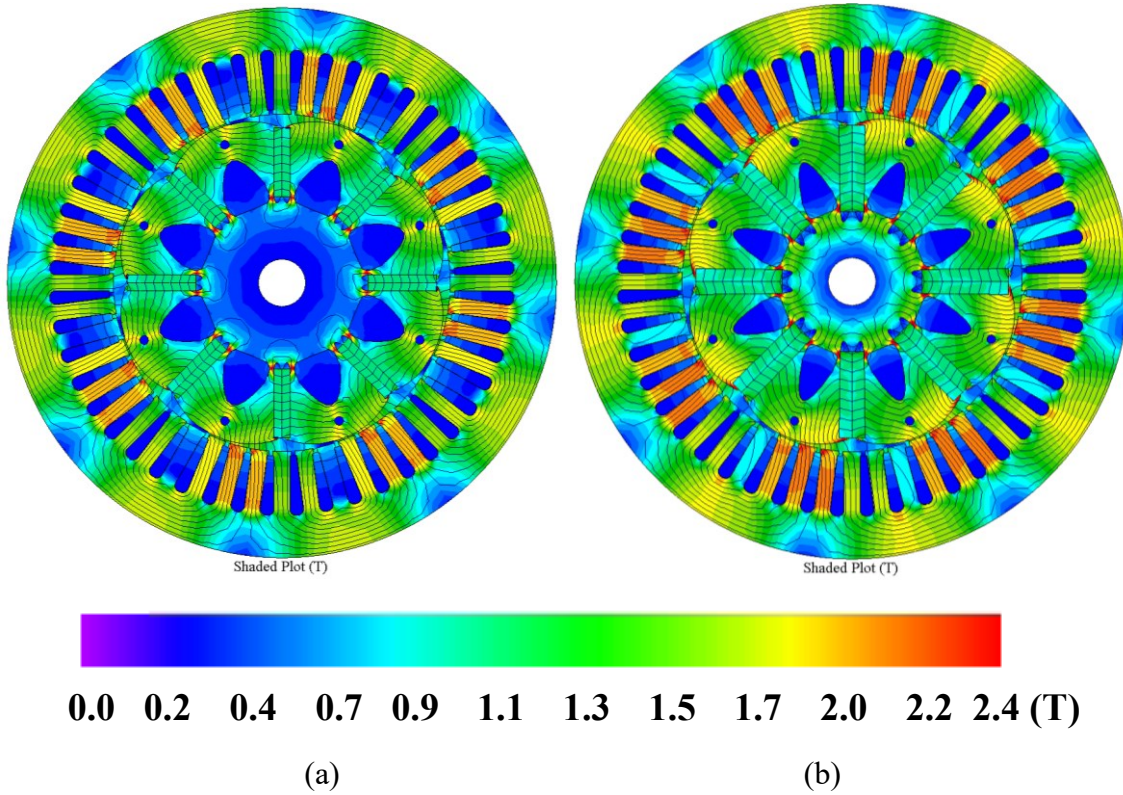


Fig. 5. 26. (a) Toyota Prius stator with proposed rotor design (a) Design-3_1(same magnet mass) (b) Design-3_2(increased magnet mass)

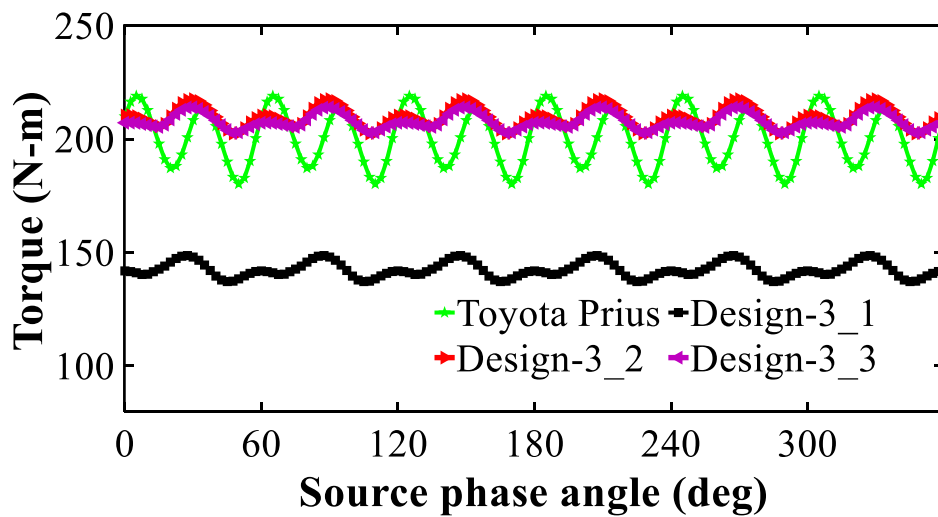


Fig. 5.27. Electromagnetic torque of Toyota Prius, Design-3_1(same magnet mass), Design-3_2(increased magnet mass), & Design-3_3(increased magnet mass with SMC).

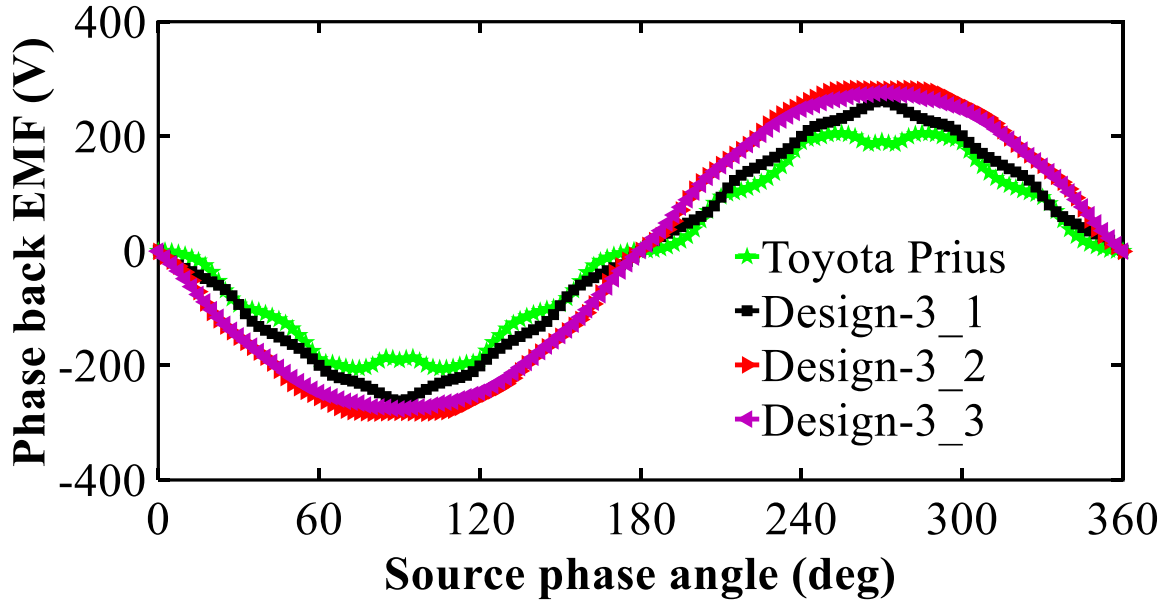


Fig. 5.28. Phase back EMF of Toyota Prius, Design-3_1 (same magnet mass), Design-3_2 (increased magnet mass), & Design-3_3 (increased magnet mass with SMC).

TABLE 5.13 – PERFORMANCE METRICS OF CASE STUDY WITH TOYOTA PRIUS

Items	Toyota Prius 2010	D-3_1	D-3_2	D-3_3
Back EMF THD (%)	26.5	16.4	7.5	4.29
Average torque (N-m)	200.7	142.3	209.7	207.8
Torque ripple (N-m) (%)	19.3	8.0	7.2	5.41

TABLE 5.14 - TOYOTA PRIUS COST COMPARISON WITH 48-SLOT/8-POLE

Item	Toyota Prius 2010	D-3_1	D-3_2	D-3_3
Stack length (mm)	50	50	50	54
The total cost of rotor core (\$)	321.75 (Lami)	321.75 (Lami)	321.75 (Lami)	348.75 (Lami)
The total cost of stator core (\$)	321.75 (Lami)	321.75 (Lami)	321.75 (Lami)	82 (SMC)
Total Magnet cost (\$)	115.2	115.2	223.5	237
Total cost (\$)	758.7	758.7	867	666.7

The schematic and flux density plot of the Design-3_3 (increased magnet mass with SMC) motor remains the same as Design-3_2 (increased magnet mass). Table 5.13 shows the performance metrics of the four designs. The torque ripple and phase back EMF are plotted without skewing the rotor or stator. The designs with same and increased magnet mass have lower torque ripple (%) and less phase back EMF THD (%).

This proves the effectiveness of the rotor design. Table 5.14 shows the cost comparison for the proposed designs such as Design-3_1(same magnet mass), Design-3_2(increased magnet mass) and Design-3_3(increased magnet mass with SMC). All prices are estimated using USD (United States Dollar). The price of neodymium is estimated as \$150/kg [51]. The price of rotor and stator laminations cores are obtained from the EMERF laminations database [52] which includes the manufacturing cost such as wire cut and assembly. The cost of the SMC material is obtained from the Rio Tinto [53] which includes the raw material for SMC and it also includes the processing cost.

The proposed rotor design is based on the spoke type PMSM which does not utilize the reluctance torque component [54], it only has a magnet torque component. In the present case study, the magnet mass is increased to match the torque rating of the baseline design. The phase current and the turns per coil can be changed to obtain the same torque as the Toyota Prius, but in this benchmarking study, the stator parameters are fixed to be the same as the Toyota Prius motor.

The proposed rotor design is also analyzed with a SMC stator core. The SMC material has lower permeability than the laminated stators, so the stack length of the motor is increased from 50mm to 54 mm to obtain the same torque rating as the baseline design. Though the magnet mass is higher than the baseline design, the overall cost of the Design-3_3 (increased magnet mass with SMC) motor is lower than the baseline design due to lower cost of the SMC stator core. Also, the proposed rotor design has very low torque ripple, and lower harmonics in phase back EMF even without skewing the rotor and stator. To further prove the effectiveness of the proposed rotor design, it's fair to compare it with a commercial motor with concentrated windings.

B. Case Study with Honda Accord 2005

Honda Accord is one of the publicly available [55] well- analyzed model. Also, this is one of the best model which has concentrated winding.

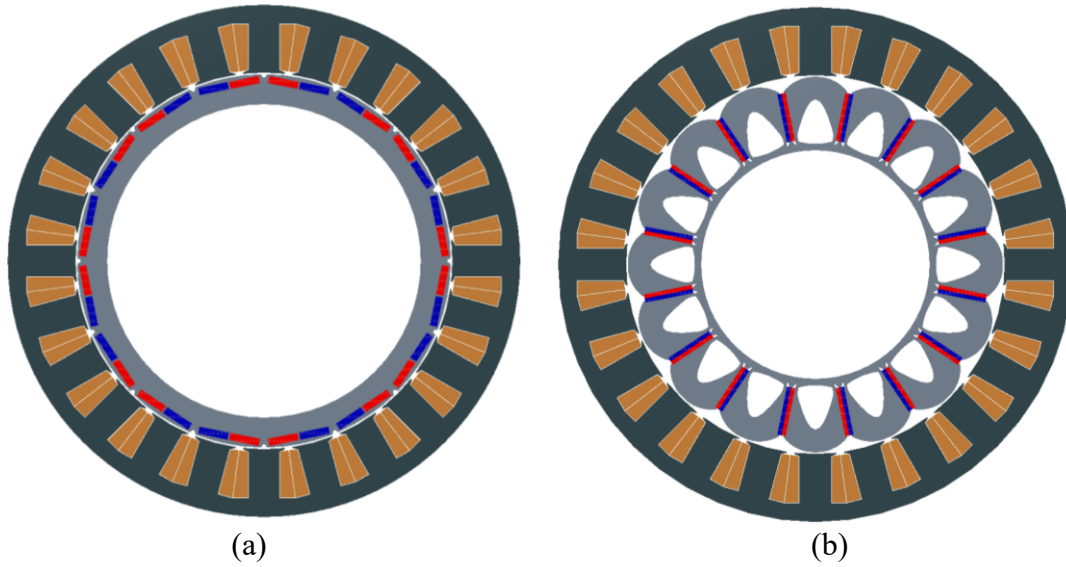


Fig. 5.29. (a) Honda Accord Rotor (b) Design-3 rotor.

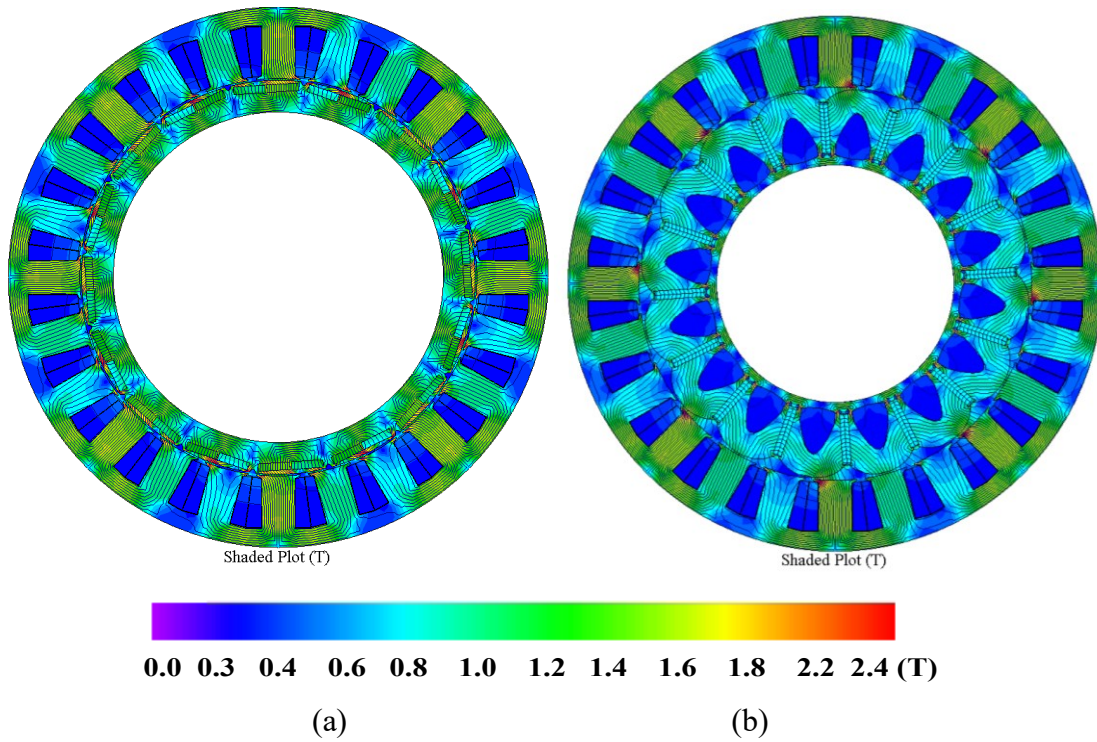


Fig. 5.30. Full load flux density plot (a) Honda Accord Rotor (b) Design-3 rotor.

TABLE 5.15 – KEY DIMENSIONS OF THE HONDA ACCORD & PROPOSED DESIGNS

Items	Honda Accord 2007	Design-3 rotor
Stator outside diameter (mm)	316	316
Stator inside diameter (mm)	232	232
Rotor outside diameter (mm)	230	230
Stack length (mm)	40	40
Air gap length (mm)	1	1
Turns per coil	52	52
Number of parallel path	8	8
Mass of permanent magnet (kg)	0.79	0.79
Poles	16	16
Number of stator slots	24	24
Slot per pole per phase	0.5	0.5
Slot depth (mm)	30.6	30.6
Slot opening (mm)	4.75	4.75
Rated speed (rpm)	850	850
Current density (A/mm ²)	16	16

A design case is presented to highlight the benefits of the Design-3 without the hub arrangement. The Honda Accord stator is fixed, and the Design-3 rotor design is scaled up to fit into the Honda Accord stator design which is shown in Figure 29. Table 5.15 shows the key dimensions of the Honda Accord design and the case with the Design-3 rotor.

TABLE 5.16 – PERFORMANCE METRICS OF CASE STUDY WITH HONDA ACCORD
MOTOR

Items	Honda Accord	Design-3 rotor
Back EMF THD (%)	24.12	12.15
Average torque (N-m)	134.7	163.4
Torque ripple (N-m) (%)	37.8	12.6

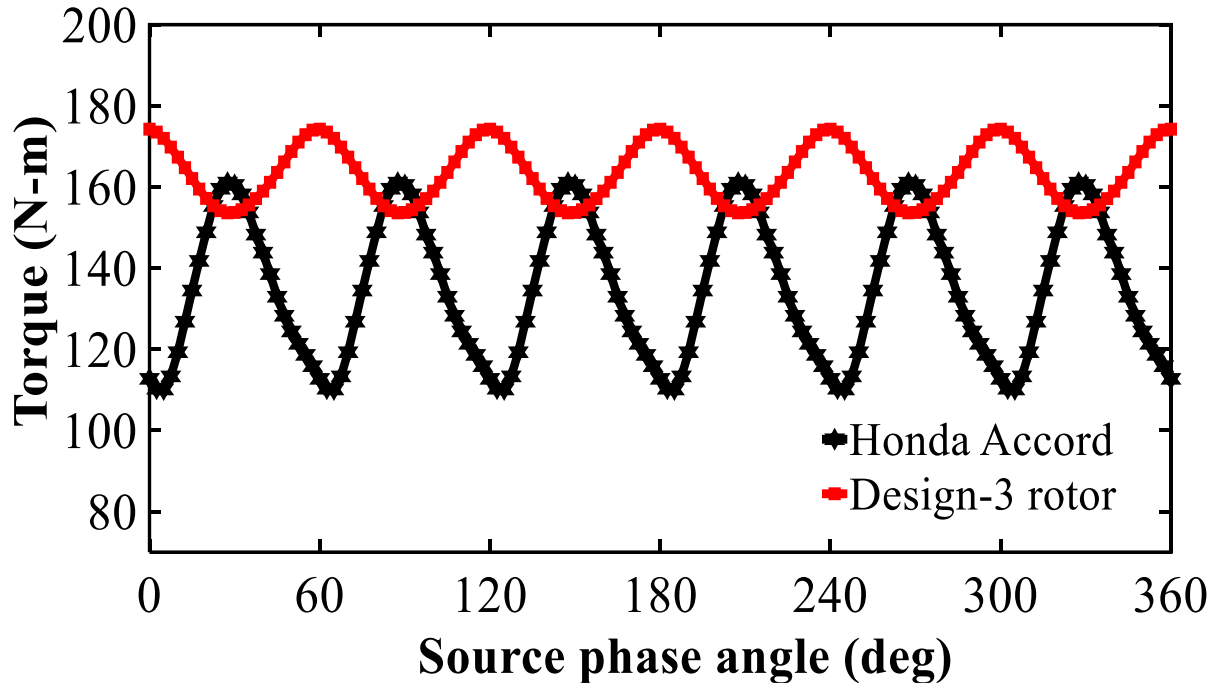


Fig. 5.31. Electromagnetic torque of Honda Accord and Design-3 rotor.

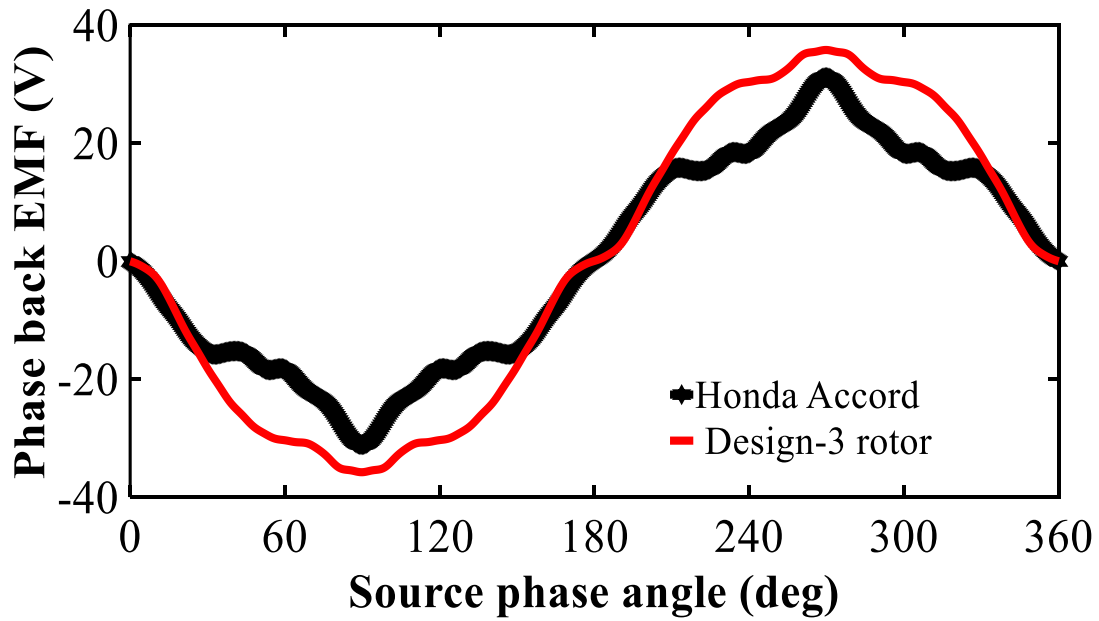


Fig. 5.32. Phase back EMF of Honda Accord and Design-3 rotor.

The Honda Accord stator is fixed with the same electric loading, and the Design-3 rotor is scaled up with the same magnet mass to make a fair comparison. Figures 5. 30, 31 and 32 show the full load flux density plot, electromagnetic torque, and phase back EMF of both the designs. Electromagnetic performances are plotted without skewing either the rotor or the stator. The

Design-3 rotor has lower back EMF THD (%) compared to the Honda Accord design. Also, the average torque is higher in the case of the Design-3 rotor. Torque ripple is reduced substantially with the Design-3 rotor. The performance metrics shown in Table 5.16 clearly show the better performance of the Honda Accord with a Design-3 rotor. This proves the effectiveness of the proposed rotor design. According to

5.7. *Conclusion*

This chapter compares seven different PMSM designs. Three FEA packages have been used for the analysis: Simcenter MotorSolve 2D, Ansys Motor-CAD 2D and JMAG Designer 3D. Firstly, a spoke type rotor PMSM has been designed and analysed with different slot/pole combinations such as 12-slot/4-pole, 36-slot/6-pole, 12-slot/8-pole and 12-slot/10-pole. The different slot/pole combinations are analyzed without skewing the rotor or stator. Air gap flux density, phase back EMF, cogging torque, losses, and efficiency maps are plotted for all the slot/pole configurations. Though the iron losses and efficiency are better for the lower slot/pole combinations, the electromagnetic torque ripple and peak-peak cogging torque values are found to be higher. Also, traction motors need to be operated in the flux weakening regions, it can be stated that the higher pole configurations such as 12-slot/10-pole are better for flux weakening and wide speed range. From this analysis 12-slot/10-pole configuration is chosen as a best candidate for high-speed traction applications. Key results of the analysis are depicted below.

- 1) The selected 12-slot/10-pole configuration is called Design-1, two other rotor designs are considered. Design-2 has a novel barrier which completely eliminates the need for the hub arrangement. Along with the novel barrier Design-3 has a rotor pole shape which reduces the electromagnetic torque ripple and cogging torque, both an optimization and a sensitivity analysis were utilized to determine the parameters of Design-3. The peak-peak cogging torque with Design-3 is 91.29% reduced from Design-1. The average torque and power rating is maintained the same for all the three rotor designs. The torque ripple with Design-3 is 80.59 % reduced from Design-1. The electromagnetic torque ripple and the cogging torque are significantly reduced in Design 3. Design -3 with the laminated stator is selected for further analysis with the SMC stator core design.

2) Design-3 rotor is scaled up and analyzed with a Toyota Prius stator core and Honda Accord stator core to prove the effectiveness of the proposed rotor design. The torque with the Honda Accord stator and Design-3 rotor is 17 % higher than the original Honda Accord motor for the same magnet mass. A cost comparison between the baseline Toyota Prius motor and the proposed rotor design with SMC material has been presented. It proves that the overall cost of SMC motor is cheaper than the baseline motor. This proves the effectiveness of the proposed rotor design.

CHAPTER – 6

Design of a SMC Stator Core for Traction Applications for Twizy Car

This chapter presents an introduction to soft magnetic composite (SMC) stator core. Three different SMC materials are compared for the same machine specification. Higher pole designs such as 24slot/16-pole and 36-slot/30-pole has been designed and analyzed with laminated and SMC stator design. The tooth body length of SMC stator is varied from 36 mm to 56 mm to analyze the performance of the motor. Finally it presents a detailed analysis such as electromagnetic , thermal and mechanical performances for the SMC motor design.

6.1. Introduction to soft magnetic composite stator (SMC)

Electric steels are classified into two types: soft magnetic alloys and amorphous metal [56-57]. Laminated steel is limited primarily to two-dimensional (2D) flux paths. There is a lot of wasted material while cutting the rotor and stator parts from the steel sheets [58]. Soft magnetic composites (SMC) stator cores can have as low as 5% wastage whereas laminated stator cores can have more than 20% wastage. SMC materials are produced from iron powders of high quality, which can be compressed without losing their inherent properties. SMC powder core has lower permeability than laminated steel. Permanent magnet machines are a good target for SMC motors because lower permeability is not as significant a barrier to designing low-cost machines [59]. SMC cores suffer from low mechanical strength; they can be used as a replacement for laminated stator cores by using laminated steel for the rotor. SMC motors can be designed with less materials and lower manufacturing costs than laminated steel sheet motors [60-62].

Due to magnetic and thermal isotropy, SMC is suitable for designing three-dimensional (3D) magnetic flux electric machines. Due to this advantage, various kinds of machines can be designed such as axial flux machines (AFM) [63-64], transverse flux machines (TFM) [65-66], and claw pole machines (CPM) [67-68]. In radial machines it is possible to reduce the tooth body length with SMC stators to allow the end winding to fit within the stack length of the machine. The reduced tooth body is possible because SMC allows 3D flux paths. The SMC motors with reduced tooth body will have lower winding turn length for the same flux linkage. This helps to

achieve lower phase resistance, hence lower copper losses. Also, the 3D flux path in SMC motors improves the torque density in terms of motor volume. A radial SMC machine with the 3D flux path has been designed and compared with a laminated steel design. In this case, one laminated steel motor is compared with two SMC motors. However, all three motors are designed with different slot/pole configurations and also with different torque and power ratings [69]. Also, the machines were not analyzed in 3D. Four different motors with silicon steel stator and SMC stator were analyzed with 60 mm and 40 mm stack lengths, this study concludes that the silicon steel machines are higher efficient than the SMC machines, but the SMC machines were found to have higher torque per rotor volume [70-71]. The cogging torque has been presented, however, the torque ripple is not analyzed between the SMC and laminated motor, which varies between the laminated motor and SMC motor with reduced tooth body. Three different SMC machines such as radial flux machine, axial flux machine and transverse flux machine were compared, the radial machine with SMC core was found to have lower cogging torque and lower losses than the other two motors. Finally axial machine with SMC core has been manufactured and tested [72].

However, it doesn't focus on the comparison between the laminated motor and SMC motor for the same specifications with electromagnetic, thermal and mechanical analysis. The concentrated non-overlapping windings are proved to be the best candidate for SMC machines [73]. The SMC tooth is designed with a reduced tooth body on both sides [74], the manufacturing and assembly of the SMC tooth parts were not presented. However, for the higher stack length, axial segmentation of the stator cores has to be considered. Also, introducing a protrusion and extrusion in the SMC stator tooth will enable the flux concentration between the tooth parts. Laminated and SMC motors have been compared; the SMC stator core performs better at high-frequency applications due to reduced core losses at higher frequencies [75]. However, SMC motors have to be analyzed with a multiphysics approach to validate the thermal and mechanical behaviors along with the electromagnetic performance. A detailed cost analysis is an important aspect while designing an SMC motor which is not presented in the literature.

This thesis focuses on comparing three different SMC materials for traction applications using loss analysis and efficiency maps. The selected SMC material is further compared with a laminated steel design. The characteristics of the selected SMC material are analyzed in FEA and verified experimentally with toroid testers. Higher pole designs were not analyzed by fixing the

stator outer diameter with the same torque and same current density. Designs such as 24-slot/20-pole and 36-slot/30-pole are analyzed with laminated stator and SMC stator. In both cases the current density is fixed as the same. The final SMC design is analyzed using 3D FEA with different tooth body lengths which allows the possibility of the 3D flux path. Also, SMC stator is designed and analyzed in 3D FEA with and without back iron to compare the electromagnetic performances. The mechanical stress analysis is performed for the final SMC stator design.

6.2 SMC material properties and machine specification

TABLE 6.1 - MACHINE SPECIFICATIONS

Specifications	Values
Rated Power	7.1 kW
Rated Torque	20 N-m
Rated Speed	3400 rpm
Maximum Speed	10,000 rpm
Supply Voltage	96 volts
Cooling type	Air Cooled
Magnet material	NdFeB(N30SH)
Stator material	SMC
Rotor material	Laminated steel

The characteristic of SMC depends on the material manufacturing methods. Generally, SMC is chosen only for the stator core due to its low strength. The SMC stator core has lower permeability when compared to laminated silicon steel. Saturation has to be considered while designing the SMC stator core. A 12 slot 10 pole spoke -type PMSM has been emerged as the best candidate from the analysis carried out in the previous chapter. Table 6.1 shows the specifications of the spoke-type machine. The machine is rated at 3400 rpm with a 20 Nm torque. The maximum speed of the motor is 10000 rpm with a field weakening operation. The current density of the motor is rated at 5 A/mm² to eliminate the forced cooling requirement. Iron loss is the deciding factor for selecting a material for traction applications. Iron loss is further classified into two types such as

hysteresis loss and manufacturing techniques, and it greatly varies from one material to other. Three different types of SMC materials have been considered for the analysis to select the best material for traction application. Table 6.2 shows the properties of the three different SMC materials [76]. The stator core material selection mainly depends on permeability, resistivity, hysteresis loss and low eddy current loss. It is not possible to produce an SMC stator core that inhibits all these properties, always a tradeoff must be done to select a material.

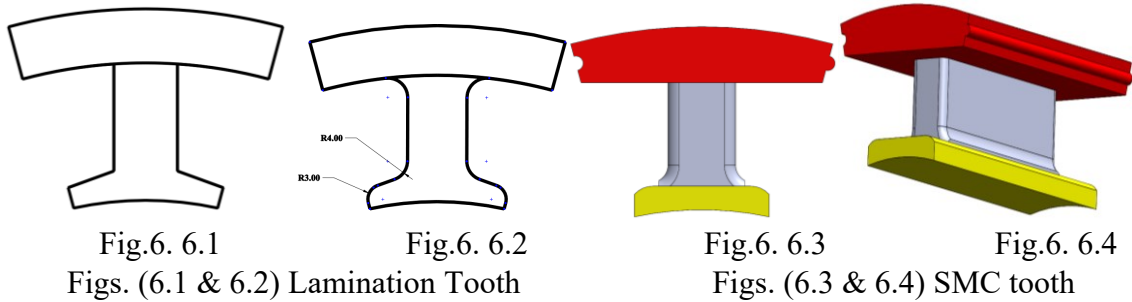


TABLE 6.2 – SMC MATERIAL PROPERTIES

Items	SMC-A	SMC-B	SMC-C
Relative permeability	220	440	720
Hysteresis loss per cycle (mWatt.sec/kg)	143.12	95.48	1000
Resistivity ($\mu\text{Ohm.m}$)	7600	1000	90
Density (kg/m^3)	7260	7450	7500
Young's Modulus (MPa)	70000	65000	140000
Poisson's ratio	0.23	0.23	0.23

6.3. SMC material comparison using 3D FEA method.

Three types of SMC materials are compared for the same machine specification which is presented in Table 6.1. Table 6.3 shows the design parameters of the three different SMC materials. The electromagnetic torque and phase back EMF of the three designs are shown below. The spoke type rotor design is chosen from the previous section. Machine parameters such as turns per coil, stator OD and stack length are maintained the same for all the designs. The torque is maintained same

for all the designs by changing the phase current. Fig.6. 5 (a) & (b) shows the electromagnetic torque and phase back EMF of the SMC designs A, B, and C.

TABLE 6.3 – DESIGN PARAMATERS OF SMC MATERIAL (A,B,C)

Items	SMC-A	SMC-B	SMC-C
Stator OD (mm)	180	180	180
Rotor OD (mm)	115	115	115
Stack length (mm)	80	80	80
Turns per coil	9	9	9
Phase resistance (Ω)	0.00214	0.00214	0.00214
Phase current, Peak (A)	170	160	152
Base speed (rpm)	3400	3400	3400
Torque (Nm)	20.4	20.4	20.4

SMC-A has lower permeability when compared to the SMC-B and SMC-C has lower permeability when compared to the SMC-B and SMC-C. Figs. 6 (a, b and C) shows the eddy current density of the SMC-A, B and C at 3400 rpm. The SMC-C has high eddy current loss which can be seen in Fig.6. 6(c). The loss analysis of the three designs at rated speed (3400 rpm) and maximum speed (10000 rpm) are shown in Fig.6. 7 and 8. Fig.6. 9 shows the copper loss, magnet loss, hysteresis loss, eddy current loss, total iron loss, mechanical loss and total loss at 3400 rpm. The copper loss is higher in the SMC-A, and lower in the SMC-C designs. The magnet loss in SMC-A, B and C are 10.48 W, 11.9 W, and 11.6 W.

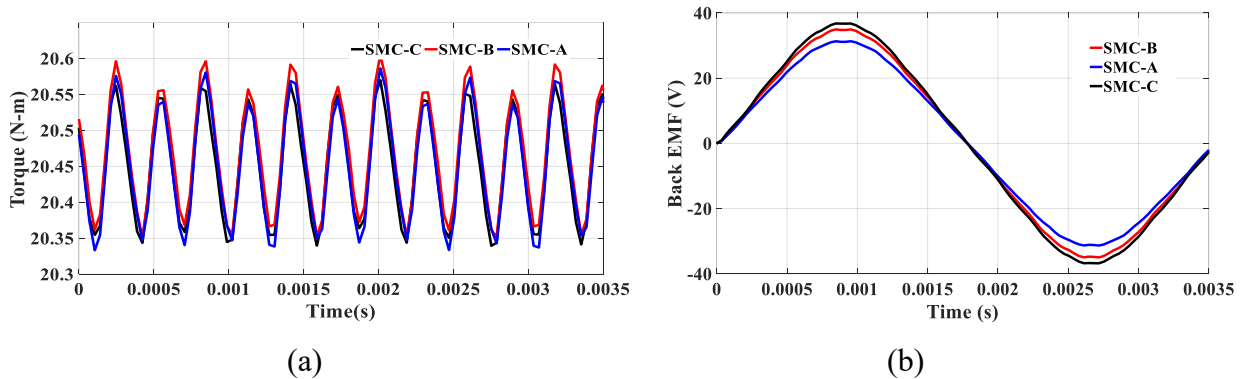


Fig.6. 5 (a&b). Electromagnetic torque of SMC (A,B,C) and Phase Back EMF at 3400 rpm

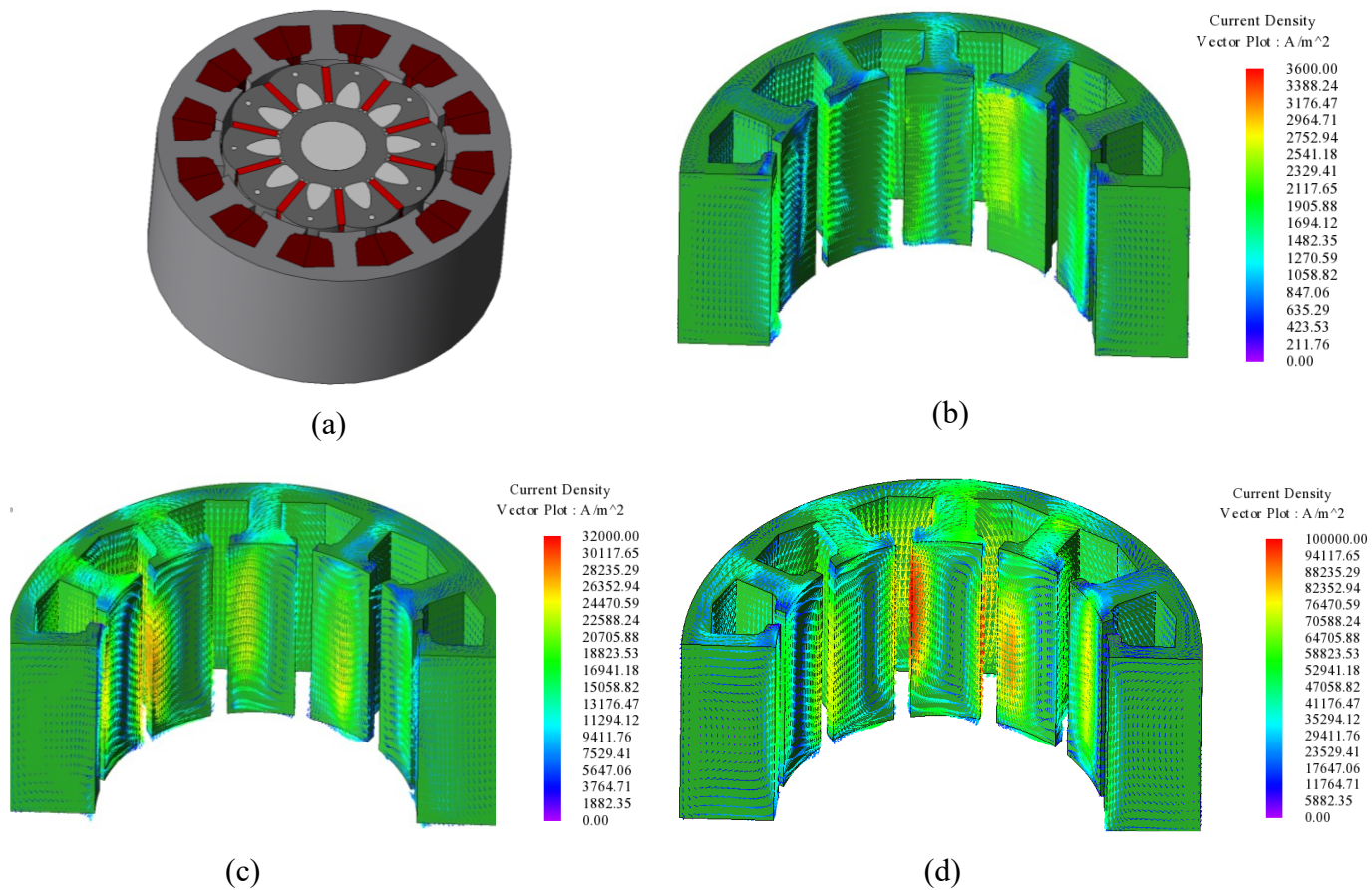


Fig.6. 6. (a) Selected spoke type rotor (b, c & d) Eddy current density of SMC – A, B & C at 3400 RPM

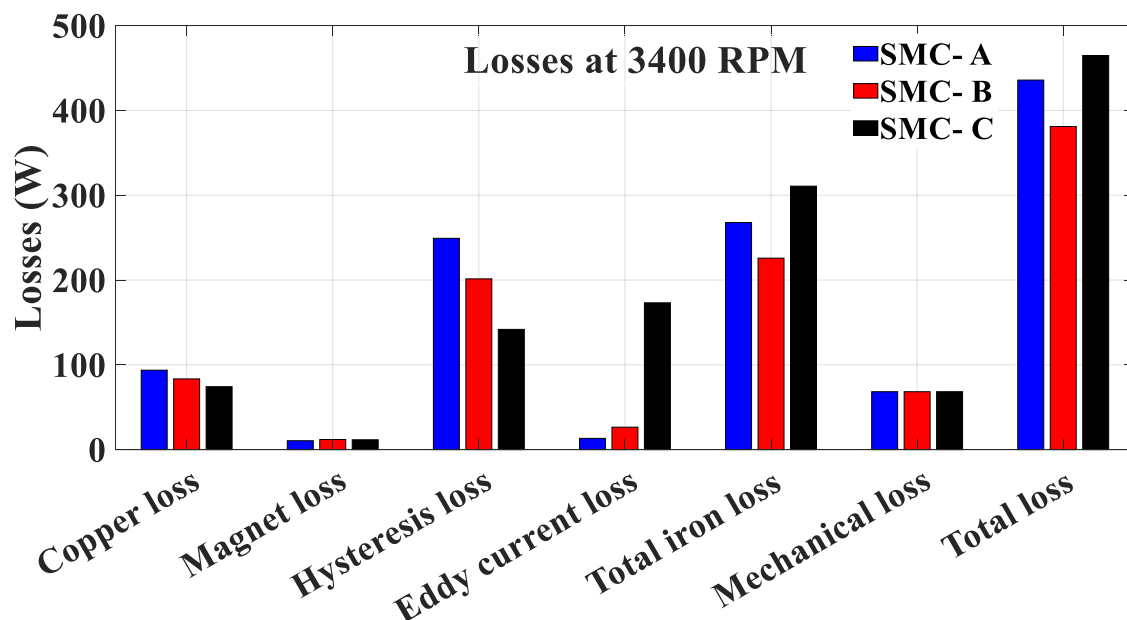


Fig.6. 7. Loss analysis of SMC (A,B,C) at 3400 RPM

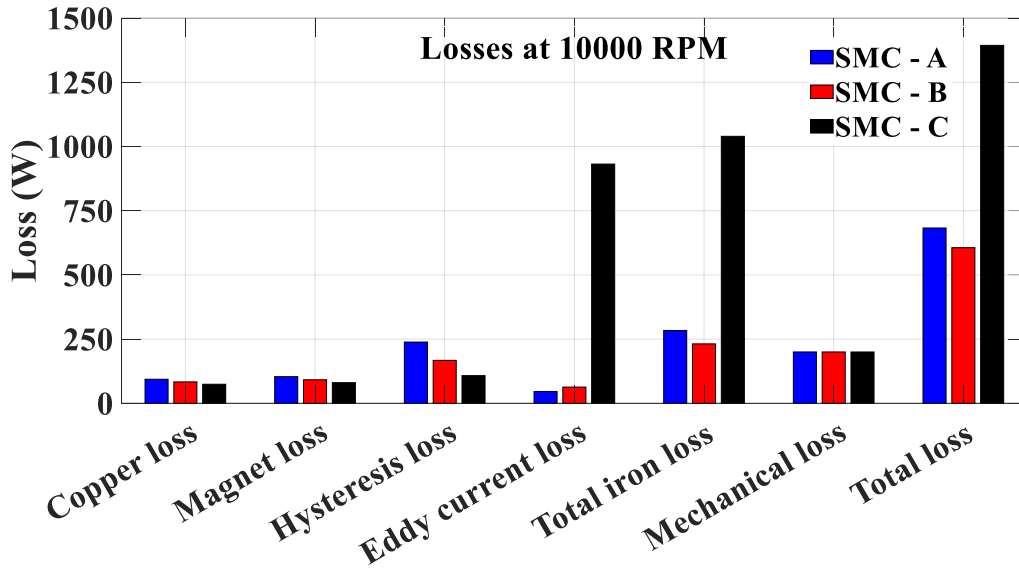


Fig.6. 8. Loss analysis of SMC (A,B,C) at 10000 RPM

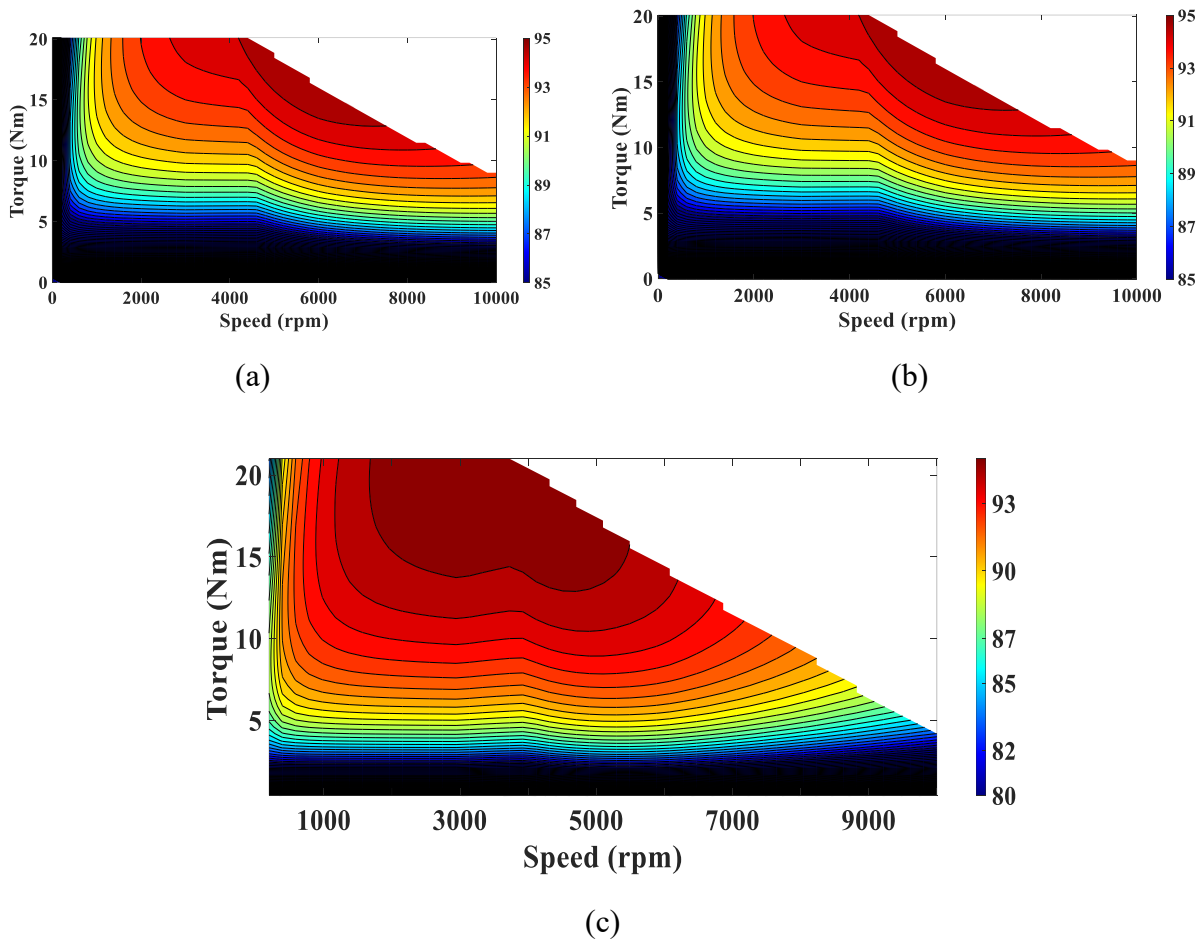


Fig.6. 9. Efficiency map (a) SMC-A (b) SMC-B (c) SMC-C

The SMC-A has lower magnet losses compared to the SMC-B & C. The hysteresis losses of the three materials are 249.2 W, 201.37 W, 141.8 W. The SMC-C has lower hysteresis losses due to the lower resistivity. The eddy current losses of the three materials are 13.27 W, 26.46 W, 173.13 W.

The eddy current loss is substantially increased in the SMC-C design due to the lower resistivity. Mechanical loss is kept as 68.3 W for all the three different designs. The total losses of the three designs are 435.8 W, 381.04 W and 464.8 W. At 3400 rpm, the SMC-B has lower losses than the other designs. Fig.6. 8 shows the loss analysis of SMC-A,B, and C at the maximum speed of 10000 rpm. The copper losses remain same. The magnet losses of the three designs are 103.75 W, 91.7 W, 80.33 W. The magnet losses are found to be higher with the SMC-A design. The hysteresis losses of the three designs are 238.54 W, 167.3 W, 107.8 W. The SMC-C has lower hysteresis loss than the other designs. The eddy current losses of the three designs are 46.14 W, 63.22 W, 931.5 W. The eddy current loss is increased in the SMC-C. The total losses of the three designs are 682.65 W, 606 W, 1393.7 W.

The SMC-B has lower losses at both the rated speed (3400 rpm) and the maximum speed (10000 rpm). Fig.6. 9. shows the efficiency map of the three designs. The efficiency of SMC-A at the rated speed is 93.8 % and at the maximum speed is 90.38 %. The efficiency of SMC-B at the rated speed is 95.0% and at the maximum speed is 91.46%. The efficiency of SMC-C at the rated speed is 93.45% and at the maximum speed is 80.37 %. From the loss analysis and efficiency map, it is found that the efficiency of SMC-C is lower than the other two designs due to the increase in eddy current loss as a result of lower electric resistivity. SMC-B is chosen for further analysis.

6.4. Characterization of SMC-B material

Fig.6. 10 shows the material characterization setup with a toroid testers for the SMC-B material sample. The SMC-B sample has inner diameter of 43.2 mm and outer diameter of 52.48mm. The length of the sample is 7.448 mm. The primary and secondary have 120 turns each. The magnetic field and the flux density are derived from the magnetizing current, and the voltage is induced in the secondary side.

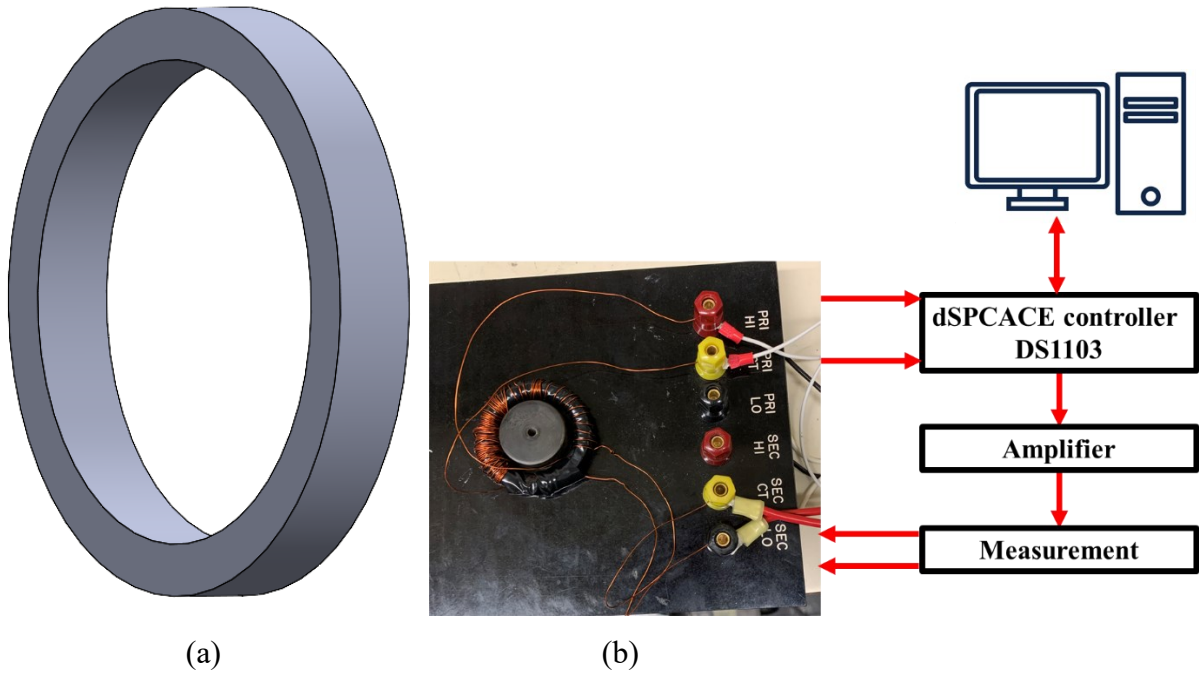


Fig.6. 10. (a) SMC-B sample ring (b) Experimental setup with a SMC-B toroid sample

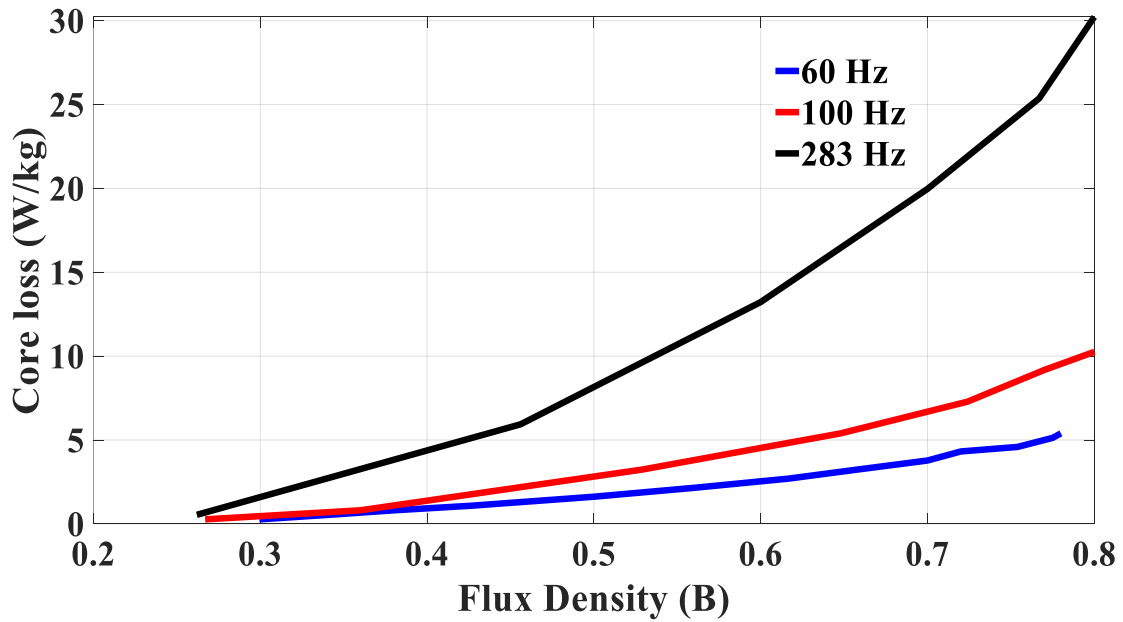


Fig.6. 11. Measured iron loss values of SMC-B material

A custom-made program is used with dSPACE to measure the iron loss following an ASTM standard using wattmetric method. Fig.6. 11 shows the measured core loss values of the SMC-B material at 60 Hz, 100 Hz and 283 Hz (3400 rpm).

6.5. Performance comparison of higher poles with SMC-B stator and laminated stator for the same specifications with same current density

In this section four different higher pole configurations are designed in FEA and analyzed. The conventional spoke type rotor is chosen for this analysis.

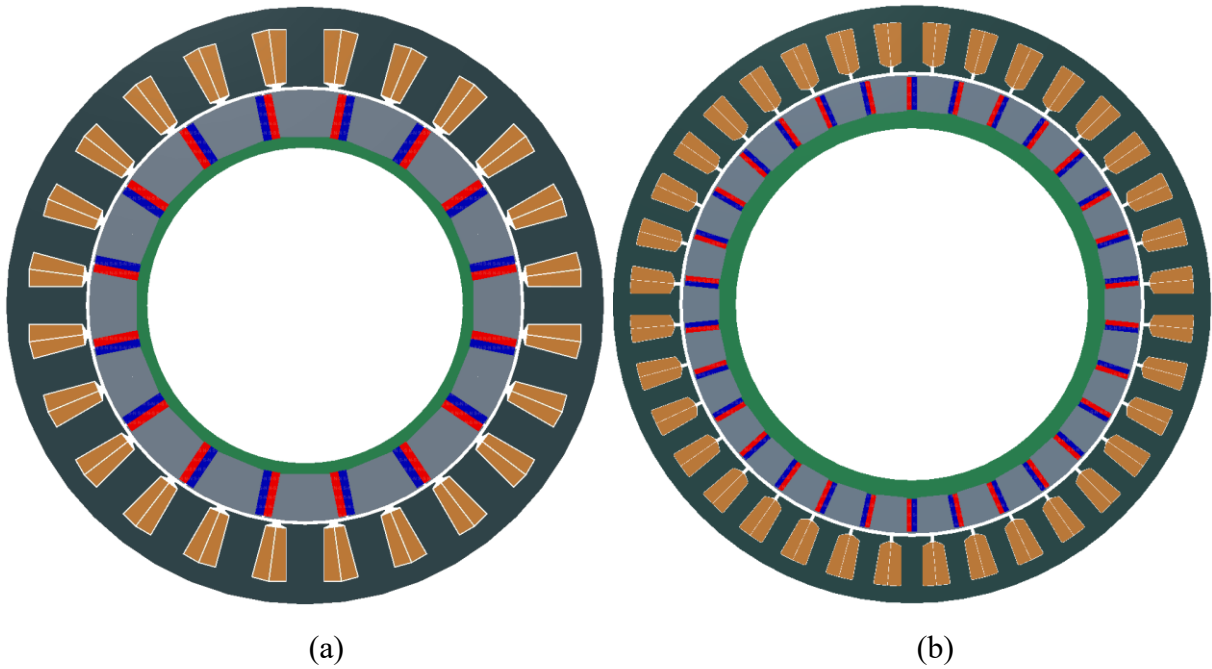


Fig.6. 12. Higher slot/pole designs (a) 24-slot/16-pole (b) 36-slot/30-pole

Table 6.4 – Design parameters of 24/20 and 36/30

Items	24/20	24/20	36/30	36/30
	LAMI	SMC	LAMI	SMC
Stator OD (mm)	180	180	180	180
Rotor OD (mm)	130	130	138	138
Stack length (mm)	100	80	110	80
Turns per coil	10	13	5	6
Copper fill factor (%)	40	60	40	60
Base speed (rpm)	3400	3400	3400	3400
Maximum speed (rpm)	10000	10000	10000	10000
Torque (Nm)	20	20	20	20
Current density (A/mm ²)	3.8	3.8	3.8	3.8

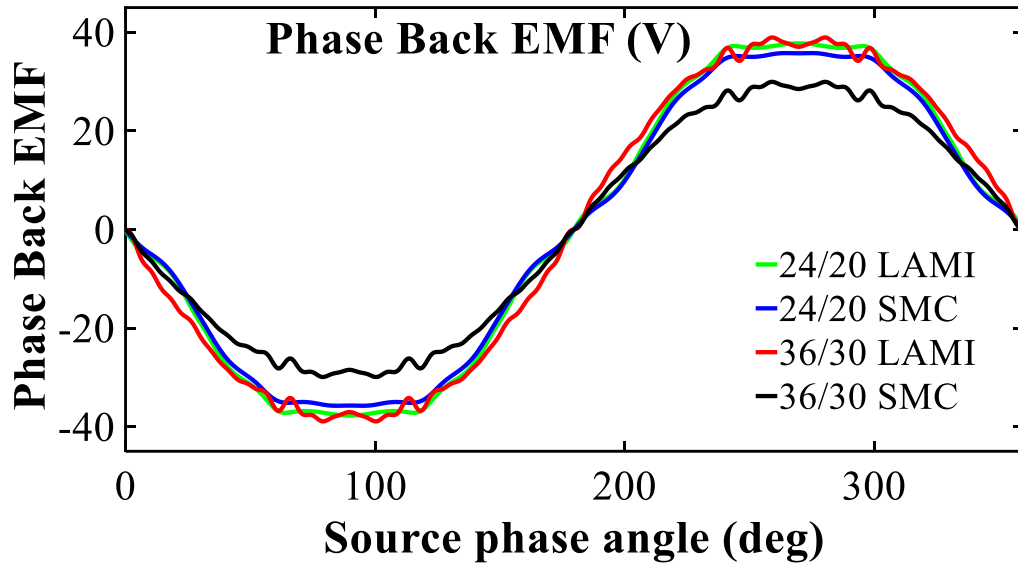


Fig.6. 13. Phase Back EMF of 24/20 & 36/30 with lamination & SMC stator

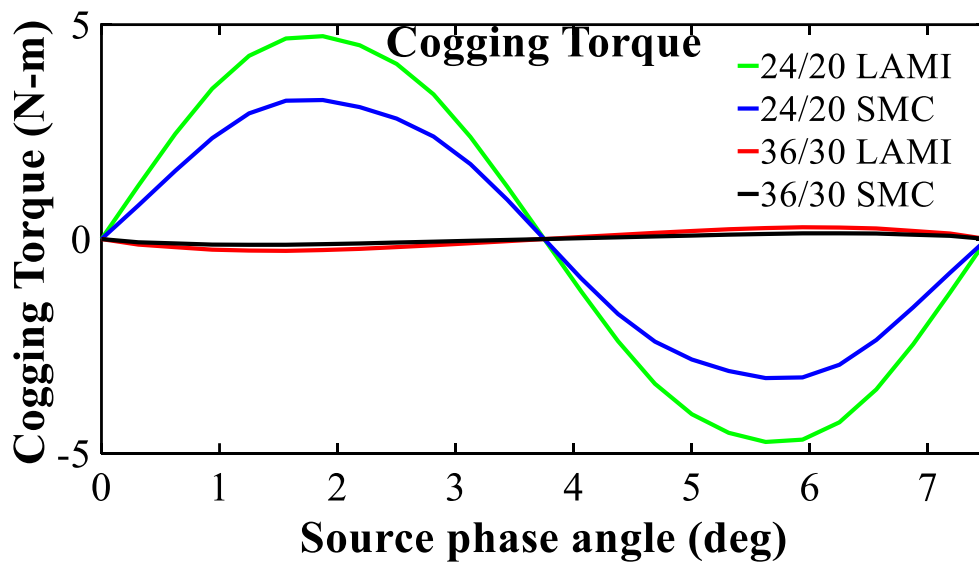


Fig.6. 14. Cogging torque of 24/20 & 36/30 with lamination & SMC stator

Fig.6. 15 shows the schematic of the higher pole configurations. Figs. 13,14 & 15 show the phase back EMF, cogging torque and electromagnetic torque of 24-slot/16-pole and 36-slot/30-pole with laminated and SMC stator designs. Table 6.5 shows the loss comparison of all four designs at 3400 rpm and 10000 rpm. It shows that the iron loss of laminated designs at higher speeds is much higher than that of SMC motors. This proves that the SMC motors will perform better at higher frequencies. Also, all the machines are designed to operate at the same current density.

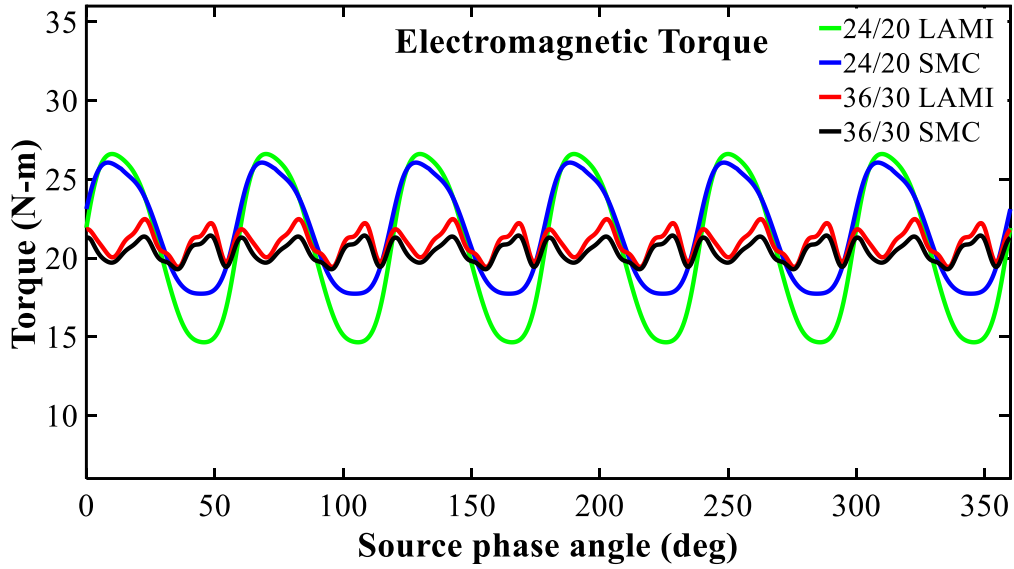


Fig.6. 15 Electromagnetic torque of 24/20 & 36/30 with lamination & SMC stator

Table 6.5 – FEA based Iron loss comparison of SMC – B & M-36 29 Ga at 3400 rpm

Items	24/16 LAMI	24/16 SMC	36/30 LAMI	36/30 SMC
Copper loss at 3400 rpm (W)	44	51.9	45.1	52.6
Copper loss at 10000 rpm (W)	44	51.9	45.1	52.6
Iron loss at 3400 rpm (W)	359	386	392	495
Iron loss at 10000 rpm (W)	1500	899	1320	589

SMC motors with higher fill factor always perform better than laminated motors due to lower phase resistance. Considering the challenges in manufacturing and testing the higher pole motors, a 12-slot/10-pole motor is chosen for manufacturing.

6.6. Selection of tooth body length for the smc stator design

From section 6.3, 12-slot/10-pole design with SMC-B is chosen as the best material in the SMC stator core. The SMC stator core is analyzed with various tooth body length such as 36mm, 40mm, 48mm, and 56mm. The simulation is carried out in 3D FEA using JMAG software [77].

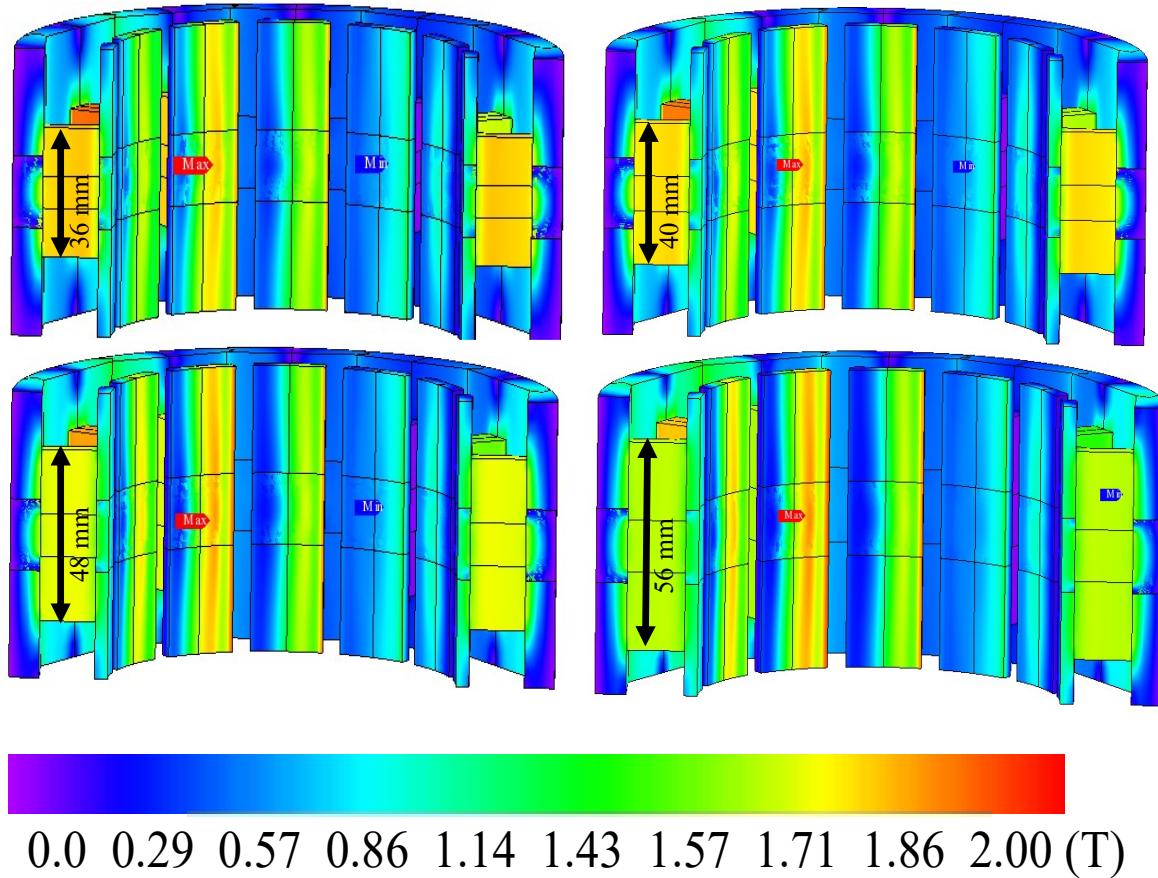


Fig.6. 16. Flux density plot of SMC stator different tooth length

Fig.6. 16 shows the flux density plot of the SMC tooth for four different tooth body lengths. Fig.6. 17 shows the electromagnetic torque for the four designs. Figs, 18 and 19 show the phase back EMF and its harmonics. Fig.6. 20 shows the cogging torque. Figs. 21 and 22 show the complete SMC stator and its flux density plot for designs with 56 mm tooth body length with back iron and without back iron. The phase back EMF harmonics, THD (%) (Table 6.7) reduces with an increase in the tooth body length. Table 6.6 shows the average torque and cogging torque for all the designs.

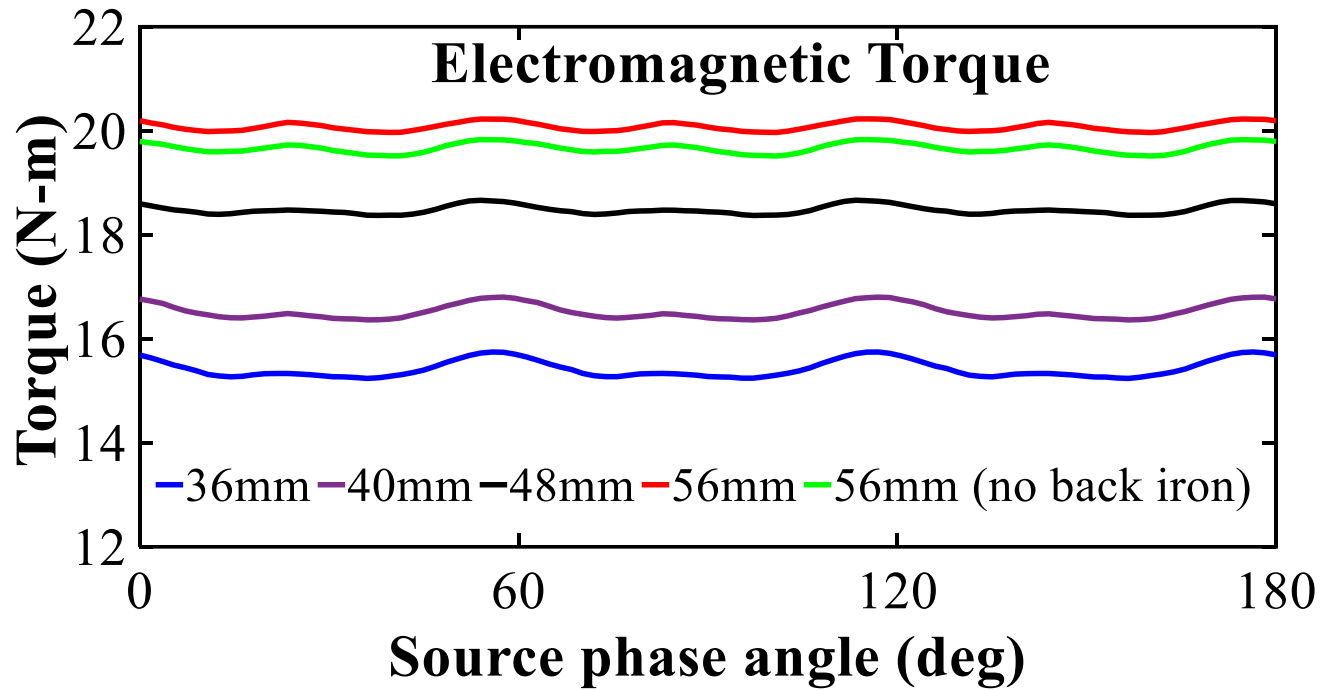


Fig.6. 17. Torque of SMC stator with different tooth length

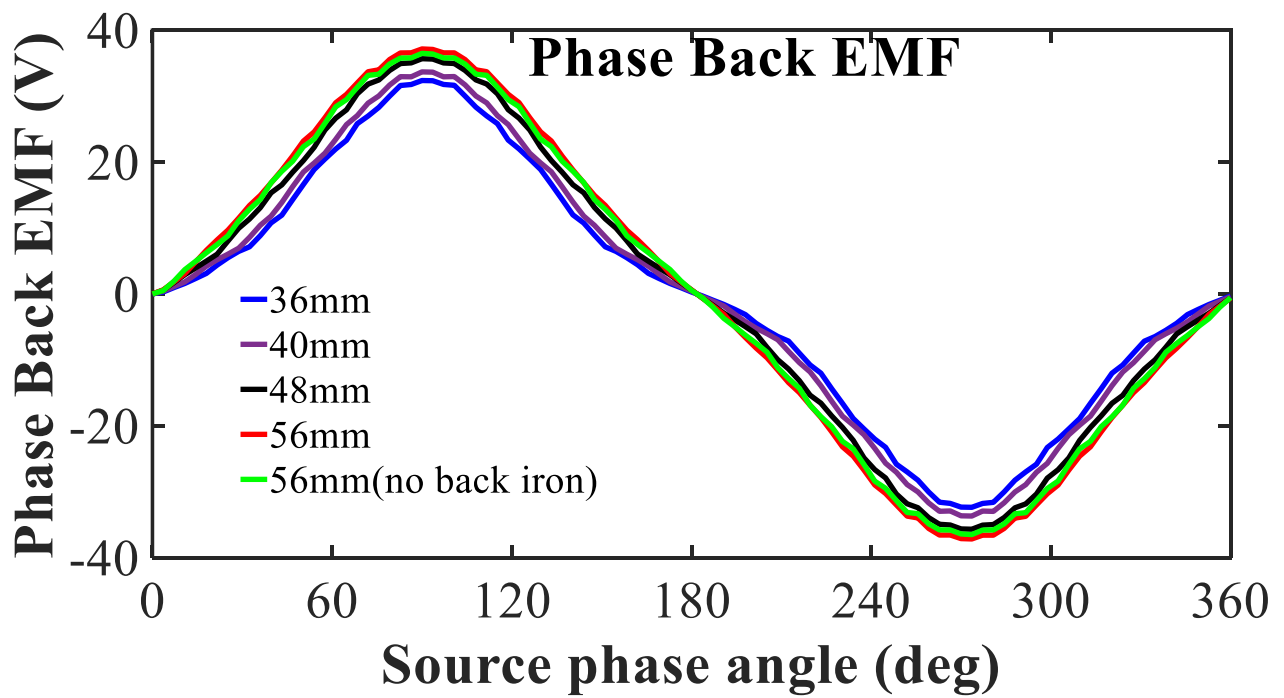


Fig.6. 18. Phase Back EMF of SMC stator with different tooth length

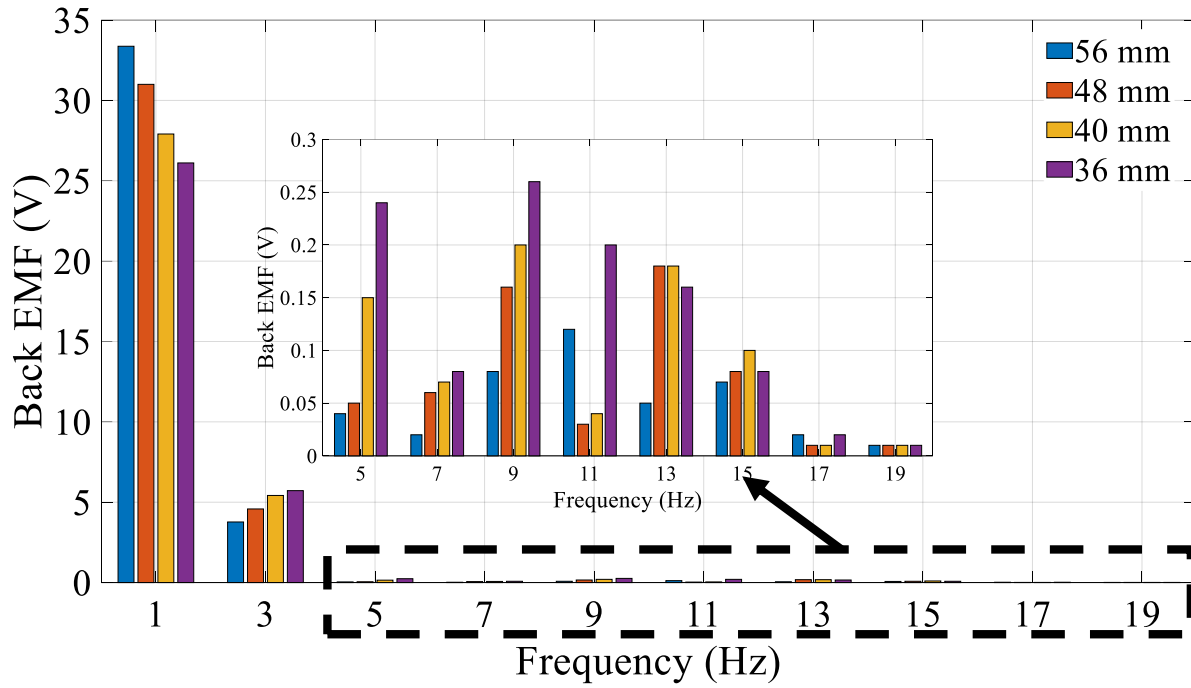


Fig.6. 19. Back EMF harmonics of SMC stator with different tooth length

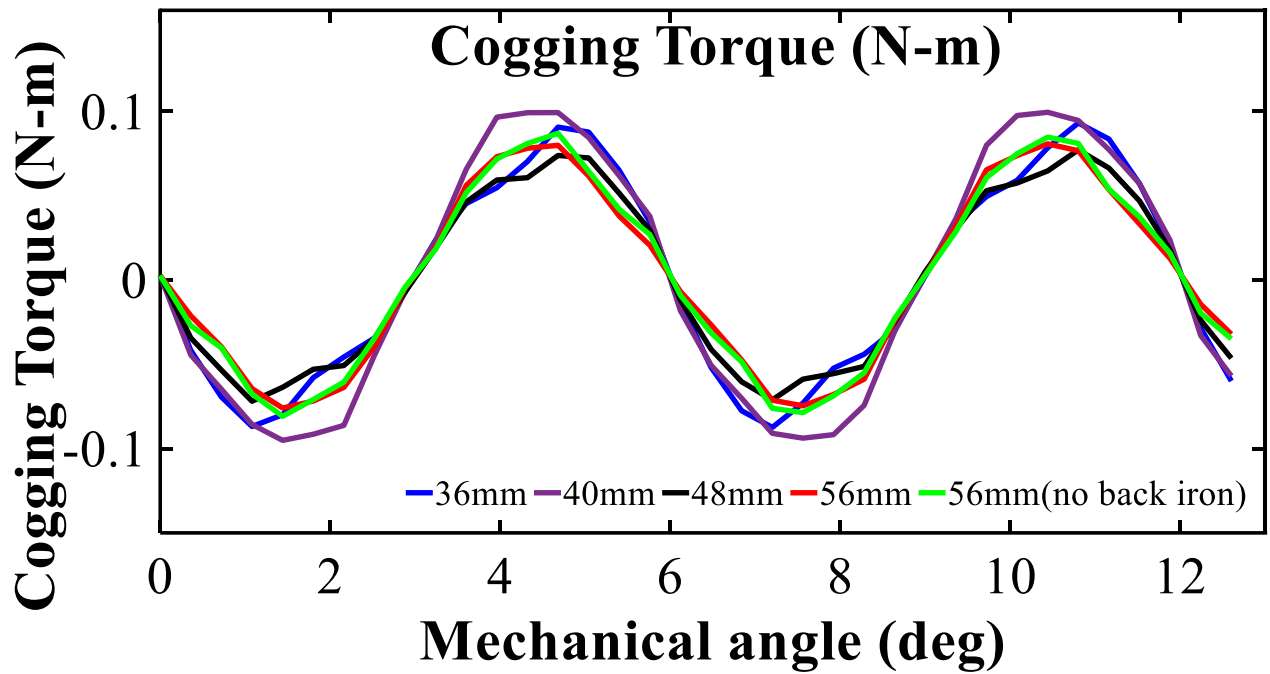


Fig.6. 20. Cogging torque of SMC stator with different tooth length

Table 6.6– Performance metrics of SMC stator with different tooth body length

Items	36mm	40mm	48mm	56mm	56mm no back iron
Average torque (N-m)	15.42	16.52	18.48	20.08	19.66
Torque ripple (N-m) (%)	3.29	2.65	1.58	1.30	1.60
Peak cogging torque (N- m)	0.09	0.09	0.07	0.08	0.08

Table 6.7– Phase back EMF harmonics of SMC stator with different tooth body length

Harmonic order	36mm	40mm	48mm	56mm
1 st	26.1	27.91	31	33.37
3 rd	5.72	5.42	4.58	3.77
5 th	0.24	0.15	0.05	0.04
7 th	0.08	0.07	0.06	0.02
9 th	0.26	0.2	0.16	0.08
THD (%)	21.9	19.4	14.7	11.3

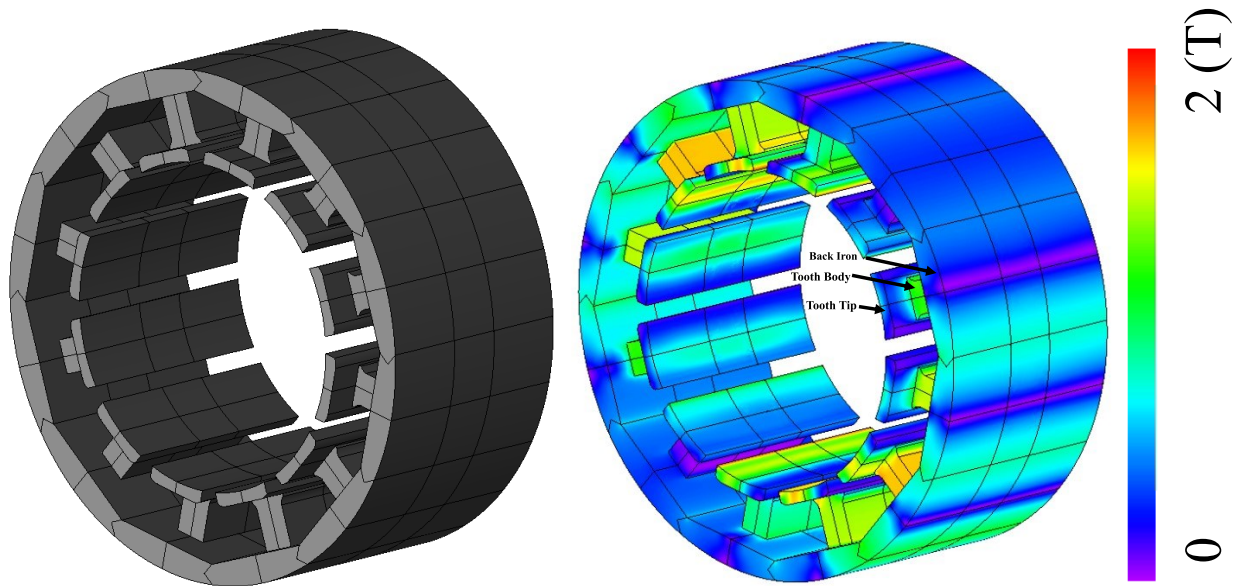


Fig.6. 21. Complete SMC stator and its flux density plot with 56 mm tooth body length with back iron.

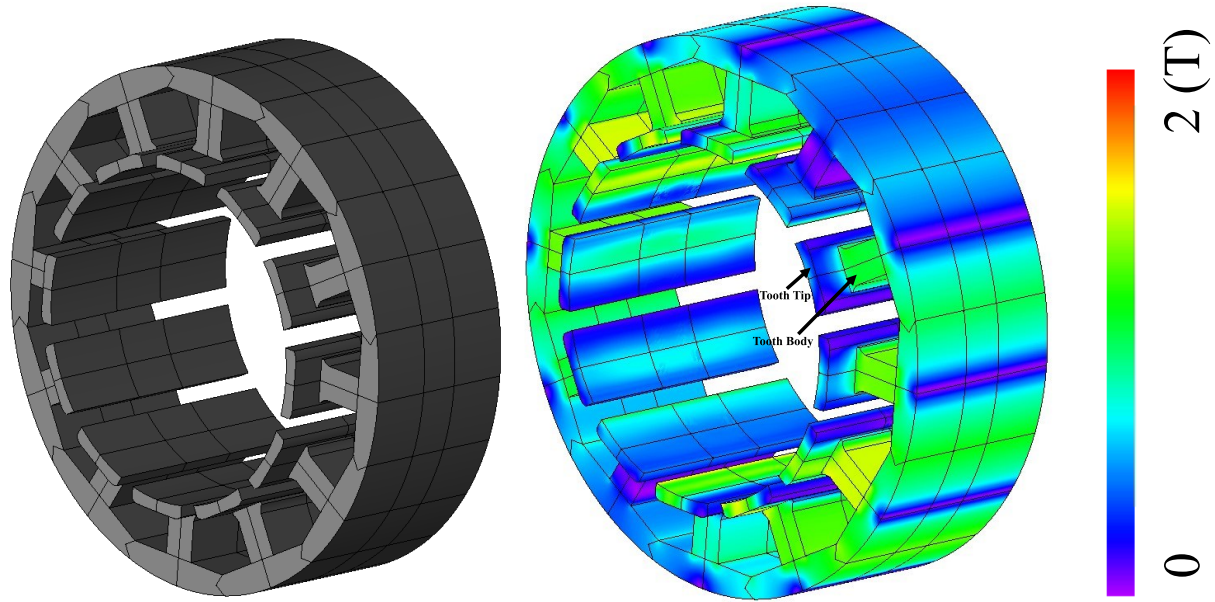


Fig.6. 22. Complete SMC stator and its flux density plot with 56 mm tooth body with no back iron.

The SMC stator with 56 mm tooth body length has an average torque of 20.08 N-m with a torque ripple of 1.3% which is better than the other four designs. Peak cogging torque is almost same for all the designs. Also, the SMC stator is designed with no back iron, in which the tooth tip is extended but the back iron height is fixed the same as the tooth body length. In this case, the average torque is reduced by 2% from the design with back iron. This design is a better candidate for additive manufacturing of stators with direct cooling.

6.7. 3D FEA design of smc stator core and comparison with the laminated steel design for the required specifications

From this section onwards SMC stator with 56 mm tooth body length with SMC-B material is used for further analysis with laminated stator designs. In chapter 5, Design-3 rotor with laminated stator emerged as the best candidate. Design-3 with the laminated stator core is selected for further comparison with the SMC stator core (Design-4). Fig.6. 25 shows the flux path for the laminated stator and SMC stator. Figs. 26 and 28 show the B-H curve and magnetic loss curves for the laminated and SMC stators. Also, it shows the single SMC tooth. As seen in Fig.6. 26, the magnetic flux density of the SMC material is lower than the laminated steel. The SMC stator can utilize 3D flux paths which is not possible with laminated steel designs.

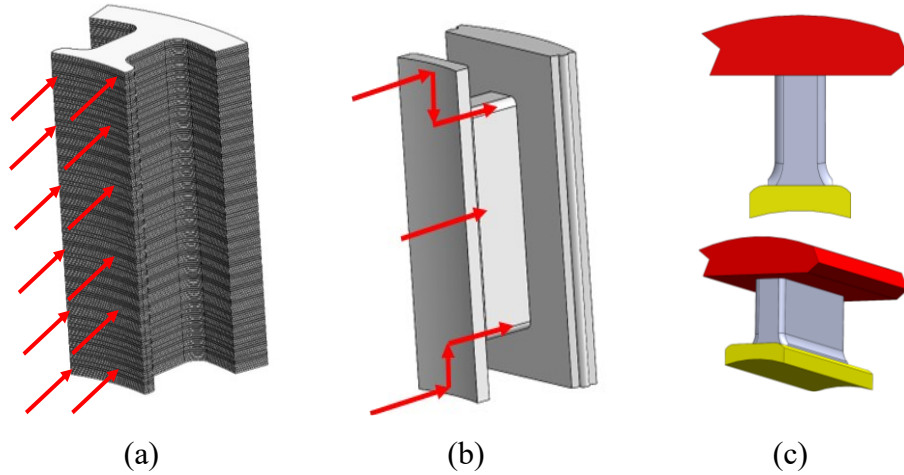


Fig.6. 23. (a) Laminated steel flux path (b) SMC flux path (c) SMC tooth

The 3D flux path of the SMC stator opens new stator designs for traction applications. Design-3 with the laminated stator is analyzed and compared with a SMC stator design with a 3D FEA. Table 6.8 shows the design specifications for the laminated stator and the SMC stator.

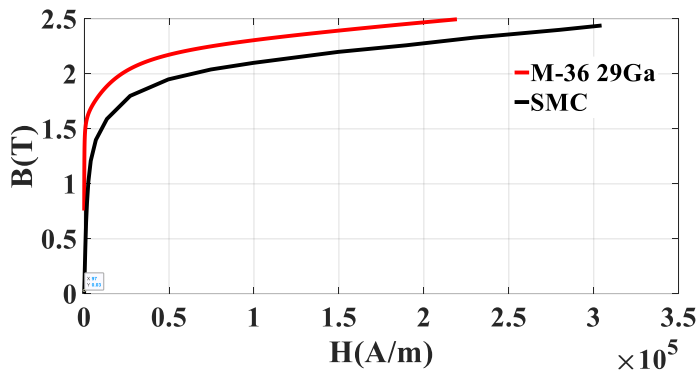


Fig.6. 24. B-H Curve of laminated Steel & SMC



Fig.6. 25. SMC stator

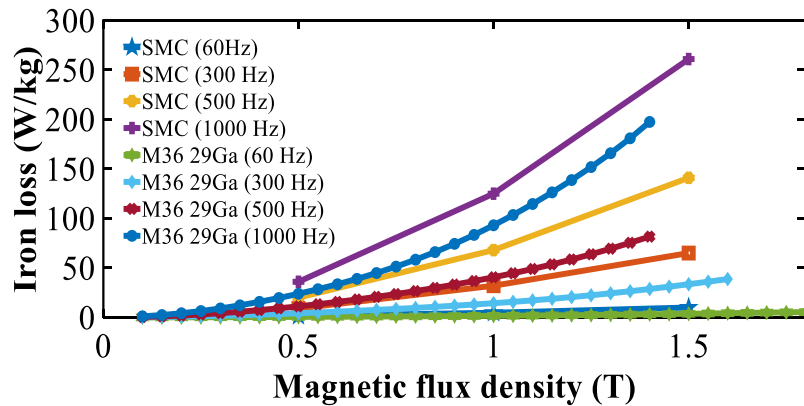


Fig.6. 26. Loss curves of laminated and SMC stator.

Table 6.8- laminated & smc stator specifications

Item	Laminated stator (Design -3)	SMC stator (Design -4)
RMS phase current	107 A	107 A
Stator OD	180 mm	180 mm
Rotor OD	113 mm	113 mm
Stack length	65 mm	80 mm
Overall stack length	95 mm	80 mm
Copper fill factor	40 %	60 %
Torque density (motor volume) at 3400 rpm	7.85 KNm/m ³	9.82 KNm/m ³

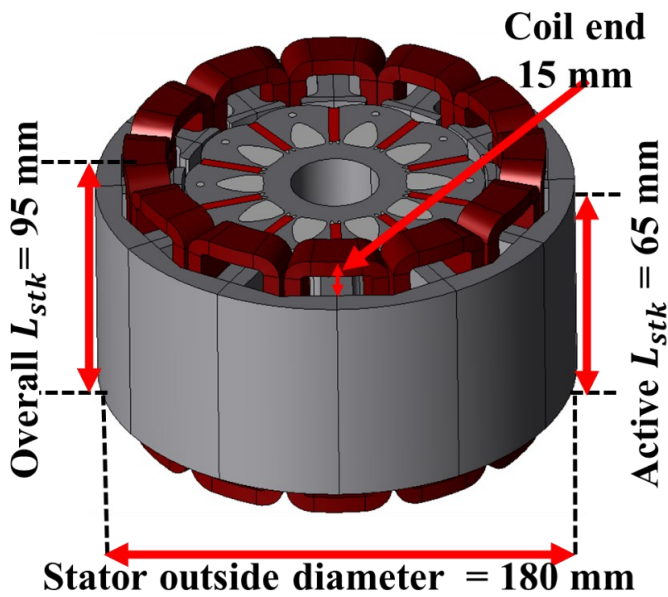


Fig.6. 27. Design – 3 (Laminated steel with coil end winding)

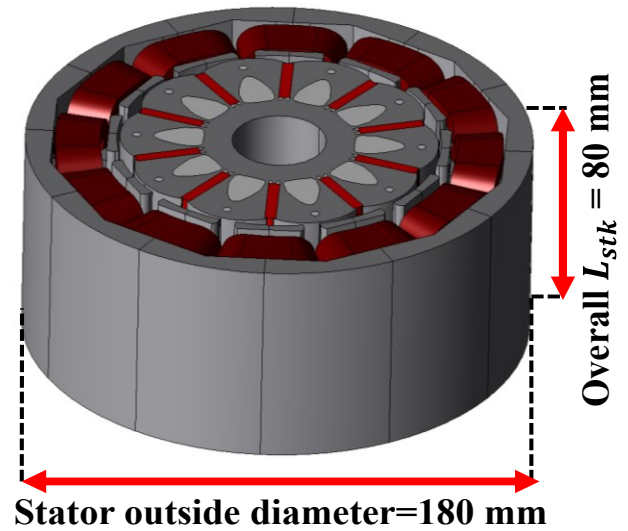


Fig.6. 28. Design-4 (SMC stator with compacted end winding)

Figs. 27 and 28 show the laminated and the SMC stator designs with the coil end windings. The laminated stator has projected end windings of about 15 mm on both sides. The tooth body of the SMC stator core is reduced on both sides to hold the copper within the stack height of the stator core. Figs. 29 and 30 show the full load flux density plot of both the designs with rotor and stator. Fig.6. 31 shows the full load flux density plot for the laminated and SMC stator cores.

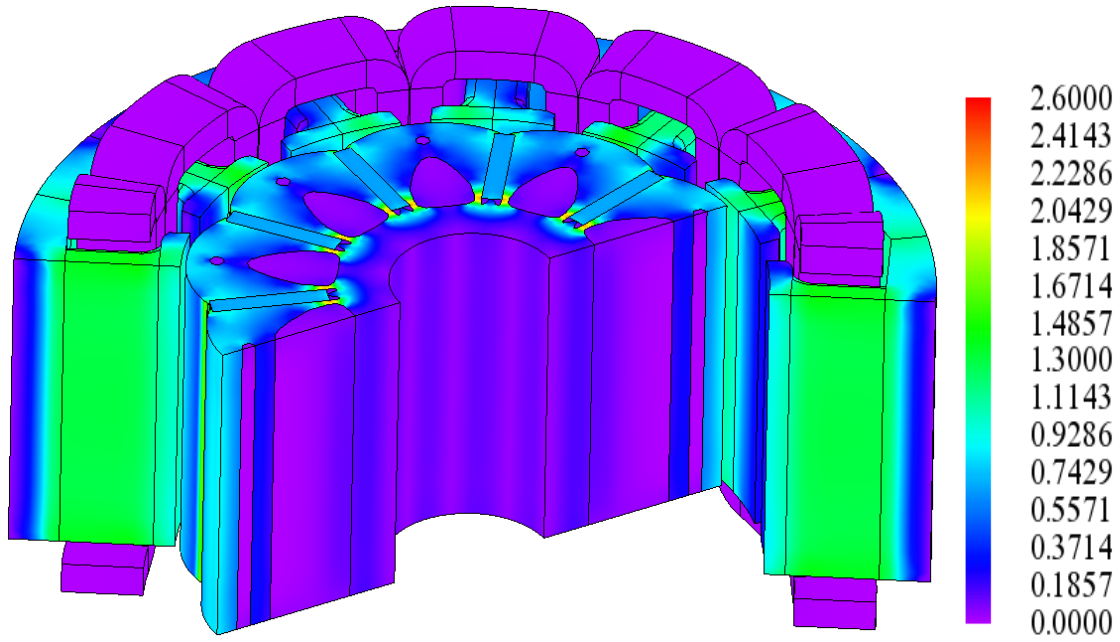


Fig.6. 29. Design -3 (Flux density plot for both stator and rotor)

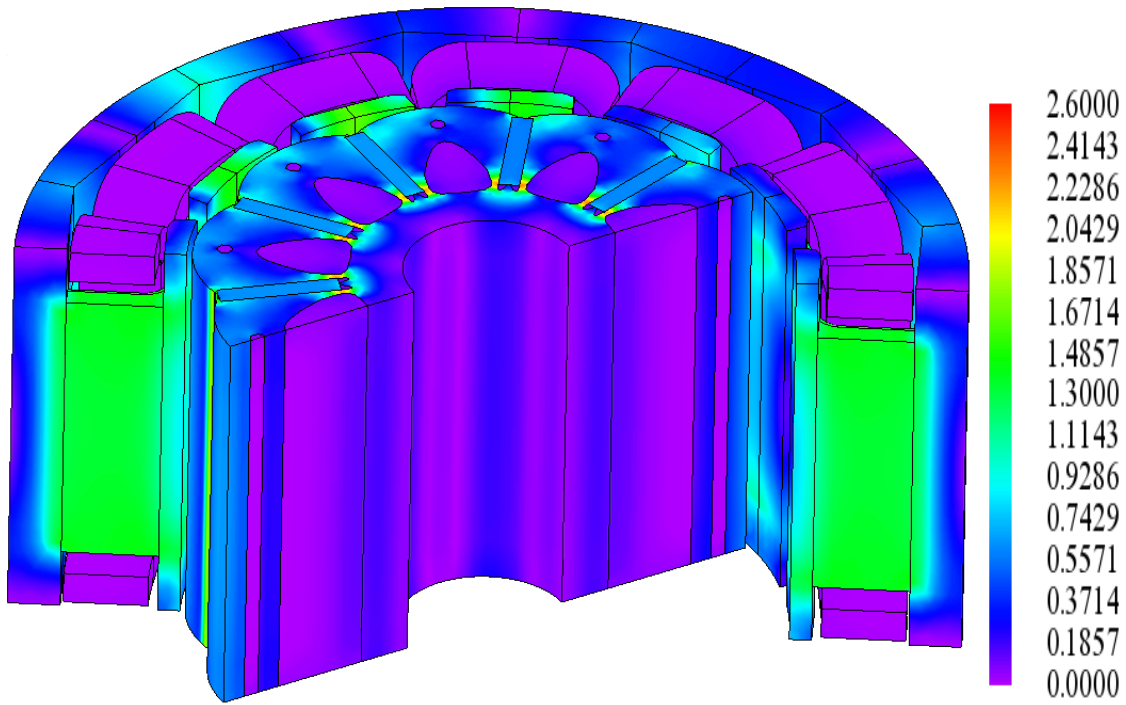


Fig.6. 30. Design -4 (Flux density plot for both stator and rotor)

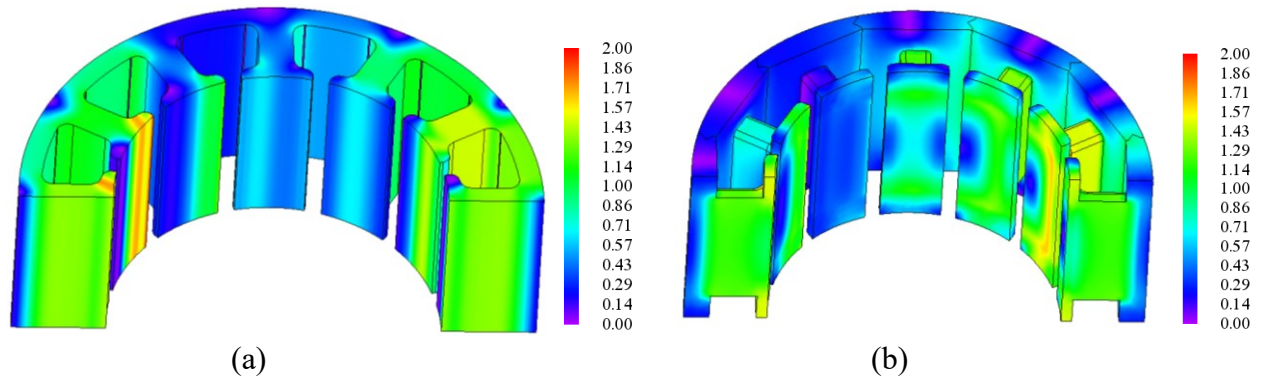


Fig.6. 31. Full load flux density plots (a) Laminated stator (b) SMC stator

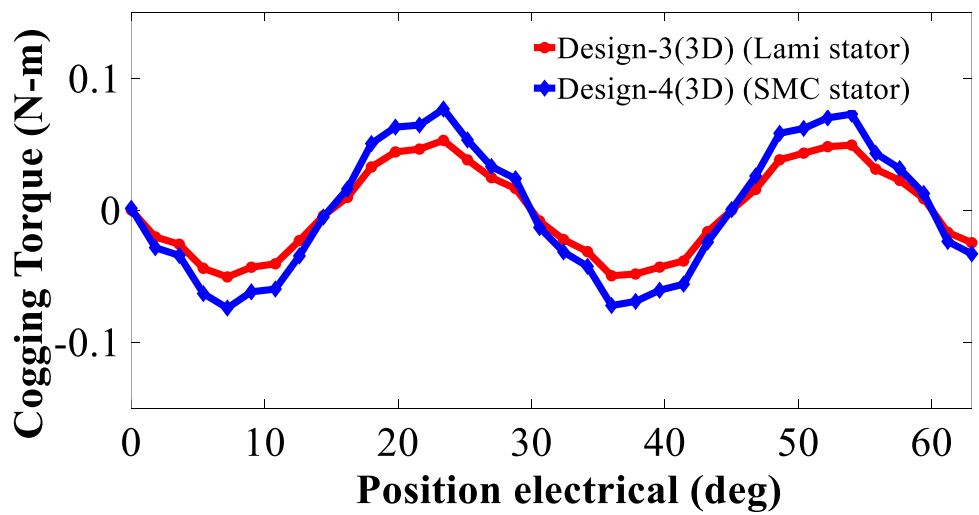


Fig.6. 32. 3D Cogging torque of Design -3 & 4 (Laminated and SMC)

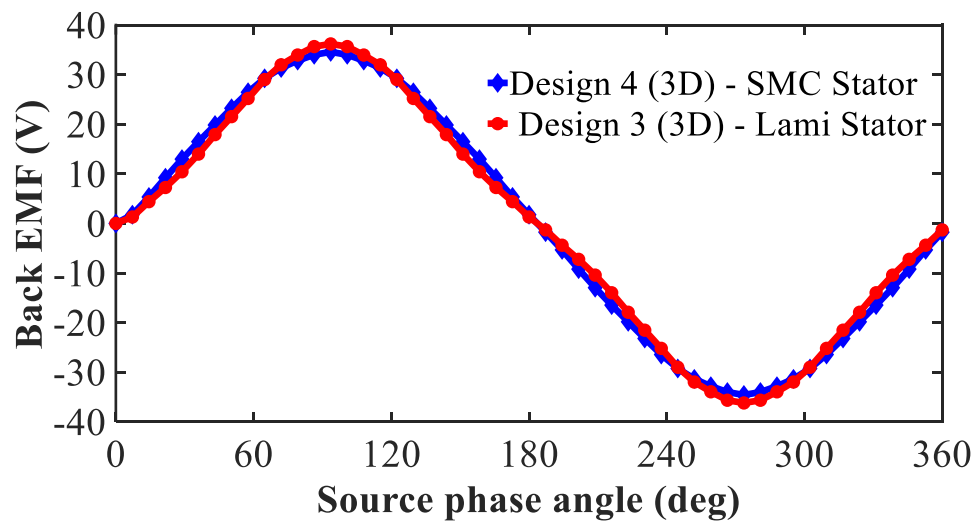


Fig.6. 33. 3D Phase back EMF of Design-3&4 (Laminated and SMC).

Figs. 32 and 33 show the cogging torque and phase back EMF of both stator designs. The electromagnetic performances are plotted for both designs using JMAG 3D FEA package [77]. The average torque is maintained the same for both designs. The torque ripple shown in Fig.6. 34 is almost the same for both stator designs.

Table 6.9– Performance metrics of slot/pole selection

Harmonic order	Design-3 (3D)- Lami	Design-4 (3D) - SMC
1 st	33.09	32.46
3 rd	1.31	3.48
5 th	0.07	0.01
7 th	0.060	0.02
9 th	0.0845	0.009
THD (%)	6.0%	11.9 %

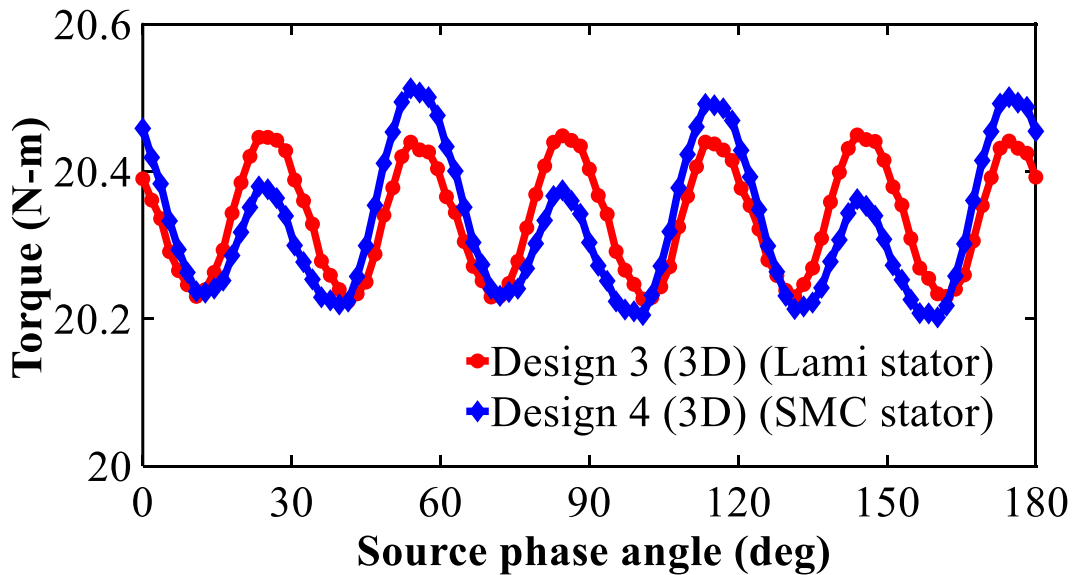


Fig.6. 34. Electromagnetic torque of Design -3 & 4 (Laminated and SMC)

Table 6.10 - Design 3 & 4 (laminated and SMC)

Item	Design-3 (3D)- Lami	Design-4 (3D)- SMC
Average torque (N-m)	20.41	20.32
Torque ripple (%)	1.11	1.55
back EMF THD (%)	6.07 %	11.8 %
Cogging torque (peak)	0.049 N-m	0.076 N-m

Table 6.9 shows the detailed comparison of back EMF harmonics for the laminated stator. The back EMF THD (%) with the SMC stator is increased 8.5% from the laminated stator. It is due to reducing the tooth body to hold the end winding within the stack height. The cogging torque is shown in Fig.6. 32 which is similar for both designs. The torque ripple and cogging torque with the SMC stator is significantly improved when compared to Design-1. Table 6.10 shows the overall electromagnetic performance comparison for the laminated stator and SMC. The torque density in terms of motor volume is higher by 20% in the SMC motor when compared to the laminated motor.

6.8. Loss analysis of SMC and laminated stator designs

This section focuses on comparing losses for the laminated and SMC stator designs. The electromagnetic performance dictate the operating efficiency of the motor.

A. Iron losses and copper loss

The iron losses in electrical machines account for a significant amount of the total losses. The iron losses of a PMSM machine can be calculated using the formula below:

$$P = K_h f B^n + K_e f^2 B^2 \quad (6.1)$$

Where K_h , K_e , n are the loss coefficients which are dependent on the material. B is the flux density, and f is the frequency. The eddy current in the SMC is divided into two types such as intra particle eddy current (P_{ei}) and overall eddy current (P_{oi}). The hysteresis loss and the intra particle eddy current (P_{ei}) can be calculated from toroid SMC samples. The total eddy current is due to the

manufacturing process which can create a random contact between the particles. The overall eddy currents can be determined by measuring the conductivity of the SMC material. The eddy current is analyzed in 3D FEA with the measured conductivity value of the SMC materials. The hysteresis loss is given as [76]

$$P_h = \sum_{e=1}^{e=n} k_h f B^a V_e \quad (6.2)$$

where, e is the element number, and n is the total element in the material, f is the fundamental frequency, B is the peak value of the flux density waveform, V_e is the element volume, k_h and a are the hysteresis loss coefficients.

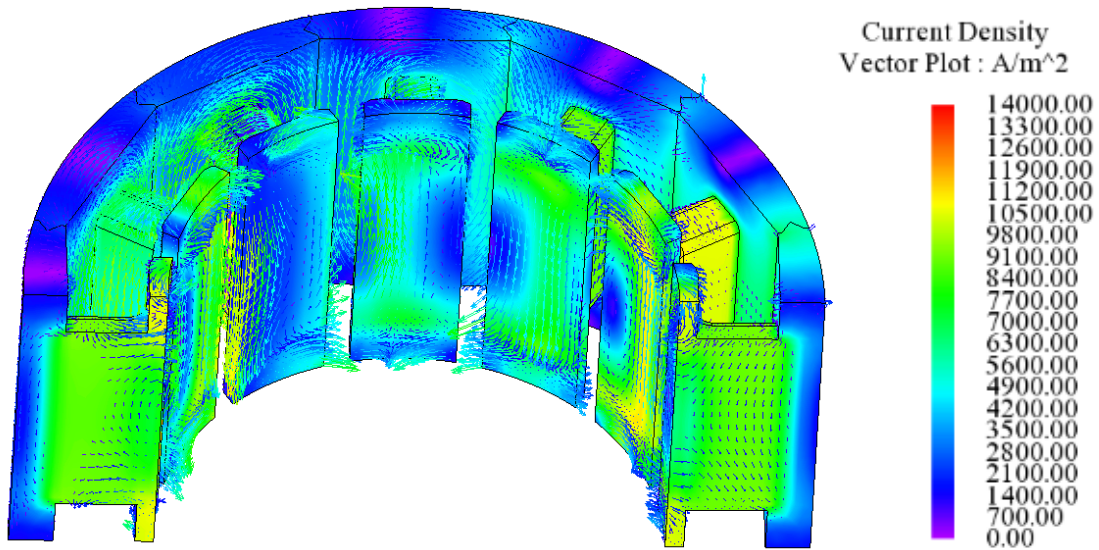


Fig.6. 35. 3D eddy current density plot of SMC stator with reduced tooth body

The intra particle eddy current can be calculated by the following equation:

$$P_{ei} = \sum_{e=1}^{e=n} \sum_{k=1}^{k=N} k_e f_k^2 B_k^2 V_e \quad (6.3)$$

where k is the harmonic order, N is the maximum considered harmonic order, f_k is the harmonic frequency, B_k is the harmonics flux density magnitude and K_e is the eddy current loss coefficient. The overall eddy current can be calculated using the eddy current density of each mesh element and also with the electric resistivity of the SMC material [76],

$$P_{oi} = \sum_{e=1}^{e=n} J_e^2 \rho V_e \quad (6.4)$$

Table 6.11 - Design 3 & 4 (Loss comparison)

Item	Design – 3 (laminated)	Design-4 (SMC)
Hysteresis coefficient (k_h)	0.0081168	0.0414204
Eddy current coefficient (k_e)	5.43843419	2.20796519
Flux density exponent (n)	2.18579142	1.78983980
Total Iron loss (3400 rpm)	136.8 W	219.2 W
Eddy current loss (3400 rpm)	60.8 W	24.7 W
Hysteresis loss (3400 rpm)	75.9 W	194.4 W
Iron loss (10000 rpm)	237.5 W	272.4 W
Eddy current loss (10000 rpm)	186.8 W	67.9 W
Hysteresis loss (10000 rpm)	50.7 W	203.4
Copper loss (3400 rpm)	104.8 W	88.6 W
Copper loss (10000 rpm)	70.1 W	64.7 W
Total loss (3400 rpm)	241.6 W	307.8 W
Total loss (10000 rpm)	307.6 W	337.1 W

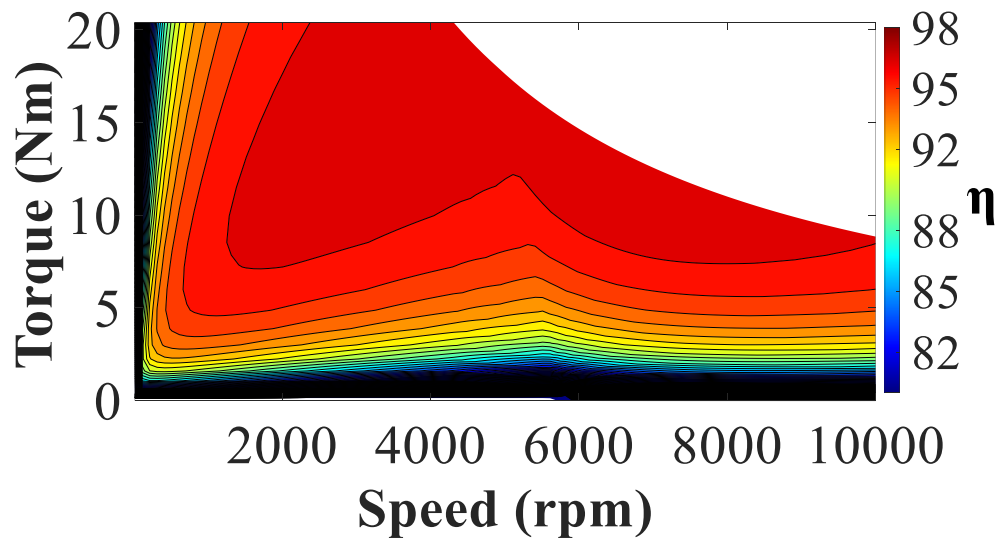


Fig.6. 36 (a) Efficiency map of Laminated stator

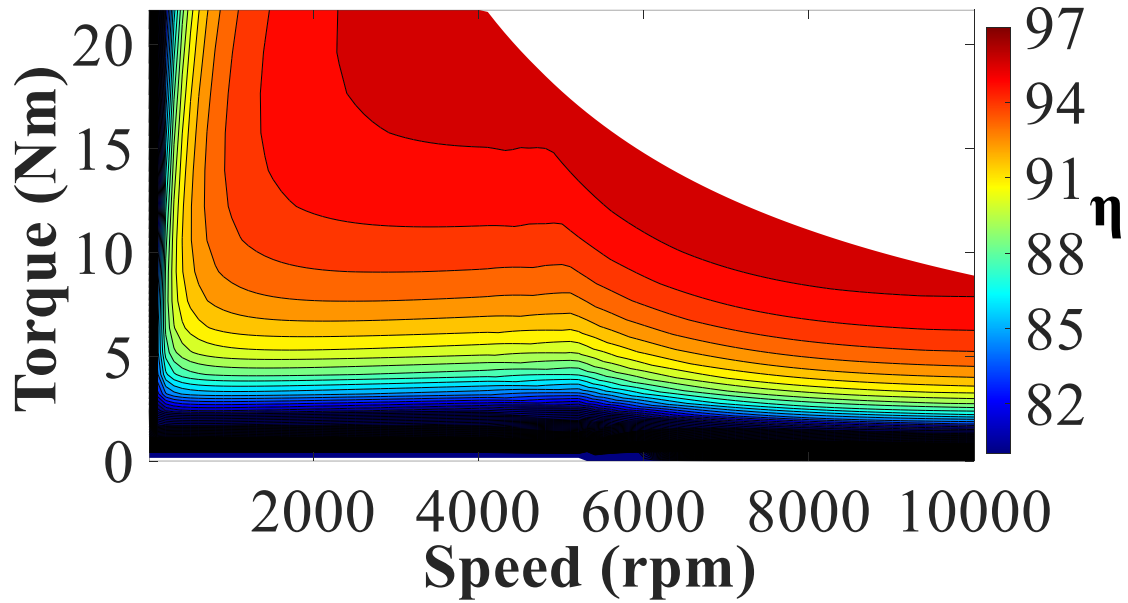


Fig.6. 36 (b) Efficiency map of SMC stator

Fig.6. 35 shows the eddy current density plot of the SMC stator core. Table 6.11 shows the comparison of iron loss comparison and Fig.6. 36 shows the efficiency maps for both designs.

6.9. Thermal analysis of (Design-3) laminated and (Design-4) SMC stator design at the base speed

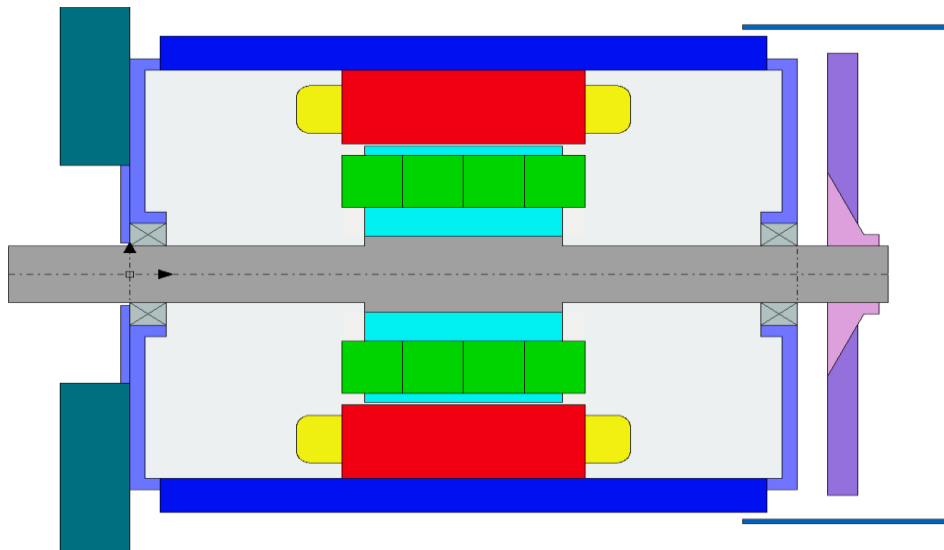


Fig.6. 37. Schematic for cooling with a fan coupled to the shaft

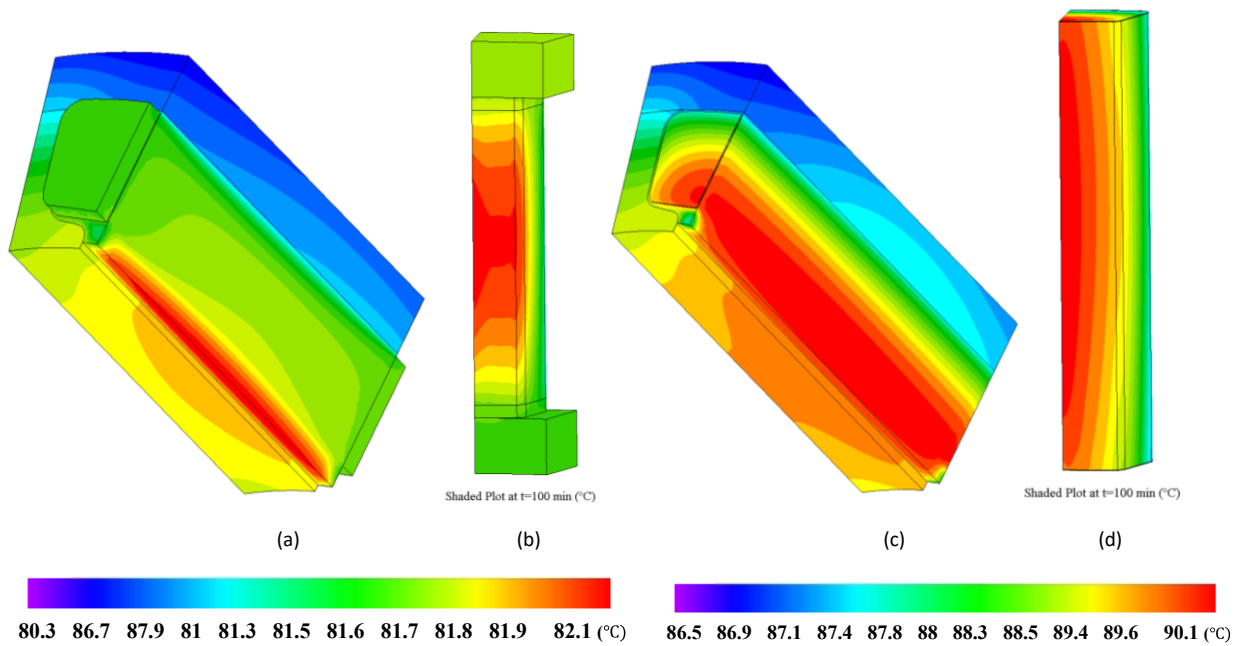


Fig.6. 38. (a) Temperature distribution in laminated steel stator (b) Temperature distribution in one coil side of a laminated stator (c) Temperature distribution in SMC stator (d) Temperature distribution in one coil side of a SMC stator.

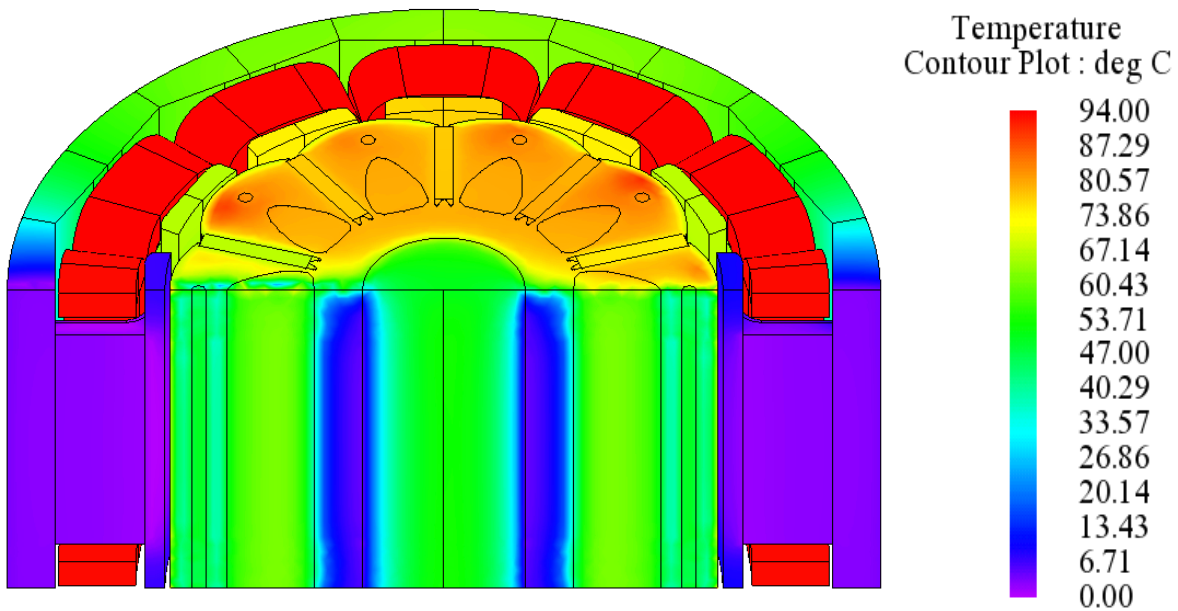


Fig.6. 39. Thermal analysis of the SMC stator design

Motor performance is governed by electromagnetic and thermal design [78]. The iron losses and copper loss are the main sources of heat generation. The primary concern of the motor design is the current density (A/mm^2). The current density values depend on the cooling conditions of the

motor. Epoxy resin is used as an insulating material. The motors are designed with natural convection with a current density no greater than 5 A/mm². Fig.6. 37 shows the schematic for cooling. Fig.6. 38 shows the temperature distribution of the laminated stator design and the SMC stator design. Fig.6. 39 shows the thermal distribution of the SMC stator design for a half model. Both machines are simulated with totally enclosed fan cooled (TEFC) cooling conditions.

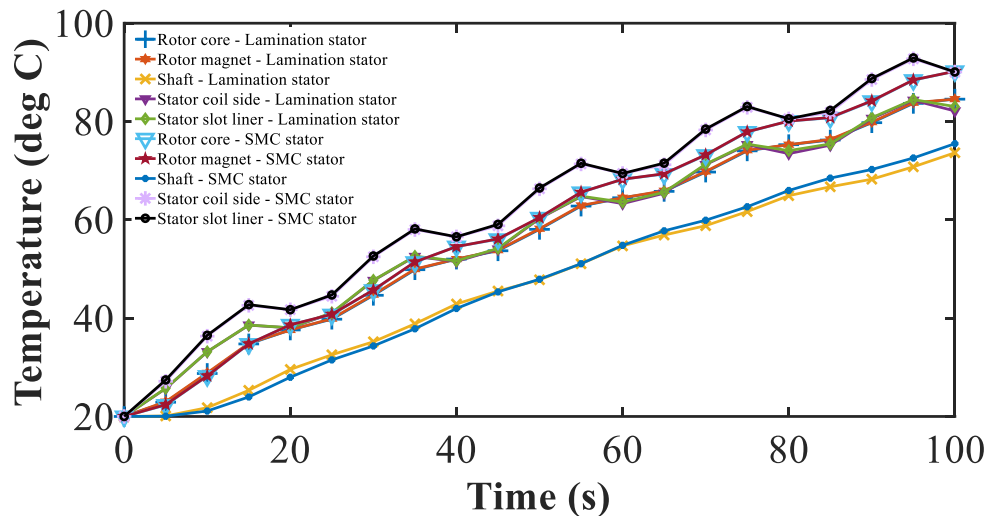


Fig.6. 40. Thermal comparison between the laminated stator and SMC stator design.

Fig.6. 40 shows the temperature distribution of various parts between the laminated stator design and SMC stator design for one tooth with one coil side. The outer circumference of the enclosure consists of fin channels, and the fan blades are mounted on the non-driven section of the machine shaft which provides the airflow into the enclosure fin channels during the operation of the motor shaft.

6.10. Electromagnetic and thermal analysis of design-5 (Laminated stator) with higher current

Section 6.7, 6.8, and 6.9 presents the laminated stator design and SMC stator designs to operate with the same RMS current value. This section firstly compares the laminated stator and SMC stator design with different current values, secondly presents the electromagnetic and thermal analysis of laminated stator design with higher current value. The phase resistance of SMC motor is lower than the phase resistance of the laminated motor due to the higher fill factor. The iron loss

of the laminated motor is lower than the SMC motor at the base speed, a case study is performed at different current values to equate the losses of both motors at the same temperatures.

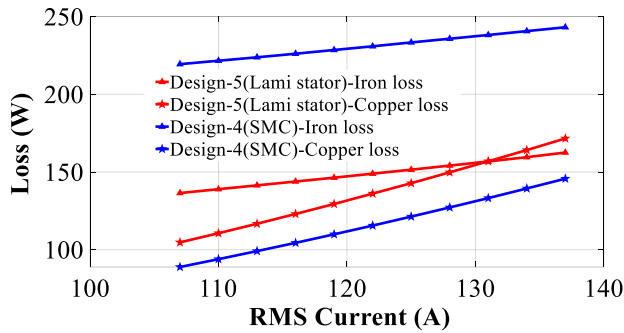


Fig.6. 41. RMS current Vs copper and iron loss at the base speed (3400 RPM) for Design-4(SMC stator) & Design-5(Lami stator)

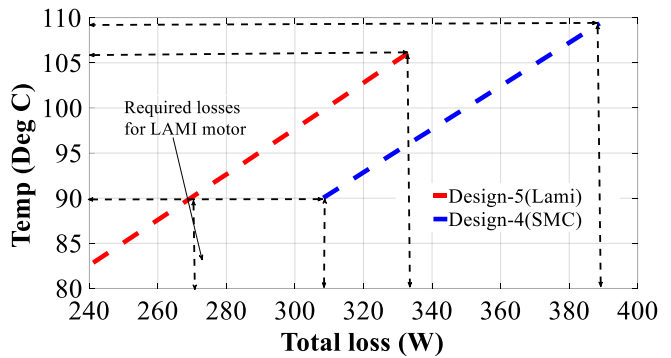


Fig.6. 42. Total loss Vs temperature at the base speed (3400 RPM) for Design-4(SMC stator) & Design-5(Lami stator)

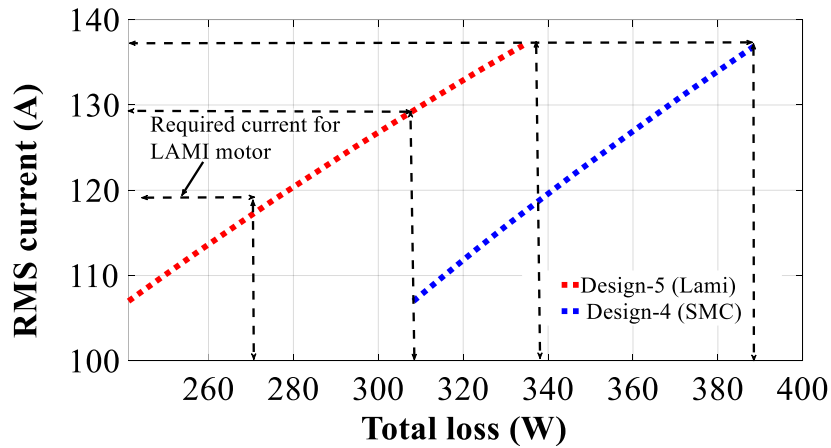


Fig.6. 43. RMS current Vs copper and iron loss at the base speed (3400 RPM) for Design-4(SMC stator) & Design-5(Lami stator)

The laminated motor with higher current is Design-5 (laminated stator). Fig.6. 41 shows the impact of copper loss and iron loss for the two designs. There exists a difference in the distribution of the copper loss and iron loss for the two motors. For the SMC stator, iron loss dominates compared to the copper loss. Fig.6. 42 shows the temperature rise with respect to the change in loss values. From section VI the RMS current value is fixed as 107 A. Both the motors are analyzed with 107 A, at this operating point the total loss of the laminated motor is 240 W with a maximum copper

conductor temperature of 82°C. The SMC motor has a total loss of 307 W with a maximum copper conductor temperature of 90°C.

Table 6.12- Design-3(Lami stator_1) specifications

Item	(Design -5) (Lami stator)
RMS phase current	119 A
Stator OD	180 mm
Rotor OD	113 mm
Stack length	65 mm
Overall stack length	95 mm
Copper fill factor	40 %
Torque density (motor volume) at 3400 rpm	9.05 KNm/m ³

To achieve the same temperature for the laminated motor a total loss of 275 W results in an RMS current of 119 A which is shown in Fig.6. 42 and Fig.6. 43. Although the SMC motor has higher iron losses, it's less prone to temperature rise due to the low copper losses. This analysis shows that the laminated motor can be designed with a higher current rating than the SMC motor to operate with the same thermal limits. Table 6.12 shows the design specifications of Design-5(Laminated stator).

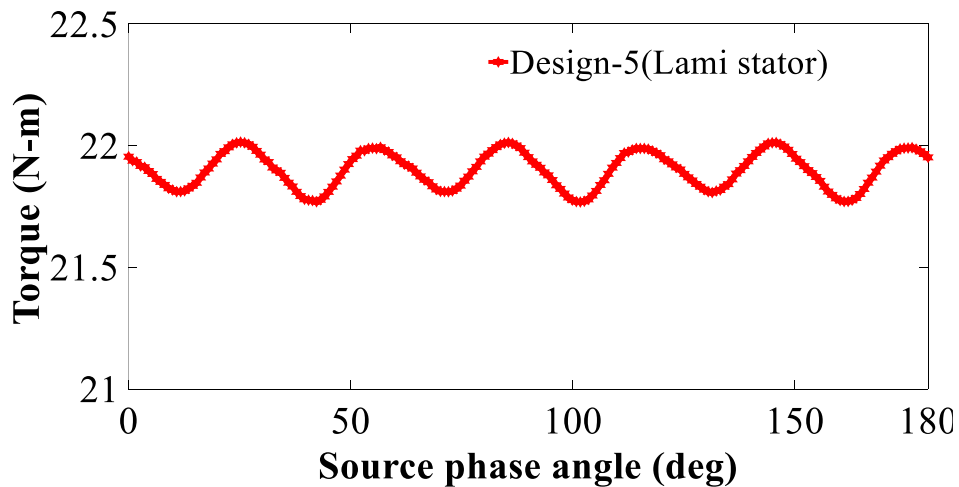


Fig.6. 44. Electromagnetic torque of Design -5 (Lami stator)

The machine parameters such as the stator outer diameter, stack length, and the copper fill factor remains same, except the current, thus the current density also will not be same. The phase back EMF and the cogging torque of Design-5 remains same as Design-3 since the turns per coil and stack length remains the same. The electromagnetic torque, efficiency map and temperature distribution for the copper conductor are presented for Design-5(Laminated stator).

Table 6.13 - Design-5 (Lami stator)

Item	Design-5 (Lami stator)
Average torque (N-m)	21.9
Torque ripple (%)	1.11

Table 6.14 - Design-5(Lami Stator) losses

Item	(Design -5) (Lami stator)
Hysteresis coefficient (k_h)	0.0081168
Eddy current coefficient (k_e)	5.43843419
Flux density exponent (n)	2.18579142
Total Iron loss (3400 rpm)	146.3 W
Eddy current loss (3400 rpm)	78.4 W
Hysteresis loss (3400 rpm)	67.9 W
Total Iron loss (10000 rpm)	218.3 W
Eddy current loss (10000 rpm)	168.1 W
Hysteresis loss (10000 rpm)	50.2 W
Copper loss (3400 rpm)	129.4 W
Copper loss (10000 rpm)	61.7 W
Total loss (3400 rpm)	275.7 W

The torque is plotted for a rated current of 119 A. The average torque and torque ripple is presented in table 6.13. The torque is increased by 7.77 % from Design-4 (SMC stator). The loss analysis is presented in table 6.14 for the Design-5(Laminated stator) motor. The iron loss also is increased from the Design-3(Laminated stator) motor due to the increase in the current.

The total loss at the rated speed is 275.7 W. Figure 45 shows the efficiency map of Design-5(Laminated stator). Figure 46 shows the temperature of the Design-5(Laminated stator) at the base speed. The copper conductor reaches 90 degrees which is same for Design-4(SMC stator) motor.

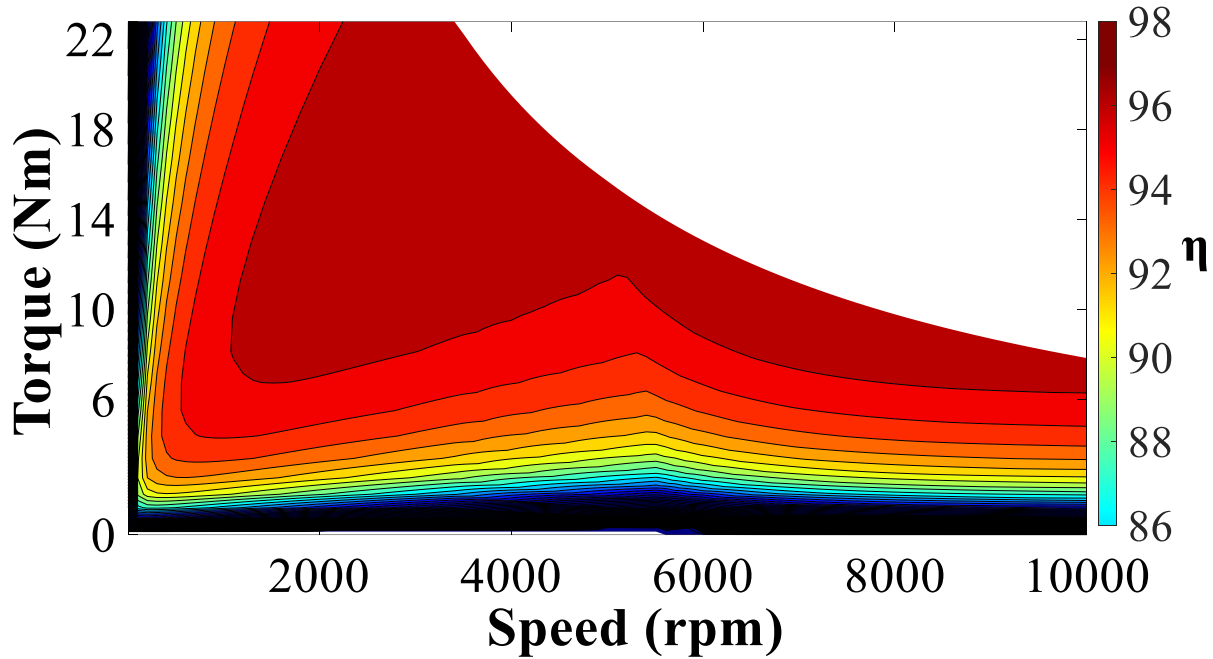


Fig.6. 45. Efficiency map of Design-5 (Lami stator) with higher current

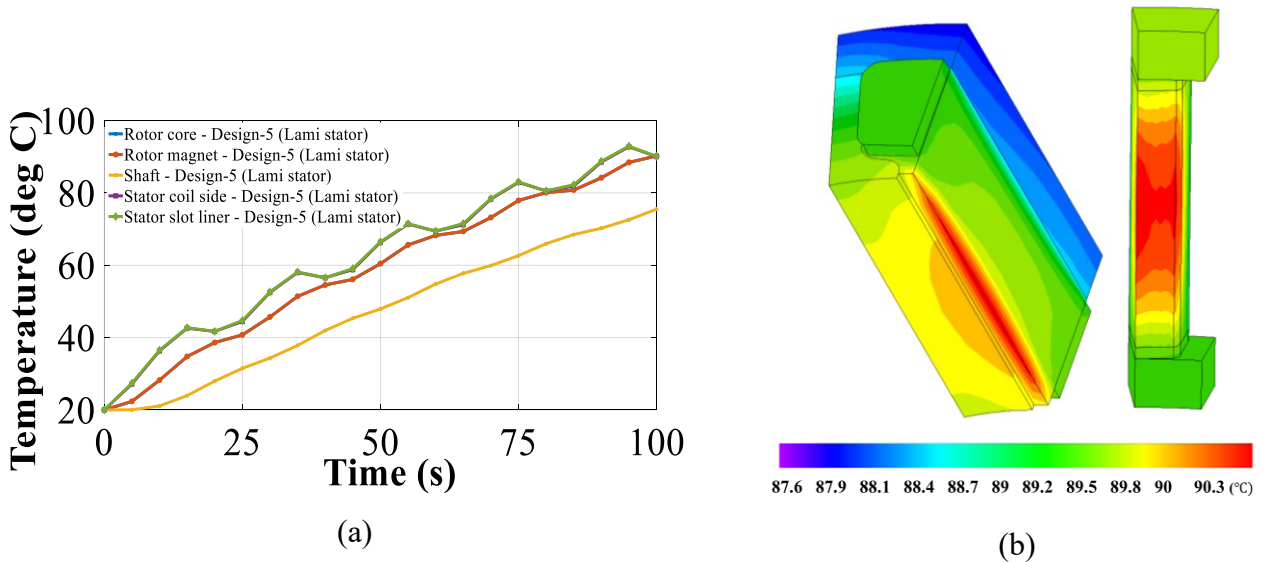


Fig.6. 46. Thermal distribution of Design -5 (Lami stator) at the base speed (a) Temperature for different parts (b) Temperature of copper conductor.

When the laminated motor is designed to operate at same thermal limits of SMC motor, the laminated motor is capable of producing higher torque. However, the torque density in terms of motor volume is 9.31 % higher in the SMC motor than the laminator motor which is made possible with the compacted end winding.

6.11. Wastage and cost comparison of laminated stator and SMC stator

According to [79] from EMERF laminations database, one method of reducing the material usage in lamination manufacture involves stamping the rotor lamination from inside the stator lamination.

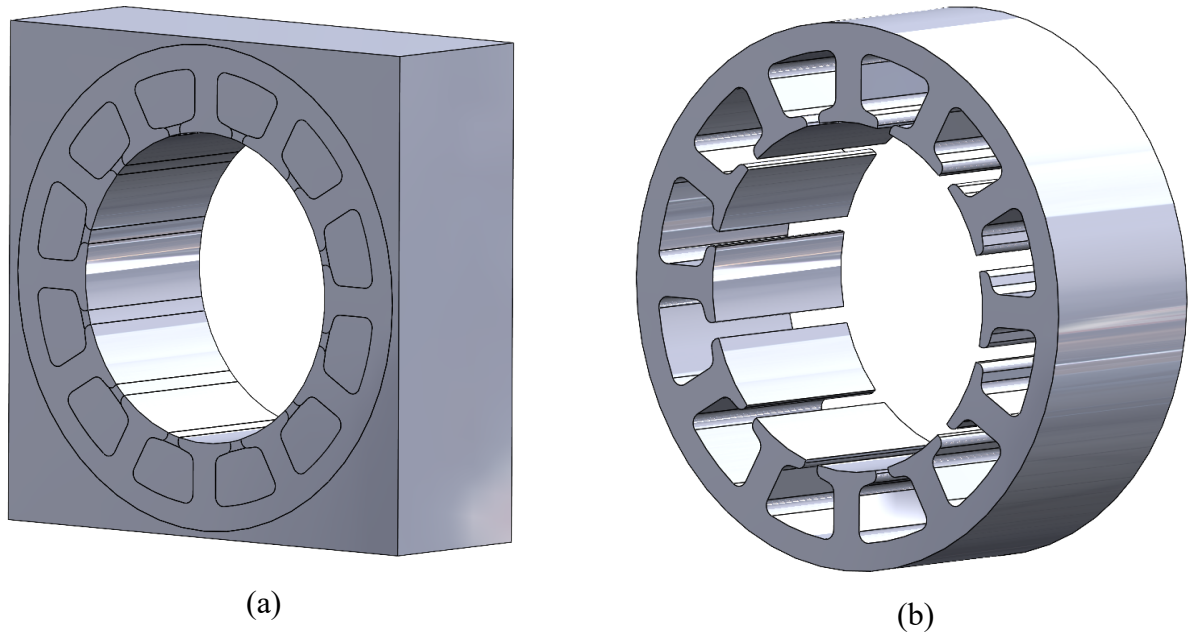


Fig.6. 47. Laminated stator (a) Square shape laminations (ready to wire cut) (b) Final laminated stator after wire cut

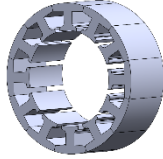
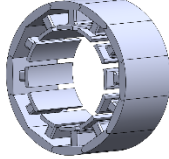
Table 6.15- Laminated steel waste

Items	Total raw material	Used raw material	Wasted raw material	Waste (%)
Laminated steel considering the whole square (kg)	12.10	4.40	7.7	63.6
Considering only the slot waste (kg)	7.54	4.40	3.14	41.6

This process eliminates the need for the second strip of raw material just for the rotor lamination. Meticulous tool work is necessary to ensure the rotor is separated without altering the stator or rotor dimensions. An extremely small air gap in the motor may not allow this technique. In this

case study, it is assumed that the middle part of the stator core is used for the rotor laminations. Usually, normal lamination manufacturing uses square shape raw materials.

Table 6.16 - Cost Comparison of Laminated motor and SMC motor

Item	Design-3 (Laminated motor)	Design-4 (SMC motor)
		
Stack length (mm)	65	80
The total cost of rotor core (\$)	418.5 (Lami)	515.2 (Lami)
The total cost of stator core (\$)	418.5 (Lami)	48 (SMC)
Magnet weight (kg)	0.47	0.55
Total Magnet cost (\$)	70.5	82.5
Total cost (\$)	907.5	645.7

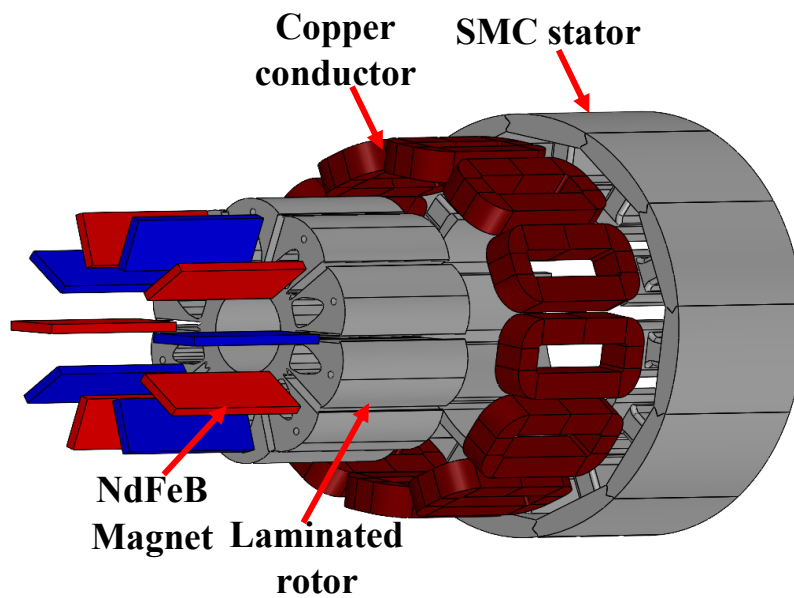


Fig.6. 48. Assembly drawing of SMC stator design

Fig.6. 47 (a) shows the normal lamination manufacturing sample in a square shape. Fig.6. 47 (b) shows the final laminated steel stator lamination after wire cut. Table 6.15 shows the laminated steel wastage in terms of wire cut, considering the whole square sheet and considering only the slot area. These values are obtained from a stator outer diameter of 180 mm with a stack length of 65 mm. The SMC will have approximately 5% wastage in the tooling process [80]. Table 6.16 shows the cost comparison between the laminator motor and SMC motor.

The use of SMC can create a revolutionary development in the electrical machine manufacturing industry. The SMC cores can be easily mass manufactured with the help of a die with desired shape and dimensions. The total price of rotor lamination and stator lamination includes wire cut and assembly. The SMC stator price includes the raw material and processing price. It's clear that the SMC motor cost is significantly lower than the laminated motor. Fig.6. 48 shows the assembly drawing of the SMC stator design.

6.12. Axial magnet segmentation, optimal flux weakening and mechanical stress analysis of SMC stator design

A. Axial magnet segmentation

This section focuses on a more detailed analysis of the SMC stator design with axial magnet segmentation, optimal flux weakening and mechanical stress analysis of SMC stator and rotor design.

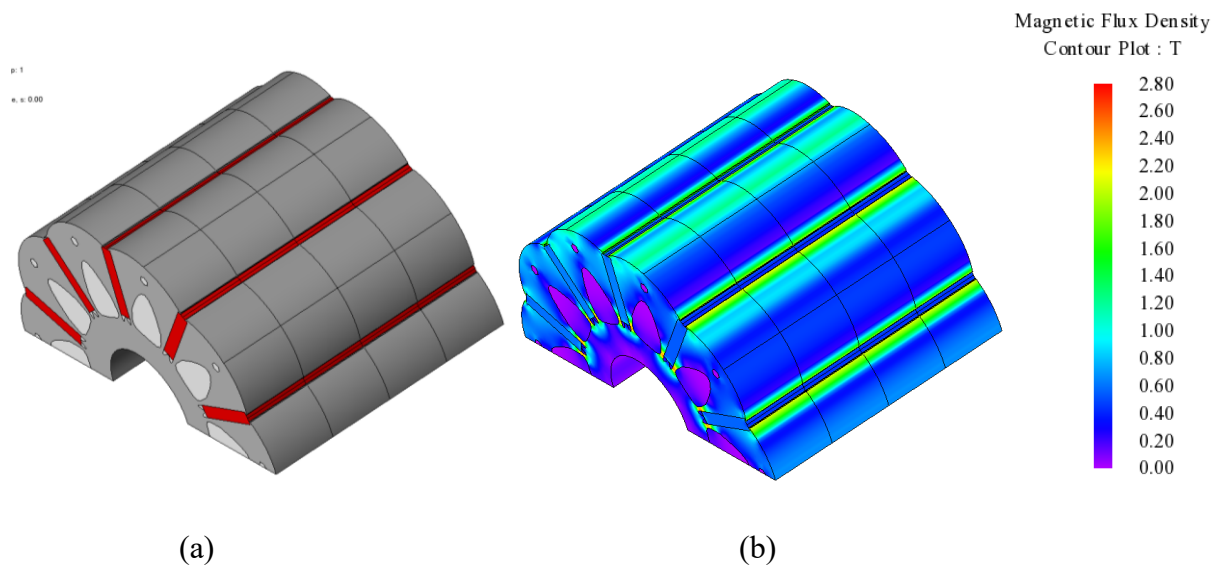


Fig.6. 49. Magnet Segments (a) Four (b) Flux plot of rotor

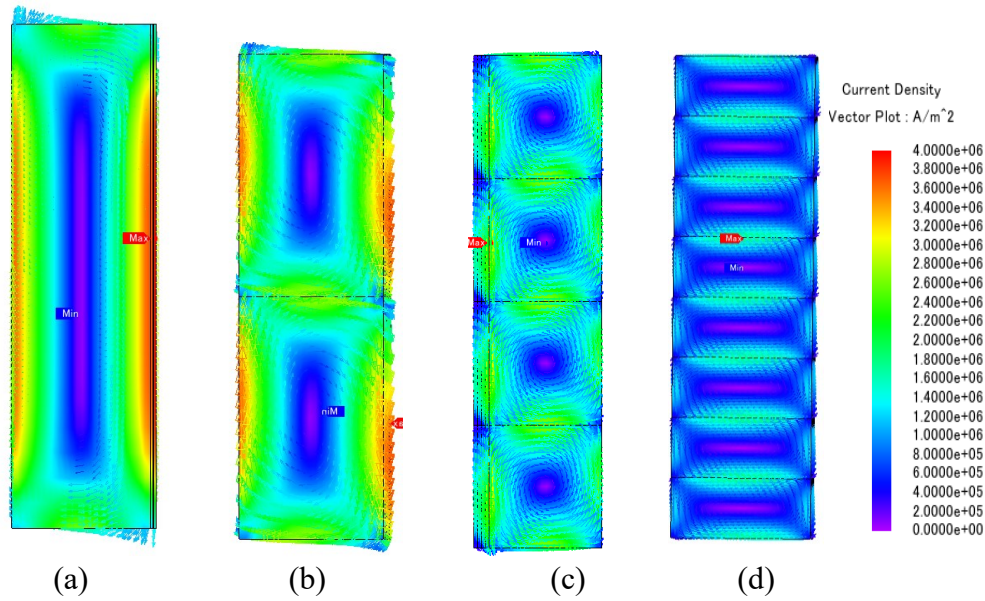


Fig.6. 50. Magnet eddy current loss density (a) No segment (b) Two segments (c) Four segments (d) Eight segments

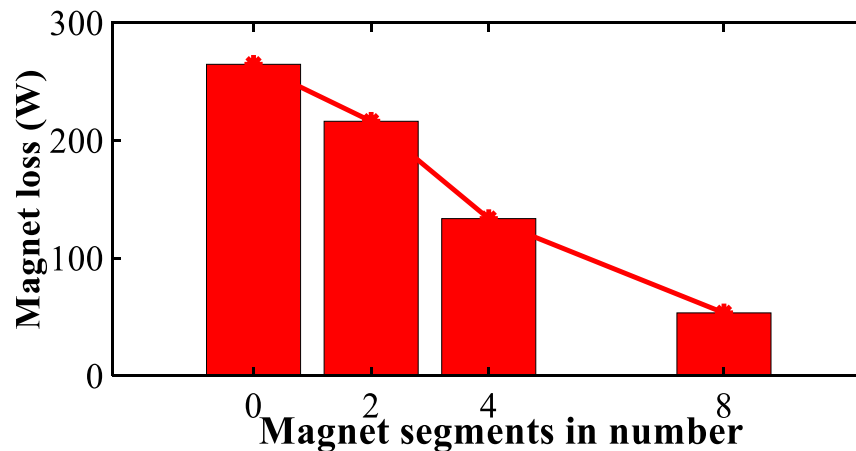


Fig.6. 51. Magnet losses of SMC stator with various segments at 10000 rpm

The permanent magnet rotors designed for high-speed application with fractional slot windings are exposed to high rate of change of flux in magnetic field which tends to produce high eddy current losses in the permanent magnets [81-82]. Axial magnet segmentation is considered to significantly reduce the magnet losses [83]. Design-4 with the SMC stator is analyzed with axial magnet segmentation. Fig.6. 49 shows the axial magnet segmentation with four segments. Fig.6. 50 shows the magnet eddy current density plot for all four different magnet segments. The eddy current density plot shows that the magnet with no segments has higher losses due to the higher eddy current loops formed at the sides. The size of the eddy current loops are reduced gradually

with increasing number of magnet segments. Fig.6. 51 shows the magnet loss of SMC stator design with various segments. The magnet losses of the four different segment scenarios are: 266.7 W, 216.3 W, 133.6 W and 53.4W. Magnets with eight segments produce low loss, considering the manufacturing and assembling issues, four segments would be an optimal choice for a traction application.

B. Optimal flux weakening

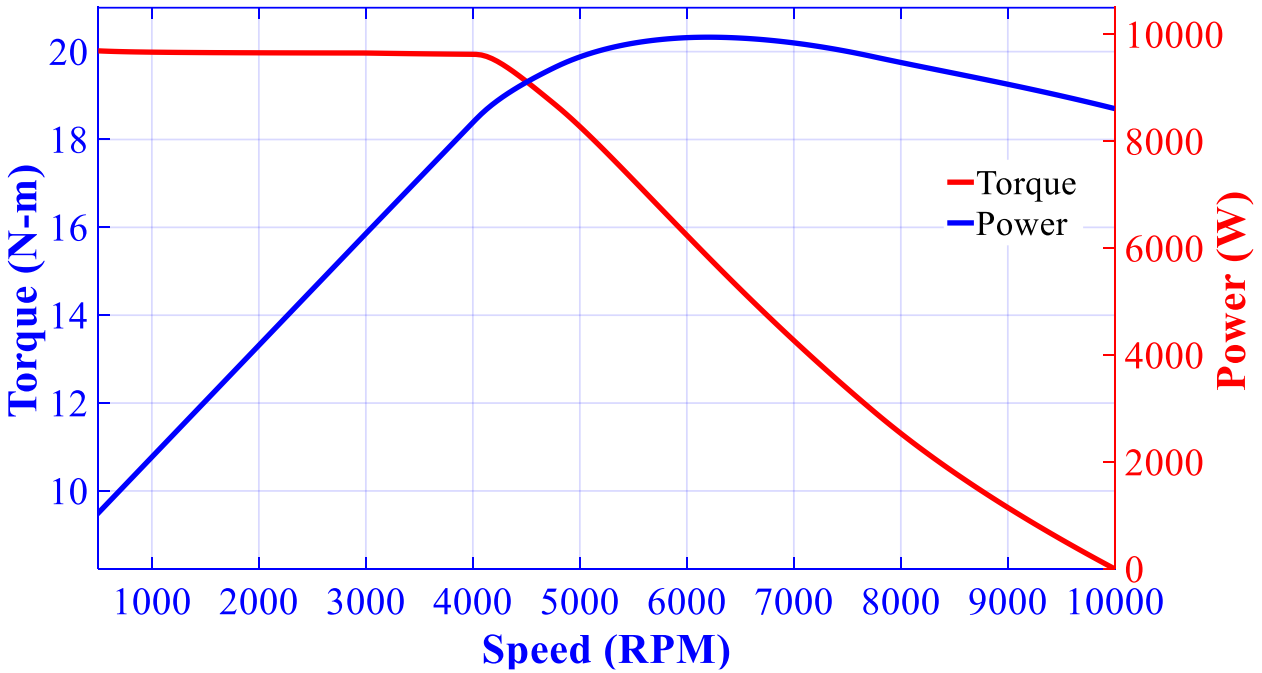


Fig.6. 52(a). Speed Vs torque & Speed Vs Power (JMAG – 3D FEA)

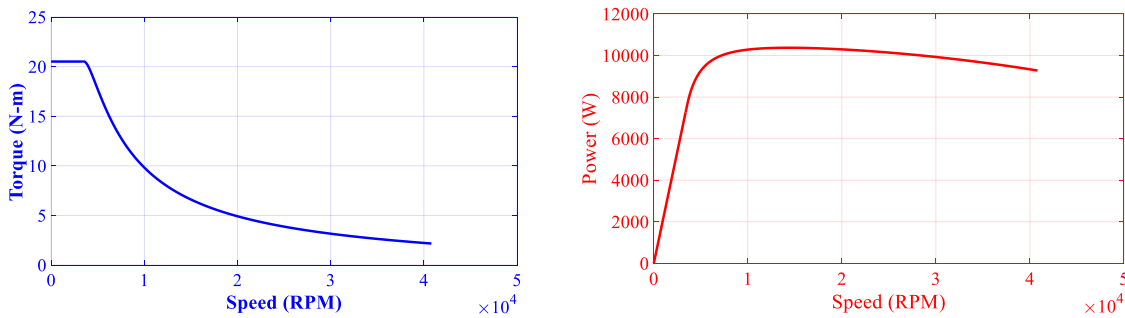


Fig.6. 52(b). Speed Vs torque & Speed Vs Power (MATLAB analytical)

Table 6.17 shows the parameters of the optimal flux weakening conditions. Fig.6. 52 shows the speed vs torque and speed vs power plotted using MATLAB equations for flux weakening.

Table 6.17- optimal flux weakening conditions

Stator	SMC stator
Winding	Concentrated
SPP slot/pole/phase	0.4
L_d d-axis inductance (mH)	0.103
L_q q-axis inductance (mH)	0.105
Lq/Ld	1.01
I_s Peak current(A	155
φ_m Flux linkage (Wb)	0.019732
Diff between φ_m & $L_d * I_s$ (% equation matched)	80.90%

The speed vs torque and speed vs power show the operating regions of the SMC stator design.

C. Mechanical Analysis

In general, the stator cores will not be subjected to high mechanical stress. Also laminated steels have high yield strength to withstand high stress whereas SMC have lower yield strength. The electromagnetic forces are calculated using 3D magnetic field transient analysis. The calculated force is applied on the stator core using a 3D structural direct transient analysis with a similar mesh pattern. Fig.6. 53 shows the SMC tooth with and without fillet.

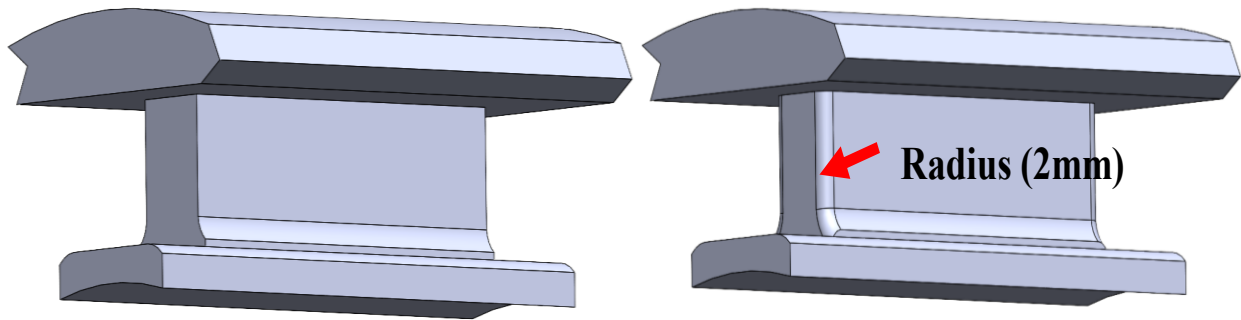


Fig.6. 53. SMC tooth (a) Without fillet (b) With fillet radius (2mm)

Fig.6. 54 shows the stress analysis of the SMC stator. The electromagnetic force of an electric motor can be analyzed from the electromagnetic force distribution obtained by mapping the transient magnetic field analysis to the structural analysis.

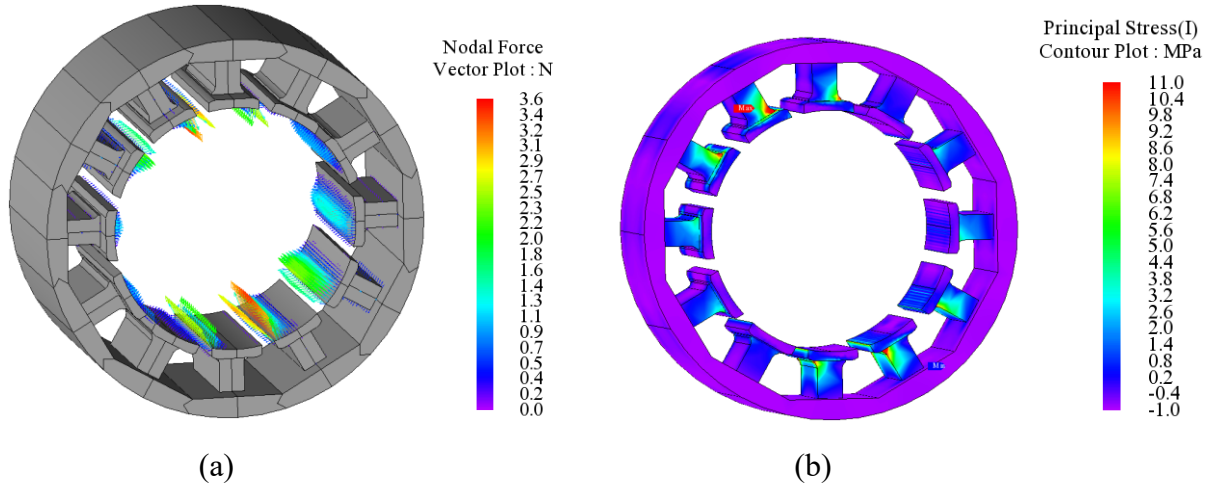


Fig.6. 54(a). Mechanical stress analysis of SMC-B stator with no fillet.

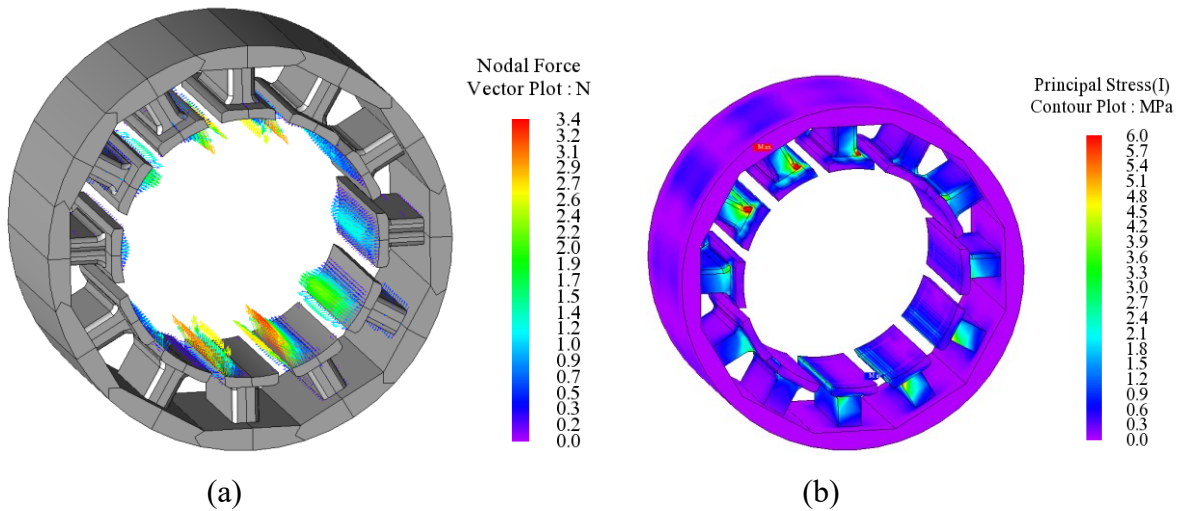


Fig.6. 54(b). Mechanical stress analysis of SMC-B stator with fillet (radius 2mm)

Nodal force condition is set up for the stator core in the magnetic field analysis. The same study is duplicated as a structural analysis, in which the electromagnetic force condition is set up for the stator core. The copper conductors and the rotor core are neglected in this study. This condition specifies the electromagnetic force obtained from the magnetic field analysis as a load. The same number of start step and end step are used from the magnetic field analysis to obtain the proper results. Also, a significant amount of mesh is added for the stator slot which is facing the air gap area. The SMC tooth without fillet at the tooth body has Mises stress of about 11 MPa whereas the SMC tooth with fillet has a Mises stress of 6 MPa. A radius of 2mm reduces 45% of the stress. The Young's modulus of the SMC material is 65000 MPa.

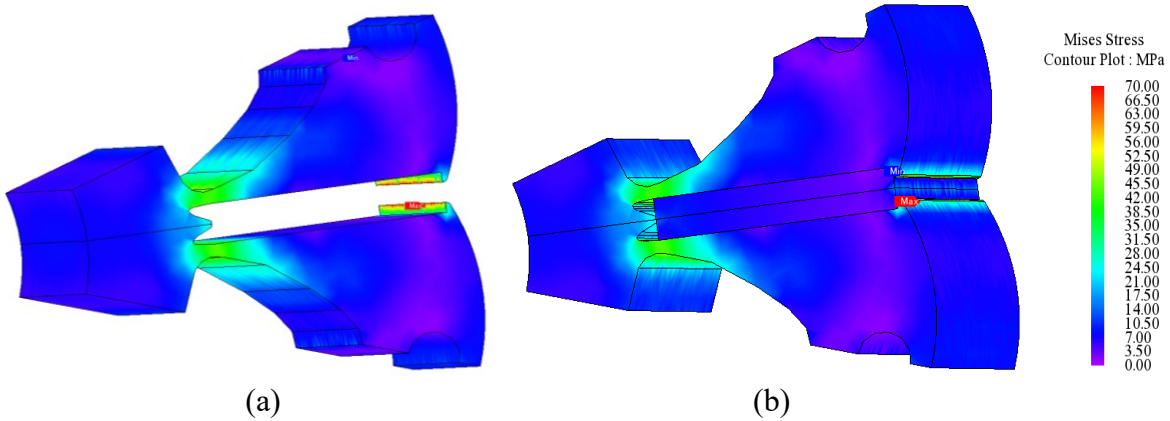


Fig.6. 55. Rotor mechanical stress at 10000 rpm (a) Rotor view without magnets (b) Rotor view with magnets.

Also, this stator stress analysis is beneficial to help choose the SMC material depending on the requirements. Centrifugal force is applied during the motoring operation. The magnets are pressed against the rotor core, thus causing stresses locally. The condition between the magnet and rotor core has to be carefully handled to obtain the precise stress distribution. A static structural study is considered for the mechanical stress analysis. The rotor core and magnets are considered targets for the centrifugal force condition. One rotor pole is considered for the centrifugal force analysis. The constraint is set up in both the X- and Y-directions. The contact condition is used between the magnets and the rotor core. Fig.6. 55 shows the mechanical stress analysis of the rotor at 10000 rpm. The rotor is made up of laminated steel which has a higher Young's modulus when compared with the SMC material. The Young's modulus of the laminated rotor is 210000 MPa. The maximum mechanical stress of the rotor at 10000 rpm is 70 MPa. This stress value is much lower than the capability of the laminated rotor.

6.13. Conclusion

This chapter compares three different SMC materials (A, B & C) with different permeability and resistivity values for a same machine specifications. Though the hysteresis loss is lower in SMC-C it has higher eddy current loss when compared to the SMC-A & B. The magnet loss, mechanical loss, and copper loss have been calculated for all the three SMC based designs using 3D FEA along with iron loss calculations. Efficiency maps are plotted for all three SMC based designs for a maximum speed range of 10000 rpm. SMC-B has the highest efficiency of 95.0 % at

the rated speed (3400 rpm) and 91.46% at the maximum speed (10000 rpm). SMC-B material is chosen to be the best material when compared to the SMC- A & C. After selecting the best SMC material, it's compared with a laminated silicon steel stator design for the same specifications. The copper loss with SMC – B stator is reduced by 26.12% from the laminated steel stator design. The torque density in SMC-B stator is improved by 15 % from the laminated stator design. The core loss of the SMC-B material is tested using a toroid tester.

Two high pole designs such as 24-slot/16-pole and 36-slot/30-pole has been analyzed with a laminated stator and SMC stator. Iron loss at 10000 rpm for the 24-slot-16-pole with laminated stator is 1.7 times higher than the SMC stator design. Iron loss at 10000 rpm for 36-slot/30-pole with a laminated stator is 2.2 times higher than the SMC stator design. This shows that the SMC stator design is a better candidate than the laminated design to operate at higher frequencies. The tooth body length SMC_B stator design is varied from 36 to 56 mm. 56 mm tooth body length is shown to have higher average torque, and lower harmonics in the phase back EMF. The average torque with the SMC stator with no back iron is 2% lower than the design with the back iron

Design-3 (3D) with the laminated stator is analyzed with a 3D analysis with the end winding overhang. Design-3(3D) is called a laminated stator design and Design-4 is called the SMC stator design. The tooth body of the SMC stator is reduced on both sides to hold the end winding within the stack height. The laminated stator design has a copper fill factor of 40% and the SMC stator design has a copper fill factor of 60%. The copper loss with the SMC stator design is 13.67% lower than for the laminated stator design. The total iron loss at rated speed (3400 rpm) with the SMC stator design is increased 31.05 % from the laminated stator design. The total iron loss at the maximum speed (10000 rpm) with the SMC stator design is increased 6.86% from the laminated stator design. The overall efficiency of the laminated stator design at the rated speed is 97% and the SMC stator is 96%. But the torque density of the SMC stator is increased 20% from the laminated stator with the help of compacted end windings and 3D flux paths.

A 3D Thermal analysis has been performed for the SMC stator design which shows that the thermal values are within the limit for a natural convection motor.

The temperature of Design-3 (Laminated stator) is lower than Design-4 (SMC stator). A case study is performed at different current values to equate the losses of both motors to the same temperature. The laminated motor with higher current is called Design-

5(Laminated stator). Design-5 (Laminated stator) reaches the same temperature of Design-4 (SMC stator) at an RMS current of 119 A. At this point, Design-5 (Laminated stator) produces higher torque than the SMC motor by 7.77 %. However, the torque density in terms of motor volume is higher in the SMC motor by 9.31% with the help of compacted end winding. A cost comparison between the laminated motor and SMC motor has been presented which clearly indicates that the SMC motor is lower cost than the laminated stator. The magnet losses with four axial segments are 50% lower than that for the magnet with zero segments. 80% of the flux weakening conditions are satisfied to achieve a wide flux weakening up to 10000 rpm.

Stator stress is reduced by 50% for SMC stator core with a fillet of radius 2mm at the tooth body. Mechanical stress analysis has been performed for the rotor: 70 MPa is the maximum stress value for a maximum speed of 10000 rpm. This study suggests that the SMC stator cores can be utilized to improve the torque density, copper fill factor and allows a 3D flux path.

CHAPTER – 7

Prototype and Experiment

This chapter presents the evolution of SMC tooth considering the manufacturing and assembling challenges. It briefly presents the SMC tooth manufacturing including the heat treatment. Also it presents the rotor manufacturing with prototype pictures. Finally, experimental results are presented for the SMC motor, along with the simulation results.

7.1. *Introduction*

Soft magnetic composite (SMC) stator cores have a higher electrical resistance than lamination steel stator cores, as noted in reference [84]. Manufacturers can produce SMC stator cores with segmented teeth and an interlocking arrangement by connecting all the teeth using an epoxy glue, which reduces the overall cost of the machine. Segmented SMC stator cores can achieve a high copper fill factor, and the manufacturing process involves punching and heat treatment. However, due to their lower mechanical strength, manufacturers use lamination steel to fabricate and stack the rotor using a cleating rod arrangement. Rotor pole shaping has been carried out to reduce the torque ripple. In a study by [89], four different machines were designed and analyzed, each operating at different power ratings and speed levels. Interestingly, the findings suggest that there are no specific guidelines available for controlling torque ripple and back EMF harmonics percentage. However, the objective of this thesis is to design, manufacture, and test a spoke-type rotor with a SMC stator that exhibits exceptionally low torque ripple. In traction applications, two types of conductor losses occur: direct current (DC) conductor losses dominate at low speed, and alternating current (AC) copper losses dominate in the higher frequency range. A comparison between finite element analysis (FEA) and a hybrid method for calculating AC losses was presented in a study [85]. Researchers analyzed the hairpin winding using the worldwide harmonized light vehicle test procedure (WLTP3) driving cycle [86], and the possibilities for manufacturing rectangular windings were presented [87]. A segmented rectangular copper wire was introduced, featuring different slot openings [88]. Although the initial design featured circular copper conductors, ribbon copper wires were used for manufacturing due to difficulties in winding assembly, which achieved a high copper fill factor. Finally, the stator and rotor are assembled into the frame, coupled with a fan to the shaft.

7.2. Evolution of SMC tooth

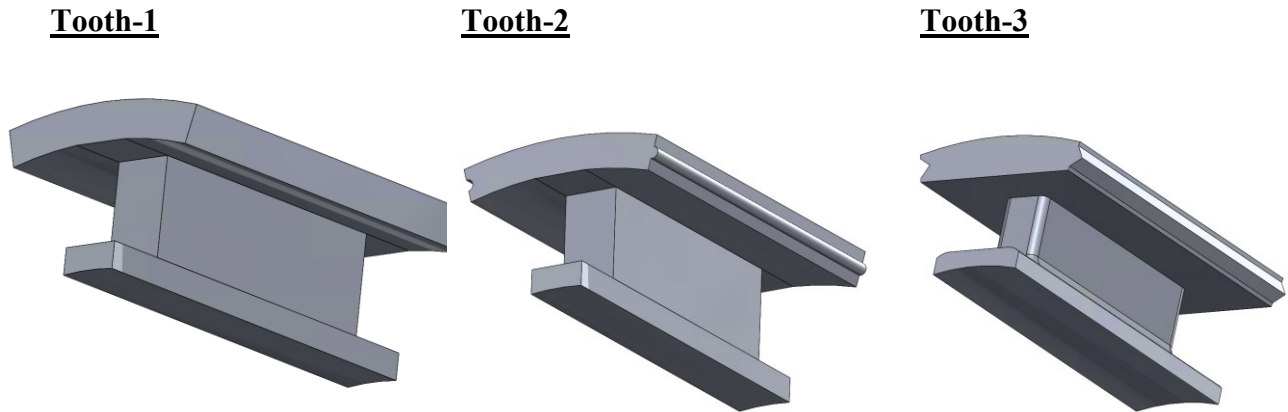


Fig. 7.1. SMC tooth evolution

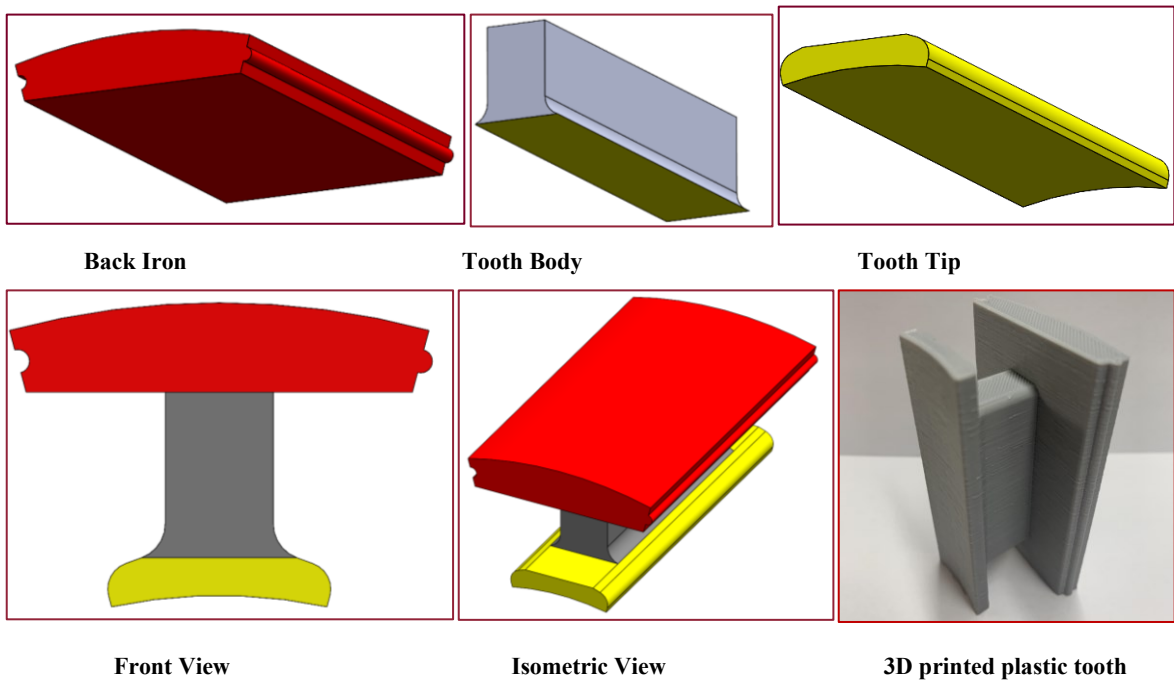


Fig. 7.2. Tooth-2 (SMC tooth) views with 3D printed plastic tooth

Fig. 7.1 shows the evolution of the SMC tooth. Initially modular SMC tooth (Tooth-1) is designed without protrusions and extrusions. This design is not well suited for assembly. The second design (Tooth-2) features protrusions and extrusions on the SMC tooth, which facilitate

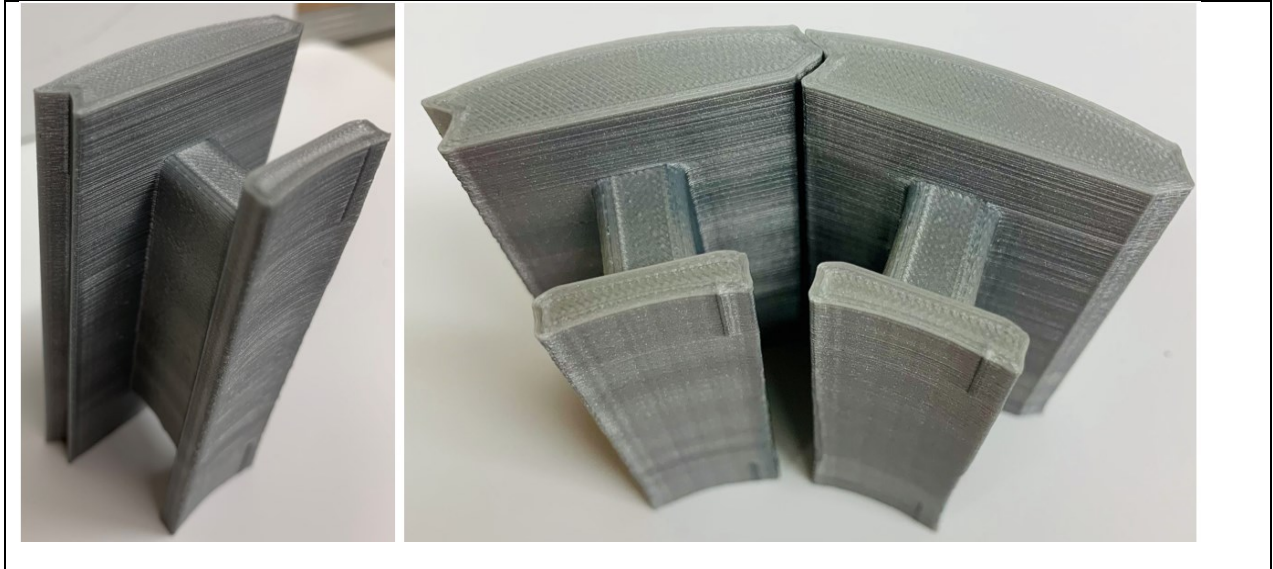


Fig. 7.3. Tooth-3 (3D Printed) SMC tooth using plastic.

easier assembly. Fig. 7.2 presents the back iron, tooth body and tooth tip for Tooth-2 design. In addition, the tooth body lacks fillets at the corners. To assess the feasibility of this design, a plastic SMC tooth was 3D printed. However, the 3D printed SMC tooth showed that for protrusions with circles, the diameter of the circle must be larger to hold the thinner back iron, which is necessary for the higher pole configuration. Therefore, the second design is also unsuitable for assembly. The SMC tooth that utilizes triangle tooth connectors, as depicted in Figure 7.3, was 3D printed using plastic material. This design proved to be the optimal choice for both assembly and flux concentrations. Unlike the previous design, complete back iron is utilized for protrusions and extrusions. In addition, manufacturers have verified that machining triangle connectors would be easier than machining circle connectors. The SMC stator has an active stack length of 80 mm, which means that each SMC tooth needs to be compressed to 80 mm if it is going to be a single piece. However, it is not feasible for the industry to compress it with one SMC material part due to the long length required. The reduced size of the tooth body and fillet pose several challenges for the compaction and machining process. The purpose of the reduced tooth body is to accommodate the end winding within the stator core's height, while the fillet is intended to protect the copper conductor from damage. If the corners are sharp, they can harm the copper conductors and lead to insulation failures. As a result, fillets are necessary to ensure that the conductors remain undamaged. Despite their benefits, these design features add complexity to the compaction and machining process. As a result, the SMC teeth prototyped here are produced in three segments manually to form an 80 mm stack length.

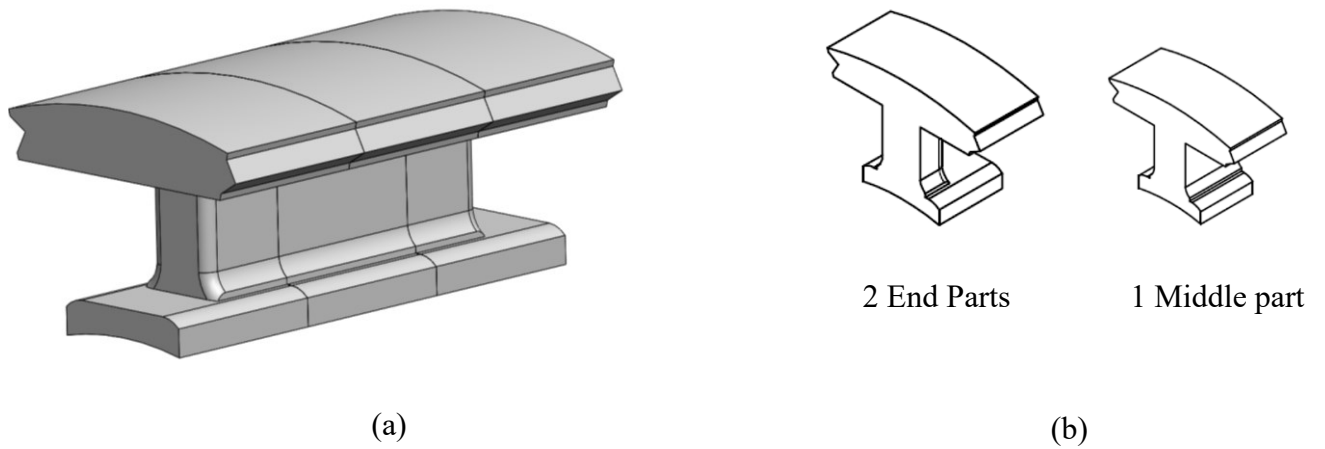


Fig. 7.4. Tooth-3 with 3 axial segments sketched using CAD software.

Fig. 7.4 shows the SMC tooth with 3 segments. The axial segmentation ensures that the flux path is not significantly affected. However, if the segmentation is done radially, it will impact the flux path.

7.3.SMC Stator fabrication

The SMC blocks are manufactured in rectangular or ring shapes and are compacted to near net shape. They are then machined to achieve the desired shape. Heat treatment is performed to enhance the material strength before the SMC teeth are assembled to form the SMC stator.

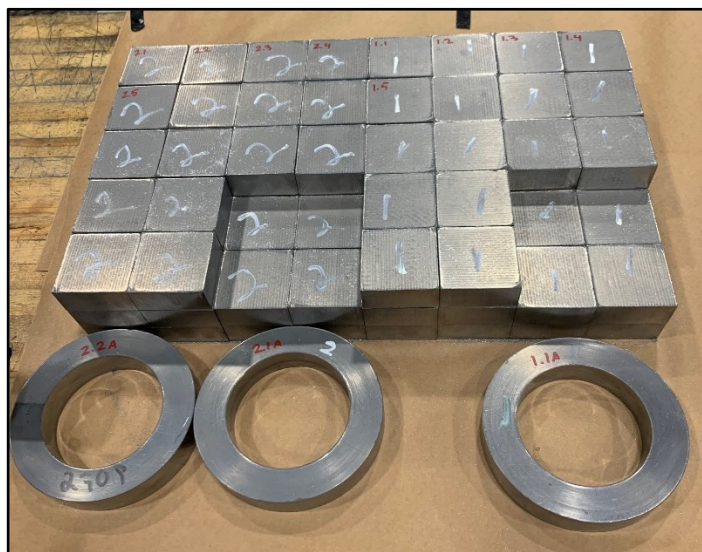


Fig. 7.5. SMC material original shape

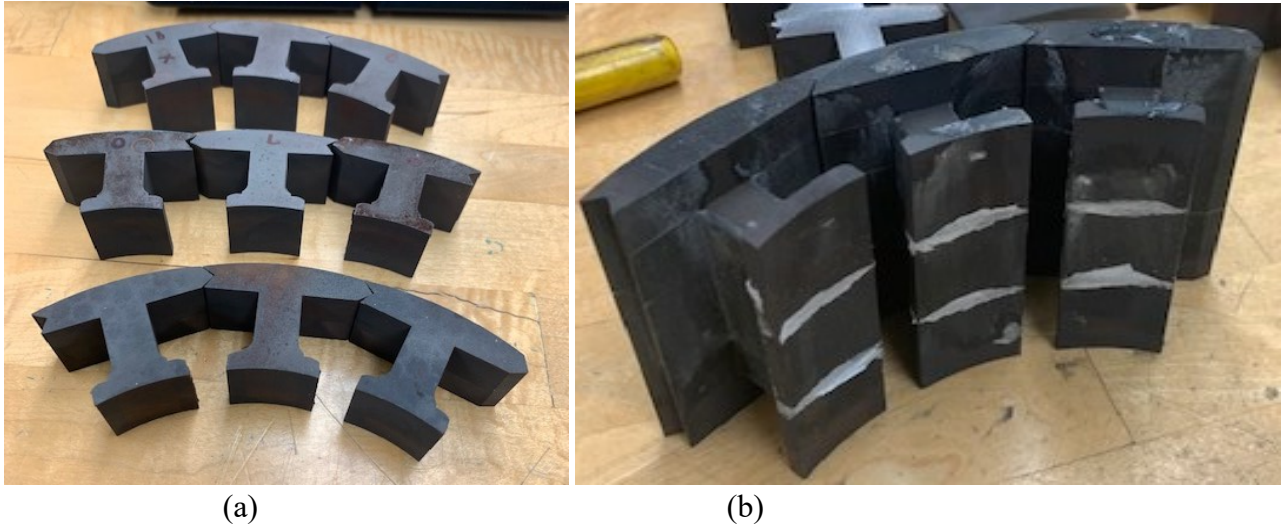


Fig. 7.6. SMC tooth (a) Manufactured tooth segments (b) Glued tooth segments.

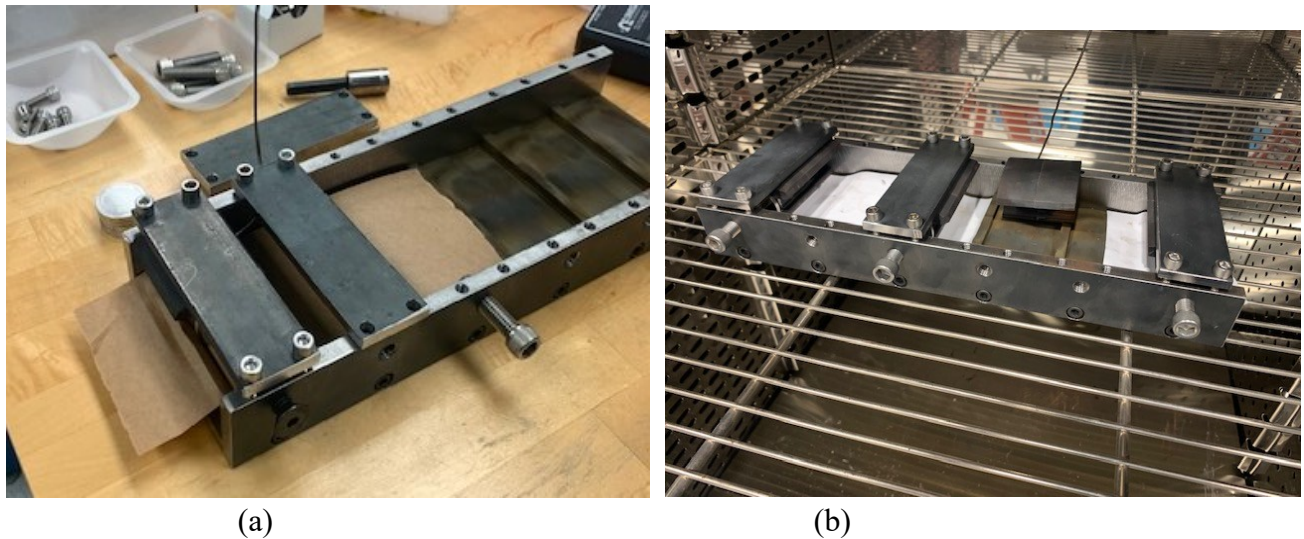


Fig.7.7 (a) SMC tooth parts in assembly with screw (b) SMC tooth assembly in the oven.

Fig. 7.5 shows the SMC material's original shape before compaction. Figs. 7.6 and 7.7 show the process of SMC tooth manufacturing. Firstly, the SMC tooth is compacted in to three segments as shown in Fig. 7.6 (a). After the 1st step, fillets of radius 2mm is added to the corners of the SMC tooth body. Secondly, the segmented teeth are connected together using an epoxy glue. Thirdly, the SMC tooth segments are assembled using a screw arrangement so that it can be placed in an oven for heat treatment. The steps are repeated for all 12 SMC teeth. Finally, the SMC teeth are assembled together to form a SMC stator core.

The following are the steps for heat treatment of the SMC stator core:

1. Gently sand the surfaces that will be in contact with each other.
2. Clean the surfaces with acetone to remove any dirt or oils.
3. Place a sheet of brown paper on the grooved bottom of the mount.
4. Apply a thin, even layer of glue (about 1mm thick) to one of the surfaces.
5. Press the parts together firmly, and wipe away any excess glue leaking from under the parts.
6. Align the parts correctly and tighten the front screw to hold them in place.
7. Check the total length of the three pieces to ensure they are identical.
8. Thoroughly clean up any remaining glue residue around the edges of the part.
9. Install the top pressure plate and evenly tighten all four screws.
10. Place the assembly in an oven preheated to 121°C (250°F), and include a control piece with a thermocouple to monitor the temperature.
11. After the glue has dried, sand any rough edges or bumps to create a smooth, even finish.



Fig. 7.8. Fabricated SMC stator core (complete) 12 slots

After heat treatment SMC teeth are assembled to form a SMC stator core. The complete SMC stator is shown in Fig. 7.8.

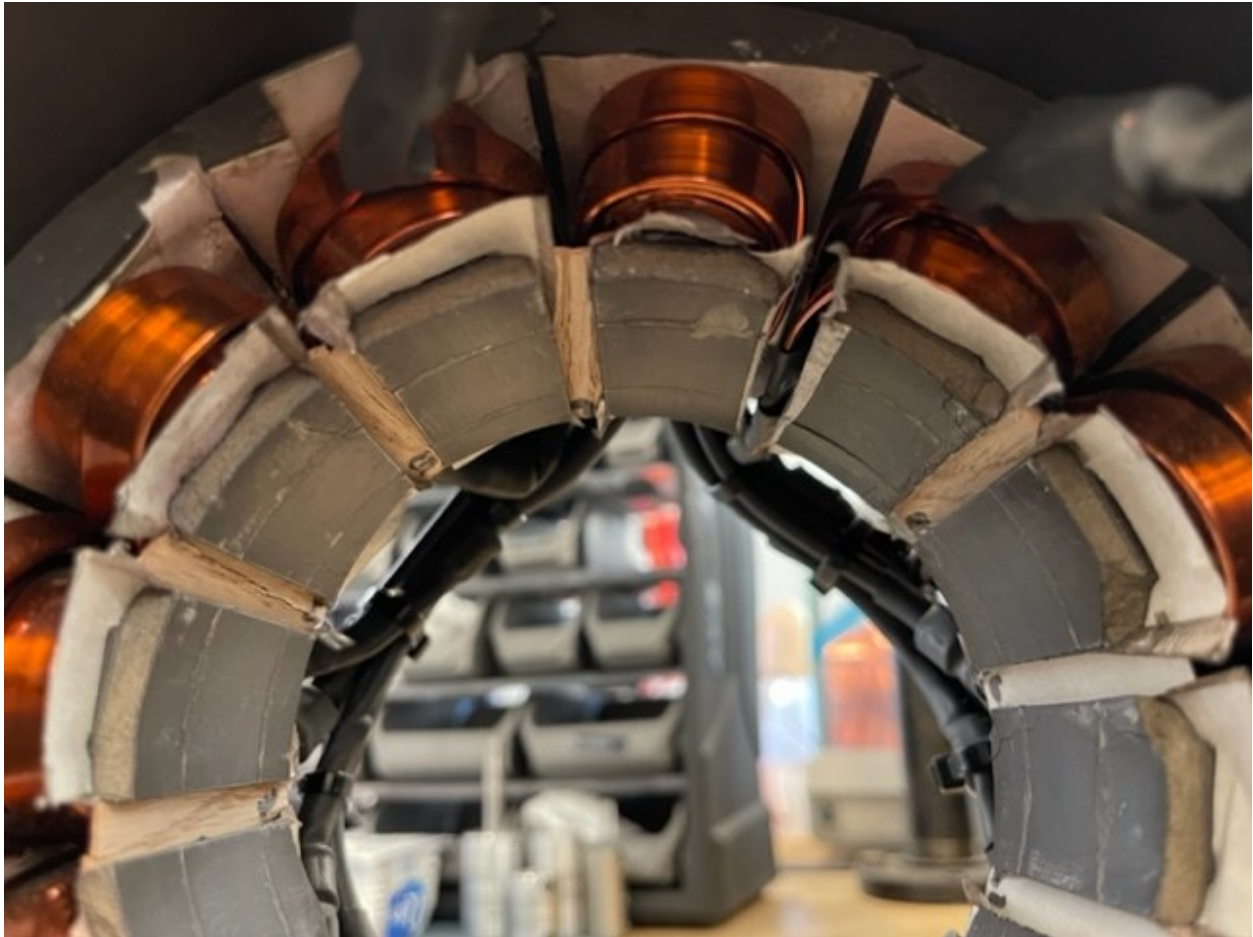
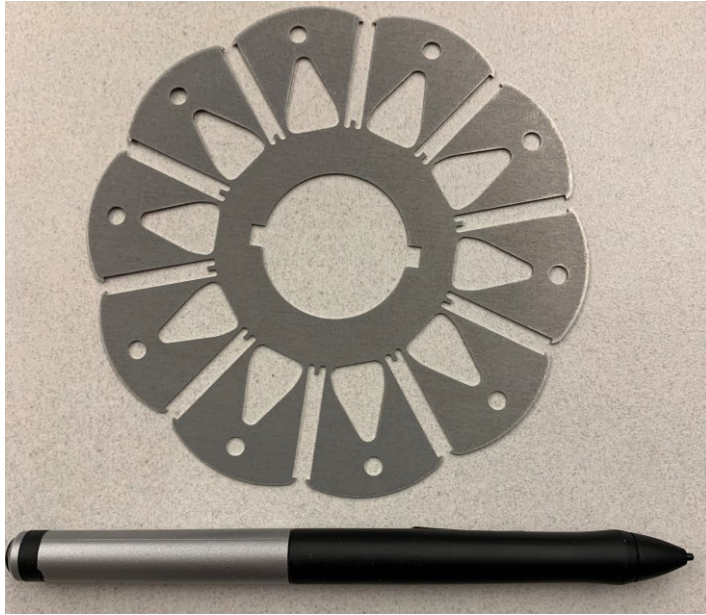


Fig. 7.9. SMC stator core is assembled and placed inside the motor frame with windings.

In Fig. 7.9, the stator core with windings is mounted inside a frame whose inner diameter is machined to match the stator's outer diameter. The winding is placed individually on each SMC tooth before the complete SMC stator is placed into the frame. The stack length of the frame is 125 mm, which is consistent with the motor's stack length. A spoke-type rotor is manufactured and assembled into the frame with the SMC stator core. The rotor is enclosed by end covers. Fig. 7.10(a) depicts the manufactured rotor lamination, while Fig. 7.10(b) shows the stacked rotor laminations with endplates, held together by a cleating rod. The magnets are then inserted into the rotor core laminations, which can be observed in Fig. 7.10(b). In addition, the figure depicts a shaft fitted into the rotor core with a bearing arrangement.



(a)



(b)

Fig. 7.10. Fabricated spoke type rotor (a) One piece of lamination (b) Stacked rotor laminations.

7.4. *Experimental validation*

The SMC motor is affixed to the test bench via mounting screws that are linked to the test bench. The motor's winding comprises two parallel paths with a total of 12 lead wires, including 3 phases. To connect it to the power supply, all neutral connections are shorted together, resulting in three lead wires. A high-speed coupling is connected between the torque transducer and the test motor. A torque transducer is connected to a display which shows the speed (RPM) and torque (N-m). The non driving end of the shaft is connected to an encoder which is connected to OPAL-RT to sense the speed of the motor. The dyno motor is supplied by a separate drive.

A. Phase Back EMF:

The spoke-type SMC motor's phase back EMF is measured. The phase back EMF is measured by simply rotating the motor using the dyno motor. The motor is rotated at six different speeds: 200, 500, 1000, 1500, 2500, and 3400 RPM, with the base speed of the motor being 3400 RPM. At each speed, the oscilloscope is connected to the motor terminal's three phases to record the phase back EMF. The test setup of the SMC motor for torque vs angle measurement is shown in Fig. 7.11.

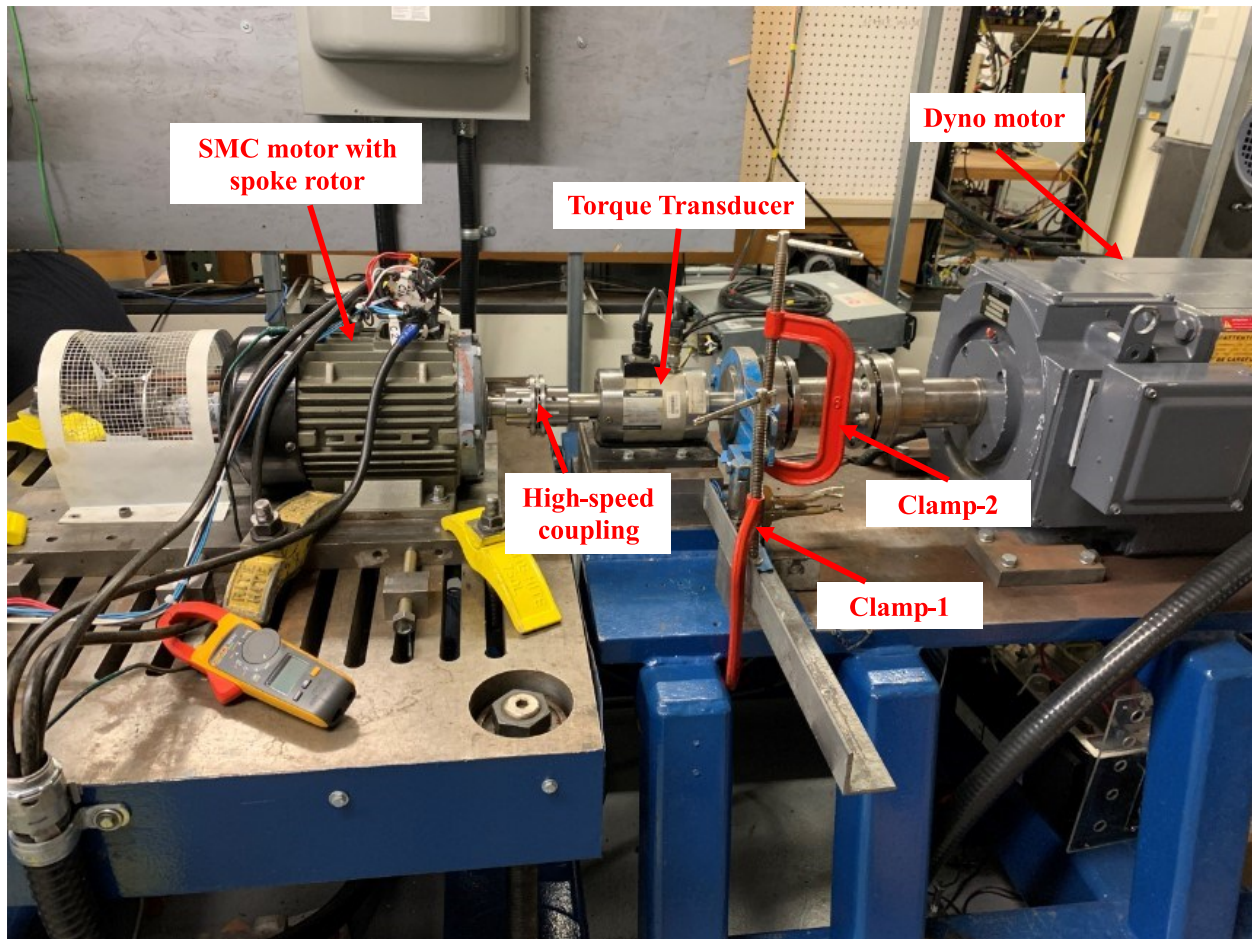


Fig. 7.11. Test setup for torque vs angle measurement

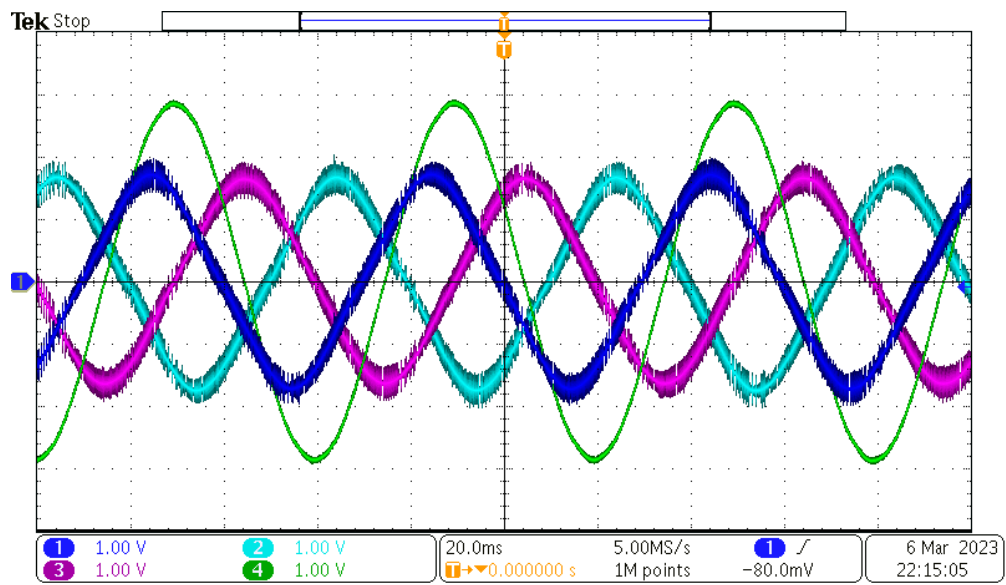


Fig. 7.12. Measured phase back EMF at 200 RPM. (Green Color is Line-Line)

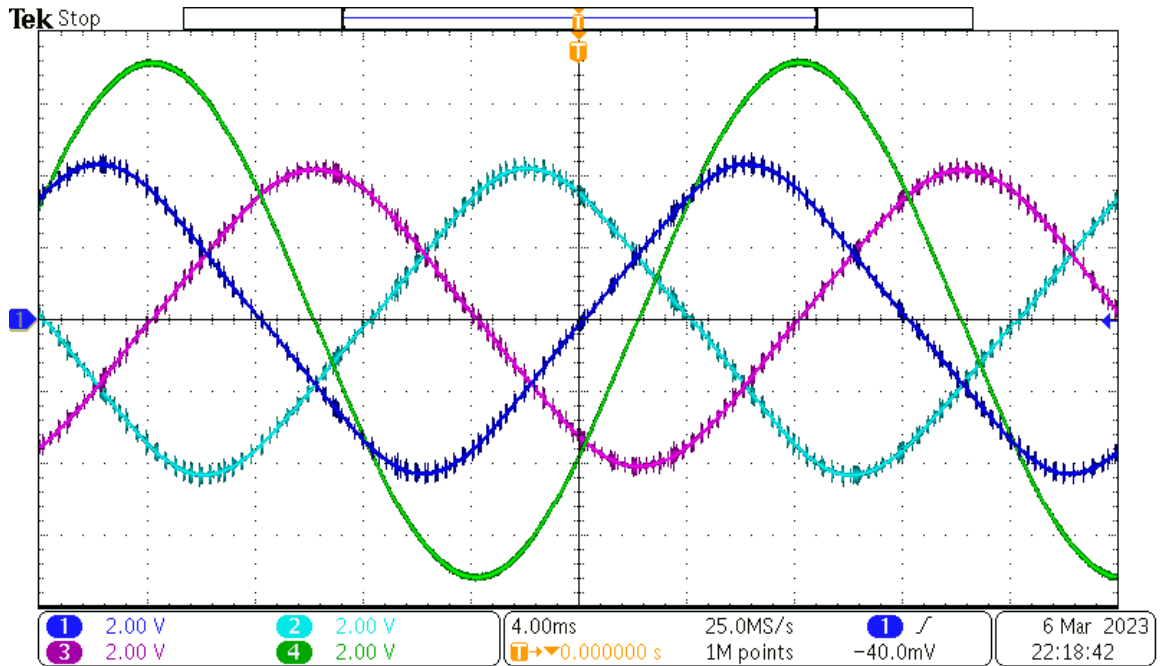


Fig. 7.13. Measured phase back EMF at 500 RPM. (Green Color is Line-Line)

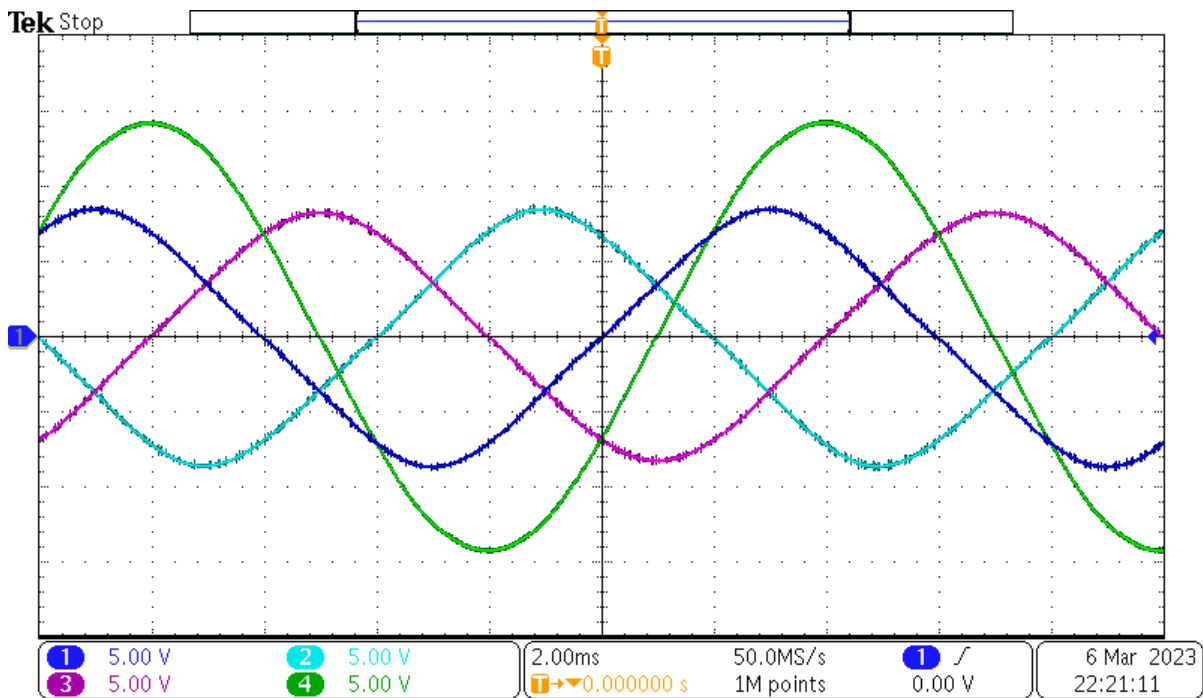


Fig. 7.14. Measured phase back EMF at 1000 RPM. (Green Color is Line-Line)

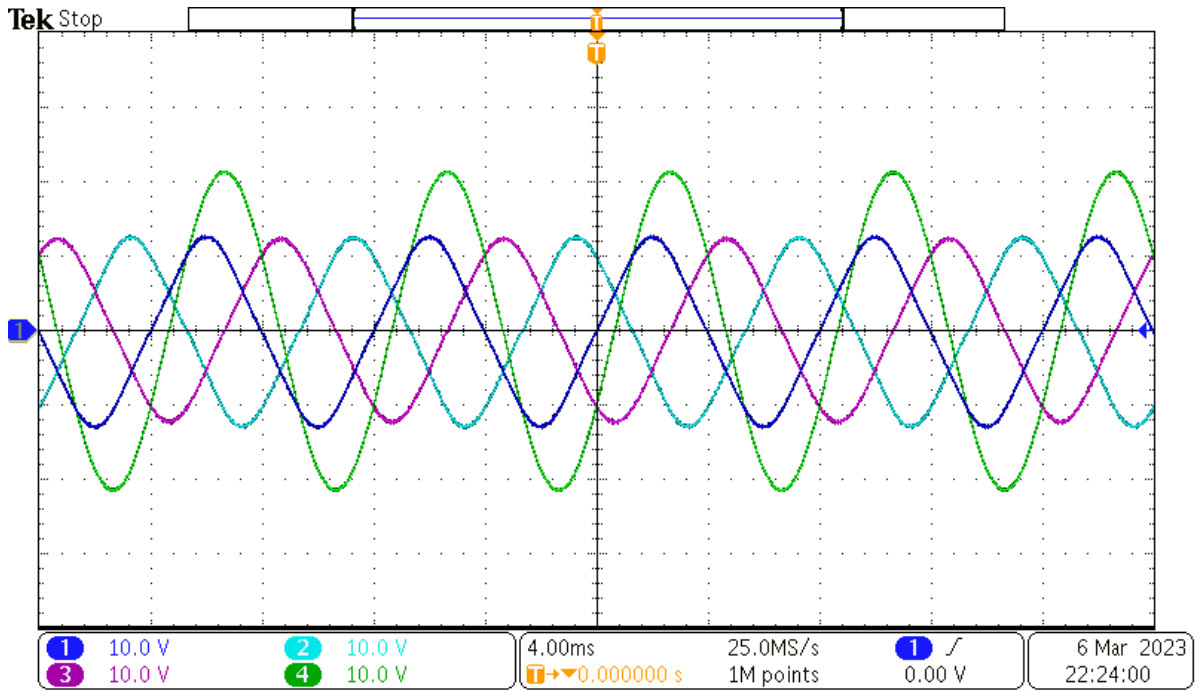


Fig. 7.15. Measured phase back EMF at 1500 RPM. (Green Color is Line-Line)

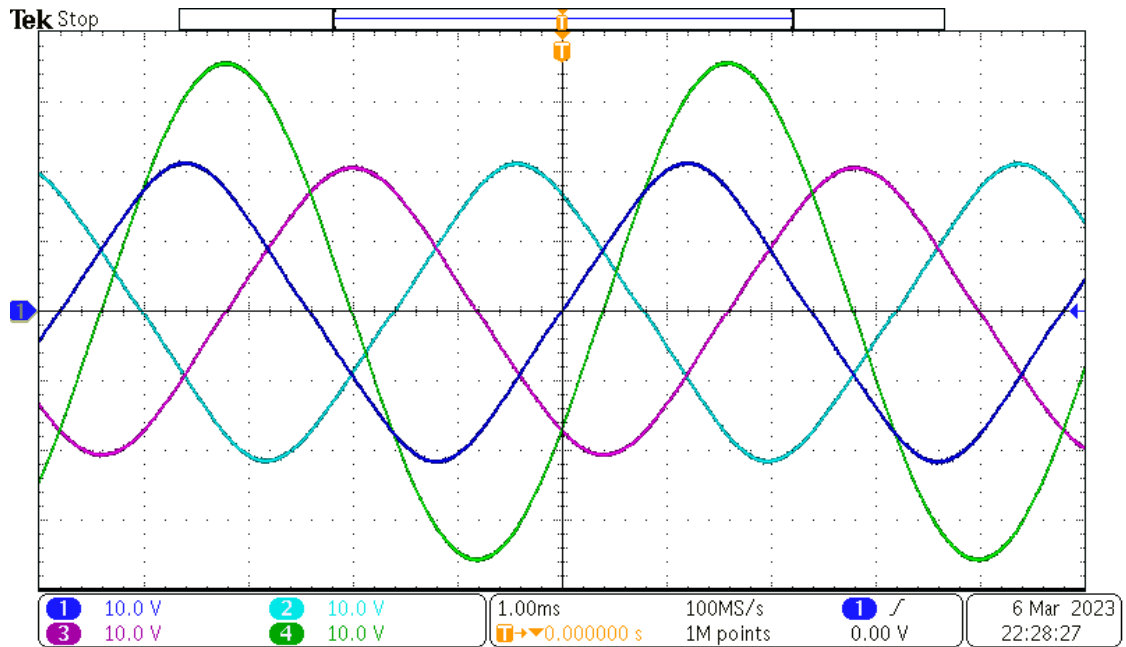


Fig. 7.16. Measured phase back EMF at 2500 RPM. (Green Color is Line-Line)

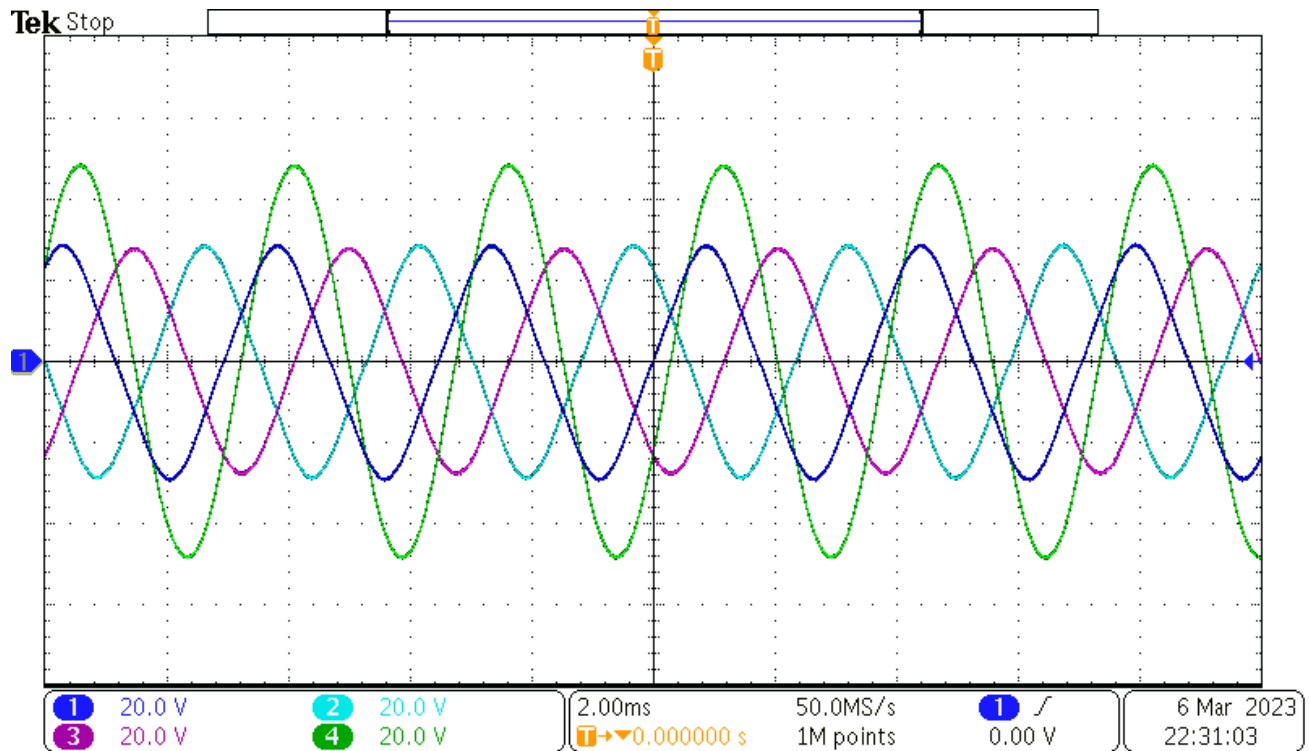


Fig. 7.17. Measured phase back EMF at 3400 RPM. (Green Color is Line-Line)

Table 7.1 Measured back-EMF vs RPM

Speed (RPM)	Back-EMF Peak Amplitude (V) (Phase to Neutral)
200	1.98
500	4.62
1000	8.73
1500	12.87
2500	21.5
3400	29.02 (FEA : 34)

Figs. 7.12 to 7.17 show the measured back EMF for different speeds. Table 7.1 shows the peak phase values of measured back EMF. Fig. 7.6 shows the phase back EMF for simulation and measurement. Table 7.2 shows the back EMF harmonics comparison between the simulation and the measurement. The measured phase back EMF peak value is lower than the simulation.

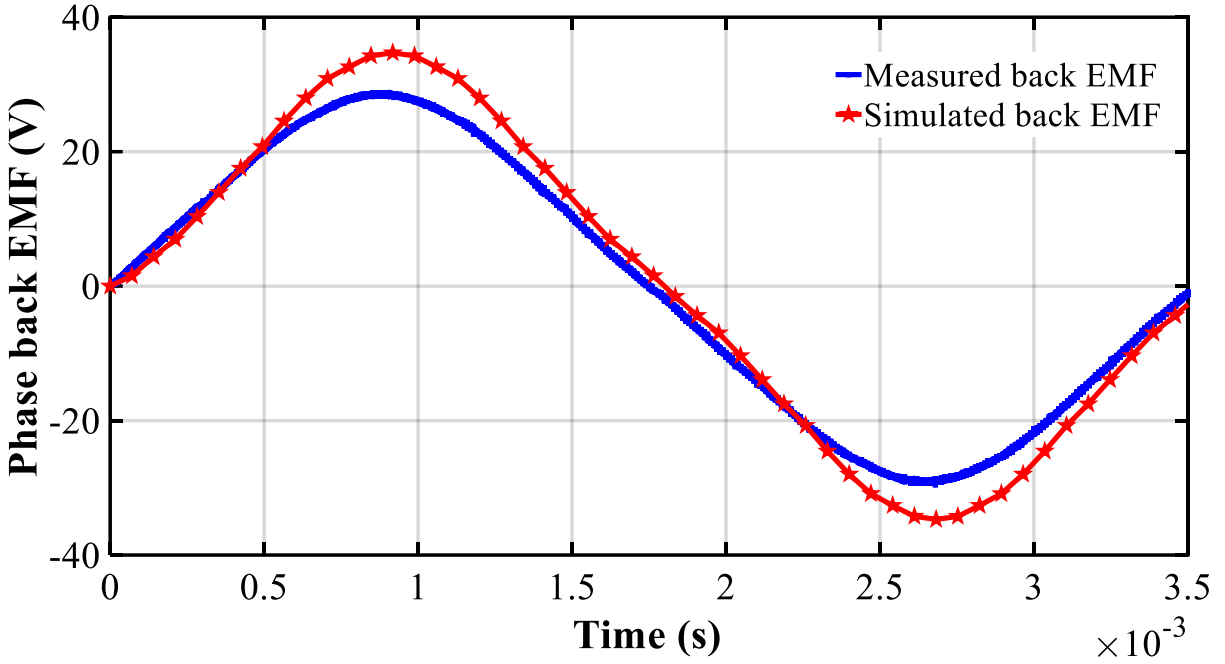


Fig. 7.18. Phase back EMF (Simulation Vs Measurement)

Table 7.2 Simulated Vs measured Back EMF

Back EMF Harmonic Order	Simulation	Measurement
Fundamental (V)	34.1	29.02
3 rd Order	2.93	1.68
5 th Order	0.07	0.04
7 th Order	0.08	0.05
9 th Order	0.07	0.04
11 th Order	0.06	0.1
13 th Order	0.15	0.01
15 th Order	0.05	0.01
17 th Order	0.04	0.01
THD (%)	8.64 %	5.80 %

The lower back EMF can be explained by several changes in the prototyping compared to the design. These include:

- The stator teeth experienced damage at the tooth ends, which would lead to an increase in reluctance and lowering of the air gap flux.
- The number of parallel strands in the winding for the prototype was one but two were used in the design.
- The SMC material performance in the prototype was not exactly the same as the one used in the design. The effect of lower density of the SMC prototype components and different manufacturing steps (machining) compared to traditional SMC components may have contributed to lower performance.

B. Torque angle measurement:

Fig. 7.11 shows the torque angle measurement setup. The rotor is locked at d-axis using two clamps. The current is fixed and then the torque angle is varied from 0 to 180 degrees with a step of 10 degrees. In this case, the speed of the motor is zero, so one phase has full current and the other two phases have half of the current. For each current, torque is measured for all the electrical degrees. Torque angle is measured for different current such as 15, 30, 45, 60, 75, 120, 150, 170 and 195 A.

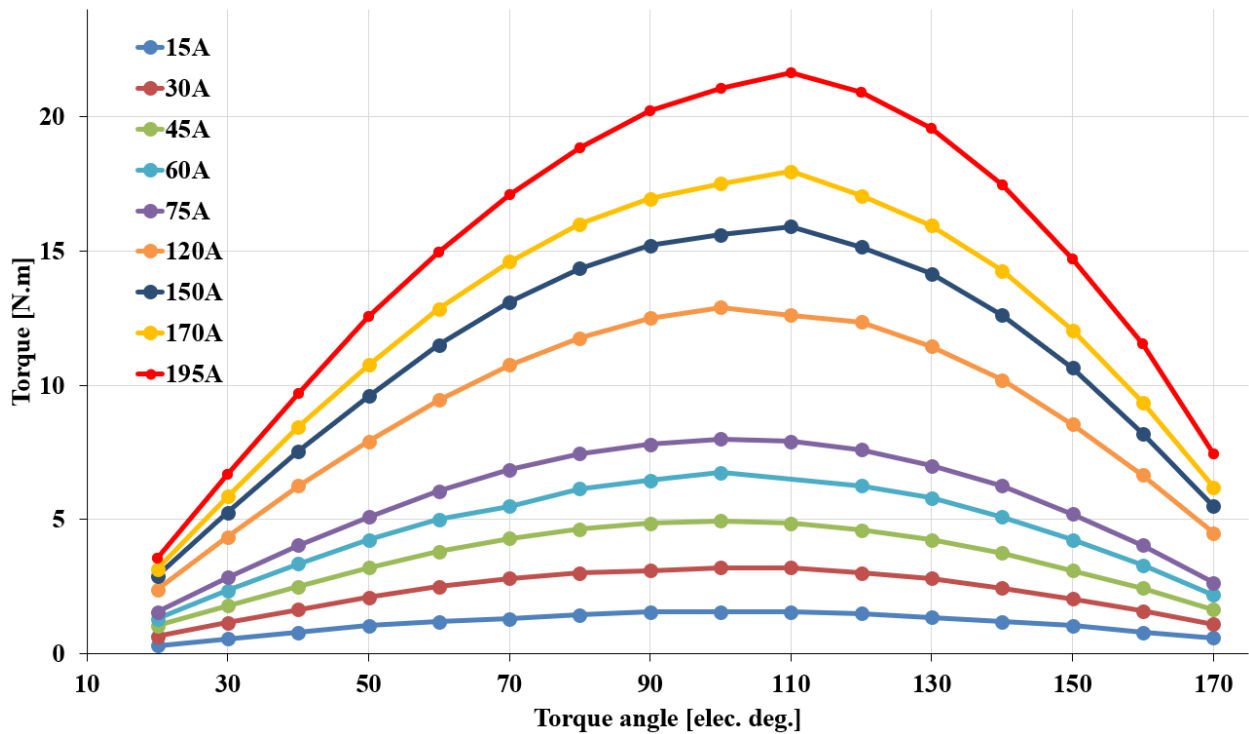


Fig. 7.19. Measured torque angle curve for SMC motor

C. Load Torque Measurement:

To measure the load torque of the motor, the test motor is loaded with a dyno motor, and the non-driving end of the test motor shaft is connected to a position encoder to track the rotor position. A high-current rating current probe is connected to the motor winding terminals to measure input current, and the test motor is driven by a high-current rating inverter using OPAL-RT and MATLAB. In MATLAB, the rotor position is monitored, and current is applied to the motor winding to measure electromagnetic torque. The torque angle is varied at each current to obtain the peak torque angle. The motor is tested at 500, 1000, 2000, and 3300 RPM, with 5 different current levels (50, 100, 130, 170, and 195 A) at each speed to evaluate torque performance. To begin testing, the test motor is rotated with the dyno motor without injecting current to the test motor. Both motors are set to a fixed speed of 500 RPM. The test motor current is then increased to 50 A, causing it to try and increase the speed of the dyno motor. However, as the dyno motor holds the test motor, its speed cannot increase, as a result of this action, torque of the test motor is measured using a torque transducer.



Fig. 7.20. Load torque measurement setup of SMC motor.

The same process is repeated for other speeds such as 1000, 2000, and 3300 RPM. Also, the current is increased varied to repeat the same process. Fig. 7.20 shows the load torque measurement setup of the SMC motor. Fig. 7.21 shows the measured load torque for different speeds and different current ratings.

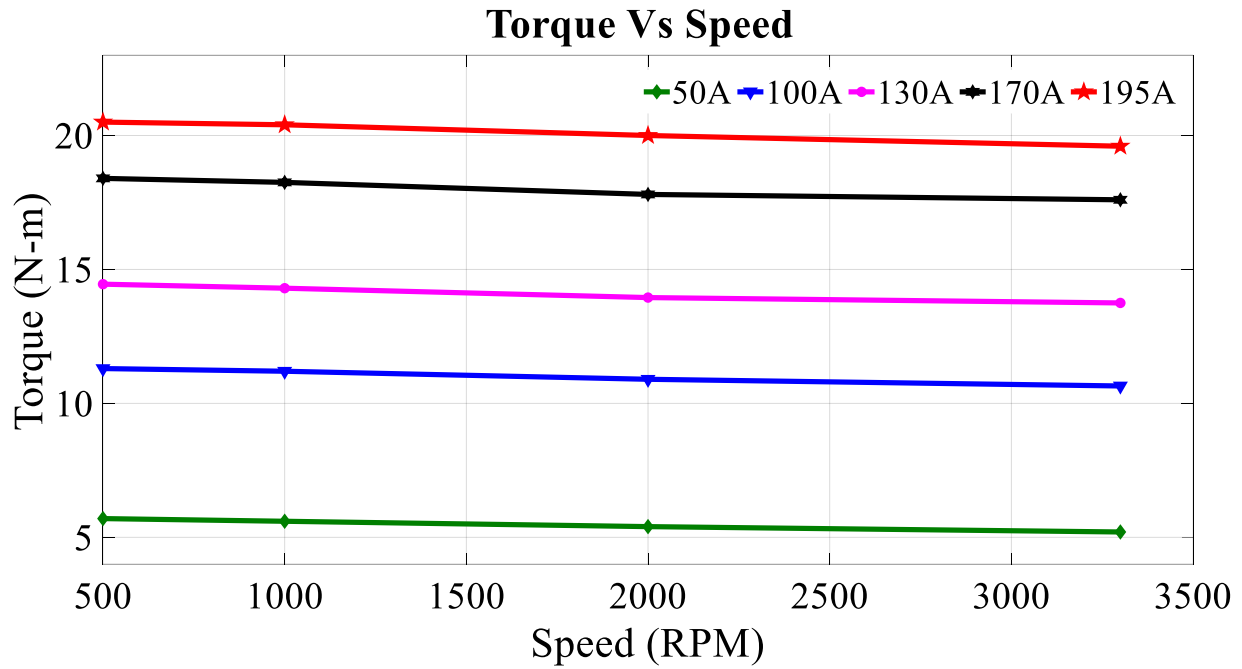


Fig. 7.21. Measured torque at various current and speed

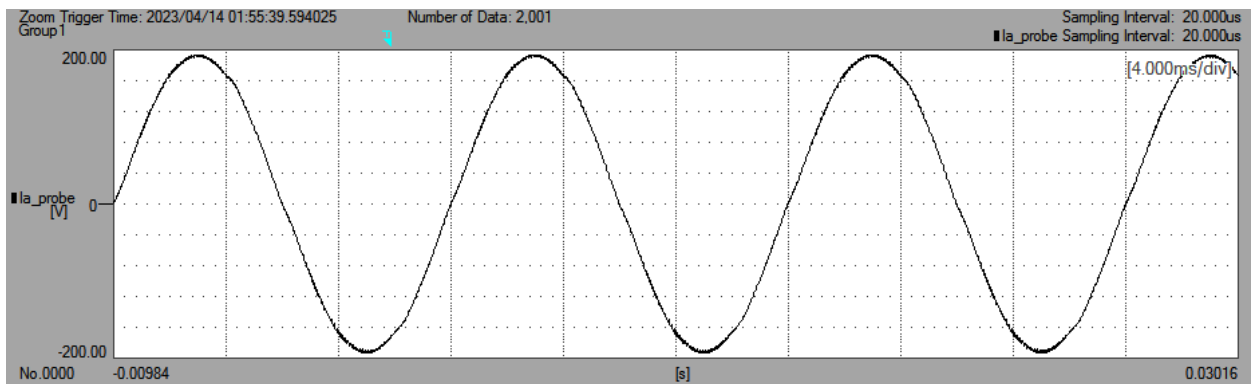


Fig. 7.22 Current waveforms at $I_s = 195$ A, 1000 rpm (83.33 Hz)

In the simulation the motor is designed to operate at a peak current of 170 A to produce 20 N-m torque. But in the measured results, the motor produces only 18 N-m torque for 170 A. Due to the reduction in phase back EMF, the peak current is increased from 170 A to 195 A to obtain the

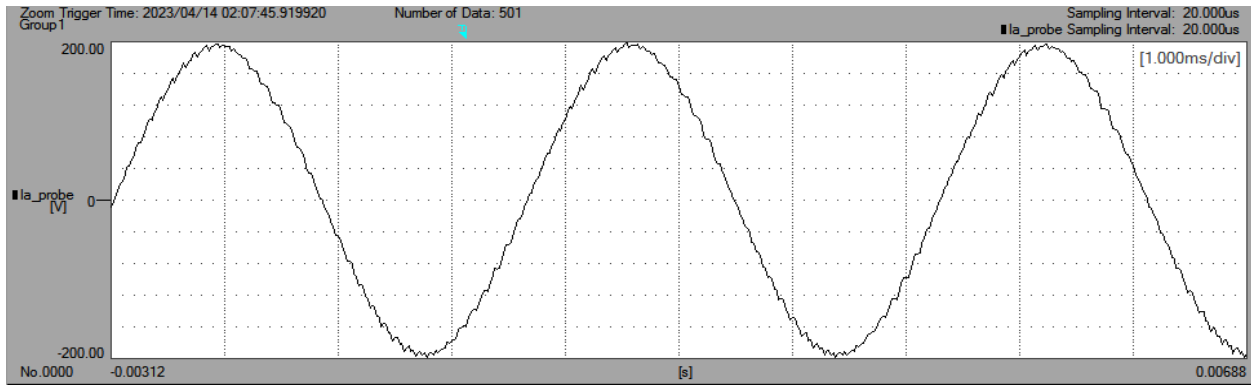


Fig. 7.23. Current waveforms at $I_s = 195$ A, 3300 rpm (275 Hz)

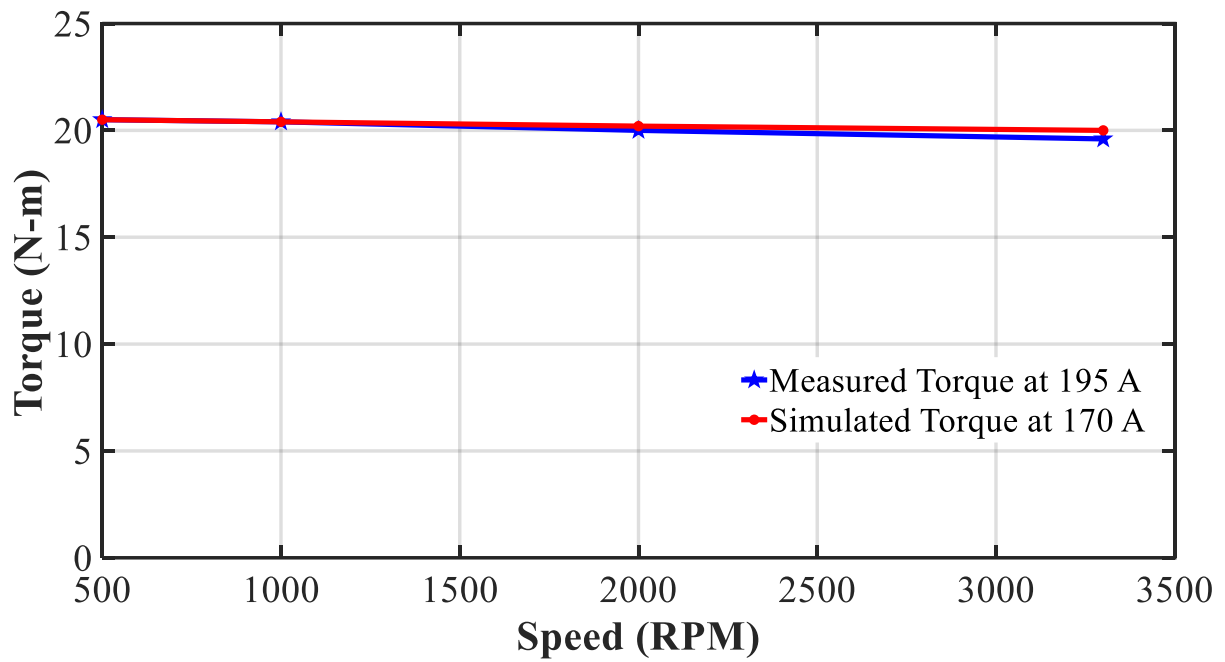


Fig. 7.24. Measured Torque vs Simulated Torque

required torque. Figs. 7.22 and 23 show the injected current waveform of the motor at 1000 and 3300 RPM. Fig. 7.24 shows the measured torque and simulated torque.

7.5. Phase resistance and copper loss calculation

The resistivity of copper is typically represented in units of ohm-meters ($\Omega \cdot m$). The standard resistivity of copper at room temperature (25°C) is approximately $1.68 \times 10^{-8} \Omega \cdot m$. The conductivity of copper is typically represented in units of Siemens per meter (S/m). The standard electrical conductivity of copper at room temperature (25°C) is approximately 5.96×10^7 S/m.

Given:

To calculate the copper loss, we need to determine the resistance of the copper conductor and then apply the power loss formula.

Given:

Resistivity of copper (ρ) = $1.68 \times 10^{-8} \Omega \cdot m$

Cross-sectional area of the copper conductor 8.36 mm^2 (or $8.36 \times 10^{-6} \text{ m}^2$)

Mean turn length (L) = 180 mm (or 0.18 meters)

First, we can calculate the resistance R_{phase} of the copper conductor using the formula:

$$R_{phase} = \frac{\rho * L}{A}$$

Calculating the expression: $R_{phase} \approx 3.62 \times 10^{-3} \Omega$ (or 3.62 milliohms)

Now, let's calculate the copper loss using the power loss formula:

Copper loss for one phase = $I^2 * R_{phase}$

Assuming an RMS current (I) of 120 A: Copper loss = $(120)^2 * 3.62 \times 10^{-3} \Omega$

Calculating the expression: Copper loss ≈ 52.224 watts

Therefore, with an RMS current of 120 A, the copper loss in the copper conductor is approximately 52.224 watts.

Copper loss for three phases = $52.224 \text{ watts} * 3$

Copper loss for three phases = 156.672 watts

7.6. Current density calculation

Current density (J) is defined as the current per unit area.

The formula for calculating current density is:

$$J = \frac{I}{A}$$

Where: J = Current density (A/m²) I = Total current flowing through the conductor (A) A = Cross-sectional area of the conductor (m²)

$$J = 137 \text{ A} / 8.36 \text{ mm}^2 = 16.38/2 = 8.19 \text{ A/mm}^2$$

So, the current density in this case would be 200 A/mm².

The initial design of the motor included two parallel strands and two parallel paths, with a conductor cross-sectional area of 16.8 mm². The copper fill factor was set at 60%, resulting in a current density of 4A/mm². However, during manufacturing, only one parallel strand was added instead of two. This reduction in the number of strands decreased the copper area, leading to an increase in the current density.

Inductance

The d-axis inductance can be calculated using the below formula,

$$L_d = \frac{\mu_0 * r_g * l_{eff}}{g} N_1^2 \frac{\pi}{3}$$

Where, L_d is d- axis inductance, r_g is the air gap radius, g is the air gap thickness, l_{eff} is the effective stack length, N₁ is the number of turns per coil.

Torque calculation

The torque equation of PMSM is given by

$$T_e = \frac{3}{2} * n_p [\lambda_m i_q + (L_d - L_q) i_d i_q]$$

Where, T_e is electromagnetic torque

n_p is number of pole pair

λ_m magnet flux linkage

i_q is q-axis current

L_d is d-axis inductance

L_q is q-axis inductance

i_d and i_q d and q axis current

From the phasor diagram of i_q and i_d we have $i_q = i_s \sin \delta$, and $i_d = i_s \cos \delta$

From the above equations $i_q * i_d = i_s^2 \sin \delta \cos \delta = \frac{i_s^2}{2} \sin 2\delta$

To find the δ (advance angle) value differentiation the torque equation and equate to zero:

For the maximum torque $\frac{dt}{d\delta} = 0$

Differentiating the above torque equation we get,

$$\lambda_{af} i_s \cos \delta + (L_d - L_q) \frac{i_s^2}{2} (\cos 2\delta) * 2 = 0$$

Simplifying the above equation, $\lambda_{af} \cos \delta + (L_d - L_q) i_s (\cos 2\delta) = 0$

$$\cos 2\delta = (2 \cos^2 \delta - 1)$$

$$\lambda_{af} \cos \delta + (L_d - L_q) i_s (2 \cos^2 \delta - 1) = 0$$

$$\lambda_{af} \cos \delta + (L_d - L_q) i_s 2 \cos^2 \delta - (L_d - L_q) i_s = 0$$

Rearranging in quadratic form we can write,

$$2 \cos^2 \delta (L_d - L_q) i_s + \lambda_{af} \cos \delta - (L_d - L_q) i_s = 0$$

$$\cos \delta = \frac{-\lambda_{af} + \sqrt{\lambda_{af}^2 + 8i_s^2 (L_d - L_q)^2}}{4i_s(L_d - L_q)}$$

7.7. Simulation Vs Measurement

The torque angle curves are plotted for the different current levels. The torque is plotted by calculating analytically with the L_d and L_q and flux linkage measured from FEA package.

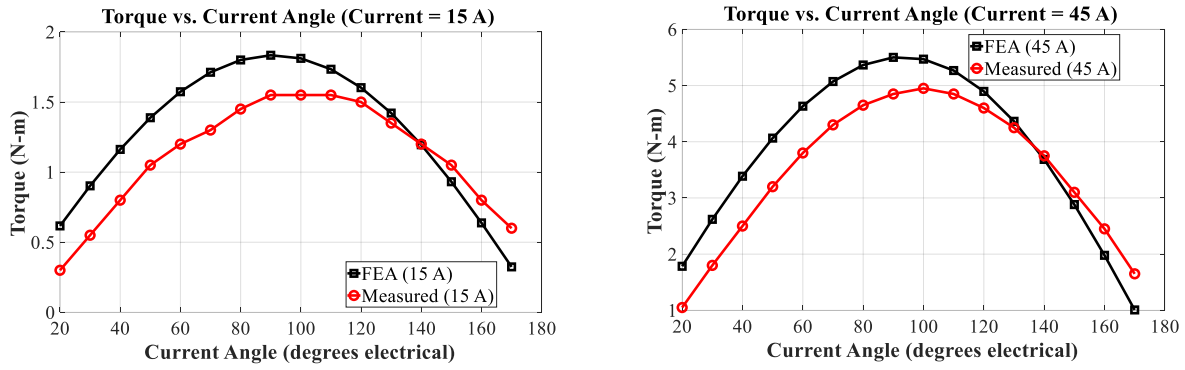


Fig.7.25. Simulated Vs Measured Torque angle curves at (Left) 15 A and (Right) 45 A

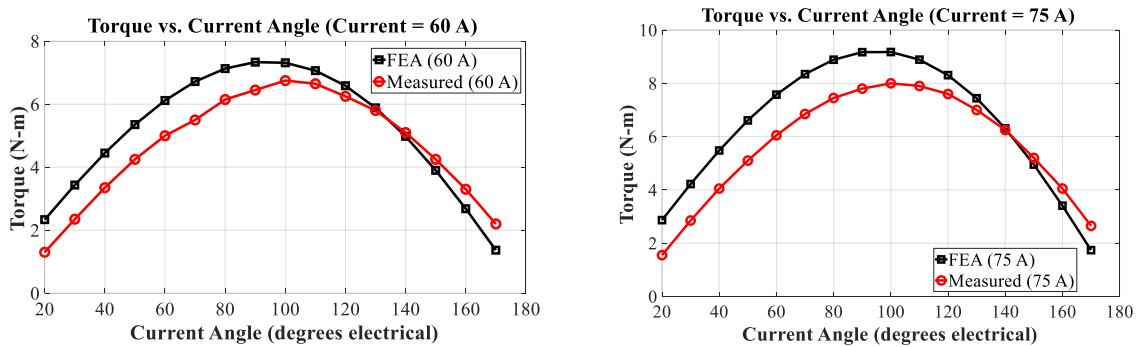


Fig. 7.26. Simulated Vs Measured Torque angle curves at (Left) 60 A and (Right) 75 A

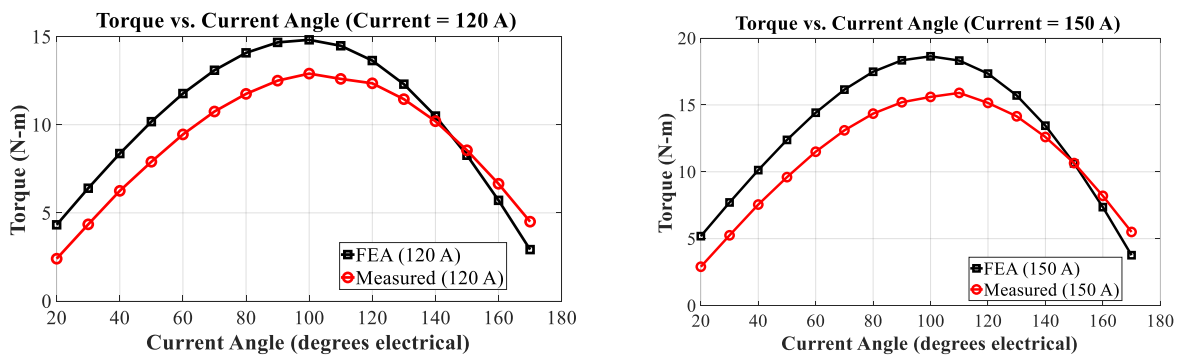


Fig. 7.27. Simulated Vs Measured Torque angle curves at (Left) 120 A and (Right) 150

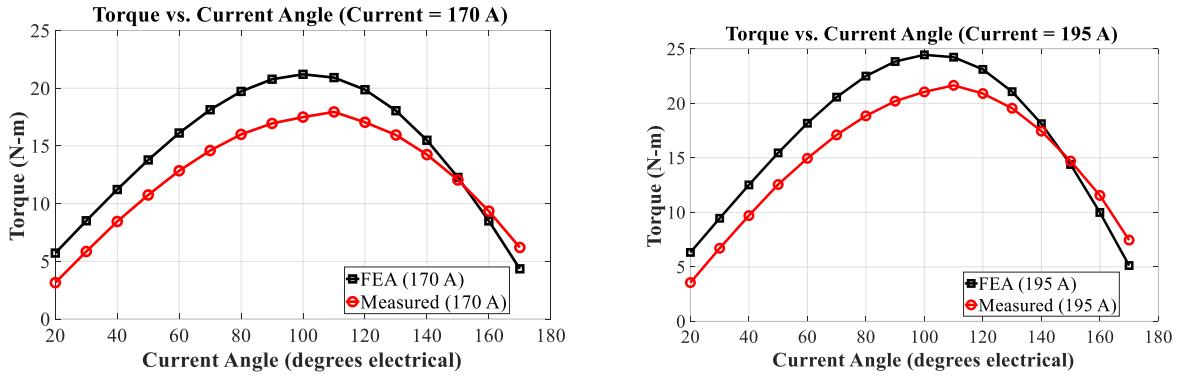


Fig. 7.28. Simulated Vs Measured Torque angle curves at (Left) 170 A and (Right) 195 A

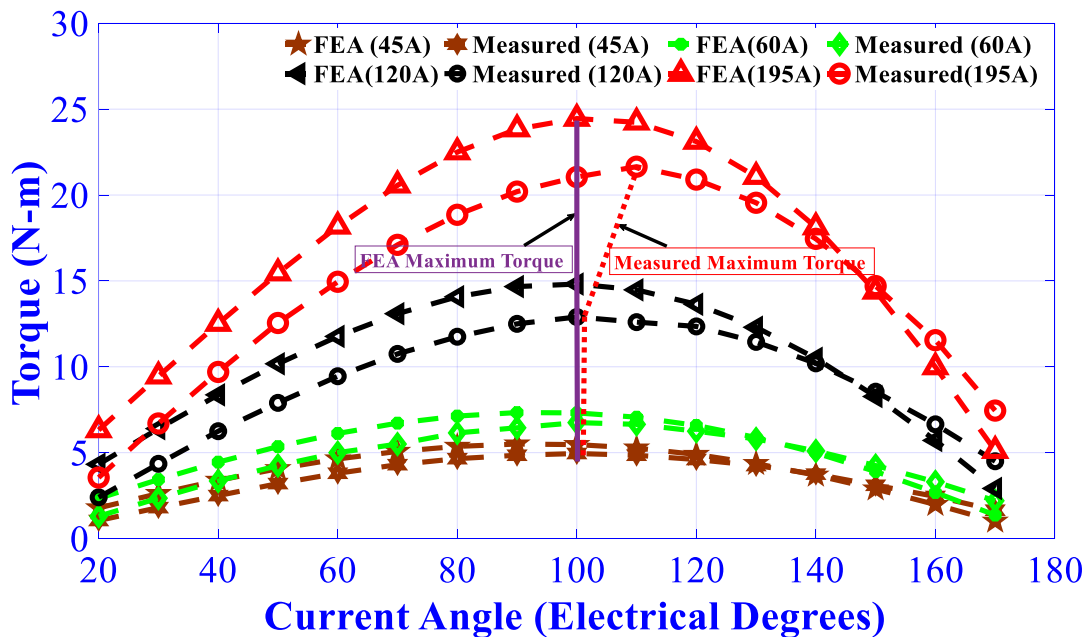


Fig. 7.29. Simulated Vs Measured Torque angle curves at 45A, 60A, 120A and 195 A

Figure 7.25 to 7.29 display the torque angle for different current levels, including 15A, 45A, 60A, 75A, 120A, 150A, 170A, and 195A. These figures illustrate the relationship between the torque and the current angle. In Figure B5, the torque angles for four specific current levels, namely 45A, 60A, 120A, and 195A, are compared. The simulation results show that the maximum torque occurs at a current angle of 100 degrees electrical. However, in the measured data, the maximum torque angle is shifted from 100 degrees to 110 degrees at higher current levels. The measured torque values are lower than the simulated values by approximately 10%.

7.8. Comparison of Simulation and measurement results with and without tooth tip:

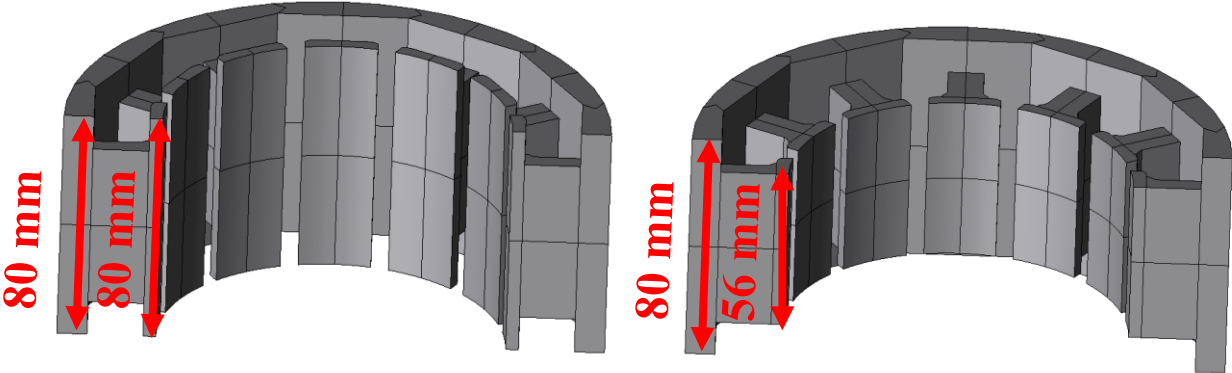


Fig. 7.30. SMC stator (Left) tooth tip length same as back iron length (Right) tooth tip length same as tooth body length.

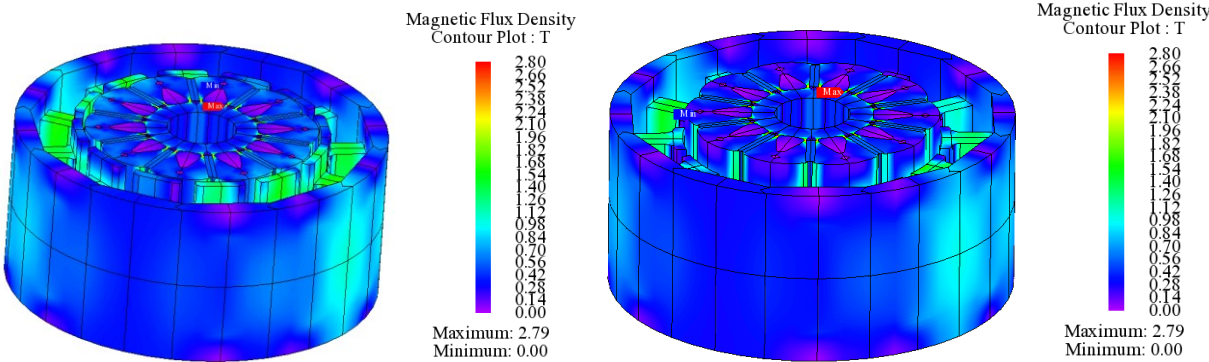


Fig. 7.31. SMC stator (Left) tooth tip length same as back iron length (Right) tooth tip length same as tooth body length.

Fig. C1 shows the SMC stator design for two different cases, with tooth tip same as the back iron length in the left side, and right side shows the SMC stator with tooth tip length same as tooth body length. Fig. C2 shows the flux density plot for the figure C1. Both the machines are analysed with the same current. This simulation will be helpful to understand the effect of tooth tip length on the electromagnetic torque.

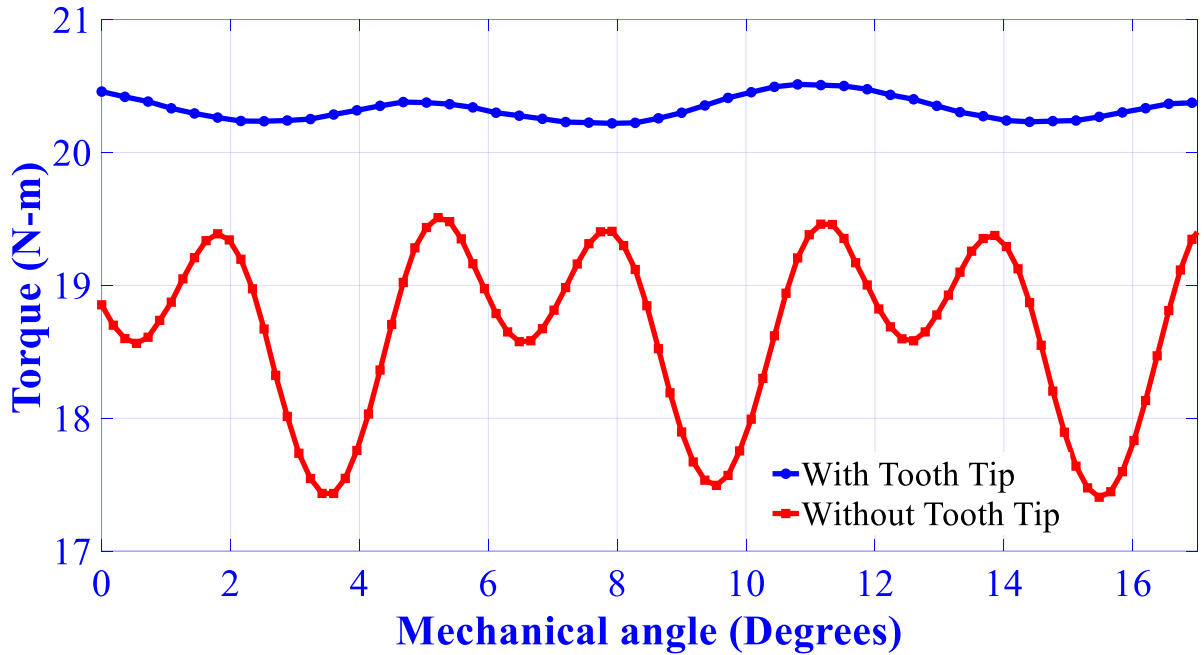


Fig. 7.32. Electromagnetic torque of SMC stator with tooth tip and without tooth tip

Table 7.3: Simulated torque components

Item	With tooth tip	Without tooth tip
Average torque	20.3 N-m	18.6 N-m

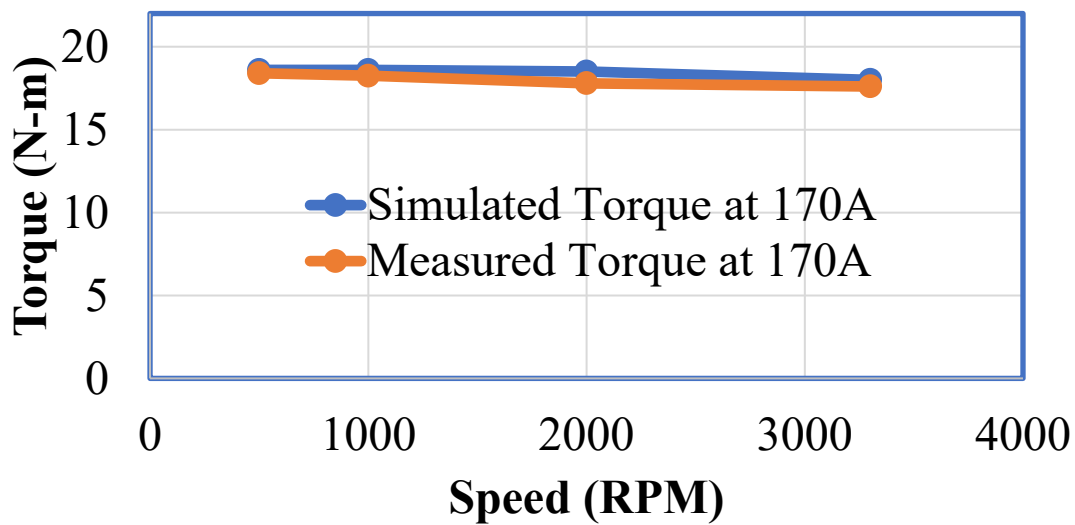


Fig. 7.33. Simulated Vs Measured torque comparison without tooth tip

Table 7.4: Simulated Vs Measured torque and phase back EMF components

Item	Without tooth tip (Simulation)	Without tooth tip (Measured)
Average torque (N-m)	18.6	18.2
Phase back EMF (Peak) (V)	30.0	29.5

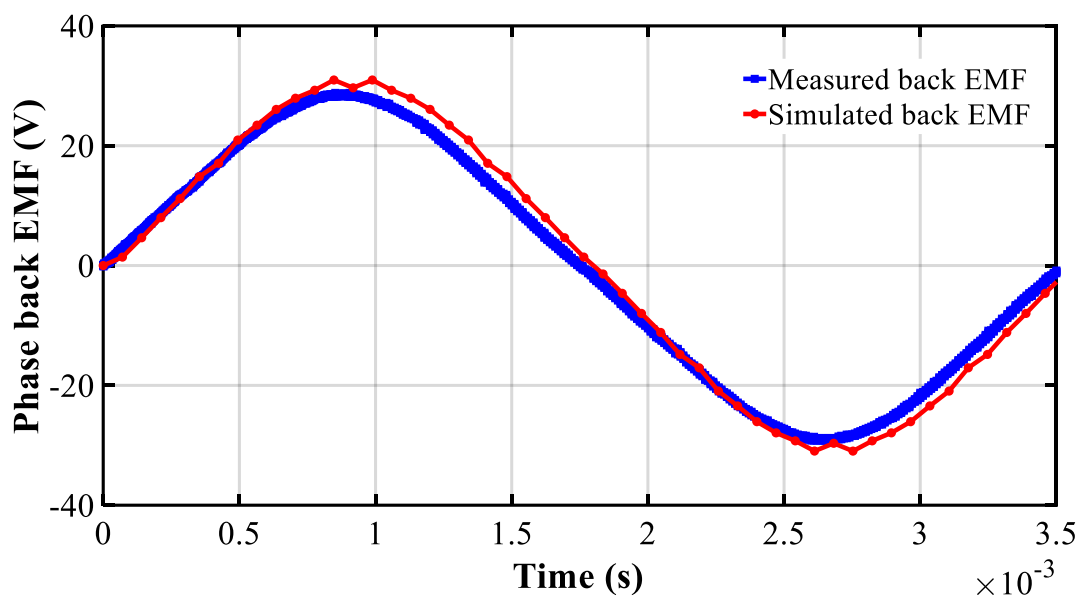


Fig. 7.34. Simulated Vs Measured phase back EMF comparison without tooth tip

Fig. 7.32 shows the electromagnetic torque of both the stator designs with and without tooth tip. It's evident that the SMC stator without tooth tip has 10% lower average torque than the SMC stator with tooth tip. This analysis proves the effectiveness of the tooth tip in terms of electromagnetic performances. Fig. 7.33 shows the comparison of simulated torque and measured torque with tooth tip as same length of the tooth body. In this case both the simulation and measured results are found to be very close. Fig. 7.34 shows the comparison of measured and simulated back EMF without tooth tip. The measured and simulated results are found to be very closer.

7.9. Conclusion

The design, simulation, prototyping and testing of SMC stator core with spoke type is presented in this chapter. Various SMC tooth designs are considered. SMC tooth design is finalized after considering the mechanical, electromagnetic, and manufacturing constraints. The rotor design is finalized based on the analysis carried out in the previous chapters which includes electromagnetic and mechanical stress analysis. The rotor is fabricated with NdFeB magnets.

The measured back EMF is 14.7 % lower than the simulated back EMF, which is due to the following reasons,

- The stator teeth experienced damage at the tooth ends, which would lead to an increase in reluctance and lowering of the air gap flux.
- The number of parallel strands in the winding for the prototype was one but two were used in the design.
- The SMC material performance in the prototype was not exactly the same as the one used in the design. The effect of lower density of the SMC prototype components and different manufacturing steps (machining) compared to traditional SMC components may have contributed to lower performance.

The prototyping and assembly of the SMC parts was challenging:

- Damage was observed on ends of the stator teeth, perhaps due to low mechanical strength of the SMC components, but also during shipping. The mechanical strength can be improved.

The motor produces 18 N-m for 170 A peak current which is 10 % lower than the simulated torque. However, the current is increased to 195 A to obtain the required torque. A novel spoke-type PMSM with a newly developed SMC grade from RTMP was designed, built and tested successfully. The designed SMC motor has a 20 % higher torque density in terms of motor volume than a simulated laminated stator motor for the same specification, assuming natural convection.

However, because of prototyping differences the prototyped motor produced 90% of torque relative to the design.

This study suggests that the SMC stator cores can be utilized to improve the torque density, copper fill factor and allows a 3D flux path. Development of the SMC powder quality is continuing in many industries to address the remaining challenges that could limit the development of the motors with SMC materials.

CHAPTER – 8

Conclusions and Future Work

The aim of this thesis was to create an affordable traction motor that utilizes a stator core made of soft magnetic composite and permanent magnets, while also enhancing its electromagnetic performance by rotor pole shaping without having to skew either the rotor or stator.

8.1. Conclusion

Chapter 1

This chapter introduces electric motors and provides an overview of various types of permanent magnet synchronous motors (PMSM). It also summarizes the types of motors used in modern electric vehicles and concludes that the majority of traction vehicles use PMSM motors, with interior PMSM motors being the most commonly utilized type.

Additionally, it provides a summary of the materials used for the stator and rotor core laminations, along with a concise explanation of the advantages of using soft magnetic composite (SMC) material. This chapter also discusses the characteristics of cold spray magnet and its advantages in designing permanent magnet synchronous motors (PMSM).

Chapter 2

In this chapter, a radial flux outer rotor PMSM is designed and compared with laminated steel (M36 26Ga) and SMC. The iron loss is reduced 32% with SMC core when it is operated at the maximum speed. The efficiency is found to be 6.5% increased with the SMC core at the maximum speed of 10,000 rpm. SMC has other advantages such as 3D flux path, less wastage of materials, higher fill factor.

The two winding techniques have been analyzed with the SMC core. The concentrated winding in design 2 with fractional SPP is found to be better in the flux weakening mode. The

difference between the flux linkage and the product of d-axis inductance and current is found to be 2 % in the concentrated winding and 45 % in the distributed winding. The lower difference in the concentrated winding makes it best suitable for traction applications.

Chapter 3

The commercial motors such as BMW i3 and Honda Accord were benchmarked and it conclude that the stator fill factor is the key element to improve the performance of the motor by reducing the copper loss of the motor.

Also, this chapter focuses on comparing the SMC and laminated steel stator core for higher pole and lower pole numbers. The SMC stator core with higher pole numbers exhibits lower iron losses at the maximum operating speed. BMWi3 rotor is utilized for the Twizy motor designs with commercial magnet and coldspray magnet. 48-slot/8-pole and 12-slot/8-pole designs are analysed with the scale down model of BMW i3 rotor design. Concentrated winding designs always performs better in the flux weakening region. However, 48-slot/8-pole distributed winding designed using coldspray magnet with a scallop design performs good in the flux weakening mode, its due to that fact that the coldspray magnet is a less B_r magnet.

In the 12-slot/8-pole configurations, three different designs are analysed. Initial 12-slot/8-pole design, 2nd design with modified stator tip thickness and sine rotor air barrier, and 3rd design with closed and open slots. In all these three designs coldspray rotors are analysed with cobra shaped magnet design. Also, for all the cases, the comparison has been done with the laminated stator and SMC stator for 12 slots 8 poles with the commercial PM and cold spray PM. The SMC stator is always simulated with a 60% fill factor. The torque density in terms of motor volume is the key parameter to define motor performance. The SMC stator has a higher torque density when compared to the laminated stator utilizing the manufacturing technique. The cobra shaped PM motor utilizes the cold spray technique to spray as a single structure without the need for two pieces of arc magnets, which increases the complexity of the mass production for traction applications. Also, this chapter concludes that 12-slot/8-pole will have higher torque ripple.

Chapter 4

A comparison between the 12-slot/8-pole and 12-slot/10-pole with conventional spoke type rotor is presented. The phase back EMF THD of the 12-slot/10-pole design is reduced by 10% from the 12-slot/8-pole design. The torque ripple with the 12-slot/10-pole design is reduced by 81 % from the 12-slot/8-pole design. The peak cogging torque with the 12-slot/10-pole design is reduced by 97% from the 12-slot/8-pole design.

Also, this chapter compares a 12-slot/10-pole conventional spoke type rotor with the 12-slot/10-pole cobra-shaped spoke type rotor. In 3-D FEA torque ripple with the cobra rotor is 66% reduced from the conventional rotor. The phase back-EMF THD of the cobra rotor is 28% reduced from the conventional rotor.

Cobra-shaped spoke type rotor is compared with the laminated stator and the SMC stator. The copper loss is 19 % reduced in the SMC stator. Efficiency maps are plotted for laminated stator and SMC stator for a maximum speed of 10000 rpm. Mechanical stress analysis has been performed for a cobra rotor at 10000 rpm. The torque density in terms of motor volume is 23 % increased in SMC stator core with cobra rotor. The optimal flux weakening equation is equated by 97% between the flux linkage and the product of d-axis inductance & current.

Finally, optimization has been carried out to select the best parameters. With the optimization technique the torque ripple is increased, however the average torque is increased by 3% from the previous design. Also, this optimization proves that the selected design is a better candidate.

Chapter 5

This chapter compares seven different PMSM designs. Three FEA packages have been used for the analysis: Simcenter MotorSolve 2D, Ansys Motor-CAD 2D and JMAG Designer 3D. Firstly, a spoke type rotor PMSM has been designed and analysed with different slot/pole combinations such as 12-slot/4-pole, 36-slot/6-pole, 12-slot/8-pole and 12-slot/10-pole. The different slot/pole combinations are analyzed without skewing the rotor or stator. Air gap flux density, phase back EMF, cogging torque, losses, and efficiency maps are plotted for all the slot/pole configurations. Though the iron losses and efficiency are better for the lower slot/pole combinations, the electromagnetic torque ripple and peak-peak cogging torque values are found

to be higher. Also, traction motors need to be operated in the flux weakening regions, it can be stated that the higher pole configurations such as 12-slot/10-pole are better for flux weakening and wide speed range. From this analysis 12-slot/10-pole configuration is chosen as a best candidate for high-speed traction applications. Key results of the analysis are depicted below.

2) The selected 12-slot/10-pole configuration is called Design-1, two other rotor designs are considered. Design-2 has a novel barrier which completely eliminates the need for the hub arrangement. Along with the novel barrier Design-3 has a rotor pole shape which reduces the electromagnetic torque ripple and cogging torque, both an optimization and a sensitivity analysis were utilized to determine the parameters of Design-3. The peak-peak cogging torque with Design-3 is 91.29% reduced from Design-1. The average torque and power rating is maintained the same for all the three rotor designs. The torque ripple with Design-3 is 80.59 % reduced from Design-1. The electromagnetic torque ripple and the cogging torque are significantly reduced in Design 3. Design -3 with the laminated stator is selected for further analysis with the SMC stator core design.

2) Design-3 rotor is scaled up and analyzed with a Toyota Prius stator core and Honda Accord stator core to prove the effectiveness of the proposed rotor design. The torque with the Honda Accord stator and Design-3 rotor is 17 % higher than the original Honda Accord motor for the same magnet mass. A cost comparison between the baseline Toyota Prius motor and the proposed rotor design with SMC material has been presented. It proves that the overall cost of SMC motor is cheaper than the baseline motor. This proves the effectiveness of the proposed rotor design.

Chapter 6

This chapter compares three different SMC materials (A, B & C) with different permeability and resistivity values for a same machine specifications. Though the hysteresis loss is lower in SMC-C it has higher eddy current loss when compared to the SMC-A & B. The magnet loss, mechanical loss, and copper loss have been calculated for all the three SMC based designs using 3D FEA along with iron loss calculations. Efficiency maps are plotted for all three SMC based designs for a maximum speed range of 10000 rpm. SMC-B has the highest efficiency of 95.0 % at the rated speed (3400 rpm) and 91.46% at the maximum speed (10000 rpm). SMC-B material is chosen to be the best material when compared to the SMC- A & C.

After selecting the best SMC material, it's compared with a laminated silicon steel stator design for the same specifications. The copper loss with SMC – B stator is reduced by 26.12% from the laminated steel stator design. The torque density in SMC-B stator is improved by 15 % from the laminated stator design. The core loss of the SMC-B material is tested using a toroid tester.

Two higher pole designs such as 24-slot/16-pole and 36-slot/30-pole has been analyzed with a laminated stator and SMC stator. Iron loss at 10000 rpm for 24-slot-16-pole with laminated stator is 1.7 times higher than the SMC stator design. Iron loss at 10000 rpm for 36-slot/30-pole with a laminated stator is 2.2 times higher than the SMC stator design. This proves that the SMC stator design is a better candidate than the laminated design to operate at higher frequencies. The tooth body length SMC_B stator design is varied from 36 to 56 mm. 56 mm tooth body length is proved to have higher average torque, and lesser harmonics in the phase back EMF. The average torque with the SMC stator with no back iron is 2% lower than the design with the back iron

Design-3 (3D) with the laminated stator is analyzed with a 3D analysis with the end winding overhang. Design-3(3D) is called a laminated stator design and Design-4 is called the SMC stator design. The tooth body of the SMC stator is reduced on both sides to hold the end winding within the stack height. The laminated stator design has a copper fill factor of 40% and the SMC stator design has a copper fill factor of 60%. The copper loss with the SMC stator design is 13.67% lower than for the laminated stator design. The total iron loss at rated speed (3400 rpm) with the SMC stator design is increased 31.05 % from the laminated stator design. The total iron loss at the maximum speed (10000 rpm) with the SMC stator design is increased 6.86% from the laminated stator design. The overall efficiency of the laminated stator design at the rated speed is 97% and the SMC stator is 96%. But the torque density of the SMC stator is increased 20% from the laminated stator with the help of compacted end windings and 3D flux paths.

A 3D Thermal analysis has been performed for the SMC stator design which shows that the thermal values are within the limit for a natural convection motor.

The temperature of Design-3 (Laminated stator) is lower than Design-4 (SMC stator). A case study is performed at different current values to equate the losses of both motors to the same temperature.

The laminated motor with higher current is called Design-5(Laminated stator). Design-5 (Laminated stator) reaches the same temperature of Design-4 (SMC stator) at an RMS current of 119 A. At this point, Design-5 (Laminated stator) produces higher torque than the SMC motor by 7.77 %. However, the torque density in terms of motor volume is higher in the SMC motor by 9.31% with the help of compacted end winding. A cost comparison between the laminated motor and SMC motor has been presented which clearly indicates that the SMC motor is lower cost than the laminated stator. The magnet losses with four axial segments are 50% lower than that for the magnet with zero segments. 80% of the flux weakening conditions are satisfied to achieve a wide flux weakening up to 10000 rpm.

Stator stress is reduced by 50% for SMC stator core with a fillet of radius 2mm at the tooth body. Mechanical stress analysis has been performed for the rotor: 70 MPa is the maximum stress value for a maximum speed of 10000 rpm. This study suggests that the SMC stator cores can be utilized to improve the torque density, copper fill factor and allows a 3D flux path.

Chapter 7

The design, simulation, prototyping and testing of SMC stator core with spoke type is presented in this chapter. Various SMC tooth designs are considered. SMC tooth design is finalized after considering the mechanical, electromagnetic, and manufacturing constraints. The rotor design is finalized based on the analysis carried out in the previous chapters which includes electromagnetic and mechanical stress analysis. The rotor is fabricated with NdFeB magnets.

The measured back EMF is 14.7 % lower than the simulated back EMF, which is due to the following reasons,

- The stator teeth experienced damage at the tooth ends, which would lead to an increase in reluctance and lowering of the air gap flux.
- The number of parallel strands in the winding for the prototype was one but two were used in the design.

- The SMC material performance in the prototype was not exactly the same as the one used in the design. The effect of lower density of the SMC prototype components and different manufacturing steps (machining) compared to traditional SMC components may have contributed to lower performance.

The prototyping and assembly of the SMC parts was challenging:

- Damage was observed on ends of the stator teeth, perhaps due to low mechanical strength of the SMC components, but also during shipping. The mechanical strength can be improved.

The motor produces 18 N-m for 170 A peak current which is 10 % lower than the simulated torque. However, the current is increased to 195 A to obtain the required torque. A novel spoke-type PMSM with a newly developed SMC grade from RTMP was designed, built and tested successfully. The prototyped SMC motor has a 20 % higher torque density in terms of motor volume than a simulated laminated stator motor for the same specification, assuming natural convection.

This study suggests that the SMC stator cores can be utilized to improve the torque density, copper fill factor and allows a 3D flux path. Development of the SMC powder quality is continuing in many industries to address the remaining challenges that could limit the development of the motors with SMC materials.

8.2. Future Work

This thesis has shown that the SMC stator cores can be utilized for traction applications with 3D flux path and high copper fill factor to obtain better electromagnetic performances. After completing this research program, there are several areas that can be identified as attractive targets for future research.

- One potential area for future research is exploring the impact of using a combination of multi-magnetic materials, such as SMC and lamination steel, for the stator core and evaluating the machine's performance across different speeds. It may be more feasible to use lamination steel in cases where manufacturing an SMC core would be complex.

- To investigate the effectiveness of the radial flux design, axial and transverse flux machines can be designed for the same specifications with SMC materials to compare the performance of all three machines.
- Coldspray magnets can be investigated with various interior PM shapes to utilize the advantage of coldspray magnets. If it becomes easier and more cost-effective to magnetize cold spray magnets, it could also enable the production of a rotor with a cobra shape.
- Interior PMSM with higher poles can be manufactured with SMC stator cores to compare the lower pole PMSM designs to prove the advantage of SMC at higher frequencies.

References

Chapter 1

1. W. Xu, J. Zhu, Y. Zhang, Y. Wang, and G. Sun. Characterization of advanced drive system for hybrid electric vehicles. In *Electrical Machines and Systems (ICEMS), 2010 International Conference on*, pages 487–492, Oct 2010.
2. A. M. El-Refaie, "Motors/generators for traction/propulsion applications: A review," in *IEEE Vehicular Technology Magazine*, vol. 8, no. 1, pp. 90-99, March 2013, doi: 10.1109/MVT.2012.2218438.
3. EMERF Steel Laminations – Third Edition.
4. Soft Magnetic Composites In Novel Designs of Electrical Traction Machines
5. Lamarre, J., Bernier, F. Permanent Magnets Produced by Cold Spray Additive Manufacturing for Electric Engines. *J Therm Spray Tech*, 2019, 1709-1717

Chapter 2

6. EMERF Steel Laminations – Third Edition.
7. Y. Enomoto, M. Ito, H. Koharagi, R. Masaki, S. Ohiwa, C. Ishihara, and M. Mita, "Evaluation of experimental permanent-magnet brushless motor utilizing new magnetic material for stator core teeth," *IEEE Transactions on Magnetics*, vol. 41, no. 11, pp. 4304–4308, Nov 2005.
8. F. Libert and J. Souldard, "Manufacturing Methods of Stator Cores with Concentrated Windings," 2006 3rd IET International Conference on Power Electronics, Machines and Drives - PEMD 2006, The Contarf Castle, Dublin, Ireland, 2006, pp. 676-680.
9. A. Boehm and I. Hahn, "Comparison of soft magnetic composites (SMCs) and electrical steel," *2012 2nd International Electric Drives Production Conference (EDPC)*, Nuremberg, 2012, pp. 1-6, doi: 10.1109/EDPC.2012.6425119.
10. C. Chiang *et al.*, "Effects of Annealing on Magnetic Properties of Electrical Steel and Performances of SRM After Punching," in *IEEE Transactions on Magnetics*, vol. 50, no. 11, pp. 1-4, Nov. 2014, Art no. 8203904, doi: 10.1109/TMAG.2014.2329708.

11. W. Soong and T. J. E. Miller, "Field weakening performance of brushless synchronous AC motor drives," *Proc. IEE—Elect. Power Appl.*, vol. 141, no. 6, pp. 331–340, Nov. 1994.
12. A. M. EL-Refaie and T. M. Jahns, "Optimal flux weakening in surface PM machines using fractional-slot concentrated windings," in *IEEE Transactions on Industry Applications*, vol. 41, no. 3, pp. 790-800, May-June 2005, doi: 10.1109/TIA.2005.847312.
13. J. Wang, X. Yuan and K. Atallah, "Design Optimization of a Surface-Mounted Permanent-Magnet Motor With Concentrated Windings for Electric Vehicle Applications," in *IEEE Transactions on Vehicular Technology*, vol. 62, no. 3, pp. 1053-1064, March 2013, doi: 10.1109/TVT.2012.2227867
14. Y. Fan, S. Chen, C. Tan and M. Cheng, "Design and investigation of a new outer-rotor IPM motor for EV and HEV in-wheel propulsion," *2016 19th International Conference on Electrical Machines and Systems (ICEMS)*, Chiba, 2016, pp. 1-4.
15. Lamarre, JM., Bernier, F. Permanent Magnets Produced by Cold Spray Additive Manufacturing for Electric Engines. *J Therm Spray Tech* 28, 1709–1717 (2019). <https://doi.org/10.1007/s11666-019-00917-6>
16. M. Ibrahim, F. Bernier and J. -M. Lamarre, "A Novel Toroidal Permanent Magnet Motor Structure with High Torque Density and Enhanced Cooling," *2020 IEEE Energy Conversion Congress and Exposition (ECCE)*, Detroit, MI, USA, 2020, pp. 4044-4049, doi: 10.1109/ECCE44975.2020.9235406.
17. S. Singh and P. Pillay, "Sinusoidal Shaped Surface Permanent Magnet Motor Using Cold Spray Additive Manufacturing," *2020 IEEE Energy Conversion Congress and Exposition (ECCE)*, Detroit, MI, USA, 2020, pp. 2089-2094, doi: 10.1109/ECCE44975.2020.9235788.
18. JMAG-Designer, (2018-2019), [Offline], Available: <https://www.jmag-international.com/products/jmag-designer/>

Chapter 3

19. Benchmarking Electric Vehicles and Hybrid Electric Vehicles, FY 2016 Annual Progress Report for Electric Drive Technologies Program
20. Hendershot Green Book, Design of Brushless Permanent-Magnet Machines, 2010
21. Evaluation Of 2005 Honda Accord Hybrid Electric Drive System, ORNL, September 2006
22. Duane Hanselman, Brushless Permanent Magnet Motor Design, 2nd Edition.
23. El-Refaie, A.; Jahns, T.; McCleer, P.; McKeever, J. Experimental verification of optimal flux weakening in surface PM Machines using concentrated windings. *IEEE Trans. Ind. Appl.* 2006, 42, 443–453.

Chapter 4

24. N. Bianchi, S. Bolognani and P. Frare, "Design criteria for high-efficiency SPM synchronous motors," in *IEEE Transactions on Energy Conversion*, vol. 21, no. 2, pp. 396-404, June 2006, doi: 10.1109/TEC.2005.853720.
25. E. Pošković, L. Ferraris, F. Franchini, A. Cavagnino and M. A. Grande, "SMC Materials in Electrical Machine Prototypes," 2019 IEEE International Electric Machines & Drives Conference (IEMDC), 2019, pp. 2042-2047, doi: 10.1109/IEMDC.2019.8785066.
26. S. Kahourzade, N. Ertugrul and W. L. Soong, "Investigation of emerging magnetic materials for application in axial-flux PM machines," 2016 IEEE Energy Conversion Congress and Exposition (ECCE), 2016, pp. 1-8, doi: 10.1109/ECCE.2016.7855218.
27. A. G. Jack et al., "Permanent magnet machines with powdered iron cores and pre-pressed windings," Conference Record of the 1999 IEEE Industry Applications Conference. Thirty-Forth IAS Annual Meeting (Cat. No.99CH36370), 1999, pp. 97-103 vol.1, doi: 10.1109/IAS.1999.799934.
28. Y. Huang, Q. Hu, J. Zhao, J. Zhu and Y. Guo, "Comparative Study of High-Speed PM Motors with Laminated Steel and Soft Magnetic Composite Cores," 2007 *IEEE Industry Applications Annual Meeting*, 2007, pp. 67-72, doi: 10.1109/07IAS.2007.81.

29. A. Jack, "Experience with using soft magnetic composites for electrical machines," IEE Half-Day Colloquium on New Magnetic Materials - Bonded Iron, Lamination Steels, Sintered Iron and Permanent Magnets (Digest NMo. 1998/259), 1998, pp. 3/1-3/4, doi: 10.1049/ic:19980331.
30. W. Zhao, T. A. Lipo and B. Kwon, "Material-Efficient Permanent-Magnet Shape for Torque Pulsation Minimization in SPM Motors for Automotive Applications," in IEEE Transactions on Industrial Electronics, vol. 61, no. 10, pp. 5779-5787, Oct. 2014, doi: 10.1109/TIE.2014.2301758.
31. A. Pouramin, R. Dutta and M. F. Rahman, "Design Optimization of a Spoke-Type FSCW IPM Machine to Achieve Low Torque Ripple and High Torque Density Under a Wide Constant Power Speed Range," 2018 IEEE Energy Conversion Congress and Exposition (ECCE), 2018, pp. 6914-6921, doi: 10.1109/ECCE.2018.8558066.
32. S. J. Galioto, P. B. Reddy and A. M. EL-Refaie, "Effect of magnet types on performance of high speed spoke interior permanent magnet machines designed for traction applications," 2014 IEEE Energy Conversion Congress and Exposition (ECCE), 2014, pp. 4513-4522, doi: 10.1109/ECCE.2014.6954019.
33. Y. Wang, R. Qu, L. Wu, H. Fang and D. Li, "Reduction of sub-harmonic effect on the fractional slot concentrated winding interior PM machines by using spoke-type magnets," 2015 IEEE International Electric Machines & Drives Conference (IEMDC), 2015, pp. 1858-1863, doi: 10.1109/IEMDC.2015.7409317.
34. S. -I. Kim, J. Cho, S. Park, T. Park and S. Lim, "Characteristics comparison of a conventional and modified spoke-type ferrite magnet motor for traction drives of low-speed electric vehicles," 2012 IEEE Energy Conversion Congress and Exposition (ECCE), 2012, pp. 3048-3054, doi: 10.1109/ECCE.2012.6342358.
35. M. M. Rahman, K. Kim and J. Hur, "Design and Optimization of Neodymium-Free SPOKE-Type Motor With Segmented Wing-Shaped PM," in IEEE Transactions on Magnetics, vol. 50, no. 2, pp. 865-868, Feb. 2014, Art no. 7021404, doi: 10.1109/TMAG.2013.2282151.
36. K. Yoon and B. Kwon, "Optimal Design of a New Interior Permanent Magnet Motor Using a Flared-Shape Arrangement of Ferrite Magnets," in IEEE

Transactions on Magnetics, vol. 52, no. 7, pp. 1-4, July 2016, Art no. 8106504, doi: 10.1109/TMAG.2016.2524505.

37. S. Singh and P. Pillay, "Sinusoidal Shaped Surface Permanent Magnet Motor Using Cold Spray Additive Manufacturing," 2020 IEEE Energy Conversion Congress and Exposition (ECCE), 2020, pp. 2089-2094, doi: 10.1109/ECCE44975.2020.9235788.
38. A. M. EL-Refaie, "Fractional-Slot Concentrated-Windings Synchronous Permanent Magnet Machines: Opportunities and Challenges," in IEEE Transactions on Industrial Electronics, vol. 57, no. 1, pp. 107-121, Jan. 2010, doi: 10.1109/TIE.2009.2030211.
39. F. Magnussen and C. Sadarangani, "Winding factors and Joule losses of permanent magnet machines with concentrated windings," IEEE International Electric Machines and Drives Conference, 2003. IEMDC'03., 2003, pp. 333-339 vol.1, doi: 10.1109/IEMDC.2003.1211284.
40. J. Cros and P. Viarouge, "Synthesis of high performance PM motors with concentrated windings," in IEEE Transactions on Energy Conversion, vol. 17, no. 2, pp. 248-253, June 2002, doi: 10.1109/TEC.2002.1009476.
41. A. M. EL-Refaie and T. M. Jahns, "Optimal flux weakening in surface PM machines using fractional-slot concentrated windings," in IEEE Transactions on Industry Applications, vol. 41, no. 3, pp. 790-800, May-June 2005, doi: 10.1109/TIA.2005.847312.
42. JMAG-Designer, (Version 21.0), [Offline], Available: <https://www.jmag-international.com/products/jmag-designer/>

Chapter 5

43. N. Bianchi, S. Bolognani, M. D. Pre and G. Grezzani, "Design considerations for fractional-slot winding configurations of synchronous machines," in IEEE Transactions on Industry Applications, vol. 42, no. 4, pp. 997-1006, July-Aug. 2006, doi: 10.1109/TIA.2006.876070.
44. R. Dutta, L. Chong and M. F. Rahman, "Design and Experimental Verification of an 18-Slot/14-pole Fractional-Slot Concentrated Winding Interior Permanent

- Magnet Machine," in IEEE Transactions on Energy Conversion, vol. 28, no. 1, pp. 181-190, March 2013, doi: 10.1109/TEC.2012.2229281.
45. A. M. EL-Refaie and T. M. Jahns, "Optimal flux weakening in surface PM machines using fractional-slot concentrated windings," in IEEE Transactions on Industry Applications, vol. 41, no. 3, pp. 790-800, May-June 2005, doi: 10.1109/TIA.2005.847312.
 46. W. Soong and T. J. E. Miller, "Field weakening performance of brushless synchronous AC motor drives," Proc. IEE—Elect. Power Appl., vol. 141, no. 6, pp. 331–340, Nov. 1994.
 47. D. G. Dorrell, M. Hsieh, M. Popescu, L. Evans, D. A. Staton and V. Grout, "A Review of the Design Issues and Techniques for Radial-Flux Brushless Surface and Internal Rare-Earth Permanent-Magnet Motors," in IEEE Transactions on Industrial Electronics, vol. 58, no. 9, pp. 3741-3757, Sept. 2011, doi: 10.1109/TIE.2010.2089940.
 48. A. Pouramin, R. Dutta and M. F. Rahman, "Design Optimization of a Spoke-Type FSCW IPM Machine to Achieve Low Torque Ripple and High Torque Density Under a Wide Constant Power Speed Range," 2018 IEEE Energy Conversion Congress and Exposition (ECCE), 2018, pp. 6914-6921, doi: 10.1109/ECCE.2018.8558066.
 49. Thomas A. Lipo "Introduction to AC machine design" 2017.
 50. Evaluation Of The 2010 Toyota Prius Hybrid Synergy Drive System (<https://info.ornl.gov/sites/publications/files/Pub26762.pdf>)
 51. Q. Ma, A. El-Refaie and B. Lequesne, "Low-Cost Interior Permanent Magnet Machine With Multiple Magnet Types," in IEEE Transactions on Industry Applications, vol. 56, no. 2, pp. 1452-1463, March-April 2020, doi: 10.1109/TIA.2020.2966458.
 52. EMERF Laminations steels, Second Printing, edited by Steve Sprague, USA.
 53. Rio Tinto, Montreal, Canada (<https://www.riotinto.com/can/>)
 54. Kwang Hee Nam, "AC motor control and applications" CRC Press, 2010.
 55. Evaluation Of 2005 Honda Accord Hybrid Electric Drive System (<https://www.osti.gov/servlets/purl/891260>)

Chapter 6

56. J. R. Hendershot & T.J.E Miller, "Design of Brushless Permanent Magnet Machines".
57. A. Krings, A. Boglietti, A. Cavagnino and S. Sprague, "Soft Magnetic Material Status and Trends in Electric Machines," in *IEEE Transactions on Industrial Electronics*, vol. 64, no. 3, pp. 2405-2414, March 2017, doi: 10.1109/TIE.2016.2613844.
58. Y. Huang, Q. Hu, J. Zhao, J. Zhu and Y. Guo, "Comparative Study of High-Speed PM Motors with Laminated Steel and Soft Magnetic Composite Cores," *2007 IEEE Industry Applications Annual Meeting*, 2007, pp. 67-72, doi: 10.1109/07IAS.2007.81.
59. J. G. Zhu, Y. G. Guo, Z. W. Lin, Y. J. Li, and Y. K. Huang, "Development of PM transverse flux motors with soft magnetic composite cores," *IEEE Transactions on Magnetics*, vol. 47, pp. 4376-4383, 2011.
60. C. Chen et al., "Cogging torque minimization of SMC motor with axially tapered stator tooth tip," *2017 20th International Conference on Electrical Machines and Systems (ICEMS)*, 2017, pp. 1-4, doi: 10.1109/ICEMS.2017.8056365.
61. Yiping Dou, Youguang Guo and Jianguo Zhu, "Investigation of motor topologies for SMC application," *2007 International Conference on Electrical Machines and Systems (ICEMS)*, 2007, pp. 695-698, doi: 10.1109/ICEMS12746.2007.4412173.
62. C. Liu, G. Lei, T. Wang, Y. Guo, Y. Wang and J. Zhu, "Comparative Study of Small Electrical Machines With Soft Magnetic Composite Cores," in *IEEE Transactions on Industrial Electronics*, vol. 64, no. 2, pp. 1049-1060, Feb. 2017, doi: 10.1109/TIE.2016.2583409.
63. G. Cvetkovski, L. Petkovska, M. Cundev and S. Gair, "Improved design of a novel PM disc motor by using soft magnetic composite material," *2002 IEEE International Magnetics Conference (INTERMAG)*, 2002, pp. DQ4-, doi: 10.1109/INTMAG.2002.1001049.

64. R. Di Stefano and F. Marignetti, "Electromagnetic Analysis of Axial-Flux Permanent Magnet Synchronous Machines With Fractional Windings With Experimental Validation," in *IEEE Transactions on Industrial Electronics*, vol. 59, no. 6, pp. 2573-2582, June 2012, doi: 10.1109/TIE.2011.2165458.
65. YouGuang Guo, Jian Guo Zhu, P. A. Watterson and Wei Wu, "Development of a PM transverse flux motor with soft magnetic composite core," in *IEEE Transactions on Energy Conversion*, vol. 21, no. 2, pp. 426-434, June 2006, doi: 10.1109/TEC.2005.860403.
66. J. G. Zhu, Y. G. Guo, Z. W. Lin, Y. J. Li and Y. K. Huang, "Development of PM Transverse Flux Motors With Soft Magnetic Composite Cores," in *IEEE Transactions on Magnetics*, vol. 47, no. 10, pp. 4376-4383, Oct. 2011, doi: 10.1109/TMAG.2011.2157320.
67. A. G. Jack, B. C. Mecrow, C. P. Maddison and N. A. Wahab, "Claw pole armature permanent magnet machines exploiting soft iron powder metallurgy," 1997 *IEEE International Electric Machines and Drives Conference Record*, 1997, pp. MA1/5.1-MA1/5.3, doi: 10.1109/IEMDC.1997.604062.
68. Y. Guo, J. Zhu and D. G. Dorrell, "Design and Analysis of a Claw Pole Permanent Magnet Motor With Molded Soft Magnetic Composite Core," in *IEEE Transactions on Magnetics*, vol. 45, no. 10, pp. 4582-4585, Oct. 2009, doi: 10.1109/TMAG.2009.2022745.
69. A. G. Jack et al., "Permanent magnet machines with powdered iron cores and pre-pressed windings," *Conference Record of the 1999 IEEE Industry Applications Conference. Thirty-Forth IAS Annual Meeting (Cat. No.99CH36370)*, 1999, pp. 97-103 vol.1, doi: 10.1109/IAS.1999.799934.
70. G. S. Liew, E. C. Y. Tsang, N. Ertugrul, W. L. Soong, D. Atkinson and D. B. Gehlert, "Analysis of a Segmented Brushless PM Machine Utilising Soft Magnetic Composites," *IECON 2007 - 33rd Annual Conference of the IEEE Industrial Electronics Society*, 2007, pp. 1268-1273, doi: 10.1109/IECON.2007.4460211.
71. Y. Ling Lim, W. L. Soong, N. Ertugrul and S. Kahourzade, "Embedded Stator End-Windings in Soft Magnetic Composite and Laminated Surface PM

- Machines," 2018 IEEE Energy Conversion Congress and Exposition (ECCE), 2018, pp. 5387-5394, doi: 10.1109/ECCE.2018.8558168.
72. Bo Zhang, "Soft Magnetic Composites in Novel Designs of Electrical Traction Machines", PhD thesis, KIT, Germany.
73. A. Reinap and M. Alakula, "Impact of Soft Magnetic Material on Construction of Radial Flux Electrical Machines," in IEEE Transactions on Magnetics, vol. 48, no. 4, pp. 1613-1616, April 2012, doi: 10.1109/TMAG.2011.2173566.
74. Gao Qilong Xie, Xhen Wang Yong, Permanent magnetic brushless based on soft magnetic materials, Chinese Patent no : CN206506370U.
75. Boehm and I. Hahn, "Comparison of soft magnetic composites (SMCs) and electrical steel," 2012 2nd International Electric Drives Production Conference (EDPC), 2012, pp. 1-6, doi: 10.1109/EDPC.2012.6425119.
76. M. Ibrahim et al., "Selection of Soft Magnetic Composite Material for Electrical Machines using 3D FEA Simulations," 2021 IEEE Energy Conversion Congress and Exposition (ECCE), 2021, pp. 3860-3865, doi: 10.1109/ECCE47101.2021.9595938.
77. JMAG Version 21.0 Material library, JSOL Corporation, Tokyo, Japan, 2022.
78. D. Staton, A. Boglietti and A. Cavagnino, "Solving the more difficult aspects of electric motor thermal analysis in small and medium size industrial induction motors," in IEEE Transactions on Energy Conversion, vol. 20, no. 3, pp. 620-628, Sept. 2005, doi: 10.1109/TEC.2005.847979.
79. EMERF Laminations steels, Second Printing, edited by Steve Sprague, USA.
80. Rio Tinto, Montreal, Canada (<https://www.riotinto.com/can/>)
81. N. Bianchi, S. Bolognani and E. Fornasiero, "An Overview of Rotor Losses Determination in Three-Phase Fractional-Slot PM Machines," in IEEE Transactions on Industry Applications, vol. 46, no. 6, pp. 2338-2345, Nov.-Dec. 2010, doi: 10.1109/TIA.2010.2070472.
82. N. Bianchi, S. Bolognani, M. D. Pre and G. Grezzani, "Design considerations for fractional-slot winding configurations of synchronous machines," in IEEE Transactions on Industry Applications, vol. 42, no. 4, pp. 997-1006, July-Aug. 2006, doi: 10.1109/TIA.2006.876070.

83. J. D. Ede, K. Atallah, G. W. Jewell, J. B. Wang and D. Howe, "Effect of Axial Segmentation of Permanent Magnets on Rotor Loss in Modular Permanent-Magnet Brushless Machines," in *IEEE Transactions on Industry Applications*, vol. 43, no. 5, pp. 1207-1213, Sept.-oct. 2007, doi: 10.1109/TIA.2007.904397.

Chapter 7

84. Y. Guo, G. Lei, J. Zhu and D. H. Pham, "Performance analysis of a permanent magnet SMC transverse flux motor with multiobjective optimization strategy," 2012 22nd Australasian Universities Power Engineering Conference (AUPEC), Bali, Indonesia, 2012, pp. 1-6.
85. G. Volpe, M. Popescu, F. Marignetti and J. Goss, "AC Winding Losses in Automotive Traction E-Machines: A New Hybrid Calculation Method," 2019 IEEE International Electric Machines & Drives Conference (IEMDC), San Diego, CA, USA, 2019, pp. 2115-2119, doi: 10.1109/IEMDC.2019.8785409.
86. 7G. Venturini, G. Volpe, M. Villani and M. Popescu, "Investigation of Cooling Solutions for Hairpin Winding in Traction Application," 2020 International Conference on Electrical Machines (ICEM), Gothenburg, Sweden, 2020, pp. 1573-1578, doi: 10.1109/ICEM49940.2020.9271026.
87. 8Y. Zhao, D. Li, T. Pei and R. Qu, "Overview of the rectangular wire windings AC electrical machine," in *CES Transactions on Electrical Machines and Systems*, vol. 3, no. 2, pp. 160-169, June 2019, doi: 10.30941/CESTEMS.2019.00022.
88. J. -H. Choi et al., "Design of High Power Permanent Magnet Motor With Segment Rectangular Copper Wire and Closed Slot Opening on Electric Vehicles*," in *IEEE Transactions on Magnetics*, vol. 46, no. 9, pp. 3701-3704, Sept. 2010, doi: 10.1109/TMAG.2010.206038
89. T. Zou et al., "A Comprehensive Design Guideline of Hairpin Windings for High Power Density Electric Vehicle Traction Motors," in *IEEE Transactions on Transportation Electrification*, vol. 8, no. 3, pp. 3578-3593, Sept. 2022, doi: 10.1109/TTE.2022.3149786.